

An In Vitro Investigation of a Novel, Two-Piece Zirconia Dental
Implant System

Ahmad Abdel Halim Abdel Hadi Jum'ah

Submitted in accordance with the requirements of

Integrated degree of Doctor of Philosophy and Master of Science
in Oral Sciences (Clinical)

The University of Leeds

School of Dentistry

June 2015

The candidate confirms that the work submitted is his own, except where work which has formed part of jointly authored publications has been included. The contribution of other authors was limited to provision of photographs of clinical cases presented in Chapter 1 and 5 which were published along with critical review of literature performed by the candidate as explicitly indicated below:

- 1- Jum'ah A., Beekmans B., Wood D., and Maghaireh H. Zirconia Implants: The New Arrival in the Armoury of Successful Aesthetic Implant Dentistry. *Smile dental journal*, 7(2), 2012.
- 2- Jum'ah A., Maghaireh H., and Wood D. Implant Dentistry: From Titanium to Zirconia. *Smile dental journal*, 6(2), 2011
- 3- Jum'ah A., Zirconia All-Ceramic Restorations: Do They Perform Well?. *Smile dental journal*, 6(2), 2011

The candidate confirms that appropriate credit has been given within the thesis where reference has been made to the work of others. This copy has been supplied on the understanding that it is copyright material and that no quotation from the thesis may be published without proper acknowledgement.

© 2015 The University of Leeds and Ahmad Abdel Halim Jum'ah

Dedications and Acknowledgements

To the man who I will cherish until the last day of my life...To every drop of sweat came off your forehead while working to put food on our table...To every moment of desperation while being battered in this hard life for your family ...To the years of your illness for our wellbeing... To the man who always believed in me... To dad... May your soul rest in eternal peace... This day would have been much happier if you were here... I am sure you are in a better place looking at me, feeling proud as your little boy kept his word and got his Masters and PhD degrees before the age of 30... Rest in peace, I am a real Doctor now, although a very different one from whom you said good bye to for the last time in 2010... As you always said, you can write a book about what you did not know, and here it is!... 315 pages of world-class and cutting edge work that I already presented across the entire world.

For my best ladies, mum, my other half and dear sister... For brothers; Khalid, Rami and Hisham... This would have not happened without your endless love and support... For my nieces and nephews, prince Omar, cheeky Ali, smiley Halim, handsome Faris, the Ironman Sami, smart Saleh, attractive, English (blond) Aboodi and their undisputed Queen, her majesty Eleen... Buying you gifts have probably been the most enjoyable time during my stay in the UK!

I would like to offer my sincerest gratitude to Professor David Wood... By the time we first met, I have never ever looked at something under a microscope... Look at me now, generating electron diffraction patterns for submicron crystals and showing Debye-Scherrer rings from Synchrotron... Would sound like Star Trek to me few years ago... Thanks for everything; help, support, consideration and proof reading papers and chapters at 3:00 AM... I simply could not wish for a better or friendlier supervisor.

I also acknowledge with gratitude University of Leeds' staff members in; School of Dentistry, Institute of Material's Research, School of Mechanical Engineering, Leeds Electron Microscopy and Spectroscopy Centre, School of Mathematics and Institute of Medical and Biological Engineering... Dr Nigel Bubb, Dr Matthew Tomlinson, Dr El Mostafa Raif, Dr Tim Comyn (the crystallography guru), Dr Andrew Keeling (the digital master), Dr Chun Wang, Dr Nagitha Wijayathunga, Dr Wieland Dietrich, Dr Michael Bryant, Dr Maria Katsikogianni, Dr Scott Finlay, Dr Marina

Malinowski, Dr William Vickers, Ms Jackie Hudson, Mr John Harrington, Dr Mike Ward and Mr Stuart Micklethwaite; I attribute what I achieved to your encouragement and support. Thanks for your help during my experimental work whilst allowing me the room to work in my own way... Dr Nicholas Silikas and Dr Hassan Maghiereh from University of Manchester, Dr Richard Langford from University of Cambridge, Dr Chris Parmenter from University of Nottingham and Dr Howie Gluckman from Implant and Aesthetic Academy; thank you all for your valuable help and input in this work.

I would like also to extend my heartfelt thanks to my clinical mentors who I worked with during the last five years, Dr Lynn Gutteridge, Dr Brian Nattress, Professor Paul Brunton, Mr Peter Nixon and Mr. Paul Gregory... All nurses and staff members in Restorative Dentistry and Clinical Photography Departments...

I also cannot forget the administrative staff at the Oral Biology Department. Claire Godfery, Ruth Kayman, Julie McDermott, Adam Steele and Gregory Baugh; thanks for bringing order to my split time between the department and hospital... Thanks for managing grants, accounts, finance, conferences and travel bookings. I will miss you when I start doing all of this by myself now...

Greatest thanks to the White Implant Development Corp. represented by Mr. Peter Kievet and Dr Bart Beekman for their generous support of the project, providing materials, grants and consultancy which allowed the production of such piece of work... I am looking forward for further cooperation in the near future.... Thanks also go to Mr Tim Palmer from Instron Company and Mr Anthony Scarratt from Struers Ltd.

In my daily work I have been blessed with a friendly and cheerful group of friends, Dr Mehrnoosh Rezapour, Dr Hani Nazal, Jihad El-Sayed, Chris Serna, Hussien EL-Enizzi and Yousef Al-Hasawi... Honestly, you were a good companion on an otherwise exhausting environment.

Special thanks to the primary sponsors for my clinical training, MSc and PhD degrees, The Jordan University of Science and Technology.

Abstract

Implant treatment is currently overriding other prosthetic solutions especially in the case of replacing anterior teeth in the aesthetic zone. Zirconia ceramics exhibit promising aesthetic, periointegration and antibacterial properties that may overcome critical drawbacks associated with titanium based dental implants. They also possess distinctive mechanical properties due to the unique transformation toughening mechanism. However, the effects of low-temperature degradation (*LTD*) or ageing on the durability of the material is of a major concern. Additionally, the currently available one-piece and two-piece zirconia dental implant designs exhibit sub-standard performance.

This study aimed to investigate ageing, mechanical properties and biofunctional characteristics of a new implant system with a novel biomechanical design. The proposed design utilises a relatively low-strength glass fibre composite abutment bonded with resin cement to an injection-moulded, soft tissue level, acid-etched zirconia implant.

Hydrothermal treatment was used to simulate *in vivo* ageing. A battery of complimentary crystallographic and imaging studies was used to characterise hydrothermally- and stress-induced phase transformation. Additionally, the effect of ageing on basic mechanical properties of standard samples was investigated at the macro-, micro- and nano-scales. Dynamic fatigue was performed in order to determine durability and reliability of various components and interfaces of the design under simulated clinical conditions. The acid-etched zirconia surface (*MDS*) was compared to a high-performance, mechanically and chemically modified titanium surface in terms of; surface topography, biocompatibility and cell biofunctional response.

The results of this study indicated that hydrothermal ageing resulted in phase transformation that was localised to the surface of the material without any involvement of the bulk. No evidence of extensive cracking was detected as a result of the used ageing conditions. The aged samples exhibited static mechanical properties that were not significantly different from the control group apart from marginal decreases in surface hardness. The implant samples restored with two different crown materials did not exhibit any premature failures. The engineered weak connection seemed to favour retrievable failures especially when low strength crown material was

used to restore the implants. The studied **MDS** zirconia surface exhibited moderate surface roughness and high biocompatibility when tested with human osteoblast-like cells and human gingival fibroblasts. Cell attachment and bone formation capacity of cells were similar or marginally higher in cells cultured on **MDS** surface when compared to titanium (**SLActive-like**) counterpart.

Within the limitations of this study, it can be concluded that the studied zirconia material was not drastically affected by hydrothermal ageing and thereby, *in vivo LTD* may be not of a concern whilst using such material. The current implant design may withstand long-term functional forces in the anterior region of the oral cavity. The **MDS** surface may reduce the time required for bone and soft tissue healing which is essential for clinical cases require immediate provisionalisation and/or early loading. Soft tissue remodelling may be of a less concern owing to the high soft tissue attachment (periointegration) capacity of the studied **MDS** zirconia surface.

Table of Contents

Acknowledgements & Dedication	Error! Bookmark not defined.
Abstract	III
Table of Contents	V
List of Figures	VIII
List of Tables.....	XIV
List of Abbreviations.....	XVI
<i>Chapter1: General Introduction</i>	1
1.1 Development of alternative implant materials: factors driving this trend	2
1.1.1 Aesthetic challenges with <i>cpTi</i>	2
1.1.2 Health related issues with <i>cpTi</i>	4
1.1.3 Metal-free prosthetic reconstructions	4
1.1.4 Breakthroughs in bioceramics' development.....	5
1.2 Ceramics in dental implantology.....	5
1.2.1 Zirconia based dental ceramics	6
1.2.1.1 Zirconium as mineral and zirconium oxide (zirconia).....	6
1.2.1.2 Zirconia as a bioceramic in dental implantology	8
1.3 Thesis aims and objectives	16
<i>Chapter 2: Crystallographic Analysis and Ageing Studies</i>	17
2.1 Introduction	17
2.1.1 Physicochemical and microstructural features of <i>LTD</i>	22
2.2 <i>LTD</i> kinetics.....	27
2.3 Macroscopic consequences of <i>LTD</i> on surgical implants.....	29
2.4 <i>In vitro</i> simulation of <i>LTD</i> process	30
2.5 Initial material characterisation	31
2.6 Ageing identification and quantification: Experimental techniques and results	33
2.6.1 <i>XRD</i> on discs and implants	33
2.6.2 Raman spectroscopy on discs and implants	49
2.6.3 Synchrotron diffraction on discs and implants.....	60
2.6.4 Direct characterisation and imaging techniques.....	63
2.6.4.1 White light interferometry or optical profilometry	63

2.6.4.2	Scanning electron microscopy	67
2.6.4.3	Transmission electron microscopy	77
2.7	Discussion	81
<i>Chapter 3: Mechanical Studies.....</i>		96
3.1	Introduction	96
3.2	Experimental procedures and results: zirconia discs.....	98
3.2.1	Accelerated <i>in vitro</i> ageing	98
3.2.2	Biaxial flexural strength.....	98
3.2.3	Edge fracture strength	107
3.2.4	Microhardness.....	112
3.2.5	Nanoindentation.....	119
3.3	Experimental procedures and results: implant samples	125
3.3.1	Accelerated <i>in vitro</i> ageing	125
3.3.2	Dynamic fatigue.....	125
3.3.2.1	Sample preparation	131
3.3.2.2	Dynamic fatigue test protocol.....	136
3.3.2.3	Post-fatigue fracture strength.....	139
3.4	Discussion	146
<i>Chapter 4: Surface Characterisation and Biological Assessment.....</i>		160
4.1	Introduction	160
4.1.1	Osseointegration	161
4.1.1.1	Factors determine the success of osseointegration	165
4.1.1.1.1	Biocompatibility of the implant material	165
4.1.1.1.2	Implant design.....	167
4.1.1.1.3	Surface topography	170
4.1.2	Soft tissue integration (Periointegration)	172
4.1.2.1	Factors determine the success of periointegration	175
4.1.2.1.1	Biocompatibility of the transmucosal material	175
4.1.2.1.2	Inflammatory status within biologic width	177
4.1.2.1.3	Surface topography of the transmucosal component	177
4.1.3	Commercially available modified implant surfaces.....	179
4.2	Experimental Procedures and Results.....	181
4.2.1	Sample preparation	181
4.2.2	SEM characterisation.....	185
4.2.3	Surface roughness analysis: Confocal laser scanning microscopy ..	192

4.2.4	Water contact angle measurements	196
4.2.5	Cell proliferation and viability studies	197
4.2.5.1	Cell culture procedures	198
4.2.5.2	Assessment of cell proliferation.....	201
4.2.5.3	Assessment of cell viability using flow cytometry	204
4.2.5.4	Expression profile of genes controlling osseointegration and periointegration.....	210
4.2.5.4.1	<i>RNA</i> extraction, quantitative and qualitative analysis	211
4.2.5.4.2	Complementary DNA (cDNA) synthesis.....	214
4.2.5.4.3	<i>qRT-PCR</i> analysis of <i>HGF</i> and <i>G-292</i> cells	214
4.3	Discussion	219
<i>Chapter 5: Clinical Relevance, Conclusions and Future Work.....</i>		233
5.1	Clinical relevance	233
5.2	Conclusions	238
5.3	Future Work	240
5.3.1	Ageing and crystallographic studies	240
5.3.2	System's reliability and performance.....	241
5.3.3	Biological Studies	243
<i>Chapter 6: References.....</i>		245
Appendix A		280
Appendix B		283
Appendix C		284
Appendix D		285
Appendix E.....		287
Appendix F.....		289
Appendix G		290

List of Figures

Figure 1. Aesthetic complications with immediately placed <i>cpTi</i> dental implant.	3
Figure 2. Custom designed and manufactured zirconia abutments.	9
Figure 3. Anatomical zirconia dental implants.	11
Figure 4. ZERAMEX-T [®] tow-piece zirconia dental implant system.	14
Figure 5. Tow-piece, hybrid zirconia dental implant system.	15
Figure 6. Schematic representation of various zirconia phases and zirconia phase transition diagram.	18
Figure 7. Schematic representation of phase transformation toughening mechanism.	21
Figure 8. <i>SEM</i> and <i>EDS</i> characterisation of the studied injection-moulded <i>Y-TZP</i> implant material.	32
Figure 9. Schematic representation of Bragg's law.	35
Figure 10. Schematic representation of the used <i>XRD</i> setup.	36
Figure 11. Refinement strategy used during Rietveld analysis of <i>XRD</i> data.	37
Figure 12. Rietveld refinement of <i>XRD</i> data obtained for a representative as-received sample.	39
Figure 13. Rietveld refinement of <i>XRD</i> data obtained for a representative aged sample.	40
Figure 14. Comparative diffraction patterns of representative samples (discs) from all experimental groups.	41
Figure 15. Comparative diffraction patterns of representative as-received disc and as-received implant.	41
Figure 16. Schematic representation of <i>GIAXRD</i> setup.	45
Figure 17. Transformation depth profile along thickness of material as estimated by <i>GIAXRD</i> .	48
Figure 18. Schematic representation of Raman confocal microscopy/spectroscopy.	50
Figure 19. Reference Raman spectra for tetragonal, monoclinic and cubic phases of <i>Y-TZP</i> .	51

Figure 20. Comparative graph of Raman spectra obtained from pure tetragonal <i>Y-TZP</i> , as-received disc and implant.	53
Figure 21. Raman spectra for aged disc and implant.	54
Figure 22. Monoclinic and tetragonal phase profile along line Raman scans in machined and machined-aged groups.	55
Figure 23. Monoclinic phase map and line profile within Vickers indentation imprint on as-received sample.	57
Figure 24. Monoclinic phase mapping and profiling around Vickers indentation imprint on aged sample.	58
Figure 25. Monoclinic phase fraction Raman map across fractured surface.	59
Figure 26. Debye-Scherrer rings obtained from representative as-received (left) and aged (right) discs.	60
Figure 27. Comparative Synchrotron X-Ray diffraction obtained for representative samples from all experimental groups.	62
Figure 28. Schematic representation of 3D optical profilometers or white light interferometer.	64
Figure 29. White light interferometry for mirror-polished <i>Y-TZP</i> discs.	66
Figure 30. Schematic representation of <i>FIB-SEM</i> setup.	68
Figure 31. Stages of <i>FIB-SEM</i> processing and imaging of zirconia dental implant.	70
Figure 32. <i>FIB</i> section from as-received implant viewed <i>SEM</i> at high magnification	71
Figure 33. <i>FIB</i> created section showing loss of homogeneity of the surface crystals (→) which could be a sign of <i>t</i> → <i>m</i> .	71
Figure 34. Comparative <i>FIB-SEM</i> image for as-received (left) and aged (right) implants.	72
Figure 35. Partial ion broad beam polishing of machined zirconia sample.	73
Figure 36. High resolution <i>SEM</i> images for ion broad beam polished as-received sample.	74
Figure 37. Elemental map for as-received sample obtained using <i>EDS</i> coupled <i>SEM</i> .	75

Figure 38. High resolution <i>SEM</i> images for ion broad beam polished aged disc sample.....	76
Figure 39. <i>TEM</i> analysis of <i>FIB</i> -prepared lamella obtained from representative as-received sample.....	79
Figure 40. <i>TEM</i> analysis of <i>FIB</i> -prepared lamella obtained from representative aged sample.....	80
Figure 41. Identical X-Ray diffraction patterns for completely different compounds.....	84
Figure 42. <i>EBSD-SEM</i> texture analysis of the injection moulded <i>Y-TZP</i> .	86
Figure 43. <i>EBSD-SEM</i> phase map for mirror polished <i>Y-TZP</i> samples.....	94
Figure 44. Weibull probability plots for <i>BFS</i> data for as-received an aged samples.....	103
Figure 45. Comparative Weibull plot for <i>BFS</i> data.....	104
Figure 46. <i>SEM</i> fractography of as-received sample.....	105
Figure 47. <i>SEM</i> fractography of representative aged sample.....	106
Figure 48 Weibull probability plots for edge fracture strength test.....	109
Figure 49. <i>SEM</i> post-mortem examination of the fractured edge of a representative as-received sample.....	110
Figure 50. <i>SEM</i> post-mortem examination of the fractured edge of a representative aged sample.....	111
Figure 51. Weibull plots for Vickers hardness data for as-received and aged groups.....	115
Figure 52. Comparative Weibull plot for Vickers indentation data.....	116
Figure 53. <i>SEM</i> examination of Vickers indentation imprint on representative as-received (unpolished) sample.....	117
Figure 54. <i>SEM</i> examination of cracks associated with Vickers indentation on polished, as-received sample.....	117
Figure 55. <i>SEM</i> examination of Vickers indentation imprint on representative aged (unpolished) sample.....	118
Figure 56. Change in contrast around Vickers indentation made on polished-aged sample.....	118

Figure 57. Representative load-displacement (depth) hysteresis curves.....	122
Figure 58. Comparative graph demonstrating the load-displacement relationship for as-received and aged groups.....	123
Figure 59. Comparative plot of hardness and Young's moduli.....	124
Figure 60. Standardised glass fibre composite (Triflor [®]) abutment design.	132
Figure 61. CAD of implant supported all ceramic crowns.....	133
Figure 62. Outline of the study and different experimental groups.....	134
Figure 63. Reproduction of internal surface of the bottom fixture (sample holder) used in dynamic fatigue test.....	135
Figure 64. . Implant-abutment-crown assembly embedded in resin block	135
Figure 65. Sample mounted and loaded during dynamic fatigue test.....	136
Figure 66. Effective load-cycle curves.....	137
Figure 67. Displacement of upper loading fixture at each loading cycle during the entire dynamic fatigue test.....	137
Figure 68. Outcome of dynamic fatigue test.....	138
Figure 69. Loading apparatus displacement during fatigue test of a sample that was debonded during loading.....	138
Figure 70. Various failure modes in representative samples during post-fatigue fracture strength test.....	140
Figure 71. Comparative graph for post-fatigue fracture strength data.....	142
Figure 72. Comparative graph of post-fatigue fracture strength for samples restored with IPS e.max Press crowns.....	143
Figure 73. Comparative Weibull plot for pooled post-fatigue fracture strength data for non-aged and aged implants sustained H failure mode.....	144
Figure 74. R-Curves for various failure modes in group 1 and 3.....	145
Figure 75. R-Curves for various failure modes in group 2 and 4.....	146
Figure 76. R-curves for zirconia implants restored with GFC abutment (H) and Lava crown compared to one-piece zirconia implant (B).	159
Figure 77. Mirror polished grade II cpTi discs.....	183

Figure 78. Grade II <i>cpTi</i> discs after two acid pickling cycles .	184
Figure 79. Sandblasted <i>cpTi</i> discs with Alumina abrasive particles (250-500µm).	184
Figure 80. <i>EDS</i> spectrum of <i>ZR-M</i> zirconia surface.	185
Figure 81. <i>SEM</i> examination of <i>Zr-M</i> disc surface.	186
Figure 82. <i>SEM</i> examination of <i>MDS</i> disc surface.	188
Figure 83. <i>SEM</i> examination of Zirconia implant surface.	189
Figure 84. Comparative <i>SEM</i> views for <i>Zr-M</i> and <i>MDS</i> surfaces.	190
Figure 85. <i>EDS</i> analysis of <i>SLActive-like</i> surface.	190
Figure 86. <i>SLActive-like</i> titanium surface topography under <i>SEM</i>	191
Figure 87. Representative 3D reconstructed topographical images for <i>Zr-M</i> (left) and <i>MDS</i> (right).	195
Figure 88. Contact angle measurements for <i>Zr-M</i> (left) and <i>MDS</i> (right).	197
Figure 89. <i>HGF</i> (left) and <i>G-292</i> (right) cells used in this study at 70-80% confluence stage.	200
Figure 90. Setup of the tissue culture procedures.	200
Figure 91. Total <i>HGF</i> and <i>G-292</i> counts.	203
Figure 92. <i>HGF</i> and <i>G-292</i> doubling times.	203
Assessment of cell viability using flow cytometry	204
Figure 93. Representative flow cytometry output for <i>HGF</i> cells.	206
Figure 94. Representative flow cytometry output for <i>G-292</i> cells.	207
Figure 95. Biocompatibility of implant surfaces as per flow cytometry	208
Figure 96. Representative <i>RNA</i> electrophoresis gels.	213
Figure 97. Expression profile of <i>VCL</i> , <i>ColA1</i> , <i>FNI</i> and <i>ITGA2</i> in <i>HGF</i> cells.	217
Figure 98. Expression profile of <i>BMP-2</i> , <i>RUNX-2</i> , <i>OSCN</i> and <i>ALP</i> in <i>G-292</i> cells.	218
Figure 99. Optical profilometry of <i>MDS</i> and <i>SLActive-like</i> surfaces.	224
Figure 100. Comparative <i>SEM</i> views for implant (A) and disc (B) samples.	225

Figure 101. Comparative analysis of surface topography of <i>MDS</i> discs and implants.....	226
Figure 102. Peri-implant mucosal soft tissue remodelling a round various implants in the aesthetic zone.....	234
Figure 103. Treatment sequence and outcome of extracted upper left central incisor tooth using zirconia dental implant.....	235
Figure 104. The protective role of the engineered weak link in the implant system.....	236

List of Tables

Table 1. Commercially available zirconia dental implant systems.....	12
Table 2. Summary of outcome of Rietveld analysis for <i>XRD</i> data.....	42
Table 3. Comparison of monoclinic phase fraction as calculated by two different methods. Mean (SD).....	42
Table 4. Summary of <i>DTZ</i> in all experimental groups.....	44
Table 5. Summary of maximum X-Ray penetration depth at various incident angles.....	45
Table 6. Peaks at Raman shifts for various, pure, single phase <i>Y-TZP</i> powders.	52
Table 7. Summary of <i>Y-TZP</i> discs polishing protocol.....	64
Table 8. Summary of mean (MPa) and Weibull parameters obtained for BFS data.....	102
Table 9. Summary of mean (N) and Weibull parameters obtained for edge fracture strength data.....	108
Table 10. Summary of mean HV , penetration depth (<i>t</i>) and Weibull parameters. Mean (SD).....	115
Table 11. Summary of mean displacement or plastic depths. (SD).....	123
Table 12. Summary of hardness (<i>H</i>) and Young's modulus (<i>E_s</i>) values obtained using nanoindentation.....	124
Table 13. Summary of post-fatigue failure modes and their respective mean loads (N±SD) in all experimental groups.....	141
Table 14. Summary of Weibull parameters for post-fatigue fracture strength data (N).....	143
Table 15. Summary of results from static mechanical studies.....	148
Table 16.. Polishing stages and sequence used prior mechanical and chemical titanium surface treatment.....	182

Table 17. Roughness parameters and their definitions (Feng <i>et al.</i> , 2002).....	193
Table 18. Mean and standard deviation values of measure roughness parameters (μm) for all experimental groups.....	194
Table 19. Summary of flow cytometry data.....	209
Table 20. <i>qRT-PCR</i> amplification protocol.....	215
Table 21. Comparison of roughness parameters (μm) of implants versus <i>MDS</i> discs. Optical profilometer (OP).....	226

List of Abbreviations

•C	Celsius
μ/ρ	Mean absorption coefficient
3D	Three dimensional
Å	Angstrom
ADS	Automatic divergence slit
AFM	Atomic force microscopy
ALP	Alkaline phosphatase
ATZ	Alumina toughened zirconia
BFS	Biaxial fracture strength
BIC	Bone implant contact
BMPs	Bone morphogenetic proteins
BSE	Back scattered electron
C	Crown chipping
CAD	Computer assisted design
CAM	Computer assisted manufacturing
CCD	Computer coupled device
cDNA	Single stranded DNA
CE	Conformité Européenne
CIM	Ceramic injection moulding
CLSM	Confocal laser microscopy
cm	Centimetre
COL1A1	Collagen alpha 1 type 1
cpTi	Commercially pure titanium
CT-XRD	Computed tomography X-Ray diffraction
DMEM	Dulbecco's modified eagle medium
DMSO	Dimethyl sulfoxide
DNA	deoxyribonucleic acid

<i>DTZ</i>	Depth of transformed zone
<i>EBL</i>	External basal lamina
<i>EBS</i>	Electron back scattered diffraction
<i>EDS</i>	Electron dispersive spectroscopy
<i>EDTA</i>	Ethylenediaminetetraacetic acid
<i>E_r</i>	Reduced modulus
<i>E_s</i>	Elastic modulus
<i>ET</i>	Everhart–Thornley
<i>FAC</i>	Focal adhesion contacts
<i>FCS</i>	Flowcytometry standards
<i>FDA</i>	Food and drug administration
<i>FDS</i>	Fixed divergence slit
<i>FGF</i>	Fibroblast growth factor
<i>FIB</i>	Focused Ion Beam
<i>FNI</i>	Fibronectin
<i>g</i>	Gram
<i>G292</i>	Osteosarcoma cell line
<i>GFC</i>	Glass fibre composite
<i>GIAXRD</i>	Glancing incident angle X-Ray diffraction
<i>GPa</i>	Giga Pascal
<i>H</i>	Hardness
<i>H_i</i>	Implant head fracture (failure mode)
<i>HAADF</i>	High angle annular dark field
<i>H_{avg}</i>	Average (Swedish) height
<i>HGF</i>	Human gingival fibroblast
<i>HIF</i>	Hypoxia-inducible factors
<i>HIP</i>	Hot isostatic pressing
<i>HR</i>	Implant head fracture and crown rupture

<i>HV</i>	Vickers hardness
<i>IBL</i>	Internal basal lamina
<i>ICCD</i>	International centre of diffraction data
<i>ISE</i>	Indentation size effect
<i>ISO</i>	International standards organisation
<i>ITGA-2</i>	Integrin $\alpha 2$
<i>JE</i>	Junctional epithelium
<i>Kg</i>	Kilogram
<i>Kv</i>	Kilo Volt
<i>L</i>	Litre
<i>LSD</i>	Least significant difference
<i>LTD</i>	Low temperature degradation
<i>mA</i>	Milliampere
<i>MAJ</i>	Mehl Avrami Johnson
<i>MCP-1</i>	Monocyte Chemoattractant Protein-1
<i>MDP</i>	Methacryloyloxydecyl phosphate
<i>MDS</i>	Maxon dental surface
<i>min</i>	Minute
<i>mm</i>	Millimetre
<i>mN</i>	millinewton
<i>MPa</i>	Mega Pascal
<i>MTT</i>	Methylthiazol Tetrazolium
<i>nA</i>	nanoampere
<i>nm</i>	Nanometre
<i>NTC</i>	No template control
<i>OSCN</i>	Osteocalcin
<i>PBS</i>	Phosphate buffer saline
<i>PD(CP)</i>	Palladium constant pressure

<i>PDF</i>	Powder diffraction file
<i>PDGF</i>	Platelet derived growth factor
<i>PDL</i>	Periodontal ligament
<i>PEEK</i>	Polyether ether ketone
<i>PI</i>	Propidium iodide
<i>PIM</i>	Powder injection moulding
<i>pm³</i>	Pico meter cubic
<i>PMN</i>	polymorphonuclear leukocytes
<i>PO</i>	Preferred orientation
<i>PSZ</i>	Partially stabilised zirconia
<i>qRt-PCR</i>	Quantitative real-time polymerase chain reaction
<i>R</i>	Crown rupture
<i>R_a</i>	Arithmetical mean deviation.
<i>RNA</i>	Ribonucleic acid
<i>R_p</i>	Maximum peak height
<i>RPM</i>	Rotation per minute
<i>R_q</i>	Root-mean-square (RMS) roughness
<i>RUNX</i>	Runt-related transcription factor
<i>R_v</i>	Maximum depth of valley
<i>R_{wp}</i>	R weighted factor
<i>S</i>	Sedimentation rate
<i>Sa/S</i>	Fold increase in surface area
<i>SE</i>	Secondary electron
<i>sec</i>	Second
<i>SEM</i>	Scanning electron microscope
<i>SLA</i>	Sandblast, large grit, acid etch
<i>t→m</i>	Tetragonal to monoclinic phase transformation
<i>TEM</i>	Transmission electron microscope

<i>TGF</i>	Transformation growth factor
<i>TIMPs</i>	Tissue inhibitor of metalloproteinases
<i>TL</i>	Twin lens
<i>T-T-T</i>	Transformation, temperature and time
<i>UV</i>	Ultraviolet
<i>VCL</i>	Vinculin
<i>VEGF</i>	Vascular endothelial factor
<i>VF</i>	Vibrational frequency
V_m	Monoclinic phase volume fraction
X_m	Monoclinic Integrated intensity ratio
<i>XRD</i>	X-Ray diffraction
<i>Y-TZP</i>	Yttria tetragonal zirconia polycrystals
<i>ZTA</i>	Zirconia toughened alumina

Chapter1: General Introduction

Despite the significant improvement of oral health, quality and accessibility of health care services, according to the Adult Dental Health Survey, in 2009; the average number of lost teeth among the dentate population in the UK was reported to be as high as six teeth (Steele *et al.*, 2012). If left untreated, tooth loss may compromise the individual's oral function and ability to socialise. Traditionally, removable and fixed partial dentures were the treatment of choice to replace missing teeth. However, such prostheses have a high biological cost and long-term complications. Replacing missing teeth with osseointegrated dental implants can be regarded as the most significant breakthrough in the dental profession (Depprich *et al.*, 2012). Implant dentistry began more than four decades ago when the first dental implant was placed by Brånemark (Brånemark *et al.*, 1977, Albrektsson, 1988).

Dental implantology is the art and science of studying surgical placement and restoration of dental implants. Endosseous dental implants can be defined as “*prosthetic devices made of alloplastic materials implanted into the oral tissues beneath the mucosal, periosteal layer and within the bone to provide retention and support for a fixed or removable dental prosthesis or as substances that are placed into the jaw bone to support a fixed or removable dental prosthesis*” (The Academy of Prosthodontics, 2005).

Dental implants have revolutionised the rehabilitation and restoration of oral health in patients suffering from complete or partial edentulism. Commercially pure titanium (*cpTi*) has been and is still, the gold standard material for such implants owing to its' excellent biological, physical and mechanical properties (Albrektsson, 1988, Adell, 1990, Taborelli *et al.*, 1997, Niinomi, 1998, González, 1999, Akagawa and Abe, 2003, Abrahamsson and Cardaropoli, 2007). The outstanding long-term serviceability of this material has been proven by high quality experimental and clinical research that is well documented in the dental literature (Albrektsson, 1988, Jemt and Johansson, 2006, Simonis *et al.*, 2010). A plethora of changes involving; design features, surface treatments and placement techniques of dental implants have evolved in an attempt to improve the outcome of this treatment modality. However, these changes spared to a large extent, materials from which implants are made.

1.1 Development of alternative implant materials: factors driving this trend

Titanium implants have a long traceable record of predictable clinical performance with a cumulative success rate of 98.8% for 15 years (Lindquist *et al.*, 1996). Only recently, there has been a move toward seeking alternatives to *cpTi*. Such a trend has been driven by several interplaying factors that were summarised by Andreiotelli *et al.* (2009) into four groups:

1.1.1 Aesthetic challenges with *cpTi*

The tremendous increase in patient's demands and expectations from dental implant treatment has made clinicians not only interested in the osseointegration and survival of implants, but also concerned with the aesthetic outcome of this treatment (Heydecke, 1999, Meijer *et al.*, 2005, Zembic *et al.*, 2009). Implant dentists are also under extraordinary pressure from their patients to speed up the process of implant treatment as patients find it difficult to cope with provisional restorations, especially when it comes to replacing missing teeth within the aesthetic zone. Therefore, more dentists are now considering the use of advanced clinical techniques such as; immediate implant placement and loading via provision of a prosthetic supra-structure.

These advances, however, come at the expense of aesthetic complications as it has been found that post-extractive placement using titanium dental implants can be associated with aesthetic compromise such as wound dehiscence and mid-facial recession (Esposito *et al.*, 2010). There is strong evidence suggesting that it is possible to successfully load dental implants immediately or early after their placement in selected patients, although it has been suggested that not all clinicians may achieve optimal results. Trends suggest that immediately loaded implants fail more often than those conventionally loaded counterparts (Esposito *et al.*, 2009).

There have been significant concerns as far as stability and longevity of soft tissue aesthetics, synonymously called 'pink' aesthetics, and subsequently patient satisfaction. This type of failure is usually encountered with immediately placed and restored dental implants. Ironically, this aspect has been found to be underexposed in the dental literature (Den Hartog *et al.*, 2008, Lang *et al.*, 2012). The aesthetic complications of immediate replacement techniques are more evident in patients with thin gingival biotype who are more prone to recession. In such patients, mid-facial

recession causes greyish shimmering through the mucosa which jeopardises the aesthetic outcome and patient' satisfaction (Ugo Covani, 2004, Cosyn *et al.*, 2008, Den Hartog *et al.*, 2008). Figure 1 shows a commonly encountered aesthetic failure following immediate implant placement in the aesthetic zone. In fact, it has been shown in a recent clinical trial that more than 30% of patients who received single immediate implant treatment needed further surgical procedure namely, connective tissue grafting, after 12 months of placement due to major alveolar process remodelling and advanced midfacial recession (Cosyn *et al.*, 2012). It is worthwhile to remark that implants were placed using flapless surgery and only patients with thick gingival biotype and intact labial bone plate after extraction were included in this study.



Figure 1. Aesthetic complications with immediately placed **cpTi** dental implant.

Mid-facial, peri-implant soft tissue recession around immediately placed and provisionalised **cpTi** dental implant in the area of upper right central incisor. Cervical margin of the crown and 2-3 mm of implant head were exposed creating significant aesthetic concern for the patient 18 months after implant placement. Used with permission from Dr. Howard Gluckman.

The correction of the aforementioned aesthetic complication is possible through using different grafting procedures (Schneider *et al.*, 2011). However, there is only limited, weak evidence in the dental literature suggesting that augmentation at implant sites with soft tissue grafts is effective in increasing soft tissue thickness improving aesthetics. Furthermore, there are a limited number of randomised controlled studies showing that surgeries used to increase the height of keratinised mucosa using autografts or an animal-derived collagen matrix were able to achieve their goal. These studies also revealed that the above intervention came at the price of a worsened

aesthetic outcome not to mention the potentially serious complications and donor site morbidity following autograft harvesting (Esposito *et al.*, 2012).

1.1.2 Health related issues with *cpTi*

Unfortunately, it is no longer the case that titanium is considered as a completely bioinert material. In contrast, titanium is thought to be the ‘New Allergen’ as demonstrated by several reports and studies. Several authors reported increased prevalence of oral allergies to metals, including inert materials like gold and titanium. This was particularly evident in patients with a history of allergy to other, less noble metals. They also maintained that titanium oral implants can induce toxicity or type I or IV allergic reactions which may account for unexplained failures of dental implants in some patients (Evrard *et al.*, 2010). A histological study on retrieved titanium hip implants showed a quite strong inflammatory response to these implants and was regarded as a contributing factor for failure (Lalor, 1991). In addition, Sicilia *et al.* (2008) reported a 0.6% prevalence of allergy to titanium in patients who received dental implants and recommended allergy tests in some cases (Sicilia *et al.*, 2008).

Significant concerns have been raised recently regarding allergies and sensitisation to titanium particles released due to corrosion and wear (Koutayas *et al.*, 2009). High concentrations of titanium ions were detected locally i.e., bone in the vicinity of implants and systemically as in regional lymph nodes, internal organs, serum and urine which is potentially hazardous to human body (Black *et al.*, 1990, Kazuhisa and Iizuka, 1993, Onodera *et al.*, 1993, Jorgenson *et al.*, 1997, Jacobs *et al.*, 1998). Despite the aforementioned findings, the significance of these concerns is not clear in light of huge amount of reports that proved safety of *cpTi* for oral use. Furthermore, testing patients for titanium allergy on regular basis still cannot be easily justified (Wenz *et al.*, 2008).

1.1.3 Metal-free prosthetic reconstructions

The steadily growing concerns about the aesthetics and potential health problems associated with metal alloys resulted in an increased number of metal-phobic dental patients (Bågedahl-Strindlund *et al.*, 1997, Andreiotelli *et al.*, 2009). This has been substantiated by the constantly emerging reports correlating systemic diseases and genetic mutations to ion release from metallic restorations (Angela *et al.*, 2008, Geier *et al.*, 2011). Nowadays, it is a routine situation that clinicians face in dental

practice, where patients are reluctant to receive metallic prostheses and demanding for metal-free alternatives. This in turn, directed large attention toward developing and studying alternative ceramic implant materials.

1.1.4 Breakthroughs in bioceramic' development

Advances in biomaterials sciences allowed the production of high strength and biocompatible implantable ceramic materials. The extensive number of zirconia based ceramics is the best example on such achievement in this field. The enormous progress in the field of ceramic manufacturing technologies enabled the production of high precision biomedical implants. The introduction of Powder or Ceramic Injection Moulding (*PIM*, *CIM*) and Hot Isostatic Pressing (*HIP*) techniques were the hallmarks of this development (Andreiotelli *et al.*, 2009, Park *et al.*, 2012a). Collectively, these two factors played an important role in the growing popularity of zirconia as a bioceramic, dental implant material (Vagkopoulou *et al.*, 2009).

1.2 Ceramics in dental implantology

Bioceramics is a term that refers to medical grade ceramic materials that can be used as implantable devices in the human body. The last half century witnessed unsurpassed progress in the field of development and innovation of ceramic implants. The large number of patents and research publications proposing or investigating such bioceramics is a strong indication on the substantial increase of interest and achievements in this field. Ceramic implants for total hip arthroplasty procedures and ceramic oral implants are major examples on the outcome of such progress. Bioceramics vary in their chemical composition and microstructure. Poly-crystalline, ceramic oxide, glass, glass ceramic and ceramic composite are all examples of materials that can be used to manufacture bioinert or bioactive ceramic implantable devices (Best *et al.*, 2008).

Ceramic endosseous implants have been advocated, investigated and used since the late 1960's. Mono- and poly-crystalline aluminium oxide were amongst the first used ceramic materials owing to their high biocompatibility and ease of manufacturing. Cerasand[®], Tübingen[®], Bionit[®], Pfeilstift[®], Münch[®], Bioceram[®] and Sapphire[®] are examples of commercially-available ceramic alumina based implants. However, such systems are currently obsolete owing to their low flexural strength and

fracture toughness particularly the mono-crystalline form. Ironically, implant fracture was among the rarest cause of implant loss in clinical studies investigated the performance of these implants (Kawahara *et al.*, 1980, Andreiotelli *et al.*, 2009).

To date, zirconia is by far the most widely used and investigated ceramic as an alternative implant material. Zirconia based dental ceramics have been subjected to thorough investigations for use as alternative material for; orthopaedic implants, fixed dental prostheses and abutments for dental implants (Piconi and Maccauro, 1999, Andersson, 2003, Paolo Francesco Manicone, 2007). The large amount of interest in zirconia is not only attributed to high strength and biocompatibility in comparison to alumina, but also due to the its potential to outperform *cpTi* in terms of aesthetic properties, soft tissue response and antibacterial characteristics.

1.2.1 Zirconia based dental ceramics

1.2.1.1 Zirconium as mineral and zirconium oxide (zirconia)

Zirconium is a transition metal located in IVB group and period number 4 in the periodic table. The atomic number of zirconia is 40, its' atomic weight is 91.22 g/mol and its' density is 6.49 g/cm³. Zirconium melting temperature is 1,855 °C and it transforms to gaseous state at 4,409 °C. It has five naturally occurring and 28 artificial isotopes which have half-lives that greatly vary between nano-seconds and hundreds of years (Rall, 1947).

Some authors referred the origin of the word zircon to the Persian word 'Zargun' which means golden in colour. Ancient Indian tales, Roman historian and some biblical writings have also mentioned naturally occurring gems containing zirconium (Christie and Brathwaite, 1999). Pure zirconium is found in either amorphous or crystalline forms. The former is blue-black powder in which atoms are not symmetrically arranged within the metal lattice in contrast to the latter, which exists as a white powder where the atoms assume symmetrical arrangement (Christie and Brathwaite, 1999).

Zirconium dioxide (ZrO_2) (alternatively called zirconia) was discovered in 1789 upon heating Jargon (old gemstone) by the German chemist, Martin Henrich Klaproth. The Swedish chemist, Jöns Jakob Berzelius isolated the impure metallic form of zirconium in 1824 using heat treatment with a mixture of potassium and potassium

zirconium fluoride in an iron tube (Christie and Brathwaite, 1999). Herzfield (1916) managed to isolate the pure zirconium dioxide using a high concentration of hydrochloric acid to convert zirconium silicate to zirconium oxychloride octahydrate (Herzfield, 1916). In 1925, van Arkel and de Boer used iodide decomposition to prepare hafnium zirconium which is considered as pure zirconium due to the difficulty of separating the two metals from each other (Heiserman, 1991).

Zirconia assumes three structurally different crystalline phases; the first one is the monoclinic phase, in which the zirconium and oxygen atoms are arranged in a deformed prism with parallelepiped sides, the second one is the tetragonal phase, in which atoms assume straight prism with rectangular sides and the third one is the cubic phase, where the atoms are arranged in the form of straight prisms and square sides (Pittayachawan, 2008). At room temperature, the stable phase is the monoclinic that remains so until 1170 °C, after which the tetragonal phase becomes stabilised up to 2,370 °C. Above that temperature, cubic phase is predominantly stabilised till the melting point is reached (Scott, 1975).

Among the three phases, tetragonal is the preferred one in terms of structural and mechanical properties and ability to be machined in the clinical environment (Gupta *et al.*, 1977). Addition of dopants like 3% yttrium oxide (Y_2O_3) made stabilising this phase at room temperature possible (Hellmann and Stubican, 1983a). However, yttria partially stabilised tetragonal zirconia polycrystals (***Y-TZP***) is a metastable compound, i.e. it may undergo phase transformation when subjected to certain stimuli. In essence, this describes the basis of the unique toughening mechanism of partially stabilised zirconia compounds which is called transformation toughening.

When subjected to heat, cracks, grinding, or sandblasting, the apparently stable ***Y-TZP*** undergoes transformation to the monoclinic phase. This process is accompanied by 3-5% volume expansion of the crystals which induces compressive stresses within the crystalline lattice that act as crack stoppers. This transformation is said to be martensitic i.e. doesn't affect dimensional stability of the material. It is proved to have a major contribution to the outstanding mechanical properties of the so-called 'Ceramic Steel' (Garvie *et al.*, 1975).

1.2.1.2 Zirconia as a bioceramic in dental implantology

The high strength and exceptional biocompatibility qualified zirconia to be one of the leading biomaterials or bioceramics. The earliest work describing the first biomedical application of zirconia as a surgical implant was in 1969 by Helmer and Driskell (Helmer and Driskell, 1969). In dentistry, zirconia was first used for endodontic posts or high strength extra-coronal, crown and bridge restorations. Later on, implant dentistry witnessed a surge in the use of zirconia as a transmucosal abutment material. This has been a direct result of the introduction and notable progress in computer assisted design and computer assisted manufacturing (*CAD-CAM*) technology.

Functional parameters are no longer the sole determinants of implant success. Great attention has been drawn to the aesthetic outcome of such treatment modality as aesthetics may be the chief and only patient' complaint (Chang *et al.*, 1999). The introduction of zirconia abutments offered improved mechanical properties, biocompatibility and radiopacity in comparison to alumina counterparts (Koutayas *et al.*, 2009). Additionally, Rimondini *et al.* (2002) concluded that zirconia surfaces accumulated significantly less bacteria when compared to titanium counterparts (Rimondini *et al.*, 2002). This *in vivo* finding has been confirmed by a human study conducted by Scarano *et al.* (2004) who utilised titanium and zirconia discs placed in the oral cavity for 24 hours (Scarano *et al.*, 2004). Furthermore, peri-implant soft tissues' response and health was found to be optimum around zirconia abutments (Brodbeck, 2003). Moreover, zirconia and titanium abutments have been clinically assessed by van Brakel *et al.* (2011) who found that there was no significant difference between the two groups. However, zirconia abutments were associated with shallower sulcus depths after three months in this study (Van Brakel *et al.*, 2011).

The fracture resistance and marginal fit of prefabricated and custom made zirconia abutments have been investigated by a number of *in vitro* and clinical studies. In their chewing simulation study, Butz *et al.* (2005) compared fracture strength of titanium reinforced zirconia, alumina and titanium abutments. Zirconia abutments showed fracture resistance similar to titanium controls and significantly higher than the alumina group. No screw loosening or detectable cracks could be found in the zirconia group after chewing simulation (Butz *et al.*, 2005). These findings were confirmed by

Gehrke *et al.* (2006) who concluded that zirconia abutments exceeded the established values for maximum incisal bite forces reported in the literature and maintained a tight fit inside titanium fixtures after five million chewing cycles (Gehrke *et al.*, 2006). Marginal adaptation of all-zirconia abutments and zirconia abutments with titanium inserts was found to be clinically adequate (Brodbeck, 2003).

CAD-CAM technology enabled manufacturing of custom-made all ceramic abutments and offered improved aesthetics and soft tissue integration (Koutayas *et al.*, 2009). Marginal adaptation and fracture strength of **CAD-CAM** processed abutments was found to satisfy clinical requirements (Canullo, 2006, Gehrke *et al.*, 2006). These virtually designed zirconia abutments are individually customised to accurately follow gingival contours. The finish line is placed just below the zenith of the peri-implant soft tissue for optimum final crown aesthetics (Figure 2).

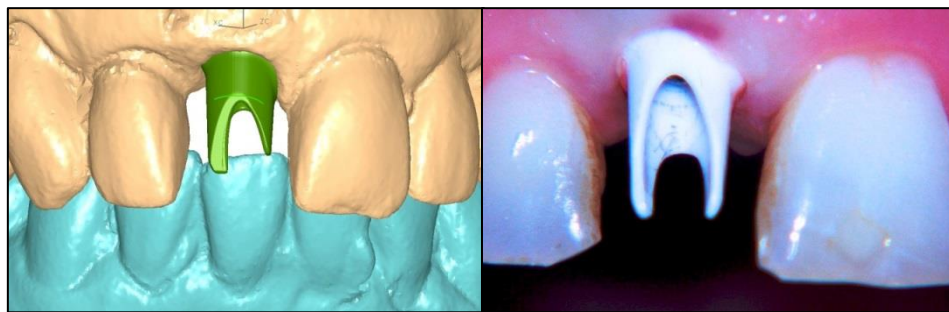


Figure 2. Custom designed and manufactured zirconia abutments.

Left, 3D **CAD** of a zirconia abutment to restore implant replacing upper right central incisor. Right, zirconia abutment fitted *in situ* with optimum margins following pre-implant soft tissue contours. Jum'ah *et al.*, (2011).

Outstanding performance of zirconia abutments has been demonstrated in a clinical study (Glauser *et al.*, 2004). A 100% four-year survival rate was reported by the authors. It is noteworthy that 70% of abutments studied, were used in implants that restored missing anterior teeth. Linkevicius & Apse (2008) systematically reviewed studies investigated zirconia abutments and only found two clinical trials that satisfied their inclusion criteria. They concluded that titanium abutments did not maintain higher bone levels when compared to zirconia counterparts (Linkevicius *et al.*, 2008). One year later, Zembic *et al.* (2009) published results of their randomised controlled trial in which 18 zirconia and 10 titanium abutments were used to restore implants in canine and posterior regions. Results showed 100% survival rate when abutments

were followed up to a mean period of 3 years. This trial also showed no difference in the biological outcome between the two groups in terms of probing depth, plaque index and bleeding on probing (Zembic *et al.*, 2009).

Nothdurft and Pospiech (2010) studied the performance of zirconia abutments for posterior single tooth replacement and found no mechanical or biological signs of failure associated with any reconstruction followed up to six months (Nothdurft and Pospiech, 2010). From an aesthetic point of view, zirconia abutments can be advantageous in many ways (Yildirim *et al.*, 2000). Frank exposure of the white zirconia abutment as a result of recession is far from perceivable by patient. Moreover, zirconia was found to be associated with less discoloration of 1.5 mm thick soft tissue when compared to titanium as reported in an animal study (Jung *et al.*, 2007). Bressan *et al.* (2011) confirmed these results in their multicentre prospective clinical study (Bressan *et al.*, 2011). However, care should be taken regarding these claims in light of the clinical trial by Zembic *et al.* (2009) who assessed colour changes by means of spectrophotometry. The authors found that both zirconia and titanium abutments induced similar visible colour changes in peri-implant soft tissues (Zembic *et al.*, 2009).

A hybrid implant design where the fixture was made of *cpTi* with a zirconia soft tissue collar or transmucosal part was introduced by a French dental implant manufacturer (TBR Group, France). In the clinical trial by Bianchi *et al.* (2004), it was found that this hybrid implant system performed better than titanium controls in terms of probing depth, bleeding on probing and plaque index. Also, rapid stabilisation of peri-implant tissues was documented in the first year and survival rate after two years was 100% (Bianchi *et al.*, 2004). However, this clinical trial seems to be at a high risk of bias as there was not enough information about randomisation and allocation concealment, a small sample size and no information about assessors' blinding. Additionally, the risk of delamination of the zirconia collar may be an issue with such design upon the long-term use.

Two case reports were published about using laser acquisition techniques to scan extracted roots and mill truly anatomic, root-analogue zirconia implants using *CAM* technology to replace extracted teeth (Figure 3). The authors claimed good performance of these implants after 30 months. They also alleged potential benefits of

being atraumatic and the fact that this procedure negates the need for bone and soft tissue augmentation surgeries (Pirker and Kocher, 2008, Pirker *et al.*, 2011). However, the presence of bone defects due to previous infections may be the major challenge to this approach. Thus; careful case selection should be warranted. In addition, damage of unsupported thin labial bone plate during insertion of the implant may be an inevitable sequel that may undermine the treatment outcome.



Figure 3. Anatomical zirconia dental implants.

Top left, X-ray showing non-restorable upper right second premolar tooth. Top right, tooth was atraumatically extracted and scanned to produce a zirconia replica. Bottom left and right, clinical and radiographic appearance of the placed implant. Reused with permission (Pirker and Kocher, 2008). License Numbers for re-use permission: 3592490908779.

One-piece and to a lesser extent, two-piece zirconia implants have emerged as viable alternatives to titanium counterparts in the last two decades. The number of clinical studies that investigated the survival of zirconia implants is considerably less than *in vitro* counterparts. In addition, it is not surprising that quality of these studies is not as high as those available for titanium dental implants. This is attributed to the short follow-up period and/or small sample size rendering the evidence supporting the use of zirconia dental implants inconclusive. Table 1 shows the most popular commercially-available zirconia dental implants systems and their manufacturers.

Table 1. Commercially available zirconia dental implant systems.

<i>System</i>	<i>Manufacturer</i>
<i>WhiteSKY® ceramic implants</i>	<i>Bredent Medical, Germany</i>
<i>CeraRoot® Dental Implant System</i>	<i>Oral Iceberg S.L, Spain</i>
<i>Zeramex-T</i>	<i>Zermax, Germany</i>
<i>Zirkolith® & Z-Look® Evo Zirconia Implant</i>	<i>Z-Systems Switzerland</i>
<i>Curavx®</i>	<i>Maxon Motor Dental, Germany</i>
<i>The Straumann® PURE Ceramic Implant</i>	<i>Straumann, Switzerland</i>
<i>SDS® Implants</i>	<i>Swiss dental solutions AG</i>

A recent systematic review on different types of dental implants found no randomised controlled trials describing implants made or coated with materials other than titanium (Esposito *et al.*, 2007). However, studies providing lower level of evidence were reviewed by Andreiotelli *et al.* (2009) who found three retrospective cohort studies on one-piece zirconia dental implants that met the inclusion criteria of their systematic review (Andreiotelli *et al.*, 2009). The first two studies investigated 189 and 100 zirconia implants and found one year survival rates of 93% and 98%, respectively. Most failed implants did so in the healing phase, in which increased mobility was noticed. Only one implant failed after prosthetic reconstruction due to implant fracture (Mellinghoff, 2006, Oliva *et al.*, 2007). Lambrich and Iglhaut (2008) observed 127 zirconia and 234 titanium implants for a mean observation period of 21.4 months. In this study, zirconia implants performed as well as titanium counterparts when inserted in mandible (98.4% vs 97.2%). Titanium implants performed significantly better in the maxilla (98.4% vs 84.4%). All failures were in the healing phase due to increased implant mobility (Lambrich and Iglhaut, 2008).

The final conclusion of the aforementioned systematic review was that scientific data from animal and human studies showed that zirconia implants osseointegrate as well as titanium. Additionally, zirconia is a promising material in implant dentistry. However, these findings should be supported by long-term clinical data before recommending zirconia implants as a viable alternative to titanium counterparts (Andreiotelli *et al.*, 2009). These findings have been confirmed recently by

Depprich *et al.* (2012) who found only 17 clinical studies on zirconia implants conducted between 2006 and 2011. Survival rate was between 74–98% after 12–56 months. The authors remarked that all of the studies had significant shortcomings and thus, well-designed controlled clinical trials are urgently needed (Depprich *et al.*, 2012).

Payer *et al.* (2010) published their results after two years follow-up of 19 immediately loaded zirconia implants. They reported 95% two-year survival according to the clinical and radiographic parameters they examined (Payer *et al.*, 2012). These results are consistent with the data published by Oliva *et al.* (2010) who followed up 831 one-piece zirconia implants placed in 371 patients for five years and found a survival rate of 95%. In the latter study, three groups of implants with different surface roughness were investigated. The acid-etched implants were found to be superior to the coated and machined ones (Oliva *et al.*, 2010).

Kohal *et al.* (2012) found that immediately restored one-piece zirconia implants had one-year cumulative survival rate comparable to titanium counterparts. However, they remarked that the incidence of bone loss around zirconia implants was considerably higher than that for titanium counterparts at the follow-up. Thus, the studied implants could not be recommended for clinical use (Kohal *et al.*, 2012). These findings were in line with data from a study by Cannizzaro *et al.* (2010). The latter authors reported high failure rate due to significant bone resorption in the healing phase around one-piece zirconia implants. Immediately placed and restored implants were at an increased risk for such complication (Cannizzaro *et al.*, 2010).

Two-piece zirconia implants where a zirconia fixture and abutment are rigidly connected by metal screw or bonded by resin cement were proposed. A prototype two-piece design was found to be potentially inadequate for clinical use. The studied implants exhibited high rate of implant head fracture (Kohal *et al.*, 2009a). This can be attributed to the large amount of stress that a rigid zirconia abutment can induce on the inner surface of an implant. In contrast, a Swiss dental implant manufacturer (Swiss dental solutions AG, Switzerland) claims in their marketing material that 3.8 mm diameter zirconia implant, zirconia abutment and associated interface could withstand dynamic fatigue testing for two million cycles at 240 N without fracture. The associated interface, or in other words the joining mechanism, can be mechanical

(utilising gold, titanium or poly ether ether ketone (**PEEK**) screws) or adhesive (luting cements) or both. The implant is machined from **Y-TZP** blocks and annealed at high temperatures.

A two-year, single-centre, longitudinal case series reported the outcome of treating 32 partially edentulous, systemically healthy patients with 49 two-piece zirconia implants (**ZERAMEX-T[®]**, Dentalpoint AG, Zürich, Switzerland). Implants were placed in the posterior region and zirconia abutments were bonded to implants with adhesive resin cement (Figure 4). In this study, two abutments had fractured and five implants were lost due to aseptic loosening. The authors concluded that the one-year cumulative survival rate after loading was 87% (Cionca *et al.*, 2014).



Figure 4. ZERAMEX-T[®] two-piece zirconia dental implant system.

Clinical (top left) and radiographic (top right) appearance of surgically placed zirconia implant and cemented zirconia abutment to replace lower right second premolar tooth. Clinical (bottom left) and radiographic (bottom right) appearance of the restored implant 12 months post-operative (Cionca *et al.*, 2014). No permission was required for re-use for non-commercial purposes.

The above cited research findings cast doubt on the sufficiency of one-piece zirconia implants owing to the possible accelerated bone loss during the healing phase. Additionally, the use of two-piece implant design utilising a zirconia abutment may also contribute to irretrievable failures such as implant head fracture or aseptic loosening owing to conveyance of excessive forces during masticatory function.

‘If something is likely to fail, place it in an accessible location’. This is a sound engineering principle that is utilised in almost all fields of industry. This principle was introduced, developed and investigated in the present study in collaboration with the

White Implant Development Corp. (The Netherlands) and Maxon Motors (Germany). The White Implant System[®] utilises a low-strength glass fibre composite (**GFC**) abutment (Triflor[®], E. Hahnenkratt GmbH, Germany) that is cemented to a soft tissue level zirconia implant (Curavex, Maxon Motors, Germany) to support an all-ceramic crown (Figure 5). In this case, the weakest part in the chain could be; (1) abutment-implant bond (via adhesive cement), (2) abutment itself or (3) the brittle all-ceramic crown. Failure of any of these parts is likely to be favourable, less drastic and retrievable. The introduction of a cemented **GFC** abutment as a substitute to zirconia may also provide a cushioning mechanism. It can prevent detrimental forces e.g. trauma, from being transmitted to the implant and surrounding bone. Such impact forces are more likely to break suprabony components rather than the implant itself. In a clinical situation, the failure of the abutment, crown or any of the adhesive bonds can be easily repaired as opposed to implant head fracture or crestal bone resorption encountered in conventional one- or two-piece implant systems. Embracing this design conforms to a treatment modality that is proven to be successful in dental practice namely, restoration of endodontically treated teeth with glass-fibre posts and all-ceramic crown restorations (Signore *et al.*, 2009).

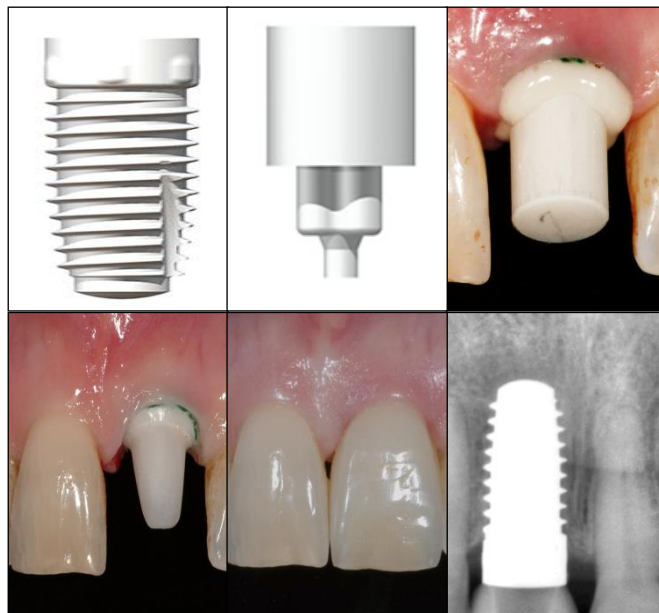


Figure 5. Two-piece, hybrid zirconia dental implant system.

The White implant system where a soft tissue level zirconia implant (top left) is bonded to a **GFC** abutment (top middle). A clinical case demonstrate the use of such design to replace an extracted upper left central incisor tooth (top right, bottom left). Bottom middle and right, clinical and radiographic appearance three years post-operative showing stable soft tissue and bone levels around the restored implant (Jum'ah *et al.*,

1.3 Thesis aims and objectives

The use of zirconia dental implants has been widely studied. While most studies concentrated on *HIP* and milled zirconia implants, *LTD* in *CIM* counterparts is as of yet unreported. Additionally, the performance of a novel, hybrid, two-piece zirconia dental implant design has not been reported in the literature. Furthermore, there are only a limited number of studies comparing the biofunctional response of cells to the proprietary '*MDS*' zirconia surface to other well-known *cpTi* surfaces. The overall aim of this multi-part project is to perform pre-clinical, *in vitro* testing of the reliability of a novel, hybrid, two-piece zirconia dental implant design. The translational aim of this project is to investigate, develop and refine this implant design to ensure optimum performance as an aesthetic alternative to conventional *cpTi* systems used to replace missing teeth in the aesthetic zone.

To achieve the aims, a multitude of crystallographic, mechanical and biological studies will be performed on standard, disc-shaped samples as well as implant-abutment-crown assemblies. Dynamic mechanical studies will also be performed on implants restored with two different crown materials with respect to their clinical applications. This project will have three main objectives that will be presented independently in the form of individual chapters; each with its own introduction, materials & methods, results and discussion sections, and consequently discussed and correlated to each other in the context of their clinical relevance:

Chapter 2: The *LTD* or ageing phenomenon will be characterised and quantified as a result of hydrothermal treatment using crystallographic and direct imaging techniques.

Chapter 3: The effect of hydrothermal ageing on basic mechanical properties of the implant material will be investigated using static mechanical testing. The second part of this chapter will examine the reliability and durability of various interfaces and materials within implant-abutment-crown assemblies under simulated clinical conditions.

Chapter 4: Surface roughness characterisation will be performed using different techniques on the smooth and roughened zirconia implant surfaces and compared to mechanically and chemically modified *cpTi* counterpart. Additionally, the biofunctional response of human gingival fibroblasts and osteoblast-like cells to these three surfaces will be compared.

Chapter 2: Crystallographic Analysis and Ageing Studies

2.1 Introduction

Zirconium oxide (ZrO_2), or zirconia, is an inorganic metal-oxide ceramic material. Pure zirconia exhibits several, chemically-identical but structurally-distinctive allotropes according to temperature:

- Below its melting point (2680 °C) and above 2370 °C, zirconia assumes the cubic crystalline system. Cubic zirconia exhibits a face-centred cubic Bravais lattice arrangement, an atomic inter-planar distance (d) of 2.94 Å, unit cell parameters ($a=b=c$) of 5.14 Å and inter-planar angles ($\alpha=\beta=\gamma$) of 90° (Katz, 1971).
- Between 1170 °C and 2370 °C, zirconia assumes a body-centred tetragonal Bravais crystalline arrangement, an atomic inter-planar distance (d) of 2.96 Å, unit cell parameters ($a=b\neq c$) of 3.598 Å and 5.185 Å and inter-planar angles ($\alpha=\beta=\gamma$) of 90° (Yashima *et al.*, 1994).
- At room temperature and below 1170 °C, pure zirconia is present as a base-centred monoclinic Bravais arrangement with an atomic inter-planar distance (d) of 3.16 Å, unit cell parameters ($a\neq b\neq c$) of 5.15 Å, 5.21 Å and 5.32 Å, respectively and interplanar angles ($\alpha=\gamma\neq\beta$) of 90° and 99.17° (Varez *et al.*, 2007, Lughì and Sergo, 2010).
- Other crystalline arrangements have been discovered in surface treated zirconia ceramics including a second cubic phase and orthorhombic phases (Scott, 1975, Pittayachawan, 2008). Basic crystalline phases and a simplified phase diagram of zirconia are demonstrated in Figure 6.

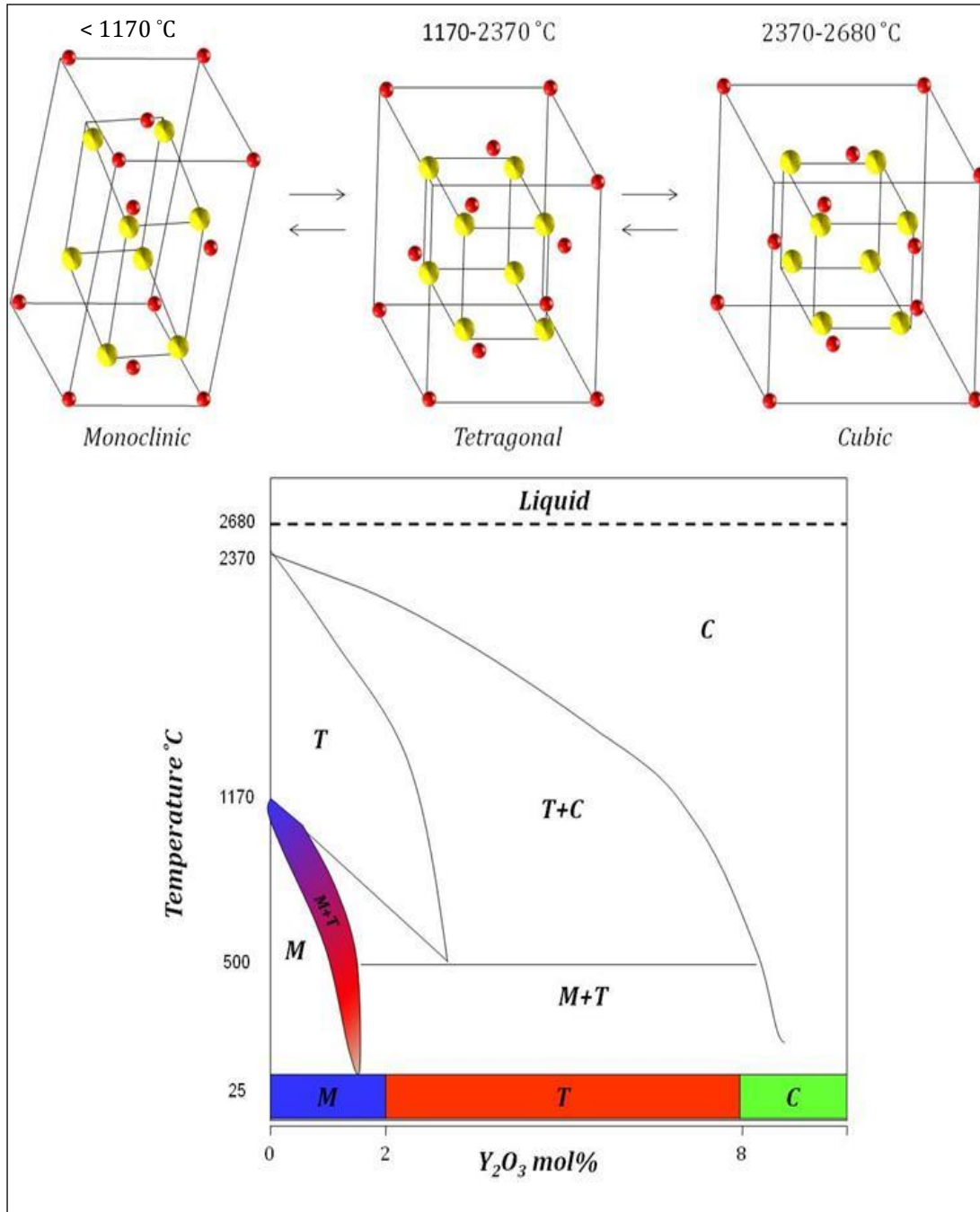


Figure 6. Schematic representation of various zirconia phases and zirconia phase transition diagram. Top, spatial arrangement of zirconium (yellow) and oxygen (red) atoms in the three principle phases of zirconia. Bottom, relationship between concentrations of Y₂O₃ stabiliser, temperature and phase stability. The diagram clearly demonstrates the proportional increase of cubic (C) phase with increasing the concentration of Y₂O₃ and temperature. Tetragonal phase (T) can be stabilised at room temperature by addition of 2-8 mol% of Y₂O₃. Monoclinic phase (M) is stable between room temperature and 1170 °C and with Y₂O₃ concentration below 1.8 mol%. Reproduced based on original phase diagram by Scott (Scott, 1975).

The transformation process from tetragonal to monoclinic ($t \rightarrow m$) allotrope exhibits the characteristics of martensitic transformation (Subbarao *et al.*, 1974, Schmauder and Schubert, 1986b, Deville *et al.*, 2004, Lughì and Sergo, 2010). According to the phenomenological theory of martensitic crystallography, a martensitic transformation can be characterised by a change in crystal structure (a phase change) in the solid state that is; athermal, diffusionless and involves the simultaneous, co-operative movement of atoms over distances less than an atomic diameter. The process should result in a microscopic change of shape of the transformed region (Deville *et al.*, 2004, Chevalier *et al.*, 2009). Despite the fact that the transformation process is diffusionless, i.e. involves only a minimal movement of atoms less than the interatomic distance, $t \rightarrow m$ results in 3-5% net volumetric expansion (Subbarao *et al.*, 1974, Bannister, 1993). This is a direct result of the difference in unit cell volume of monoclinic and tetragonal zirconia phases (140.96×10^6 vs. 67.12×10^6 pm³). Dilatation and shear (unit cell) strain subsequent to $t \rightarrow m$ process may result in excessive cracking and catastrophic failure which hindered the use of zirconia as a reliable ceramic material for many decades (Bannister, 1993, Lughì and Sergo, 2010).

In the late 1920's, stabilisation of tetragonal and cubic zirconia phases were successfully achieved at room temperature via addition of metal oxide stabilisers such as Yb₂O₃, Er₂O₃, Eu₂O₃, Gd₂O₃, Sc₂O₃, La₂O₃, CaO, MgO, CeO₂ and Y₂O₃. Alloying zirconia with the last four chemical oxides was the most widely used process to produce fully-stabilised and partially-stabilised (metastable) zirconia ceramics and received great attention among researchers (Ruff and Ebert, 1929, Ruff *et al.*, 1929, Passerini, 1939, Gupta *et al.*, 1977, Hellmann and Stubican, 1983b, Garvie *et al.*, 1984, Fassina *et al.*, 1992, Lughì and Sergo, 2010).

The required concentrations of Y₂O₃ to achieve room temperature, metastable tetragonal and fully-stable cubic phases vary among different studies. In his cornerstone work, Scott (1975) reported that stabilisation of tetragonal and cubic phases at room temperature requires addition of 4-13 mol% and > 13 mol% of Y₂O₃ respectively (Scott, 1975). However, it has been consensually cited that addition of ≥ 8 mol% Y₂O₃ to pure monoclinic zirconia can result in a fully stable, low transformation capacity cubic zirconia. Also, addition of lower concentrations of dopant or stabiliser such as 1.8-8 mol% Y₂O₃ can yield the most commonly used

zirconia based ceramics nowadays, single phase, transformable or metastable **Y-TZP** (Gupta *et al.*, 1977, Hellmann and Stubican, 1983b, Hannink *et al.*, 2000, Lughi and Sergo, 2010).

Tetragonal phase stabilisation using metal oxide dopants can be enhanced by embedding the stabilised crystals in a high elastic modulus matrix. Stabilised tetragonal zirconia phase within a matrix of cubic zirconia or the so called, partially stabilised zirconia (**PSZ**) is an example on this material. Alumina has also been used as a matrix to form the so called zirconia toughened alumina (**ZTA**) (Lughi and Sergo, 2010).

Pure cubic zirconia is difficult to process and use in the biomedical field. **PSZ** is very difficult to manufacture owing to the complexity of matrix precipitation process. **Y-TZP** is the easiest to manufacture among other forms of zirconia ceramics. It also has a superior potential for use as surgical implant material owing to; high biocompatibility, optimum aesthetic properties, machinability as well as high strength and fracture toughness (Piconi and Maccauro, 1999, Hisbergues *et al.*, 2009, Vagkopoulou *et al.*, 2009, Lughi and Sergo, 2010).

When mechanically challenged, for example by a propagating crack, the metastable tetragonal crystals can transform to the monoclinic phase ($t \rightarrow m$). This process is accompanied by 3-5% volumetric expansion of the crystals (analogous to cooling unstabilised tetragonal zirconia to room temperature) which yields radial compressive stresses that halts the crack propagation. The unique transformation toughening mechanism or, stress-induced $t \rightarrow m$ is largely responsible for the unsurpassed strength of **Y-TZP** in comparison to other ceramics (Garvie *et al.*, 1975, Gupta *et al.*, 1978). A schematic representation of stress-induced $t \rightarrow m$ is presented in Figure 7.

In order to lead to toughening of the solid matter, the transformation should exhibit the following features; (1) co-operative atom movements without the need to reconstruct the crystal structure in order for the transformation to take place in association with advancing crack, (2) high speed in order to allow for spontaneous reaction to the progressing crack and (3) a displacive component that leads to a relatively significant shape change of the transformed volume that is dominated by shear stresses (Deville *et al.*, 2004).

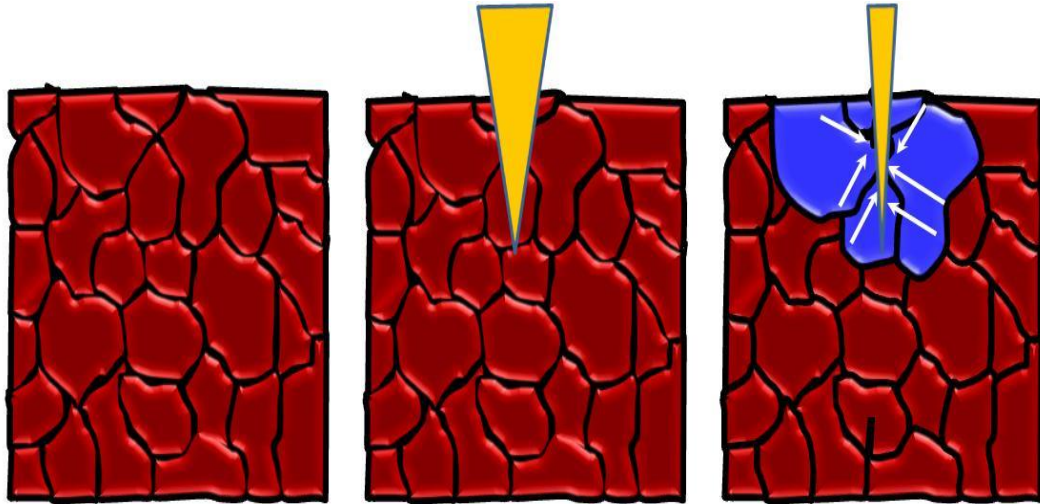


Figure 7. Schematic representation of phase transformation toughening mechanism.

The energy produced by a propagating crack can induce tetragonal (red) to monoclinic (blue) phase transformation. The monoclinic crystals are 3-5% larger in size in comparison to tetragonal counterparts. The volumetric expansion yields compressive stresses that close the crack front and halts its propagation.

Interestingly, the $t \rightarrow m$ process can take place spontaneously *in vivo* and upon exposure to a humid environment. This phenomenon has been identified as low-temperature degradation (*LTD*) or ageing. As a consequence of this process, *Y-TZP* can suffer slow, long-term, structural deterioration manifested as microcracking and/or loss of strength (Kobayashi *et al.*, 1981).

By definition, $t \rightarrow m$ during *LTD* should not be triggered by the local stresses produced at the tip of an advancing crack, as in the case of transformation toughening phenomenon (Lughi and Sergio, 2010). “Unfortunately, the remarkable advantages of the phase transformation toughening cannot be exploited without taking the risks of *LTD* process” (Chevalier *et al.*, 2007b).

From a microstructural point of view, the major shortcoming of *Y-TZP* is that once the tetragonal crystals transform to the monoclinic polymorph, they cannot exhibit phase transformation toughening mechanism anymore (Lughi and Sergio, 2010). *LTD* may have two major macroscopic adverse effects on zirconia biomedical implants:

- Cracking and monoclinic crystal pull-out may cause loss of crystalline coherence and consequently a decline in mechanical reliability.
- Surface roughening and the subsequent increase in the wear rate which may elicit an immune response against the released wear particles. This may ultimately cause aseptic bone loss and implant loosening in addition to further decline in mechanical and aesthetic parameters (Chevalier *et al.*, 2007b, Lughì and Sergo, 2010).

2.1.1 Physicochemical and microstructural features of *LTD*

According to the majority of research reports, *LTD* is a water-mediated phase transformation that propagates via a nucleation-and-growth mechanism. Several models have been proposed to elucidate the role of water and explain the physicochemical basis of *LTD*. Sato and Shimada (1985) were among the forerunners to investigate *LTD*. They demonstrated the role of corrosive and/or corrosive-mechanical stress in their pivotal work. They concluded that water and solvents with a molecular structure containing a lone-pair electron orbital opposite to a proton donor site, react with Zr-O-Zr bonds at the propagating crack front and consequently form Zr-OH bonds. The formation of the (OH⁻) bond may relieve strain/tension stabilising tetragonal phase and ultimately enhance $t \rightarrow m$ (Sato and Shimada, 1985). Similarly, Yoshimura *et al* (1987) adopted the hypothesis of anion diffusion and Zr-OH bond formation upon the exposure to water. According to their findings, such a reaction triggers $t \rightarrow m$ by chemical adsorption of water molecules followed by the formation of Zr-OH bonds at the surface. However, the latter group postulated that destabilisation of the tetragonal phase was attributed to the accumulation of lattice strains as a result of this reaction rather lattice strain relief. The accumulation of strain by the migration of (OH⁻) ions at the surface and in the crystalline lattice results in formation of nucleating defects. The nucleation of monoclinic phase in the vicinity of tetragonal grains enhances $t \rightarrow m$ and subsequently causes micro- and macro-cracking (Yoshimura *et al.*, 1987).

In their transmission electron microscopy (*TEM*) study, Lange *et al* (1986) demonstrated that water vapour reacted with yttrium in the *Y-TZP* and produced submicron clusters of Y(OH)₃. This reaction caused stabiliser (Y₂O₃) depletion and thereby, produced a monoclinic nucleus on the surface of an exposed tetragonal grain.

Monoclinic nuclei collectively grow to cause transformation of the tetragonal phase. The 3-5% volumetric expansion and shear strain associated with $t \rightarrow m$ can produce a microcrack in the case where the size of the transformed grain is larger than the critical size for microcracking. In this case, subsurface grains and bulk of the material will be exposed to corrosive action of water penetrating into deeper layers with subsequent spontaneous transformation and strength deterioration. If not, $t \rightarrow m$ will be limited by the diffusion range of yttrium to the surface and the strength is less likely to be affected. The authors concluded that catastrophic effects of *LTD* can be avoided by reducing *Y-TZP* grain size below the critical value required for microcracking (Lange *et al.*, 1986). A similar mechanism was proposed by Schubert (1986) and Li *et al.* (1996) who demonstrated the vital role of Y-OH bond formation during *LTD* process and significant synergistic effect of water (Li *et al.*, 1996, Ustundag and Fischman, 2009).

Based on data obtained from neutron diffraction and accelerated ageing dynamics, oxygen free radicals have been proposed as a more potent contributor to the *LTD* process in comparison to other water-derived species, e.g (OH^-). Water is believed to provide free radicals (O^-) that start the surface corrosive attack and cause lattice shrinkage and build-up of tensile stresses (corrosive-stress process) (Schubert and Frey, 2005). $t \rightarrow m$ starts in the most unstable areas such as grain boundaries where the largest amount of tensile stresses are present and then propagates to the centre of the grain as water attack continues (Schmauder and Schubert, 1986, Chevalier *et al.*, 2007b, Chevalier *et al.*, 2009).

A cascade of events occur after initial transformation process; the transformed grains come under compressive forces and the surrounding tetragonal phase grains come under tensile stresses which destabilises the tetragonal phase and again, favours further $t \rightarrow m$ via reduction of the strain energy (ΔU_{SE} , described later). In this way, a near-to-near mechanism or autocatalytic effect is provoked. As the tensile stresses generated by the transformation process are greatest on grain boundaries, microcracking starts in these areas and grain pull-out rate increases significantly. This in turn, facilitates diffusion of water molecules into deeper layers of the material and intensifies the acceleratory effect of water on *LTD* (Deville *et al.*, 2004). Chevalier *et al.* further concluded that a thermodynamic driving force working

synergistically with the diffusion of water-derived species is required for the transformation to occur (Chevalier *et al.*, 2007b, Chevalier *et al.*, 2009).

Despite the uncertainties and controversies surrounding the *LTD* phenomenon, it is well-established that;

- *LTD* is time-dependent process that proceeds most rapidly at temperatures of 200-300°C.
- It commences at the surface and further progresses to the bulk of the material via a nucleation-and-growth mechanism where nucleation refers to the transformation of a single grain, which can act as a nucleus for further transformation and growth refers to the preferential extension of $t \rightarrow m$ to the crystals in the vicinity of the nucleus.
- Water, vapour or moist environments have a significant role in the enhancement of this process.
- It is dependent on many other microstructural and chemical variables (Yoshimura *et al.*, 1987, Chevalier *et al.*, 1999a, Lughì and Sergo, 2010).

The crucial, obligatory prerequisite for the occurrence of $t \rightarrow m$ is that the tetragonal zirconia crystals exhibit thermodynamic metastability. Whether $t \rightarrow m$ is considered (positively) as a toughening mechanism or (negatively) part of the *LTD* process is determined by the initiative that provoked the transformation process itself. $t \rightarrow m$ induced at the propagating crack front is a stress-induced transformation and considered as toughening mechanism. Spontaneous $t \rightarrow m$ that is not associated with mechanical stress generated by propagating cracks, occurs at low temperatures and in a humid environment is considered as *LTD* or ageing process (Lughì and Sergo, 2010). In *Y-TZP*, $t \rightarrow m$ is mechanically constrained under metastable conditions.

In order for the $t \rightarrow m$ to occur, sufficient energy should be introduced to the metastable environment to end the equilibrium state and drive the transformation process. If $t \rightarrow m$ is envisioned as a chemical reaction that is controlled by pertinent free energy change ($\Delta G_{t \rightarrow m}$), the factors affecting the transformation of a tetragonal crystal to its monoclinic allotrope can be described in the Equation (1) (Lange, 1982):

$$\Delta G_{t \rightarrow m} = \Delta G_c + \Delta U_{SE} + \Delta U_s \quad (1)$$

Where;

ΔG_c : is the difference in chemical free energy between the tetragonal and monoclinic phases,

ΔU_{SE} : refers to the change in elastic strain energy associated with $t \rightarrow m$, and

ΔU_s : is the change in energy associated with the formation of new interfaces as a result of the $t \rightarrow m$ process including; microcracks, surface uplifts and volumetric expansion

The value of ΔG_c is negative whenever the temperature is below the martensite start limit. It is largely determined by the temperature, chemical composition and the amount of oxygen vacancies. ΔU_{SE} is dependent on the modulus of the surrounding matrix and the presence of internal (residual) or external (applied) stresses. ΔU_s is affected by the size and shape of the crystal (Chevalier *et al.*, 2009, Lughì and Sergio, 2010). Martensitic transformation is a non-equilibrium process. Thus, for $t \rightarrow m$ to take place, $\Delta G_{t \rightarrow m}$ should be less than zero. Tetragonal phase will be unstable or undergoing $t \rightarrow m$ where $|\Delta G_c| > |\Delta U_{SE} + \Delta U_s|$ (Chevalier *et al.*, 2009).

Y-TZP sensitivity to **LTD** is significantly affected by several interplaying factors. Some of these factors potentiate $t \rightarrow m$ by conferring a conducive environment for this process while others play a role in disrupting/stabilising the equilibrium state of tetragonal phase (meta)stability. Porosity or density plays an important role in delivering water to deeper layers of the material and thereby increasing the depth of **LTD** (Masaki, 1986, Muñoz-Saldaña *et al.*, 2003). The effect of grain size on **LTD** is complex. Increasing grain size reduces the grain boundary area where **LTD** is preferentially initiated, thus reducing the rate of **LTD**. However, increasing grain size also depresses the nucleation barrier and increases the tensile stresses (reduce ΔU_{SE}) on the grain boundaries and thereby increases sensitivity to **LTD**.

Smaller grain size can increase the nucleation rate on the abundant grain boundaries and accelerate **LTD** (Li and Watanabe, 1998). However, it is worthwhile to mention that **LTD** was significantly suppressed under extreme ageing conditions upon the use of fully dense **Y-TZP** with a critical grain size $< 0.36 \mu\text{m}$ (Muñoz-Saldaña *et al.*, 2003).

The amount of cubic phase, which is affected by sintering protocol and dopants' concentration, is directly related to the **LTD** process. Cubic grains are larger than tetragonal counterparts and can deplete the latter from stabiliser and thereby, increase

the risk of **LTD** (Chevalier *et al.*, 2004). Dopants or stabilisers should be used in an optimum way in order to maintain the balance between **LTD** and mechanical properties. High concentrations of dopant reduce the sensitivity to **LTD** by decreasing $|\Delta G_c|$ and increasing ΔU_{SE} . However, a large amount of stabiliser reduces the efficiency of transformation toughening mechanism and thereby, reliability of the material (Sato and Shimada, 1985). The type of dopant also affects the rate of **LTD**. Ceria-doped zirconia and ceria co-doped **Y-TZP** materials seem to have reduced sensitivity to **LTD** and better mechanical properties in comparison to **Y-TZP** (Tsukuma and Shimada, 1985, Wang *et al.*, 1992, Ban *et al.*, 2008). Unfortunately, ceria stabilised tetragonal zirconia is not commercially available yet due to several reasons as cited by Lughii and Sergo (2010). Firstly, reduction of Ce^{+4} to Ce^{+3} can occur spontaneously during sintering in air at room temperature as a result of stress locally generated by $t \rightarrow m$. Ce^{+3} is reported to have a significantly inferior stabilising effect on tetragonal zirconia. Secondly, ceria stabilised zirconia has a light yellow to almost brownish colour. This in turn poses an aesthetic challenge for dental applications. Thirdly, reduction of Ce^{+4} to Ce^{+3} tends to cause dark grey discoloration. This is especially relevant in the oral environment as several studies reported that some glucose and lactose containing foods have Ce^{+4} to Ce^{+3} reducing capabilities (Lughii and Sergo, 2010).

Addition of alumina particles was shown to reduce the **LTD** kinetics of **Y-TZP** as it increased densification, increased ΔU_{SE} by increasing matrix elastic modulus and enhanced tensile deformation in superplastic flow (Radford and Bratton, 1979, Chevalier *et al.*, 2009). In addition, the segregation of Al^{+3} to the grain boundary reduces $|\Delta G_c|$ by enhancing anion vacancies in the crystalline grain boundary i.e., alumina-zirconia interface can accommodate a higher concentration of oxygen vacancies in comparison to the bulk of the grain owing to the trivalent nature of aluminium (Suenaga *et al.*, 1998).

Presence of stress/strain in the crystalline lattice is an important determinant of the $t \rightarrow m$ process. It has been demonstrated that $t \rightarrow m$ does not take place in stress-free tetragonal zirconia crystals, even if the stabiliser content is significantly below that required as per the stability of the phase diagram, that is <1.8 mol% (Schmauder and Schubert, 1986b). Grinding and surface treatments affect reliability and **LTD** sensitivity of **Y-TZP** as they affect internal and residual stresses, and introduce external

stresses. Wet grinding and sandblasting seemed to have no detrimental effect on reliability (Guazzato *et al.*, 2005). Compressive stresses as a result of rough surface polishing aids **LTD** resistance. Scratches induced by fine polishing induce $t \rightarrow m$ and potentially **LTD** along the scratch line as a result of tensile stresses build up (Deville *et al.*, 2006). Internal tensile stresses act to reduce ΔU_{SE} while compressive stresses increase the value of this parameter which explains the different effect on **LTD** susceptibility (Chevalier *et al.*, 2009). The effect of various stresses can significantly alter the nature of the $t \rightarrow m$'s product. Where the transformed crystal is in a non-constrained environment such as on the surface of a solid matter or in a powder, the volumetric expansion subsequent to $t \rightarrow m$ is manifested/relaxed as a surface uplifts or the so called, martensite reliefs. On the other hand, in a mechanically constrained environment and in the presence of a stress field, such as the bulk of a solid matter, tetragonal MgO partially stabilised zirconia transformed into a stack of monoclinic allotropes (crystal twinning), which accommodated the shear component of the transformation as indicated by **TEM** studies (Chevalier *et al.*, 2009).

2.2 **LTD** kinetics

The contribution of factors affecting ΔG_c , ΔU_{SE} and ΔU_S eventually determines as to whether the equilibrium state of metastable tetragonal zirconia will be disrupted or maintained and hence whether $t \rightarrow m$ proceeds or not. Thus, in a (meta)stable tetragonal crystal, the occurrence of $t \rightarrow m$ strictly requires a kinetically driven event over an elapsed time range that alters one or more of the above variables. Tetragonal zirconia phase can be existent in a (meta)stable form even if the conditions point toward negative $\Delta G_{t \rightarrow m}$. This is attributed to the fact that a thermodynamic or a mechanical trigger is needed for $t \rightarrow m$ to take place, analogous to water remaining in liquid state just below the freezing temperature (Lughi and Sergo, 2010).

Equation 1 allows studying the boundaries of mechanical and thermodynamic stability of **Y-TZP** at a snapshot of time as the variables are time independent. Long-term stability of tetragonal phase of zirconia can however, be studied in time-dependent, kinetic terms (Lughi and Sergo, 2010). The effect of **LTD** on **Y-TZP** was overlooked until 2001 owing to the presumption that its occurrence within an *in vivo* environment was physically impossible. These thoughts were consolidated by the fact that **LTD** kinetics peak at approximately 250 °C (Chevalier *et al.*, 2009). However, it

has been demonstrated that $t \rightarrow m$ kinetics are very profoundly affected by several microstructure- and processing-related factors which if modified, will result in the kinetics being shifted by several orders of magnitude (Deville *et al.*, 2005).

The martensitic $t \rightarrow m$ process in *Y-TZP* takes place by an apparent water-controlled nucleation and growth mechanism. Several studies have shown that *LTD* kinetics follow sigmoidal laws related to the nucleation and growth mechanism. Thus, they can be initially described using the Mehl-Avrami-Johnson (*MAJ*) equation that is used for time-dependent, isothermal phase transitions (Chevalier *et al.*, 2007b, Kokubo, 2008):

$$V_m = 1 - \exp[-(bt^n)] \quad (2)$$

Where;

V_m is the monoclinic volume fraction in the volume accessible by the technique used for quantification,

t is the time,

n is the *MAJ* exponent constant, and

b is a parameter dependent on temperature

The parameter dependent on temperature (b) can be calculated from the apparent activation energy, in the 37-140°C temperature range, using Arrhenius law presented in Equation 3 (Chevalier *et al.*, 2007b, Lughì and Sergo, 2010):

$$b = b_0 \times \exp\left[-\frac{Q}{RT}\right] \quad (3)$$

Where;

b_0 is a constant,

R is the gas constant,

Q is the apparent activation energy, and

T is the absolute temperature.

The apparent activation energy is, in essence, the driving force for the $t \rightarrow m$ process. In a given material at any point of time, it is the value of $\Delta G_{t \rightarrow m}$ at which $t \rightarrow m$ process takes place. It depends on the free energy difference between the tetragonal and monoclinic phases, temperature and stress state. Various surface treatments and processing conditions largely affect the apparent activation energy by altering one or more of these factors (Chevalier *et al.*, 2007b, Lughì and Sergo, 2010).

The use of Equations 2 and 3 had substantial success in extrapolating time-temperature equivalences between *in vitro*, accelerated, high temperature **LTD** data and *in vivo* **LTD** occurring at body temperature. For instance, steam sterilisation at 134°C for 5 hours is now proposed to simulate 15–20 years of *in vivo* **LTD** (Chevalier *et al.*, 1997, Chevalier *et al.*, 1999a, Lughì and Sergo, 2010).

Y-TZP femoral implants were being used successfully since 1985 with a fracture rate of 1 per 50,000 implants (0.002%) (Cales, 2000). The premature catastrophic failure of a series of **Y-TZP** surgical implants used for total hip arthroplasty however tarnished this respectable record and imposed a paradigm shift in consideration of **LTD** phenomenon. As cited by Chevalier *et al.* (2007), **LTD** was the major suspect and the leading cause in the striking episode of femoral implants failure within ‘particular’ batches. The occurrence and distribution of these failures undoubtedly indicated awry processing. It subsequently transpired that the manufacturer utilised a new time-efficient tunnel furnace to provide a continuous sintering operation to cope with the increasing commercial demand. The newly processed femoral heads failed within months of implantation with a striking failure rate of 8%. The use of autoclave sterilisation at that period had also complicated the situation and was later forbidden by the Food and Drug Administration (**FDA**). The use of the tunnel furnace led to an uneven radial distribution of intermediate density and a highly porous core of the implants after sintering. In addition, mechanical grinding for a wedge-shaped female receptacle in the **Y-TZP** femoral head in order to receive metal male component led to accumulation of high residual stresses that lowered $t \rightarrow m$ activation threshold. Unfortunately, these flaws skipped the standard quality control checks which investigate the overall density and surface **LTD** (Chevalier *et al.*, 2007b).

2.3 Macroscopic consequences of LTD on surgical implants

Studies on retrieved femoral head surgical implants revealed that **LTD** can have two major macroscopic adverse effects on zirconia dental implants. Firstly, cracking and monoclinic crystal pull-out may cause surface roughness, loss of crystalline coherence and consequently decline in mechanical reliability. Secondly, the released particles can elicit an immune response that ultimately causes aseptic bone loss and implant loosening (Chevalier *et al.*, 2007b, Lughì and Sergo, 2010). However, as cited by Chevalier *et al.* (2007), the extent and relevance of such problems varied among

published reports owing to the complexity and multifactorial (processing and chemical composition) nature of *LTD* process (Chevalier *et al.*, 2007b). Some studies reported poor survival rates due to high wear rates and wear particles release which led to osteolysis and ultimately aseptic loosening of the implants. Analysis of the retrieved implants (implanted for up to 10 years *in vivo*) revealed significant *LTD* at the articulating surfaces. The degradation of the material's strength was associated with extensive microcracking, increased monoclinic phase fraction, reduced hardness and surface roughness parameters (Allain *et al.*, 1999, Haraguchi *et al.*, 2001, Norton *et al.*, 2002, Catledge *et al.*, 2003, Hernigou and Bahrami, 2003, Santos *et al.*, 2004).

2.4 *In vitro* simulation of *LTD* process

LTD, at accelerated rates, can be reproduced in the laboratory environment using several mechanisms. Ageing of zirconia in humid air, distilled water, saline, artificial saliva, Ringer's solution, acetic, sulphuric or nitric acid and caustic soda, at various temperatures and for different periods have been reported (Nakajima *et al.*, 1983, Drummond, 1989, Chevalier *et al.*, 1999a, Shojai and Mäntylä, 2001, Kosmać *et al.*, 2008). The most commonly reported *in vitro* ageing mechanism is hydrothermal ageing using autoclave sterilisation units or hydrothermal reactors. Nakajima *et al.* (1983) were among the first who reported the use of autoclave for *Y-TZP* ageing (Nakajima *et al.*, 1983). They have used a temperature that ranged from 100 to 180°C for less than 5 hours. Such accelerated *LTD* tests are currently used for extrapolating an estimate of *LTD* rates and, hence, the product's lifetime assuming that the transformation rate follows the same Arrhenius-like trend at room/body temperature (Lughi and Sergio, 2010). It has been suggested that 5 hours of hydrothermal ageing at a temperature of 134 °C and 2 bar steam pressure may simulate 15–20 years of *LTD* at 37 °C (Chevalier *et al.*, 2007b). Assuming comparable time–temperature equivalences, the ISO standards 13356:2008 specified that *Y-TZP* ceramic implant materials should contain less than 25% monoclinic phase fraction after the aforementioned ageing cycle (ISO 13356, 2008).

2.5 Initial material characterisation

The microstructure of the injection-moulded zirconia dental implant material was characterised using scanning electron microscopy (*SEM*). Ethylene oxide sterilised, 17.85 ± 0.011 mm diameter and 1.03 ± 0.014 mm thick *Y-TZP* zirconia discs were provided by the manufacturer (Maxon motor GmbH, Germany), (The White Implant Development Corp., The Netherlands). The steps of the production, data sheet and sterilisation process of these samples were provided by the manufacturer and included in Appendix A, B and C respectively. As-received discs were mirror polished as described in Section 2.6.4.1. Discs were sputter coated with 10 nm layer of platinum using a high resolution sputter coater (Agar scientific, UK). High resolution field emission *SEM* was used to study the crystalline structure of the material (LEOGemini 1530). Images were imported to DigitalMicrograph™ software (Gatan Microscopy Suite, UK). Images were calibrated using the software according to the scale bar embedded in the image. Five lines of known lengths were drawn to include the maximum number of complete grains. Average crystal size was calculated using the linear intercept method according to Equation (4) (Wurst and Nelson, 1972):

$$D = 1.56 \frac{C}{MN} \quad (4)$$

Where;

D is the average grain size,

C the total length of test line superimposed on micrograph,

N the number of intercepts,

M the magnification of the micrograph, and

1.56 is the proportionality constant or correction factor

Characterisation of the elemental composition of representative, as-received samples was carried out using energy dispersive X-Ray spectroscopy (*EDS*) system (Oxford Instruments, UK). The system is equipped with a silicone drift detector (X-Max®) and pulse processor (X-stream-2, Oxford Instruments, UK). Data was analysed using sophisticated elemental analysis software (AztecEnergy, Oxford Instruments, UK).

SEM revealed a homogenous and dense microstructure without any notable defects or porosity. Grains were equiaxial in shape and had clear, well-demarcated grain boundaries. Grain size varied between 200-600 nm with an average of

453.61±51.73 nm according to linear intercept method. Measurement of the average diameter of grains using software like ImageJ without any corrections revealed a smaller grain size in comparison the linear intercept method (384.27 nm Vs. 453.61 nm). It has been reported that the former technique may underestimate grain diameter due to stereological error. A correction factor of 1.56 can be used to obtain the real grain diameter as in the linear intercept method used in this study (Fullman, 1953, Deville *et al.*, 2005).

EDS analysis revealed weight percentage of 71.38%, 26.88%, 1.22%, 0.27% and 0.25% of the following atoms Zr, O, Y, Hf, and Al, respectively. Platinum was shown in the spectrum as it has the same close electron emission energy to zirconium as well as due to a weak signal present from the coating material. Figure 8 demonstrates microstructure of the studied material as seen under high magnification **SEM** and **EDS** spectrum for the same sample.

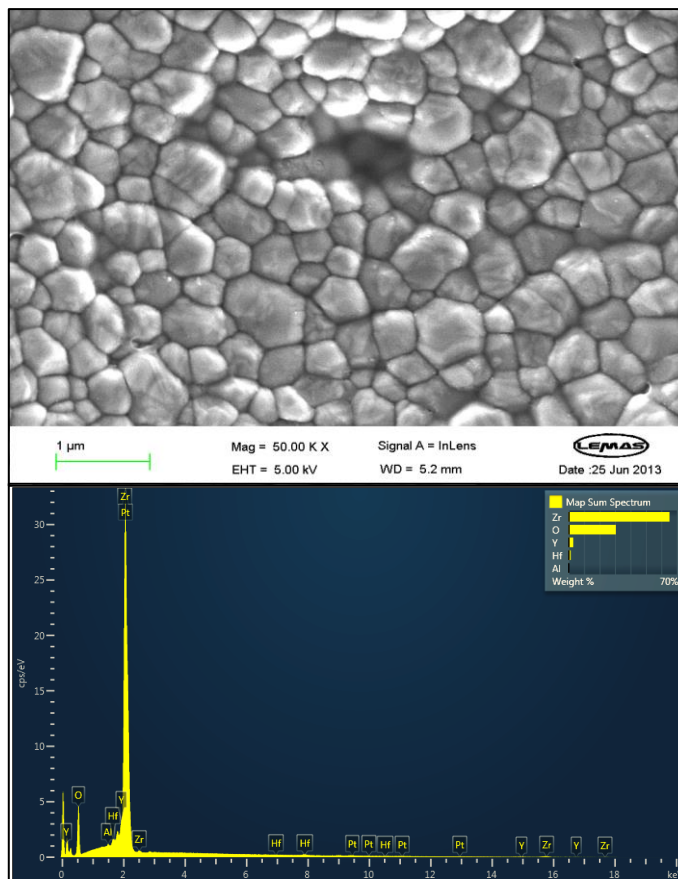


Figure 8. **SEM** and **EDS** characterisation of the studied injection-moulded **Y-TZP** implant material.

Top, high magnification **SEM** image revealing the ultrastructure of polished material which was used to calculate average crystal diameter. Bottom, elemental **EDS** analysis of the material demonstrating chemical composition that is principally consists of Zr and O.

2.6 Ageing identification and quantification: Experimental techniques and results

The bout of catastrophic failures of zirconia implants stressed the fact that *LTD* is a very complicated and delicately controlled process. Examination of *LTD* susceptibility for all produced batches of any zirconia biomedical device has been a standard procedure since then. In fact, this misfortune could have been avoided if the experimental work by Chevalier *et al* (1999) was carefully considered. They postulated and tested an analytical method for modelling zirconia *LTD* kinetics utilising X-Ray diffraction (*XRD*) and atomic force microscopy (*AFM*). In their model, it was hypothesised that *LTD* takes place by a constant nucleation of new transformation zones with time. Additionally, transformation zones increase in diameter and height at constant rate provided that an adequate space was available.

The above model was successfully applied to hot- and cold-isostatically pressed 3 mol% *Y-TZP* and commercially available Prozyr zirconia femoral heads (Chevalier *et al.*, 1999a, Gremillard *et al.*, 2004a, Chevalier *et al.*, 2007b). However, the authors reiterated that accurate prediction of *LTD* kinetics can only be performed while the nucleation-growth and *t*→*m* process is confined to the depth accessible by X-Ray (5µm). *LTD* that progressed to the bulk of the material, beyond 5µm, cannot be assessed utilising this method which explains how the failed zirconia hip implants skipped quality control process (Chevalier *et al.*, 1999a, Chevalier *et al.*, 2007b). Thus, the use of various direct imaging techniques in order to assess the extent and the consequences of *t*→*m* process has been widely adopted thereafter.

Experimental techniques used for characterising *LTD* can be generally divided to techniques which assess the crystallographic or morphological changes induced by the *t*→*m* process. The former techniques rely on differentiation between the crystallographic features of various zirconia phases. The latter however, directly examine/image the sequela of *t*→*m* such as; microcracking, crystalline pull-out, crystal twinning and formation of martensite reliefs/laths.

2.6.1 *XRD* on discs and implants

XRD is by far the most extensively used technique to characterise and quantify *LTD* in zirconia ceramics (Deville *et al.*, 2005). It is a quick, versatile, non-destructive and reliable technique to study the chemical setup and phase fractions of naturally

occurring and manufactured crystalline powders and solids. Every crystalline substance yields a characteristic pattern of diffracted X-Rays. In case of mixture of substances, each one produces its pattern independently of the others.

The X-Ray diffraction pattern of a pure substance is like a fingerprint of the substance. Thus, **XRD** is suited for identification of chemical composition and various phases within multiphase materials. **XRD** allows measuring the average spacing between layers of atoms and crystals which in turn, allows identification of orientation and spatial arrangement of crystals. Size and shape of crystals, internal stresses and chemical bonds within the crystalline lattice can all be studied utilising X-Ray diffraction (Jenkins and Snyder, 2012).

XRD largely depends on Bragg's law where the intensity and pattern of diffracted X-Ray beams indicate the electron density and inter-atomic distance of the tested material. It is firmly established **XRD** can be used to perform texture analysis which is used to identify any preferred orientation of crystals within the crystalline lattice. This is essential in solid, processed materials such as ceramics where crystals may assume a non-random distribution as opposite to powder samples. Knowledge of the texture is an important factor in understanding the mechanical, physical or chemical behaviour of the investigated material (Vanasupa *et al.*, 1999, Almer *et al.*, 2003). Bragg's law can be given as in Equation (5) (Warren, 2012):

$$n\lambda = 2d \sin \theta \quad (5)$$

Where;

n: integer,

λ: electromagnetic radiation wavelength,

d: the separation of the reflecting planes, and

θ: the angle of incidence of X-Rays

In simple words, Bragg's law states that the planes of atoms or crystals separated by a particular distance within each crystalline solid diffract incident electromagnetic radiation in specific patterns of constructive interference at certain angles of incidence. Figure 9 shows a schematic representation of the relation between incident beam wavelength, incident angle, d-spacing, production of constructive interferences and diffracted signals.

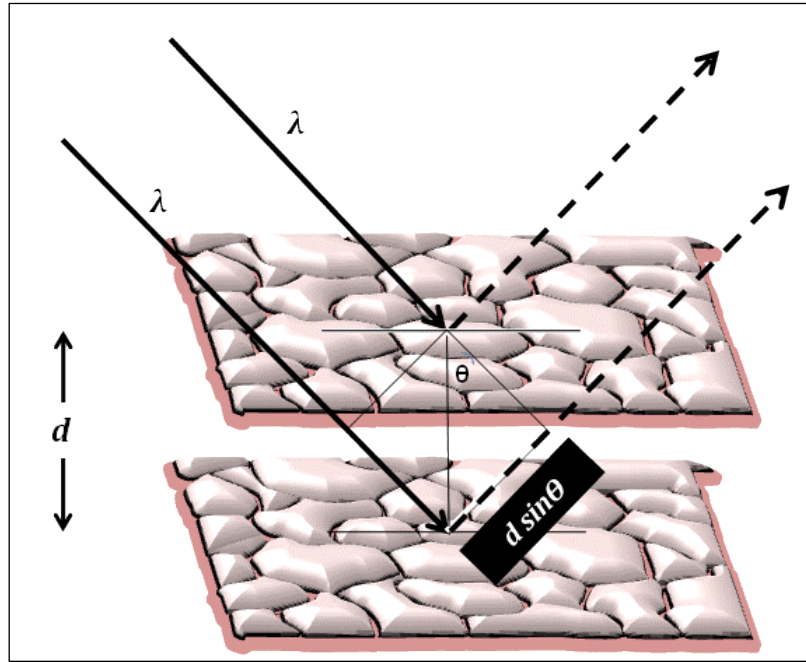


Figure 9. Schematic representation of Bragg's law.

The concept of Bragg's diffraction explains the appearance of characteristic and distinct diffraction patterns of different crystalline materials. The diffracted X-rays interfere constructively when they travel a distance inside the material that is different by a whole number multiplied by their wavelength ($n\lambda$). The relation between constructively interfered diffracted signal $n\lambda$, d and θ can be given by the equation $n\lambda=2d \sin\theta$.

In this project, **XRD** analysis was performed on as-received and aged ($n=3$) discs using a PANalytical X'Pert Powder diffractometer (Panalytical B.V, The Netherlands) with Ni filtered Cu $K_{\alpha 1}$ (1.5406 \AA) at generator voltage and tube current of 40Kv and 40 mA, respectively.

Samples were mounted to an ultra-low background, custom made aluminium holder utilising a minimum amount of plasticine that was completely masked under the sample. A 10 mm fixed incident beam mask was used to collimate the width of the exposed area and the beam length was adjusted to 2 mm. Diffraction data was collected in a classical Bragg-Brentano geometry from 27° to 33° 2θ with step size of 0.033° and dwell time of 175 sec. Automatic divergence slits (**ADS**) were used in order to ensure equal irradiated area over the entire 2θ range. Outputs were charted using the X'Pert Data Collector software (Panalytical B.V, The Netherlands). Figure 10 shows a schematic representation of the described diffractometer.

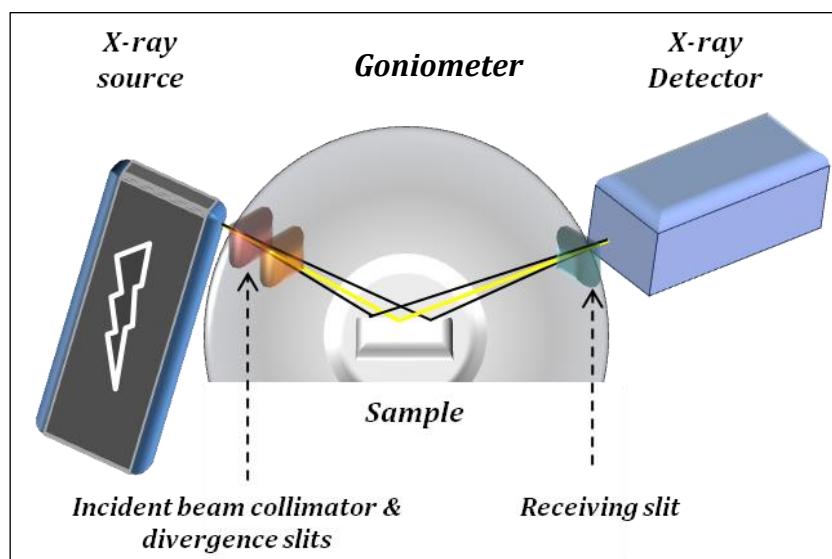


Figure 10. Schematic representation of the used *XRD* setup.

Classic Bragg-Berntano *XRD* setup involves irradiating a stationary sample from an X-ray source that simultaneously moves along 2θ range with the X-ray detector.

The volume percentage of monoclinic phase was determined in all samples according to two different methods. Firstly, High Score Plus software (Panalytical B.V, The Netherlands) was used to perform a search match using the elemental restrictions determined from the product information sheet and *EDS* data of obtained for representative samples. Diffraction patterns were matched with reference powder diffraction files (*PDF*) obtained from the International Centre of Diffraction Data (*ICDD*) database. *PDFs* with best match probability and highest quality were included in one calculated model. The model contained tetragonal yttria stabilised zirconia diffraction data based on Yashima *et al* (1994) with a P42/nmc space group and lattice parameters of $a = 3.6029 \text{ \AA}$ and $c = 5.1716 \text{ \AA}$ (Yashima *et al.*, 1994). Additionally, the model contained diffraction data of baddeleyite (monoclinic) zirconia phase based on Varez *et al* (2007) with a space group of P21/nmc and lattice parameters of $a = 5.1514 \text{ \AA}$, $b = 5.2098 \text{ \AA}$ and $c = 5.3204 \text{ \AA}$ (Varez *et al.*, 2007, Yamashita *et al.*, 2008).

The matched phases were added into a pseudo Voigt distribution to perform Rietveld refinement on diffraction data. Rietveld refinement is a technique in which a calculated model is fitted to a diffraction pattern. The model includes reference powder diffraction data of various components, pattern line shape, background and phase composition. The model parameters are then adjusted via least-squares

refinement to best match the raw data (Ilavsky and Stalick, 2000). Refinement proceeds with treatment of raw diffraction data by transforming from *ADS* to fixed divergence slits (*FDS*), using a trigonometric algorithm in the software. Refinement of all global variables was carried out including; specimen displacement (mm), polynomial background correction, flat background, and other background coefficients. Zero shift (2θ) and wavelength (\AA) were the exception and kept unrefined.

Variables related to individual phases including; scale factor, preferred orientation, peak shape variables, asymmetry (Rietveld) factor and cell parameters were refined one by one. Refinement was performed systematically, according to a strategy so as to treat all specimens consistently. The refinement was deemed successful as far as it did not cause convergence of fit or yielded impossible values such as peak shape of 1 or size broadening factor less than zero. Weighted-profile *R*-factor (R_{wp}), an agreement index that measures the degree of convergence in the fit, was used as a guide to the quality of fit. The refinement process was accepted as long as R_{wp} was less than 10. Figure 11 summarises the refining strategy used in this study.

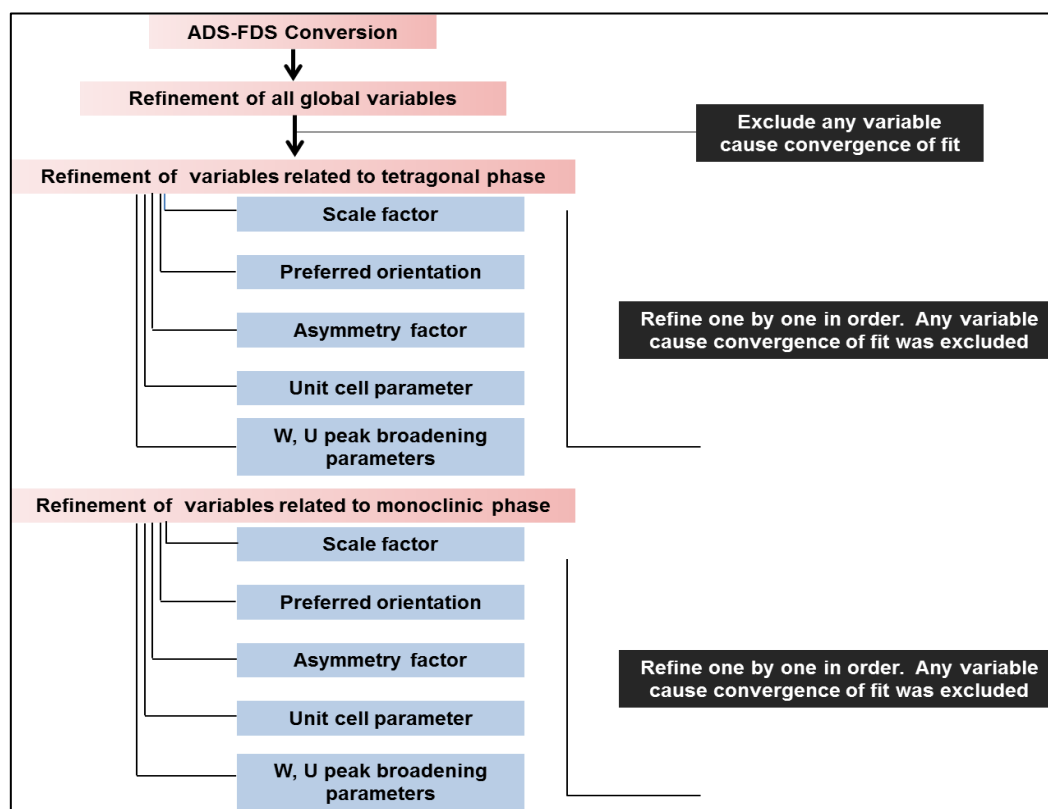


Figure 11. Refinement strategy used during Rietveld analysis of *XRD* data.

Secondly, the monoclinic volume fraction was determined from scans for all samples according to the Toraya's modification of the Garvie and Nicholson method. Experimental integrated intensity ratio of monoclinic phase (X_m) and monoclinic volume fraction (V_m) were determined using Equations (6 and 7) (Garvie and Nicholson, 1972, Toraya *et al.*, 1984):

$$X_m = \frac{I_{m(-111)} + I_{m(111)}}{I_{m(-111)} + I_{m(111)} + I_{t(101)}} \quad (6)$$

$$V_m = \frac{1.311X_m}{1 + 1.311X_m} \quad (7)$$

Where;

I_t : integrated intensity or the area under the tetragonal peaks, and
 I_m : integrated intensity or the area under the monoclinic peaks

In this project, twelve discs were divided into; as-received, aged, machined and machined-aged groups (n=3 per group). Aged samples received hydrothermal treatment in a 1.2 litre high pressure hydrothermal reactor (Series 4540 Parr, U.S.A) with 300 ml of distilled water. The ageing cycle lasted for 5 hours at operating temperature and pressure equal to 134 °C and 2 bar, respectively. Samples were left in the hydrothermal reactor upon completing the cycle until 50 °C temperature was reached. The cooling rate was estimated to be 0.011 °C/sec. Samples were dried using compressed air and stored in a desiccator until further testing.

In order to examine the effect of mechanical grinding on $t \rightarrow m$, a 'machined' group was created by preparing a central, rectangular, 8 mm wide and 0.5 mm deep area in six discs using fine grit, multi-layer gold diamond burs (45 µm, Diatech, Coltene, Switzerland) fitted in a high-speed handpiece (400,000 rpm, Synea®, W&H Dental WerksBürmoos GmbH, Germany) with continuous water cooling.

Depth of preparation was continuously checked with digital micrometer (Mitutoyo Ltd, Hampshire, UK). Half of the prepared discs were exposed to the above mentioned hydrothermal treatment 'machined-aged group'.

XRD data of as-received discs after ethylene oxide sterilisation displayed a wide, anisotropic peak at approximately $2\theta = 30.3^\circ$ related to (101) tetragonal phase with lattice parameters $a, b = 3.597 \text{ \AA}$ and $c = 5.197 \text{ \AA}$. A very low intensity peak was also noticed at $2\theta = 28.1^\circ$ corresponding to the $(\bar{1}11)$ peak of the monoclinic phase with lattice parameters $a = 5.14 \text{ \AA}$, $b = 5.23 \text{ \AA}$ and $c = 5.32 \text{ \AA}$. Rietveld analysis revealed a principal tetragonal phase (94.41 ± 0.67 volume %) and minor moderately textured monoclinic phase (5.59 ± 0.67 volume %) as shown in Figure 12.

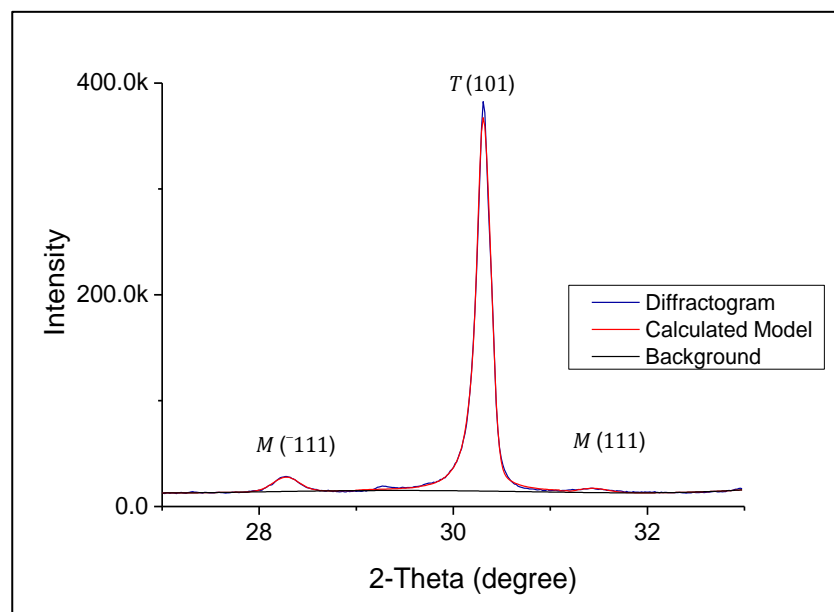


Figure 12. Rietveld refinement of **XRD** data obtained for a representative as-received sample.

Diffraction pattern (blue) was obtained by plotting intensity of diffracted signal against 2θ . Calculated model (red) from reference diffraction patterns for monoclinic and tetragonal phases was fitted to raw **XRD** data. Background (black) was calculated and refined by the software to fit bases of different peaks. Numbers above each peak corresponds to Miller indices that indicate the spatial orientation of each phase.

After 5 hours of hydrothermal ageing, intensity of the $(\bar{1}11)$ monoclinic peak had noticeably increased. In addition, a further small peak at $2\theta = 31.4^\circ$ appeared corresponding to the (111) peak of the monoclinic phase. Rietveld analysis revealed that the monoclinic phase fraction increased to 13.43 ± 2.11 volume %. Hydrothermal ageing caused notable surface texture (preferred orientation) as indicated by Rietveld analysis (Figure 13).

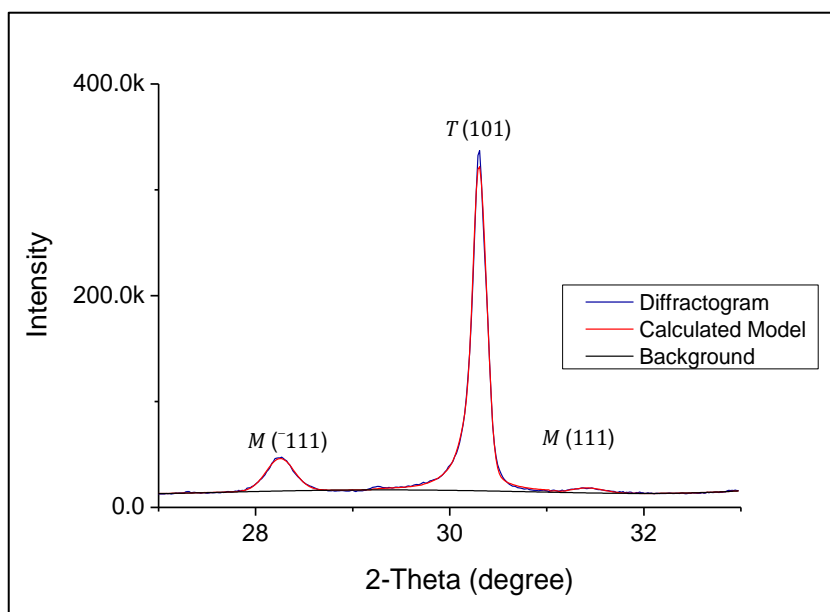


Figure 13. Rietveld refinement of *XRD* data obtained for a representative aged sample.

Machined samples displayed slightly different diffraction patterns. The monoclinic $\bar{1}11$ peak at $2\theta=28.1$ was less intense in comparison to the as-received group. The tetragonal peak at $2\theta=30.1$ was wider and more asymmetrical which is indicative of microstrain. Rietveld refinement revealed that the machined group had a mean monoclinic volume fraction of $1.73\pm 0.38\%$ and the rest was tetragonal phase. Hydrothermal ageing of machined samples (machined-aged) yielded a mean monoclinic phase volume fraction of $5.75\pm 0.91\%$.

With regard to implant samples, they exhibited similar crystallographic features to disc samples. However, some differences were noticed in monoclinic phase fractions. The mean monoclinic phase volume fraction in as-received, 5 mm diameter, ethylene oxide and sterilised implants was found to be 8.77 ± 1.32 . Hydrothermal ageing resulted in tripling of the monoclinic phase fraction of the studied implants (24.74 ± 1.41).

Diffraction patterns of representative samples from the four experimental (disc) groups are presented in Figure 14. Comparative plots for diffraction patterns of as-received disc versus implant are presented in Figure 15. Table 2 summarises the outcome of Rietveld analysis of all experimental groups.

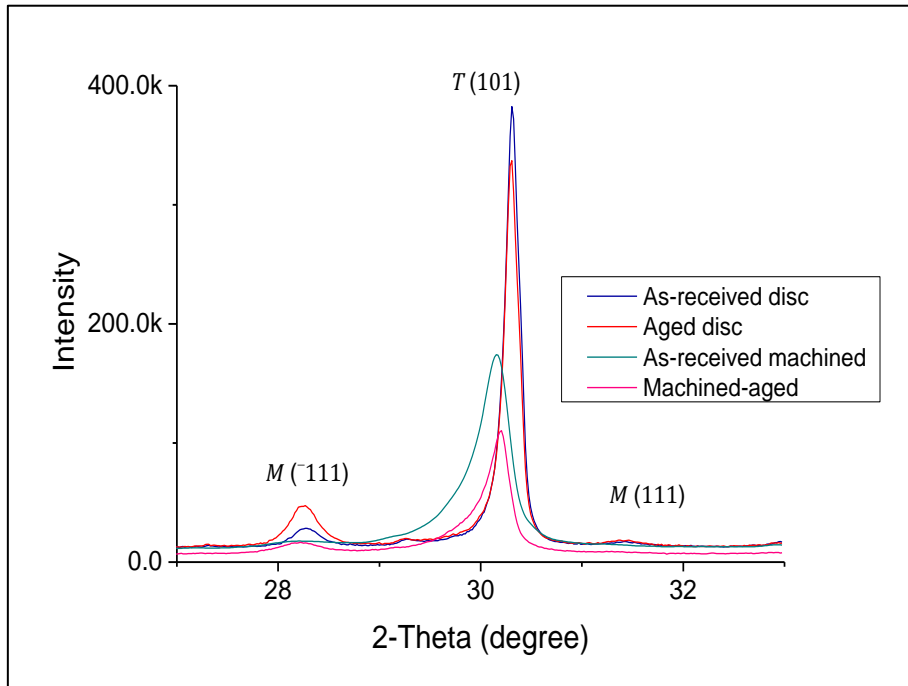


Figure 14. Comparative diffraction patterns of representative samples (discs) from all experimental groups.

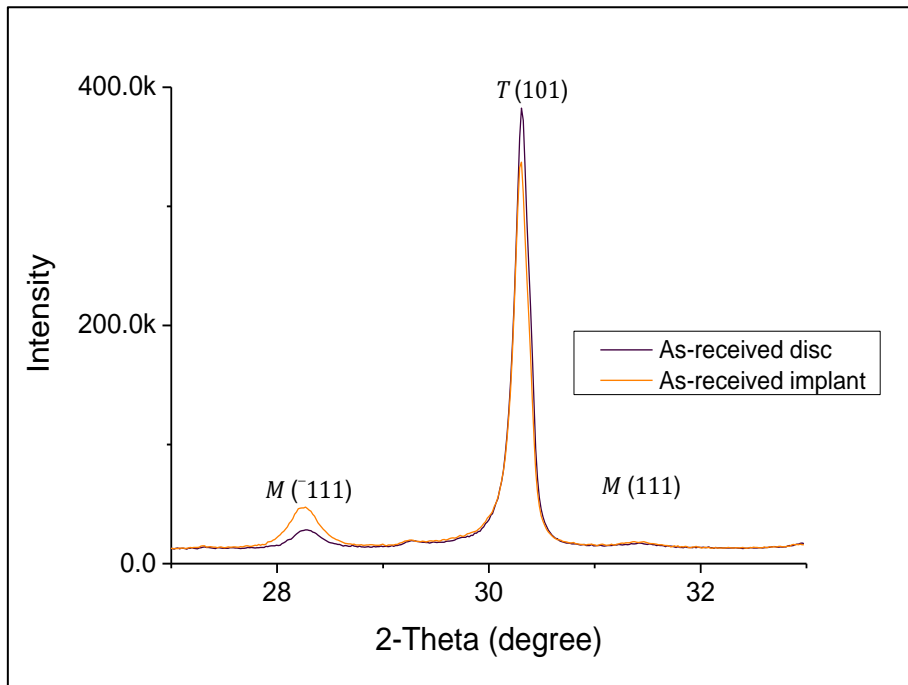


Figure 15. Comparative diffraction patterns of representative as-received disc and as-received implant.

Table 2. Summary of outcome of Rietveld analysis for **XRD** data.

V_m: monoclinic phase volume percentage, **PO** : preferred orientation

Sample	Group	V_m	PO	Microstrain
Discs	<i>As-received</i>	5.59(0.67)	Moderate	N/A
	<i>Aged</i>	13.43(2.11)	High	N/A
	<i>Machined</i>	1.73(0.38)	N/A	High
	<i>Machined-aged</i>	5.75(0.91)	N/A	Moderate
Implants	<i>As-received</i>	8.77(1.32)	Moderate	N/A
	<i>Aged</i>	24.74(1.41)	High	N/A

Analysis of diffraction data according to the Toraya’s modification of the Garvie and Nicholson method was performed. The overestimation of monoclinic volume fraction was notable with this method in comparison to Rietveld refinement. As-received discs had volume percentage of monoclinic phase of $10.77 \pm 2.28\%$. Aged discs group had a mean monoclinic volume fraction of $27.46 \pm 1.11\%$. Machined group had a mean monoclinic volume fraction of $5.25 \pm 2.02\%$. Machined-aged group had a mean monoclinic volume fraction of $9.54 \pm 1.81\%$. As-received and aged implants had a mean monoclinic volume fraction of $7.82 \pm 1.44\%$ and $30.91 \pm 3.39\%$, respectively. Table 3 compares the monoclinic phase fraction values calculated from the two different methods.

Table 3. Comparison of monoclinic phase fraction as calculated by two different methods. Mean (SD)

Sample	Group	M% (Toraya)	M% (Rietvled)
Discs	<i>As-received</i>	10.77(2.28)	5.59(0.67)
	<i>Aged</i>	27.46(1.11)	13.43(2.11)
	<i>Machined</i>	5.25(2.02)	1.73(0.38)
	<i>Machined-aged</i>	9.54(1.81)	5.75(0.91)
Implants	<i>As-received</i>	7.82(1.44)	8.77(1.32)
	<i>Aged</i>	30.91(3.39)	24.74(1.41)

Conventional **XRD** provides pivotal crystallographic information regarding zirconia **LTD**. However, only a limited thickness of the material can be studied owing to the limited X-Ray penetration ($\sim 5\mu\text{m}$) in **Y-TZP** materials. Thus, **LTD** involving the bulk of the material cannot be investigated. Also, conventional **XRD** may be of limited use to assess early stages of surface **LTD** as a result of the low precision of the technique for monoclinic contents lower than 5%. Furthermore, the technique provides no information on the distribution of transformed zones (monoclinic phase) along the studied depth of the material.

The depth of the **LTD** affected layer of **Y-TZP** (known as depth of transformed zone, **DTZ**) can be calculated utilising a method originally proposed by Kosmać *et al* (1981) (Kosmać *et al.*, 1981, Kosmać *et al.*, 1999). **DTZ** (μm) can be conservatively estimated using Equation 8:

$$DTZ = \frac{\sin \theta}{2 \mu/\rho} \ln \frac{1}{1 - X_m} \quad (8)$$

Where;

θ : the reflection angle and equals 15° ,

μ/ρ : mass absorption (attenuation) coefficient (0.0642), and

X_m : experimental integrated intensity ratio of monoclinic phase calculated from Equation 6

DTZ was significantly increased by the hydrothermal ageing process. As-received samples had a mean **DTZ** of $0.45 \pm 0.10 \mu\text{m}$ while aged samples had **DTZ** of $1.29 \pm 0.06 \mu\text{m}$. Machining of discs apparently removed part of the transformed layer ($0.21 \pm 0.08 \mu\text{m}$) and induced minimum $t \rightarrow m$. Machining seemed to minimise the tendency to $t \rightarrow m$ as a result of hydrothermal ageing. This was clear from the lower X_m , V_m and **DTZ** ($0.39 \pm 0.08 \mu\text{m}$) values of machined-aged group in comparison to aged group. Mean values of **DTZ** of as-received and aged implants ($0.32 \pm 0.06 \mu\text{m}$, $1.49 \pm 0.21 \mu\text{m}$) were not significantly different from **DTZ** values for as-received and aged discs, respectively. .

The major assumption of this method is, within the transformed surface layer, all the tetragonal grains have transformed into the monoclinic phase. However, pilot work performed utilising electron back scattered diffraction (**EBSD-SEM**) indicated that this was rarely the case with short **LTD** periods as will be discussed in Section 2.7.

Thus, such assumptions can be a major critique for such methods. Table 4 summaries **DTZ** for various experimental groups according to this method.

Table 4. Summary of **DTZ** in all experimental groups

Sample	Group	DTZ (μm)
Discs	<i>As-received</i>	0.45 ± 0.10
	<i>Aged</i>	1.29 ± 0.06
	<i>Machined</i>	0.21 ± 0.08
	<i>Machined-aged</i>	0.39 ± 0.08
Implants	<i>As-received</i>	0.32 ± 0.06
	<i>Aged</i>	1.49 ± 0.21

The aforementioned limitations of conventional **XRD** can be ameliorated. A more informative **LTD** data can be extrapolated utilising **XRD** at fixed incident angles or the so called, glancing incidence angle **XRD** (**GIAXRD**). The principle of this technique relies on the fact that penetration depth of X-Rays decreases with decreasing the X-Ray beam incident angle (Chevalier *et al.*, 2007b, Gremillard *et al.*, 2010). At each incident angle, X-Ray penetration depth can be defined as the thickness of the sample contributing to 99% of the diffracted intensity (**T**) for a given incident angle θ . It can be given by Equation (9):

$$T = 0.5 L \sin \theta \quad (9)$$

L is the X-Ray path length which is the length the X-Ray travels through a material with the given characteristics, until 99% of the intensity is absorbed and only 1% of the initial intensity is transmitted. **L** can be derived from mass absorption (attenuation) coefficient (μ/p) and true density of the material (ρ) using the following equation:

$$I_L = I_0 \times \exp^{-\left(\frac{\mu}{p}\right)\rho L} \quad (10)$$

μ/p is expressed as a combination of the specific gravity of the material and the estimated packing density (Panalytical, 2011). Table 5 summarises penetration depths at incidence angles of 1-15° as calculated by the penetration depth calculator within the HighScore Plus software (Panalytical B.V, The Netherlands). Figure 16 demonstrates a schematic representation of **GIAXRD** setup.

Table 5. Summary of maximum X-Ray penetration depth at various incident angles.

<i>Incident angle</i>	<i>Depth (μm)</i>	<i>Incident angle</i>	<i>Depth (μm)</i>
1	0.641	9	5.745
2	1.282	10	6.377
3	1.922	11	7.007
4	2.562	12	7.636
5	3.201	13	8.261
6	3.839	14	8.885
7	4.476	15	9.505
8	5.111		

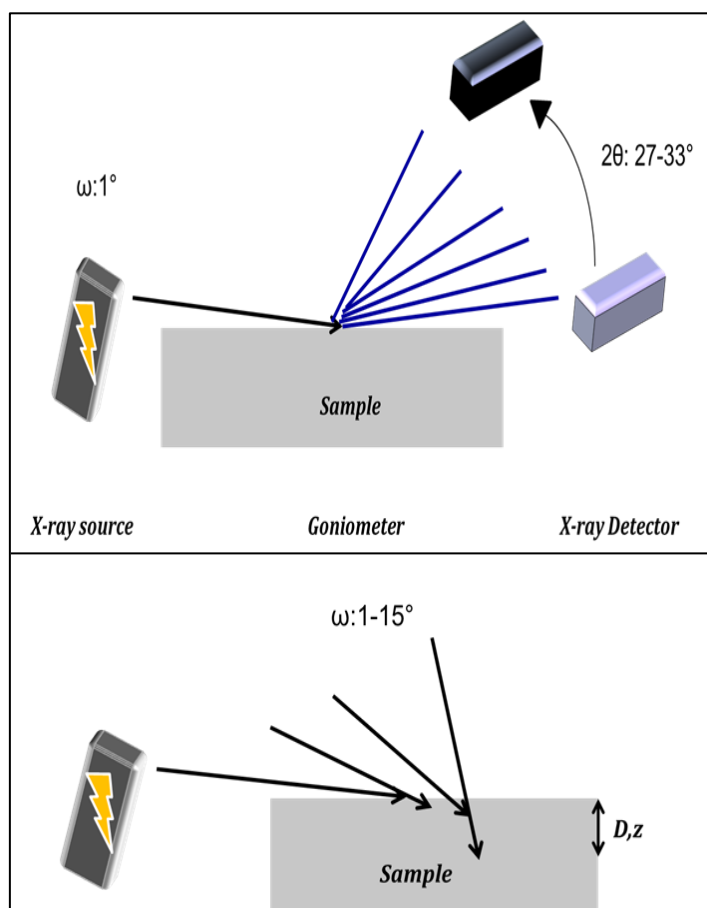


Figure 16. Schematic representation of *GIAXRD* setup.

GIAXRD setup is similar to conventional *XRD* with one exception that X-ray source remains stationary at low incident angles (ω). Diffracted signal is collected along the whole 2θ range (top). The X-ray incident angle is increased gradually to increase the depth of X-ray penetration and thereby the investigated thickness of the material (D,z).

Simple plotting of monoclinic phase fraction obtained utilising **GIAXRD** versus calculated X-Ray penetration depth at each incidence angle can provide limited qualitative information. This is attributed to the fact that most of the crystallographic information provided by the diffracted beam come from the near sub-surface, even at high incidence angles (Gremillard *et al.*, 2010). Additionally, at lower incidence angles, the surface-bulk signal ratio increases. This may lead to overestimation of the monoclinic phase fraction as the analysed depth is smaller at such small angles (Chevalier *et al.*, 2007b).

Gremillard *et al* (2010) proposed a **GIAXRD** based method to evaluate monoclinic phase fraction depth profile in zirconia ceramics. They relied on the fact that the contribution of the total diffracted X-Ray beam intensity from a small volume located at certain depth (Z), is proportional to the volume itself (d_z), monoclinic phase fraction at the same depth ($f_m(z)$) and to the transmitted beam intensity by the material ($i(z)$). They mathematically derived that the real transformation depth profile F_m can be given as an inverse Laplace transform of the fitted function of X_m -penetration depth data points or $\frac{X_m(u)}{u}$, where (u) is the reciprocal of penetration depth. Experimentally, the calculation of real transformation depth profile (F_m) begins with plotting X_m (acquired from the Garvie and Nicholson Equation (6)) versus penetration depth at different incidence angles. The second stage is to fit X_m with an appropriate mathematical function. F_m can be then calculated as the inverse Laplace transform of the fitted function (Gremillard *et al.*, 2010).

In this project, **GIAXRD** was performed on as-received and aged discs using a Phillips X'Pert Powder diffractometer (Panalytical B.V, The Netherlands) with Ni filtered Cu K $_{\alpha 1}$ (1.5406 Å) at generator voltage and tube current of 40Kv and 40 mA, respectively. Samples were mounted to a cut-off, ultra-low background, custom-made aluminium holder utilising a minimum amount of plasticine that was completely obscured from the X-Rays under the sample. A 10 mm fixed incident beam mask was used to determine the width of the exposed area and the beam length was adjusted to 2 mm. Diffraction data was collected in a classical Bragg-Brentano geometry from 27° to 33° 2θ at fixed incident angles between 1-15°. Step size of 0.05° and dwell time of 100 sec were used. **FDS** were used at $1/32$ and active detector length was reduced to $1/4$ (0.528) in order to decrease air scattering and enhance resolution. Outputs were

charted using the X'Pert Data Collector software (Panalytical B.V, The Netherlands). X_m was calculated using Equation (6) for each diffraction data set. X_m values were plotted against calculated penetration depths and fitted, using Gnuplot software (version 4.2, UK), to an exponential function given by Equation 11:

$$X_m^{fit} = \frac{Df_{mb} - \ln(1-S)f_{m0}Z_0}{D - Z_0\ln(1-S)} \quad (11)$$

Where;

D is the calculated X-Ray penetration depth contributing for a fraction S to the diffracted intensity, F_{m0} : maximum monoclinic phase fraction at the most superficial layer of the material, and F_{mb} : lowest monoclinic phase fraction at depth Z_0

Inverse Laplace transform was obtained for the fitted function using MATLAB 22 software (version 7.9, MathWorks, UK). Real transformation depth profile F_m is given by Equation 12:

$$F_m(Z) = H(Z) \left[(f_{m0} - f_{mb}) \exp^{-\frac{Z}{Z_0}} + f_{mb} \right] \quad (12)$$

Where;

H is the heaviside function, and Z is the corrected transformation depth

Quantitative analysis regarding the spatial distribution of the monoclinic phase within the examined thickness of the material was carried out. The monoclinic fraction F_m was deduced from an inverse Laplace transform of an exponential fit of X_m . The fit of X_m data suggested that $F_{mb}= 5.71 \times 10^{-10}$, $F_{m0}= 0.21$ and $Z_0= 0.81$. These findings can be interpreted as the monoclinic fraction F_m at the surface layer was 20.99% and decreased exponentially to a negligible concentration within the first 0.81 μm (Z_0) which is equivalent to a layer that is 2-3 crystals thick.

Aged sample was analysed according to the above method. Fitting of X_m data revealed that $F_{mb}= 0.032$, $F_{m0}= 0.23$ and $Z_0= 1.31$. The findings can be interpreted as the monoclinic fraction F_m at the surface layer was 22.93% and decreased exponentially within the first 1.31 μm (Z_0). As both curves of exponential degradation did not cross the x-axis, the estimation of Z_0 from the fitting function was confirmed using first derivative (tangent line) fitting the data points obtained and incidence angle of 2° and 3°. Z_0 was 0.93 and 1.2 μm for as-received and aged samples, respectively. Experimental (X_m) and the real transformation depth profiles (F_m) of the monoclinic

phase in as-received and aged samples as well as a comparative plot of F_m of both samples are depicted in Figure 17. Complete script including commands of fitting and inverse Laplace transform deduction is presented in Appendix D.

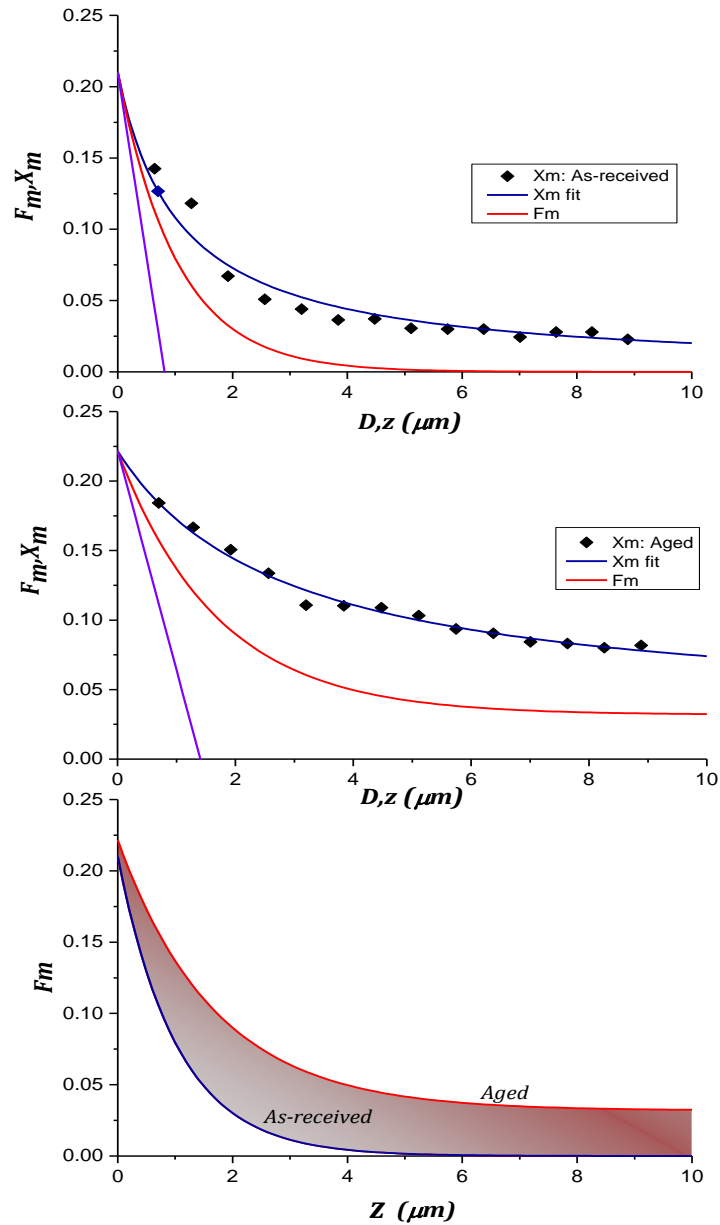


Figure 17. Transformation depth profile along thickness of material as estimated by *GIAXRD*.

X_m (\blacklozenge) is plotted against maximum penetrations depth of X-rays (D) at each incidence angle. Exponential function is fitted to X_m data (blue) to calculate experimental phase transformation depth profile. An inverse Laplace transform was created (red) to determine real phase transformation depth profile (F_m) along corrected depth (z). The depth of transformed zone was estimated using a first derivative linear function fitted to F_m profile (Amber). Top graph represent data from as-received sample, middle represent aged sample and bottom is a comparative graph of F_m for both samples.

2.6.2 Raman spectroscopy on discs and implants

Raman spectroscopy is a non-invasive spectroscopic technique that is used to identify chemical composition of various substances and detect phase changes of multi-phasic and pleomorphic materials. It utilises monochromatic light in the *UV*/visible region, usually a laser, to illuminate a sample. It relies on the inelastic scattered irradiation to determine the vibrational and rotational status which is exclusive for each molecule (Colthup *et al.*, 1990).

When irradiated with a laser beam, Raman active materials undergo inelastic and elastic (Rayleigh) scattering. The former constitutes less than 1×10^{-5} of the scattered radiation beam and it is different from the original beam in terms of frequency. This sort of scatter is very relevant as it can be detected by a spectrometer after being amplified. The molecular basis of this process can be explained by the deformation of the electric field caused by laser beam interaction/excitation with electron clouds in the atomic structure. This eventually causes changes in the polarisability of the molecules with respect to its vibrational motion. The Raman spectrum is composed of Stokes ($\mathbf{VF}_0 - \mathbf{VF}_m$) and Anti-Stokes ($\mathbf{VF}_0 + \mathbf{VF}_m$) beams which have lower and higher frequencies than the original monochromatic beam (\mathbf{VF}_0), respectively. \mathbf{VF}_m is the vibrational frequency of the molecule (Colthup *et al.*, 1990, Ferraro and Nakamoto, 2012).

On the other hand, elastic (Rayleigh) is the dominant type of scatter. The scattered radiation has the same frequency of the original monochromatic beam. This type of scatter poses a challenge to detect the weaker inelastic spectrum which can be masked by the predominant Rayleigh scattering. Instruments such as notch filters, tuneable filters, laser stop apertures, double and triple spectrometric systems are used to reduce Rayleigh scattering (Colthup *et al.*, 1990, Ferraro and Nakamoto, 2012).

Raman spectroscopy has been widely used to investigate $t \rightarrow m$ phenomenon in zirconia ceramics. Having a confocal microscope arrangement linked to it, Raman spectroscopy has wide application in studying stress and/or hydrothermally induced $t \rightarrow m$ within Vickers indentation imprints and fractured surfaces (Clarke and Adar, 1982, Bowden *et al.*, 1993, Magnani and Brillante, 2005, Gogotsi *et al.*, 2007, Pittayachawan *et al.*, 2007). The major advantages of Raman spectroscopy are its versatility and non-invasiveness. The shape, physical state, geometry and colour of the

sample are not critical when using this testing method. In addition, samples do not require mounting or preparation steps such as coating or polishing. This is of a major importance in studying zirconia based dental ceramics as mechanical grinding and polishing can induce $t \rightarrow m$ and undermine the reliability of the technique.

Raman spectroscopy also allows studying small samples and confined areas within the same sample which is a pivotal feature that allows studying curved implant threads where the majority of stress concentration is believed to be present (Sanon *et al.*, 2013). However, materials with strong fluorescent characteristics can interfere with the quality of results (Ferraro and Nakamoto, 2012). A simplified schematic representation of micro Raman spectroscopy is shown in Figure 18.

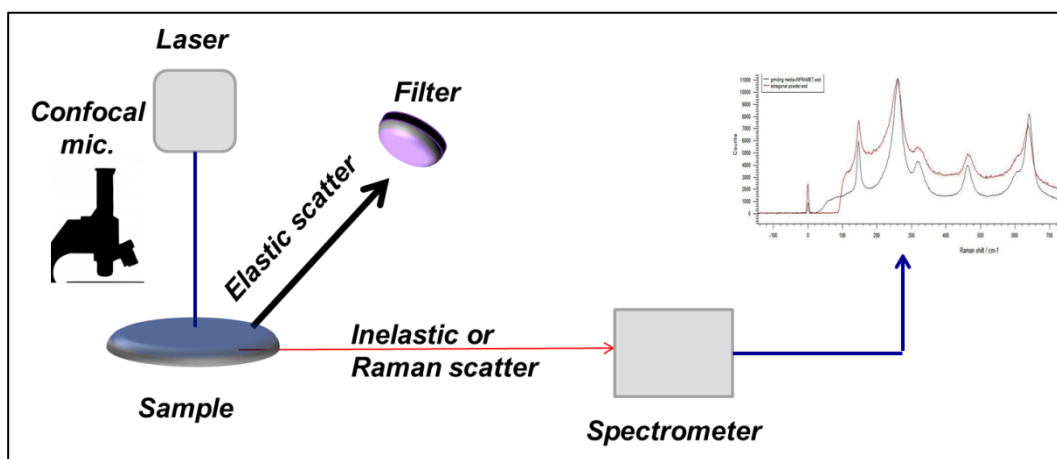


Figure 18. Schematic representation of Raman confocal microscopy/spectroscopy.

In this project, Raman spectroscopy was used to investigate hydrothermally and stress-induced $t \rightarrow m$ in both injection moulded disc and implant *Y-TZP* samples. A Renishaw inVia confocal Raman microscope operating with a 488 nm Ar⁺ laser at 10% power was used (Renishaw Gloucestershire, UK). The machine was equipped with an ultra-low noise, high sensitivity RenCam CCD detector. Images of the regions of interest were acquired using the $\times 20$ and $\times 50$ objectives of the coupled Leica confocal microscope. Machine calibration was done before scanning samples using a reference silicone material. Reference material was scanned using 488 nm Ar⁺ laser for one accumulation and for 1 sec acquisition time at full laser power.

All samples were scanned for two accumulations, 30 sec acquisition time, 2400 l/mm (vis) grating and 0% laser focus. Raman spectra of pure monoclinic, tetragonal and cubic zirconia powders (Tosoh, The Netherlands) were generated and used as reference samples for phase identification. Pure tetragonal powder was obtained from sintering 84% tetragonal and 16% monoclinic powder (TZ-3-YSE, Tosoh, The Netherlands). Sintering process was performed in a standard furnace (Elite, Leicestershire, UK) with heating rate of 100 °C/hour until target temperature of 1350 °C that was maintained 2 hours. The sintered powder was left to cool down at room temperature.

WiRE3.4 software was used to identify the distribution and quantify different phases in the created area maps (Renishaw, Gloucestershire, UK). Raman spectra of pure monoclinic, tetragonal and cubic powders are depicted in Figure 19. Characteristic peaks for each phase tabulated against Raman shifts are summarised in Table 6.

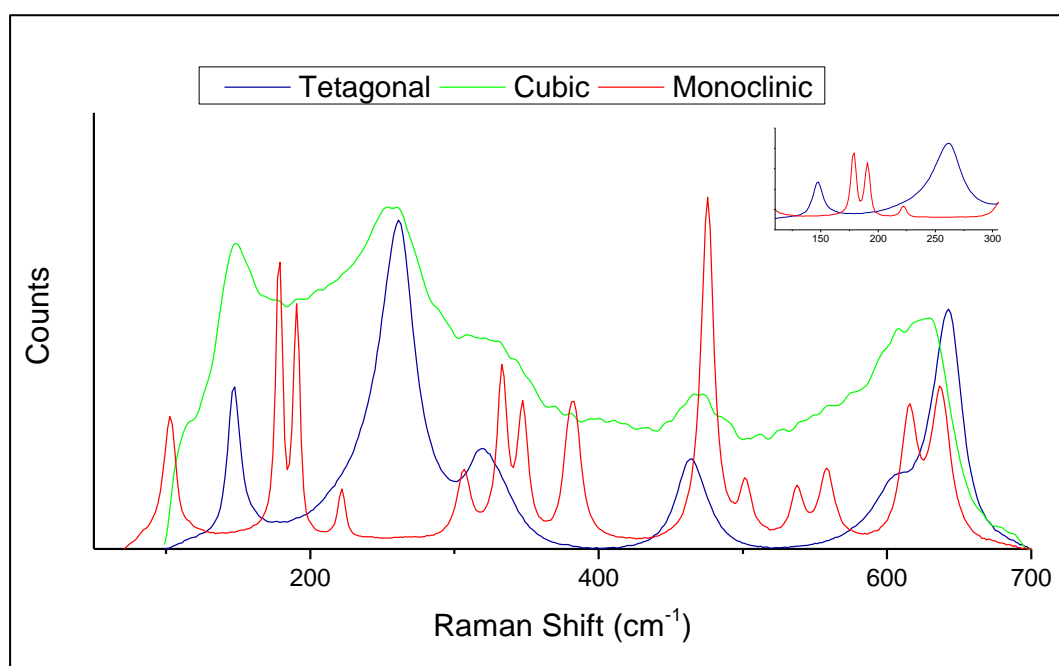


Figure 19. Reference Raman spectra for tetragonal, monoclinic and cubic phases of *Y-TZP*. Intensity of Raman scatter is plotted against Raman shifts for pure, single phase *Y-TZP* materials. Peaks of the Raman spectrum of cubic phase completely overlap with peaks in the tetragonal phase spectrum. Monoclinic phase has a distinct spectrum in the Raman shift range 100-400 cm^{-1} as shown in the inset.

Table 6. Peaks at Raman shifts for various, pure, single phase *Y-TZP* powders.

<i>Raman shift (cm⁻¹)</i>		
<i>Monoclinic</i>	<i>Tetragonal</i>	<i>Cubic</i>
102.77	147.00	146.41
178.39	260.67	256.74
190.68	321.08	330.64
221.89	463.96	469.59
306.45	642.20	525.55
333.01	607.88	631.51
347.54		
381.98		
475.45		
501.99		
537.46		
558.33		
615.24		
637.24		

Representative as-received and aged discs and implants were studied. Point scans and individual spectra within map scans were analysed using WiRE 3.4 software. When an area scan was done, 56 Raman spectra were acquired from 400 μm^2 areas in as-received and aged discs. For area scans, WiRE3.4 software was used to calculate overall monoclinic phase fraction within the entire scanned area based on basic component analysis model.

The model was constructed based on reference spectra for pure powder samples. Statistical adjustment of lack of model fit and background (second degree polynomial function) was performed automatically by the software. For point scans and individual spectra within area scans, WiRE3.4 software was used to calculate area under tetragonal peaks at Raman shifts ≈ 145 and 260 cm^{-1} and monoclinic peaks at Raman shifts ≈ 178 and 190 cm^{-1} .

The amount of monoclinic phase volume fraction (V_m) was calculated using Equation 13, originally described by Clarke and Adar (Clarke and Adar, 1982):

$$V_m = \frac{I_m^{178} + I_m^{190}}{I_m^{178} + I_m^{190} + 0.97(I_t^{145} + I_t^{260})} \quad (13)$$

Where;

I_m represents the area under monoclinic peaks at specific (superscripted) Raman shifts, and I_t represents the area under tetragonal peaks at specific (superscripted) Raman shifts

Analysis of Raman spectra obtained from point scans revealed pure tetragonal phase composition of as-received disc and implant samples. Aged discs and implants had mean monoclinic phase volume fraction of $3.52 \pm 1.32\%$ and 4.82 ± 0.19 , respectively. Representative Raman spectra obtained for as-received and aged discs and implants are presented in Figure 20 and Figure 21, respectively. Obtained spectra were compared to reference Raman spectrum for pure tetragonal **Y-TZP** powder.

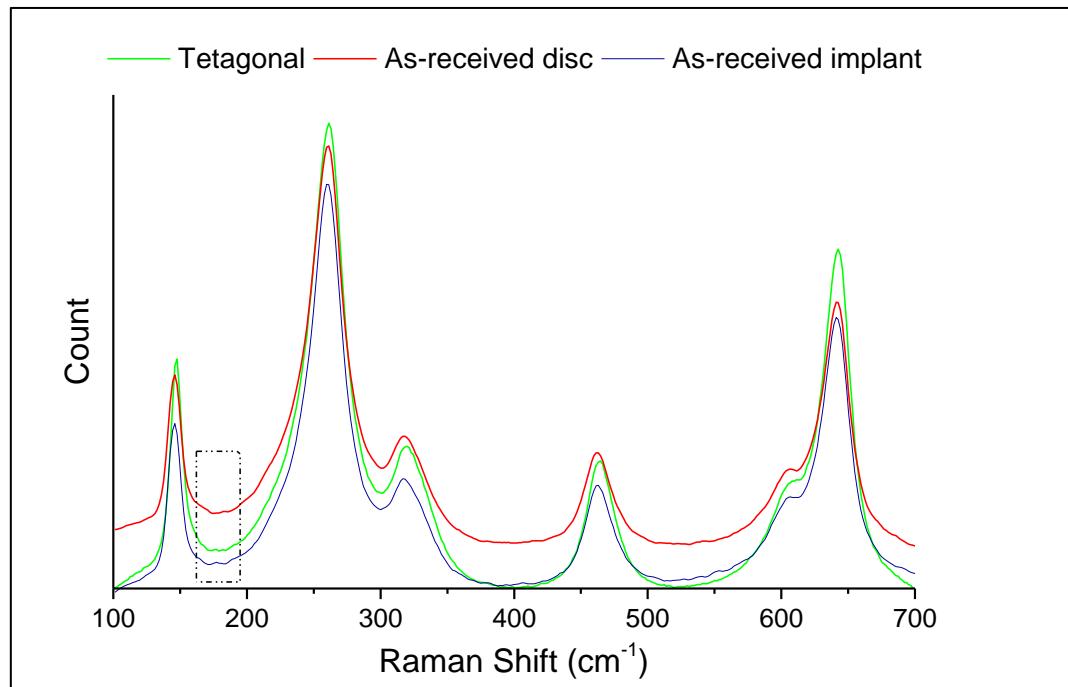


Figure 20. Comparative graph of Raman spectra obtained from pure tetragonal **Y-TZP**, as-received disc and implant.

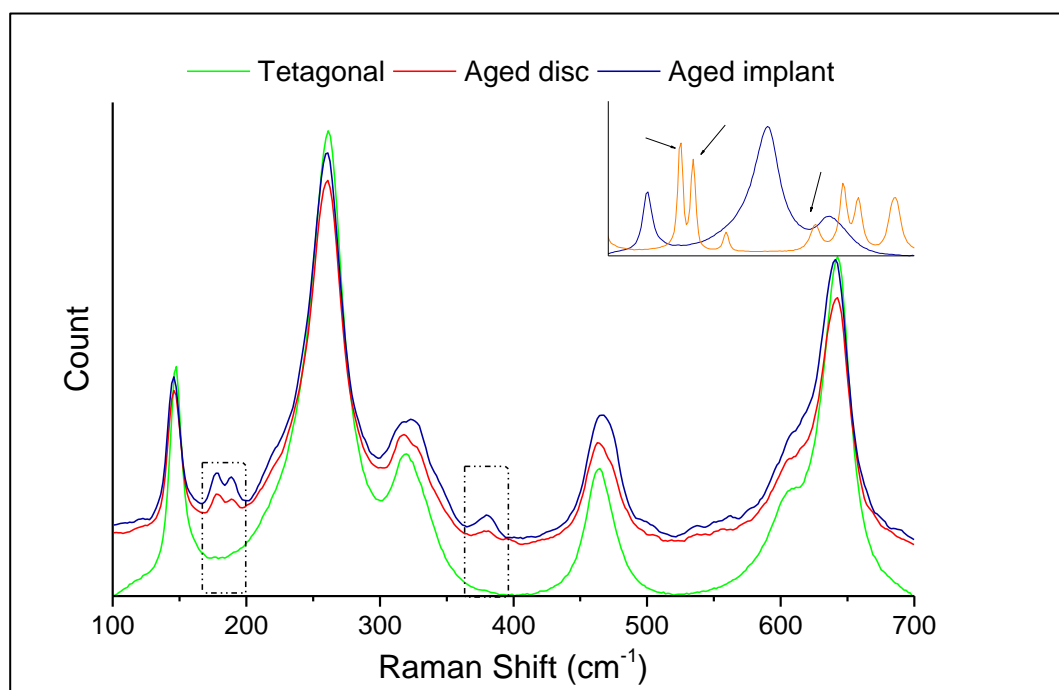


Figure 21. Raman spectra for aged disc and implant.

The composite graph demonstrated the appearance of peaks at Raman shifts characteristic for monoclinic phase (delineated with dashed rectangles) as a result of hydrothermal ageing. Spectra from aged disc (red) and implant (blue) samples are compared to pure tetragonal powder (green). Inset demonstrates the unique difference between Raman spectra of monoclinic (orange) and tetragonal (blue) phases in Raman shift range of 100-400 cm^{-1} .

Analysis of Raman spectra of the area scans obtained for as-received discs and implants revealed that less than 1% of the scanned area was composed of monoclinic phase. The studied area in the aged discs and implants contained $5.84 \pm 0.35\%$ and $6.17 \pm 0.71\%$ of monoclinic phase, respectively. These values were calculated by WiRE3.4 software based on the reference spectra from the powder samples.

The effect of machining on $t \rightarrow m$ was investigated using Raman spectroscopy. A scan along a line extending from unprepared to machined area was performed before and after hydrothermal ageing. Analysis of acquired Raman spectra was performed utilising WiRE3.4 software similar to area scans. For machined samples, highest concentration of monoclinic phase (approximately 2%) was noticed in the interface between machined and non-machined surfaces.

Similarly, the highest concentration (approximately 4%) of monoclinic phase was in the area of interface in the machined-aged samples. This may be attributed to the difference in the nature of residual stresses and microstrain introduced in the interface (tensile stresses) and inside of the machined area (compressive stresses).

Furthermore, machined areas exhibited relatively less monoclinic phase after ageing in comparison to interface and non-machined areas. Monoclinic and tetragonal phase profiles were plotted along the line scan and presented in Figure 22 for representative machined and machined-aged samples.

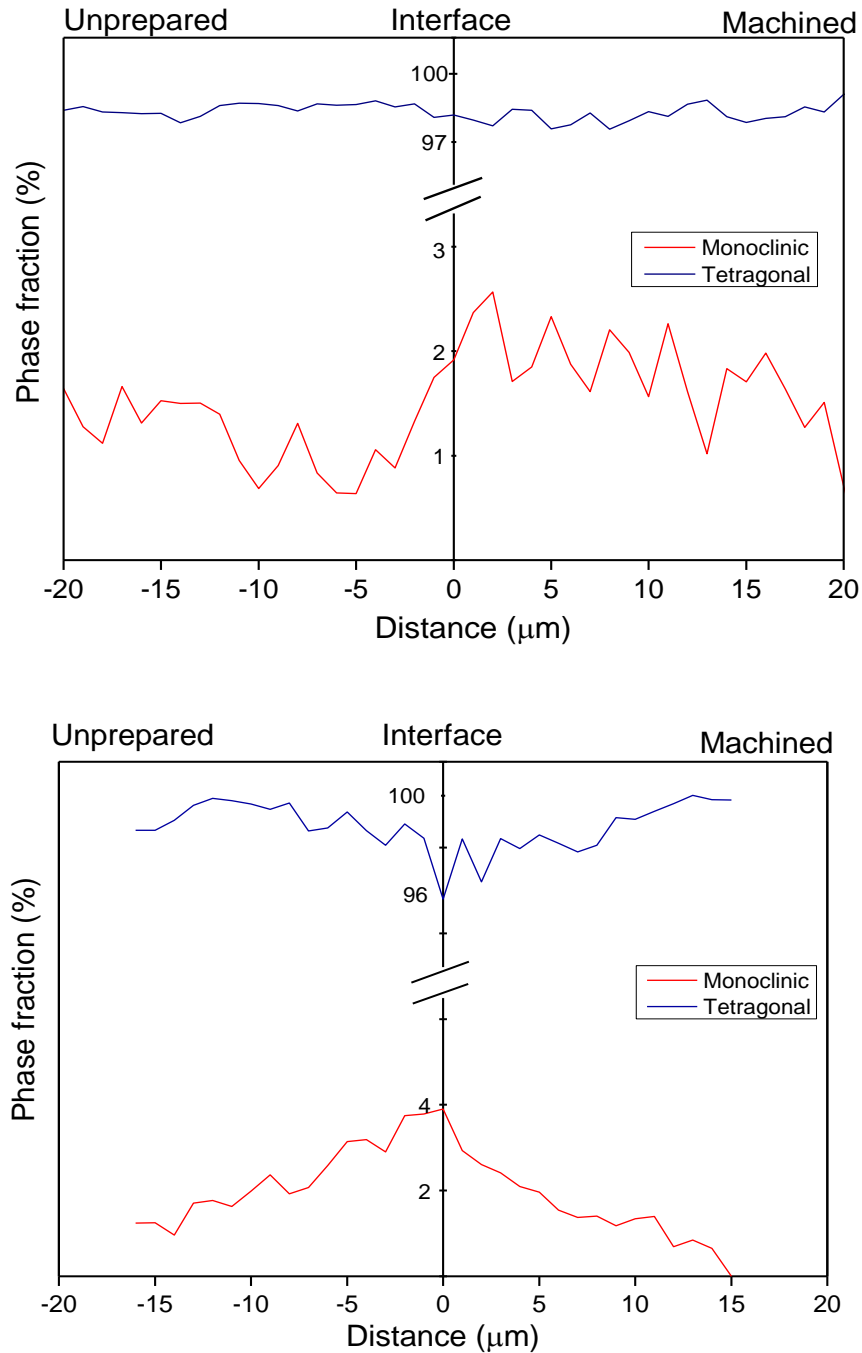


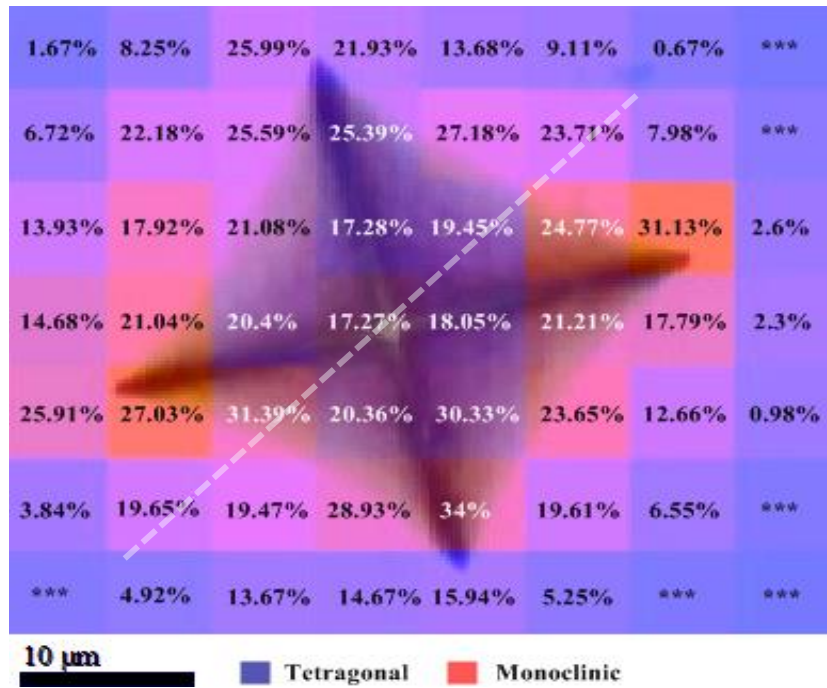
Figure 22. Monoclinic and tetragonal phase profile along line Raman scans in machined and machined-aged groups.

Raman spectra obtained along the line crossing mechanically ground and sound areas of as-received (top) and aged (bottom) disc samples. Monoclinic (red) and tetragonal (blue) phase fractions were calculated at 1 μm intervals using Clarke and Adar equation.

The effect of mechanical stimuli such as Vickers microindentation was also studied (microindentation procedure explained in Section 3.2.4). Vickers indentations were made in as-received and aged samples. The indenter's imprint and surrounding area was studied using Raman spectroscopy. Area scans were performed and analysed as described earlier in this Section. The area including the Vickers indentation in the as-received sample revealed that 20.36% of the material was permanently transformed to monoclinic phase as a result of stress-induced $t \rightarrow m$. The overall value was calculated directly utilising basic component model constructed using WiRE3.4 software. Individual Raman spectra within the area scan were analysed according to Equation (13) to calculate monoclinic phase fraction at specific points within the area.

Values were used to construct a phase fraction map that was overlaid on the indentation imprint micrograph obtained during Raman spectral acquisition. Highest amount of monoclinic phase was noticed at the corners of the imprint where cracks propagate most of the time. Moreover, a high percentage of monoclinic phase was notably present in the area where the side planes of the indenter applied the load. Diagonal line scans across the centre and the sides of the indentation imprint were acquired to confirm the above findings. Similar to area scans, the sides of the imprints exhibited the higher monoclinic phase fraction in comparison to the centre in both, as-received and aged samples. Monoclinic phase fraction along the line scan for as-received and aged samples was profiled and data indicated that the monoclinic phase diminished in areas away from the indent. Figure 23 shows mapped and line-profiled monoclinic phase fraction around Vickers indentation imprint made on as-received sample.

Hydrothermal ageing and Vickers indentation had similar pattern and amount of $t \rightarrow m$ where 23.12% was permanently transformed to monoclinic phase as a result of the two processes combined. The monoclinic phase fraction along the line scan for an aged sample was also profiled and results were similar to map data as the monoclinic phase diminished in areas away from the indent. Figure 24 shows the monoclinic phase fraction map and line profile overlaid on Vickers indentation imprint made on aged sample.



Vickers indent: as-received

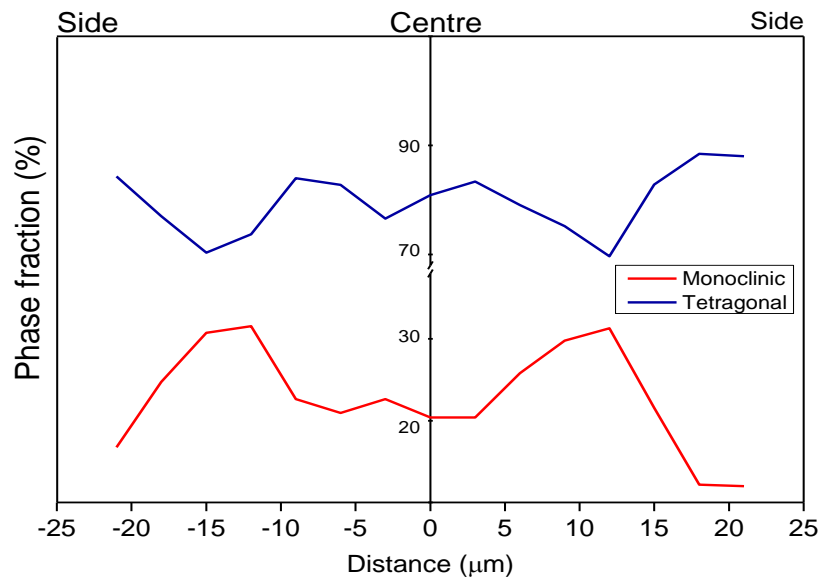
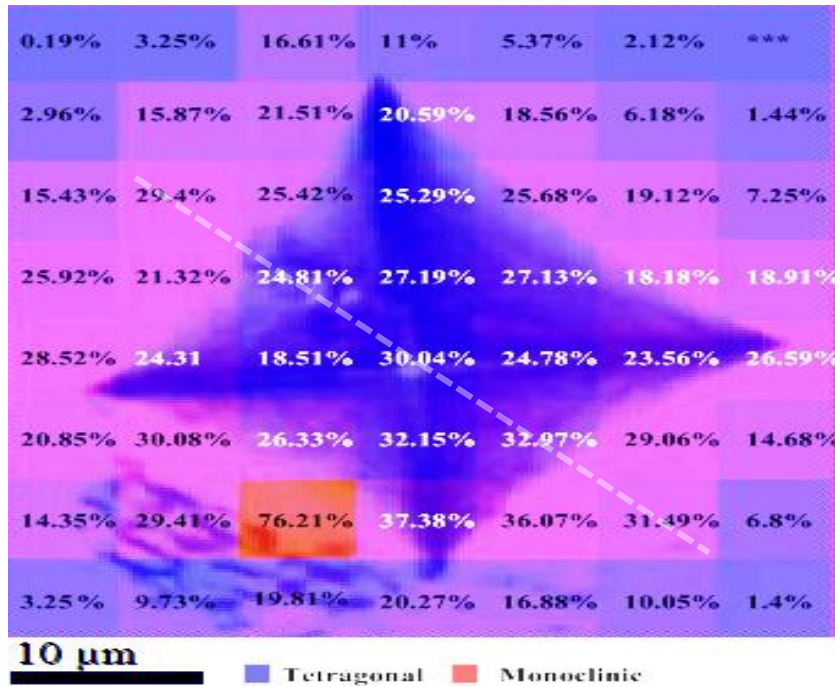


Figure 23. Monoclinic phase map and line profile within Vickers indentation imprint on as-received sample.

Top, phase transformation map around indent. The increase in red hue demonstrate higher monoclinic phase. Areas marked with (***) indicated pure tetragonal phase or monoclinic phase below detectable level. Bottom, line profile of monoclinic and tetragonal phase fractions along diagonal running outside the indent, crossing two sides and the centre (---).



Vickers indent: Aged

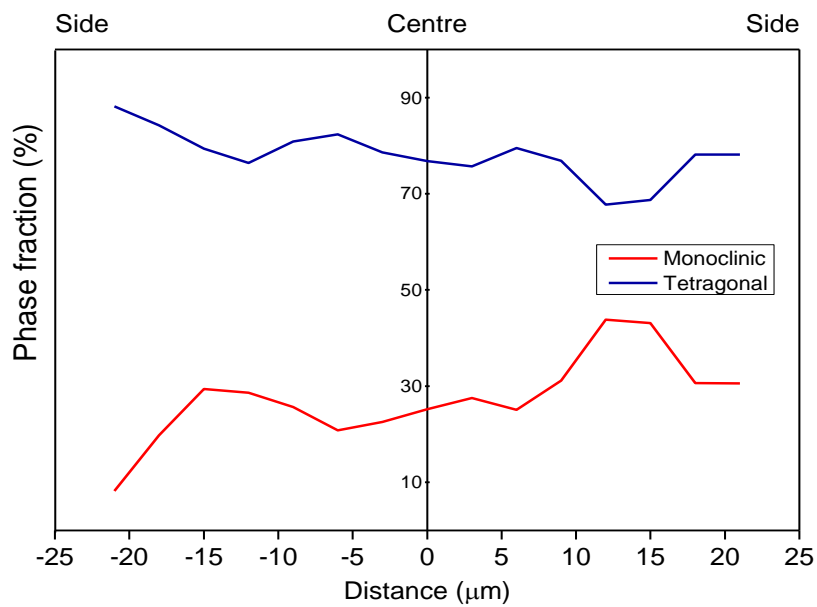


Figure 24. Monoclinic phase mapping and profiling around Vickers indentation imprint on aged sample.

Fractured surfaces obtained from biaxial flexural strength test (Section 3.2.2) were also examined using Raman spectroscopy. The distribution of monoclinic phase was determined in the area of fracture origin and along the whole thickness of the fractured surface using point and area scans in as-received and aged samples. Point scan of the fracture origin in as-received sample revealed that 7.29% of the studied area was permanently transformed to monoclinic phase. An area scan of the whole fracture origin in the same sample revealed an approximately similar value, 5.15%. An aged sample exhibited higher monoclinic phase fraction in the fracture origin. Analysis of Raman spectra revealed 15.27% and 12.07% of monoclinic phase fraction in the fracture origin according to point and area scans, respectively. Mapping of the monoclinic phase across the whole thickness of the fractured surfaces was performed using WiRE3.4 software. Monoclinic phase was concentrated in the areas of fracture origin (the area subjected to tensile stresses) and in the centre of the fractured surface where primary Wallner line propagated. Figure 25 shows monoclinic phase distribution across the thickness of fractured an as-received sample.

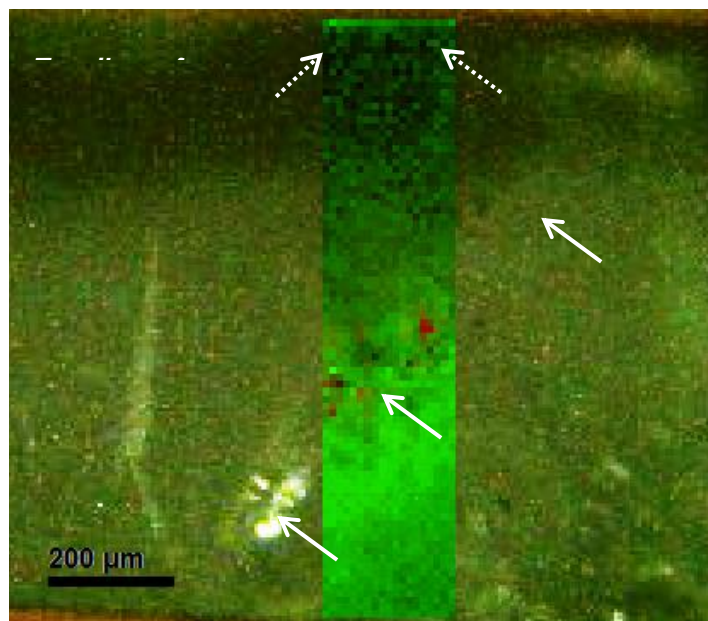


Figure 25. Monoclinic phase fraction Raman map across fractured surface.

MicroRaman map of monoclinic (red black hue) and tetragonal (green) phase fractions. Monoclinic phase concentrated in area of primary Wallnar line (→) and tensile surface of the as-received fractured disc (--->)

2.6.3 Synchrotron diffraction on discs and implants

Synchrotron radiation is a type of electromagnetic radiation that is generated from charged particles (electrons or positrons) moving along curved trajectories, with a large radius of curvature at ultra-relativistic speeds. Synchrotron radiation is intrinsically superior to laboratory generated X-Rays used in bench *XRD* techniques due to higher beam brightness and intensity in several hundred orders of magnitude in comparison to laboratory X-Ray tubes (Willmott, 2011).

Synchrotron radiation can be invaluable in studying the *LTD* phenomenon in *Y-TZP* dental ceramics. The high energy and intensity beams have the ability to penetrate the whole thickness of the sample and thereby, provide essential information about the crystalline structure of the surface as well as the bulk of the studied material.

Synchrotron X-Ray diffraction data was collected using Beamline I15 at the Diamond Light Source, UK. A $100 \times 100 \mu\text{m}^2$ Synchrotron X-Ray beam, 67 keV, was used to penetrate through discs and implants. A 2D detector array (Perkin Elmer 1621 AN) was used to collect Debye-Scherrer rings from each sample. Representative Debye-Scherrer rings obtained from as-received and aged discs are presented in Figure 26.

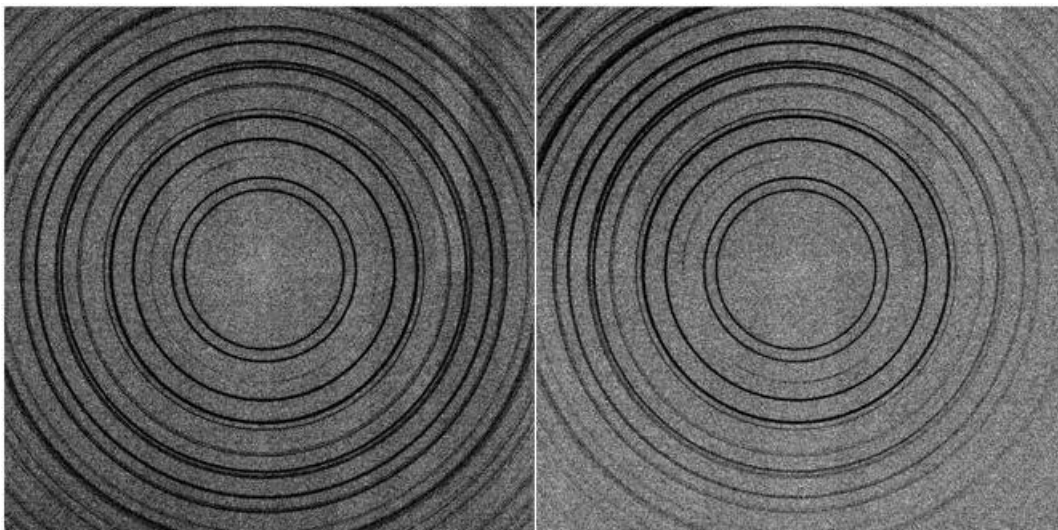


Figure 26. Debye-Scherrer rings obtained from representative as-received (left) and aged (right) discs.

The program Fit2D was used in order to generate 2θ /intensity plots from the image plate. 2θ data was converted to D-spacing (d) and further to laboratory **XRD**, 2θ data according to Equation 14:

$$2\theta = \frac{360}{\pi} \text{ASIN}\left(\frac{1.5406}{2d}\right) \quad (14)$$

Synchrotron diffraction data was plotted for as-received, aged, machined and machined-aged discs in addition to as-received and aged implants. Beam was incident on the samples and diffraction patterns were collected in transmission geometry for 1.6-11.8 2θ range (or 10-110 2θ range according to conventional lab **XRD** parameters using Cu radiation). Data was plotted using OriginPro software (version 9.1, OriginLab, USA).

An X-Ray diffraction pattern for pure tetragonal **Y-TZP** powder was obtained for 2θ range (10-110°) using a Phillips X'Pert Powder diffractometer (Panalytical B.V, The Netherlands) with Ni filtered Cu $K_{\alpha 1}$ (1.5406 Å) at generator voltage and tube current of 40 Kv and 40 mA, respectively. The obtained diffraction pattern was used for comparison with Synchrotron diffraction data.

Synchrotron diffraction patterns for all samples were completely indistinguishable. Upon comparison with the **XRD** pattern of pure tetragonal **Y-TZP** powder they were identical. All diffraction patterns were compared to reference, stick diffraction pattern obtained from **ICCD** (Yashima *et al.*, 1994). Synchrotron and laboratory **XRD** of all experimental groups and reference samples are presented in Figure 27.

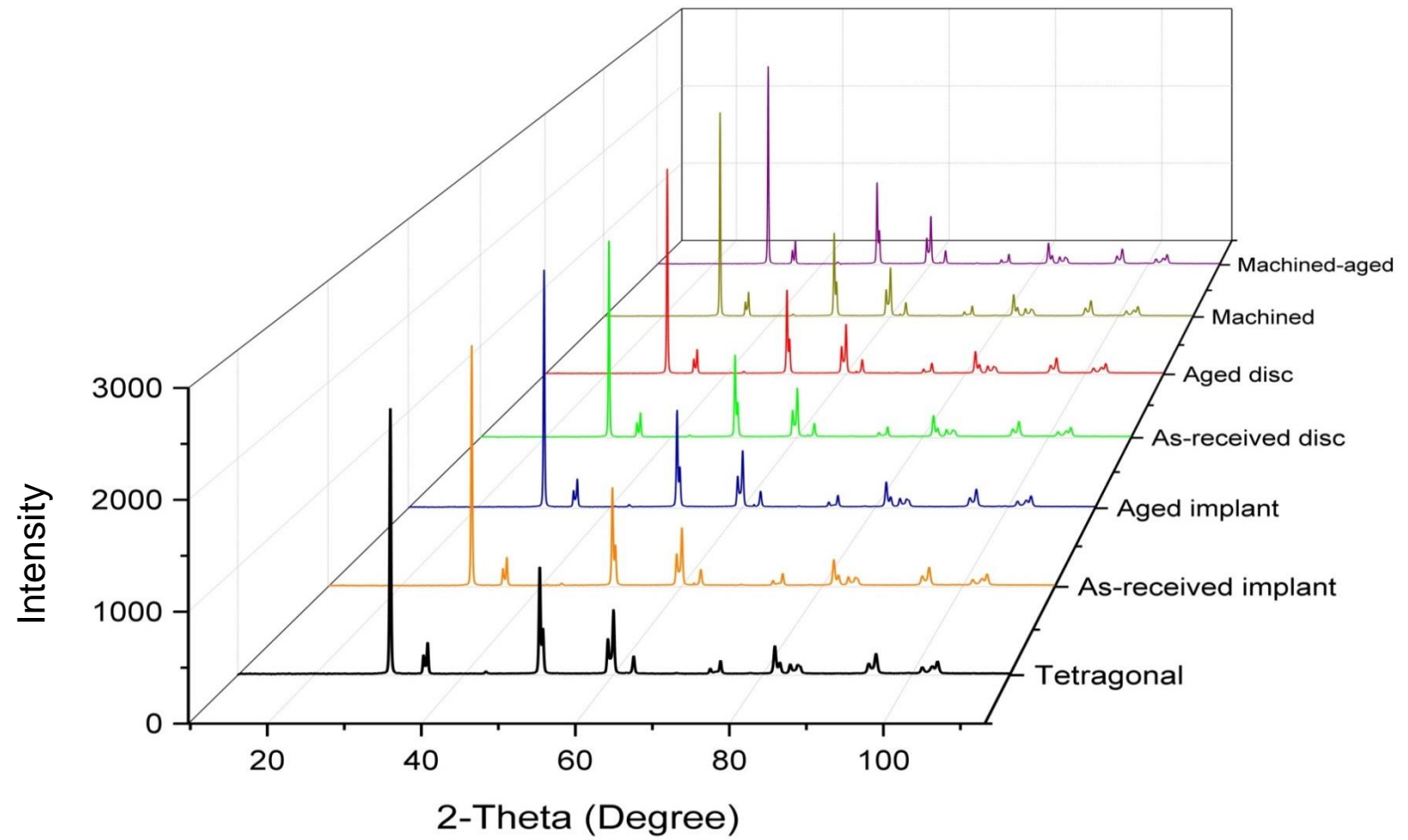


Figure 27. Comparative Synchrotron X-ray diffraction obtained for representative samples from all experimental groups.

2.6.4 Direct characterisation and imaging techniques

Crystallographic techniques detect the crystallographic changes as a result of hydrothermally- or stress-induced $t \rightarrow m$. Surface profilometry and *SEM*, can however be used to image directly the effect of *LTD* and its subsequent morphological and structural changes in the transformed layer. The transformed layer appears rougher owing to uplifts, microcracking and extensive crystalline pull-out among the transformed crystals. Additionally, *LTD* can be identified by *SEM* as microcracking increases the contrast of the transformed area (Chevalier *et al.*, 2007b). High resolution transmission electron microscopy (*TEM*) can also be used in a similar fashion. Additionally, it can be used to collect diffraction patterns of single or multiple crystals that can be further analysed and matched to monoclinic or tetragonal reference patterns.

2.6.4.1 White light interferometry or optical profilometry

Surface profilometers produce a high resolution surface map of a studied sample. Profilometers can be divided into contact and non-contact types. The former utilises a diamond stylus to analyse surface topography. The movement of the stylus along the sample dictates the surface profile. Non-contact or optical profilometers utilise light and optical systems for data acquisition. The relative difference in the vertical position of the tested surface with respect to the optical system and difference in light reflection dictate the surface profile. Optical profilometers are widely used for surface characterisation owing to their extremely high, sub-micron resolution and the ability of maintaining the integrity of the sample as opposed to stylus based, contact counterparts. Simplified schematic representation of optical interferometry profilometer is shown in Figure 28.

In this project, four discs were mounted using a transparent acrylic resin (ClaroFast, Struer, UK) utilising an electro-hydraulic programmable dual cylinder hot mounting press (CitoPress-20, Struer, UK). Samples were then mirror polished using Tegamin preparation system-20 (Struer, UK). The process comprised of four stages, plain grinding, fine grinding, polishing and oxide polishing. Various stages and products used are shown in details in Table 7. Optical microscopy at $\times 1000$ magnification using Dark Field and Differential Interference Contrast was used to assess levels of remaining deformation (BXiS, Olympus, UK). Two discs were hydrothermally aged according to the protocol described in Section 3.3.1.

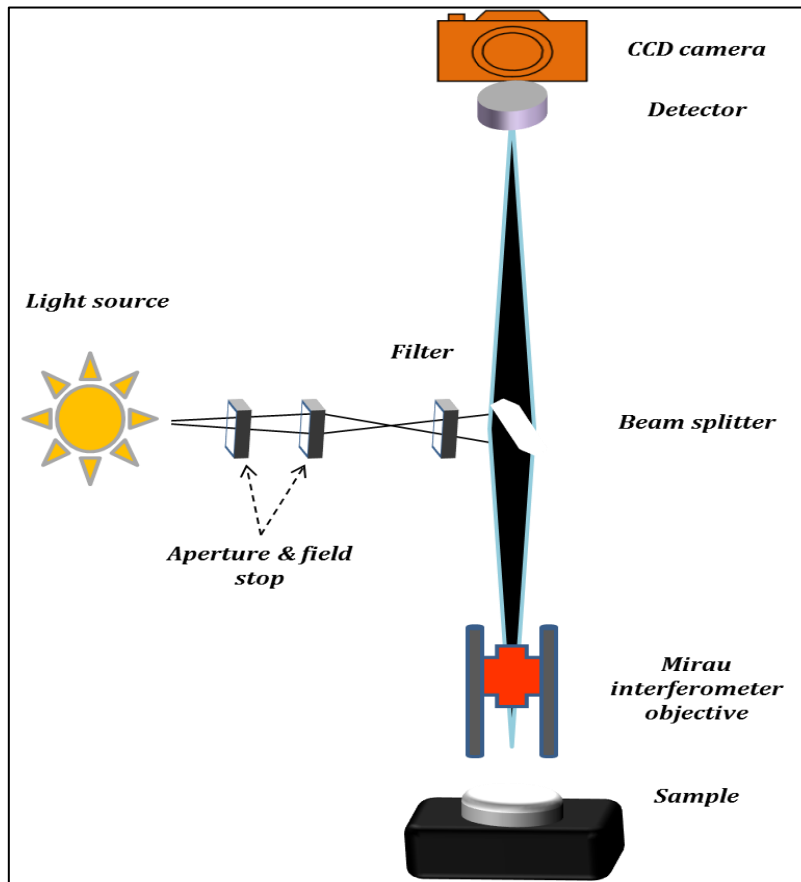


Figure 28. Schematic representation of 3D optical profilometers or white light interferometer.

Table 7. Summary of *Y-TZP* discs polishing protocol.

<i>Stage</i>	<i>Cloth</i>	<i>Speed (rpm)</i>	<i>Suspension</i>	<i>Pre-dosing (ml/min)</i>	<i>Dosing (ml/min)</i>	<i>Lubricant</i>	<i>Force</i>	<i>Time (min)</i>
Plain grinding	MD-Piano 220	300	N/A	N/A	N/A	H ₂ O	25	Until flat
	MD-Piano 1200	300	N/A	N/A	N/A	H ₂ O	25	
Fine grinding	MD-Largo	150	DiaPro Allegro/Largo 9mm	1	10		20	4
	MD-Largo	150	DiaPro Largo 3mm	1	10		20	4
Polishing	MD-Dac	150	DiaPro Dac 3mm	1	9		15	3
	MD-Dur	150	DiaPro Dur 1 mm	1	9		15	3
Oxide polishing	MD-Nap	150	OP-S 0.04 mm				20	10

Surface roughness was assessed using a 3D white light, optical (interferometry) profilometer (NPFLEX, Bruker, UK). Three random areas (1 mm×0.84 mm) within each sample were scanned. All measurements were made using vertical scanning interferometry mode, scan speed of 1 mm/sec and a standard working distance objective of ×100. Vision64[®] software (Bruker, UK) was used to analyse acquired data and apply a Gaussian filter to flatten the acquired images. The mean 3D, aerial roughness-height descriptive parameter (S_a), and its 2D roughness parameter analogue (R_a) were calculated for polished and polished-aged groups samples (n=2 per group).

S_a represents the arithmetic mean of the absolute values of the surface departures from the mean plane. R_a represents arithmetic mean of calculated roughness height calculated over the entire a measured line profile length.

Polished samples exhibited a mean S_a and R_a values of 19.23 ± 1.24 nm and 19.83 ± 0.81 nm, respectively. Polished aged samples had significantly higher mean S_a and R_a values as indicated by one-way ANOVA test, $p < 0.05$ (23.11 ± 0.88 nm and 23.74 ± 1.27 nm, respectively). In contrast to polished samples, scans from polished-aged samples revealed 3-10, bead-like structures. Such structures may represent the uplifts, crystalline pull-outs or martensite reliefs associated with the hydrothermally induced *LTD*.

Topographical maps and surface roughness profile of representative areas in as-received and aged samples are presented in Figure 29.

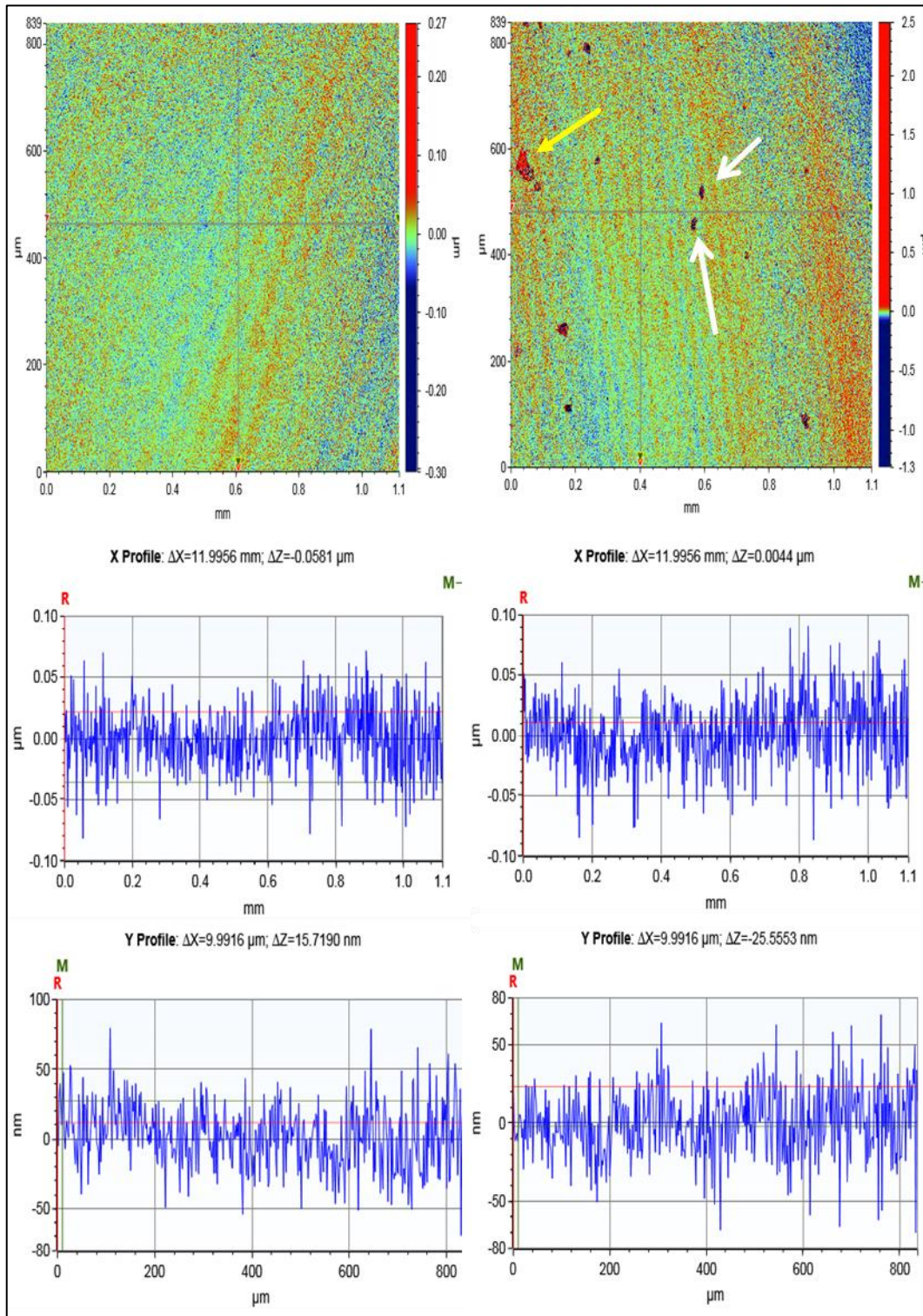


Figure 29. White light interferometry for mirror-polished *Y-TZP* discs.

Surface roughness map (top), x-axis line profile (middle) and y-axis line profile (bottom) of as-received (left) and aged (right), mirror-polished *Y-TZP* discs. Arrows point at martensite reliefs or surface pull-outs as a result of hydrothermally induced $t \rightarrow m$.

2.6.4.2 Scanning electron microscopy

SEM can be used to examine the effects of **LTD** on the surface of **Y-TZP** materials. It can detect uplifted, transformed zones and microcracks. However, the high depth of field of **SEM** renders them suboptimal with regard to detection and quantification of early stages of **LTD** (Chevalier *et al.*, 2007b). In order to study the depth/extension of **LTD** in the material, a cross section of the material should be prepared. This, in fact, poses a challenge as grinding and polishing of **Y-TZP** material may cause further stress induced $t \rightarrow m$ and subsequent microcracking.

Under **SEM**, areas unaffected by **LTD** exhibit a dark grey or black colour while transformed zones have bright white colour owing to the increased contrast as a result of microcracking and loss of crystal cohesion (Chevalier *et al.*, 2007b). Under high magnifications, intergranular cracks can be seen as a result of **LTD**. Crystal twinning is another sign of $t \rightarrow m$ that can be seen in subsurface layers upon imaging a cross section of the material (Sanon *et al.*, 2013). Crystal twinning can be looked at as the subsurface polymorph of surface uplift. It occurs as the transforming tetragonal grain is mechanically constrained within the dense crystalline lattice and the formation of martensite relief is not possible. Loss of grain boundaries is a notable consequence to such an event. The combination of these changes causes the transformed layer to appear distinctively heterogeneous in comparison to the homogenous tetragonal crystals (Keuper *et al.*, 2014).

A non-invasive cross section preparation that has minimal potential to induce $t \rightarrow m$ on **Y-TZP** sample has been made feasible with the introduction of focused ion beam (**FIB**) systems. Addition of an electron beam column and integration of **SEM** to **FIB** systems (Dual beam **FIB-SEM**) have revolutionised preparation and imaging of delicate and sensitive samples and opened novel avenues for preparing samples for material analysis (Langford and Clinton, 2004).

FIB-SEM has been widely used to study hydrothermal and stress-induced $t \rightarrow m$ in zirconia ceramics. This is attributed to the versatility of such systems that allow studying **LTD** in irregular, non-flat samples such as the threads of dental implants. Additionally, **FIB-SEM** enabled studying $t \rightarrow m$ induced at micron scale within nano- and micro-indentations (Gaillard *et al.*, 2008, Niu *et al.*, 2008, Helmick *et al.*, 2011, Jiménez-Piqué *et al.*, 2012, Massimi *et al.*, 2012, Nickel *et al.*, 2013, Sanon *et al.*,

2013, Keuper *et al.*, 2014). In a classical geometrical arrangement of **FIB-SEM** systems, **FIB** milling is performed perpendicular to the sample surface. The sample is tilted at 52° in relation to the **SEM** electron beam as shown in the oversimplified schematic representation (Figure 30).

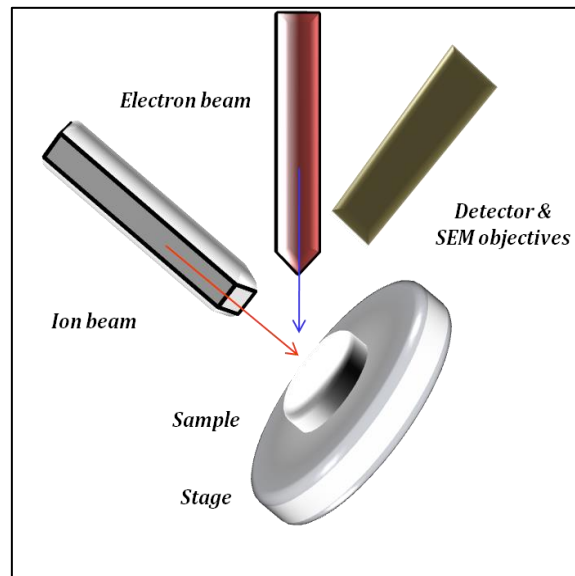


Figure 30. Schematic representation of **FIB-SEM** setup.

In this project, a **FIB-SEM** system was used to investigate the effect of hydrothermal ageing on the studied discs and implants. The work was performed at the Leeds Electron Microscopy and Spectroscopy Centre in the University of Leeds. The **FIB-SEM** system was comprised of precise **FIB** and a high resolution **SEM** with etch and deposition capabilities and equipped with a Schottky field emission source (Nova 200NanoLab, FEI, USA). A liquid gallium ion source was used to operate the **FIB** at a voltage of 30 kV.

For the disc samples, a random area in the centre of the sample was chosen for investigation. Whereas in implants, acquisition was performed in the tip of the first thread in the endosseous part of the implants. Samples were sputter coated with 20 nm thick layer of platinum using a high resolution sputter coater (Agar scientific, UK). A 1 µm thick protective layer of platinum was deposited on the area of interest. This layer helps to maintain the fine details of the top most surface of the studied slice by preventing ion induced damage and milling artefacts. Milling currents varied from 0.3–3 nA for large material volume removal. Taking into account the wedging effect and redeposition of milled particles, a volume of 15×30×30 µm was

removed initially in order to produce a milled slice that was at least 20 μm deep and 10 μm wide. A lower current (10–50 pA) was used for cleaning and refining the area of interest from artefacts and re-deposited material. Ion beam etching was performed to enhance contrast of the grain boundaries. *SEM* images were acquired at high magnifications in secondary electron (*SE*) and backscattered electron (*BSE*) modes using conventional Everhart–Thornley (*ET*), the lens (*TL*) and Palladium constant pressure (*PD(CP)*) detectors. A low primary beam voltage of 3–5 kV was used for acquisition to minimise sample charging. Figure 31 demonstrates step by step the technique to prepare a single slice using *FIB*.

The as-received discs and implants demonstrated similar crystalline features when imaged at high magnifications. *SE* and *BSE* imaging revealed homogenous and dense crystalline structure. No porosity or voids could be detected within the studied cross sections. Crystals demonstrated a diameter less than 500 nm with well-defined grain boundaries. Al_2O_3 particles were scarcely dispersed over the examined areas of interest. The obtained slices were thoroughly examined for any of the reported signs of *LTD* including; microcracking, crystal twinning, crystal pull-out or loss of material homogeneity. Within as-received implants and discs, none of these signs could be detected upon using various types of detectors. These features are demonstrated in Figure 32.

Examination of hydrothermally aged samples revealed minimal surface changes. The superficial 1-2 μm were distinctively different from the underlying material which can be attributed to $t \rightarrow m$. The layer looked heterogenous, crystals exhibited ill-defined boundaries, the appearance of some areas suggested presence of crystal twinning and/or pull-out. The transformed area had different contrast and poor resolution upon imaging which made detection of microcracks unfeasible. The material below the transformed zone exhibited features similar to those for as-received samples as shown in Figure 33. Figure 34 compares *FIB-SEM* slices from as-received and aged implants.

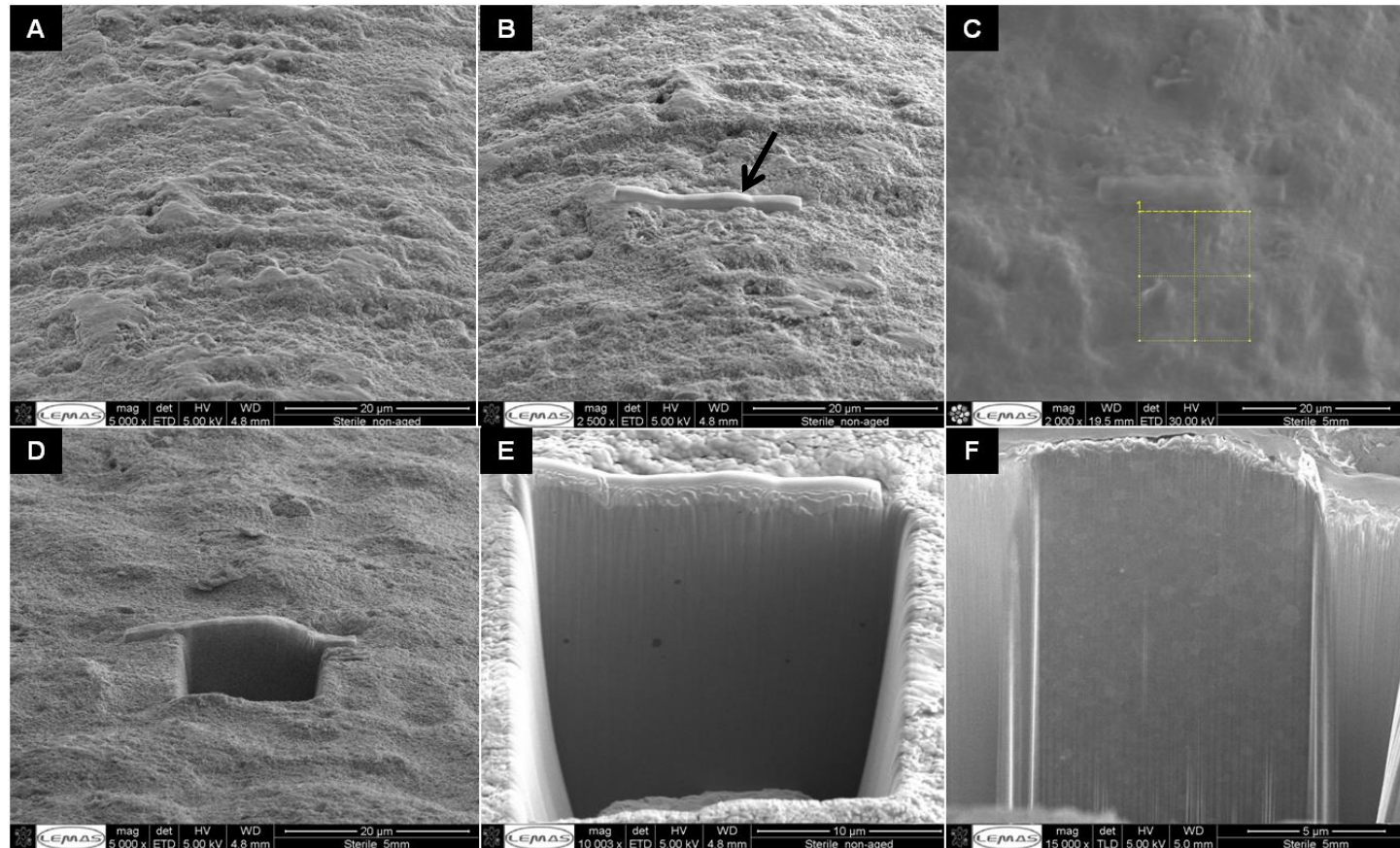


Figure 31. Stages of **FIB-SEM** processing and imaging of zirconia dental implant.

A, Determination of area of interest at the zenith of first implant thread. B, Deposition of platinum layer (→). C, Defining dimensions of area to milled. D, Initial high current ion beam milling. E, Further material removal to expose larger area for higher **SEM** magnification. F, Appearance of the section of interest after first low voltage ion etching cycle.

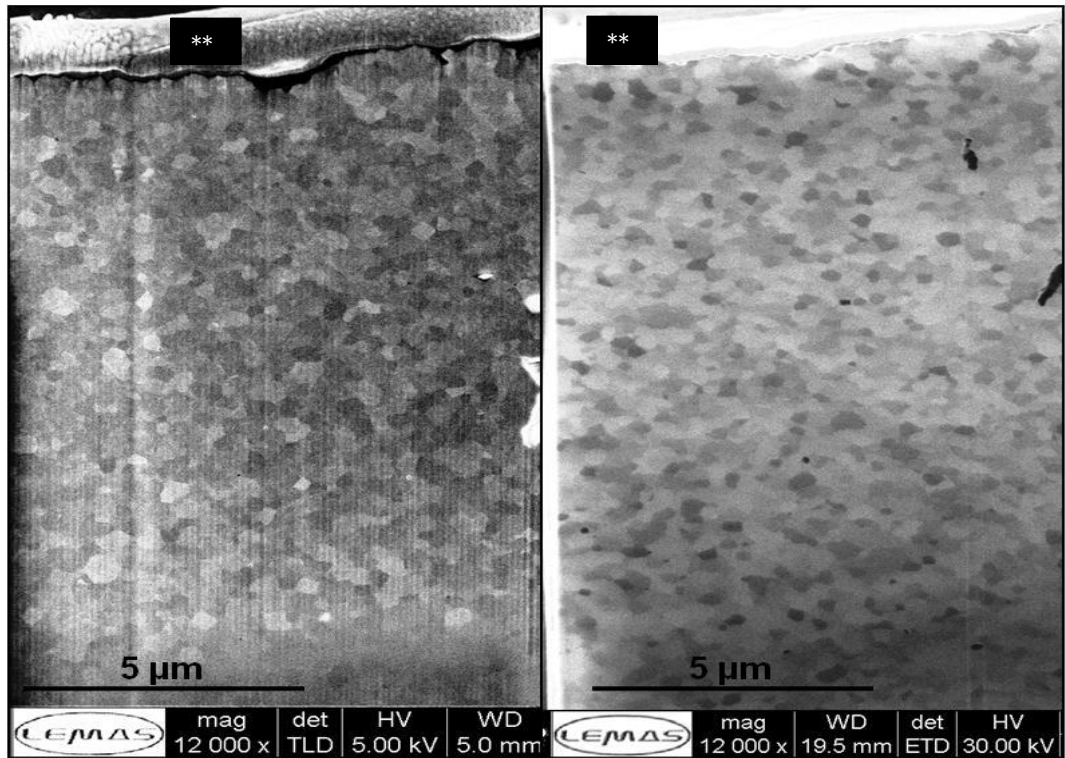


Figure 32. **FIB** section from as-received implant viewed **SEM** at high magnification **FIB** created section showing densely packed, well-defined, homogenous crystals. Platinum layer is annotated with (**). No signs of $t \rightarrow m$ could be detected in the surface, subsurface or bulk layers of the material. Views were captured using **TLD** (left) and **ETD** (right) detectors

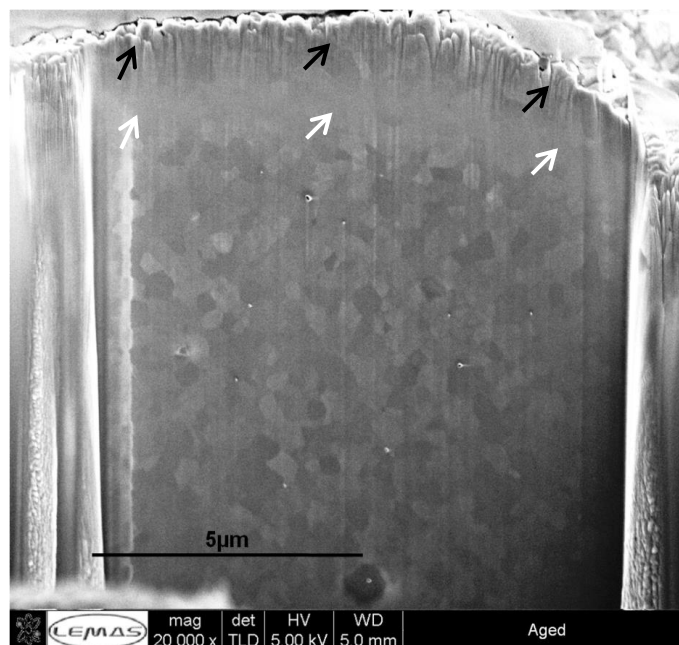


Figure 33. **FIB** created section from aged sample showing loss of homogeneity of the surface crystals (\rightarrow) which could be a sign of $t \rightarrow m$. The subsurface and bulk layers of the material demonstrated characteristics similar to as-received counterpart. Area annotated with (\rightarrow) is an artefact.

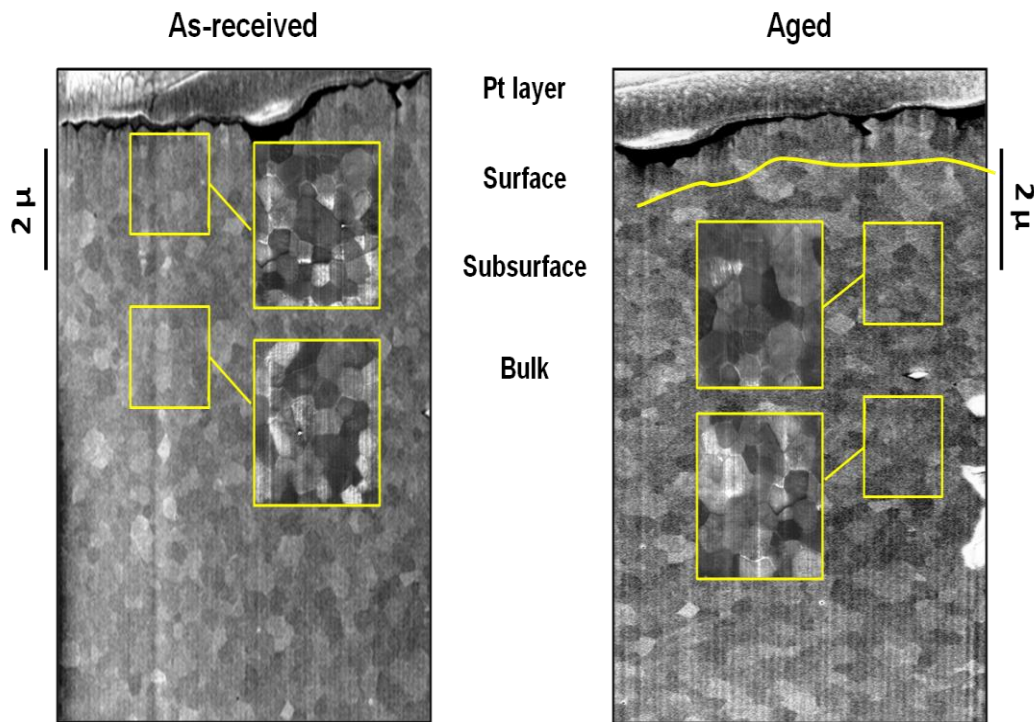


Figure 34. Comparative **FIB-SEM** image for as-received (left) and aged (right) implants.

Aged sample demonstrated transformed $< 1\mu\text{m}$ layer as indicated by the loss of crystal homogeneity, ill-defined boundaries or the so called, crystal twinning. The bulk of the material was still untransformed in both samples.

The use of **FIB-SIM** enables the study of a small area that may or may not be representative of the whole sample. The use of a non-invasive and damage-free preparation method was envisaged to image larger areas. Ion beam milling systems are essentially similar to **FIB** but perform at a larger scale. They can be used for cross-section polishing of **SEM** samples, such as zirconia, that can be adversely affected by mechanical polishing. In this project, a vacuum load-lock and liquid nitrogen cold stage ion polishing system was used to prepare as-received and aged discs for **SEM** analysis (Ilion⁺ II System, model 697, Gatan, UK). Prior to ion beam polishing, as-received and aged discs were cross sectioned using metal electroplated diamond cutting wheel operated in table top cut-off machine at 0.1 mm/sec feed speed and rotational speed of 1000 rpm (Accutom-5, Struers, UK). Copious amount of water cooling was used during the process. The broad beam ion polishing system was used to prepare a triangular area (150 μm deep, 600 μm wide at the base) from the cross section of the as-received and aged samples as shown in Figure 35.

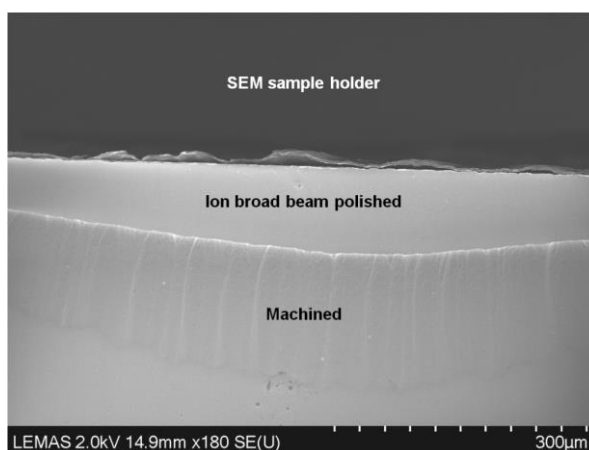


Figure 35. Partial ion broad beam polishing of machined zirconia sample.

The polished triangular zone intervening between mounting screw and machined part of the sample

The system operated with dual Ar^+ guns (0.29 and 0.32 μA), beam energy of 6.0 keV, 20° milling angle and operating chamber pressure of (7×10^{-5} Torr). Samples were then sputter coated with 10 nm thick layer of platinum using Agar high resolution sputter coater (Agar scientific, UK). Polished areas were examined using high resolution *SEM* equipped with cold field emission gun (Series SU8230, Hitachi, Japan). Characterisation of elemental composition of representative as-received sample was carried out using *EDS* system (Oxford Instruments, UK). The system is equipped with a silicone drift detector (X-Max[®]) and pulse processor (x-stream-2) (Oxford Instruments, UK). Data was analysed using sophisticated elemental analysis software (AztecEnergy, Oxford Instruments, UK).

The as-received sample exhibited similar crystallographic features to those observed upon using the *FIB-SEM* system. The sample exhibited a dense crystalline structure and well-defined grain boundaries. None of the characteristics signs of *LTD* was noticed in as-received sample. Figure 36 shows *SEM* images at different magnifications and with different detectors for a representative as-received sample. *EDS* analysis revealed material is composed of O, Zr, and Yt in addition to traces of Al and Hf. The black grains scarcely dispersed within the crystalline structure were agglomerates of alumina as shown in Figure 37. The aged sample exhibited minimal surface changes associated with $t \rightarrow m$. Crystal pull-out was confined to the surface of the material. The depth of the affected area did not exceed 2 μm at maximum. The bulk of the material beyond the transformed zone was completely ‘healthy’, displaying none of the signs of *LTD* as shown in Figure 38.

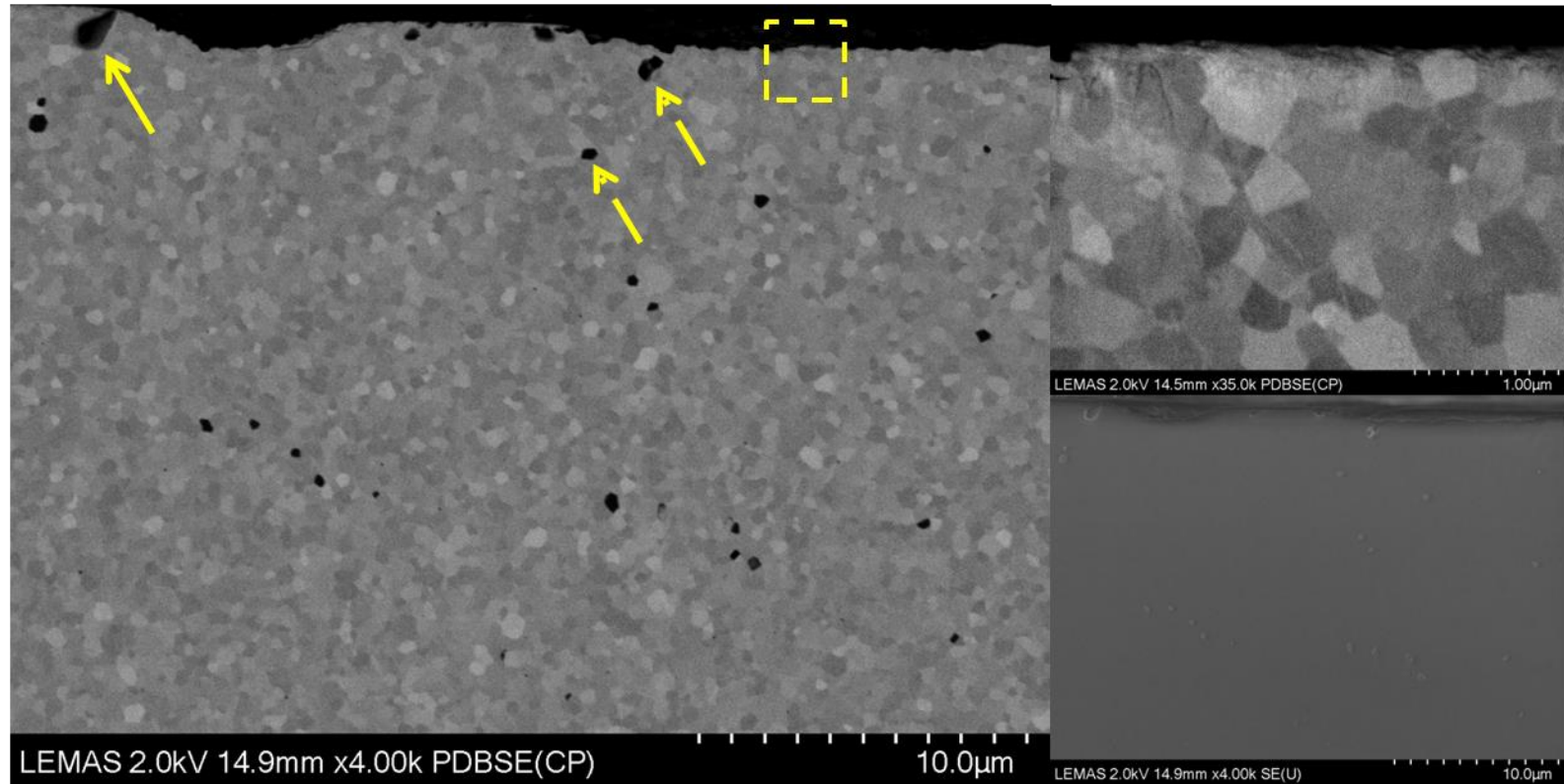


Figure 36. High resolution **SEM** images for ion broad beam polished as-received sample.

Left, larger area and number of crystals was investigated in comparison to samples studied with **FIB-SEM**. Crystals appeared homogenous and had well-defined boundaries. No signs of $t \rightarrow m$ could be detected. An evidence of crystal pull-out can be noticed on left corner of the image as annotated with (\rightarrow). Smaller black particles (\rightarrow) are composed of alumina, as will be shown in Figure 37. Top right, zoom in the area highlighted with yellow square demonstrating the integrity and well defined crystal boundaries. Bottom right, a similar magnification to (left) but using different detector. Alumina particles can be seen protruding out of the surface as they may be more resistant to ion beam polishing.

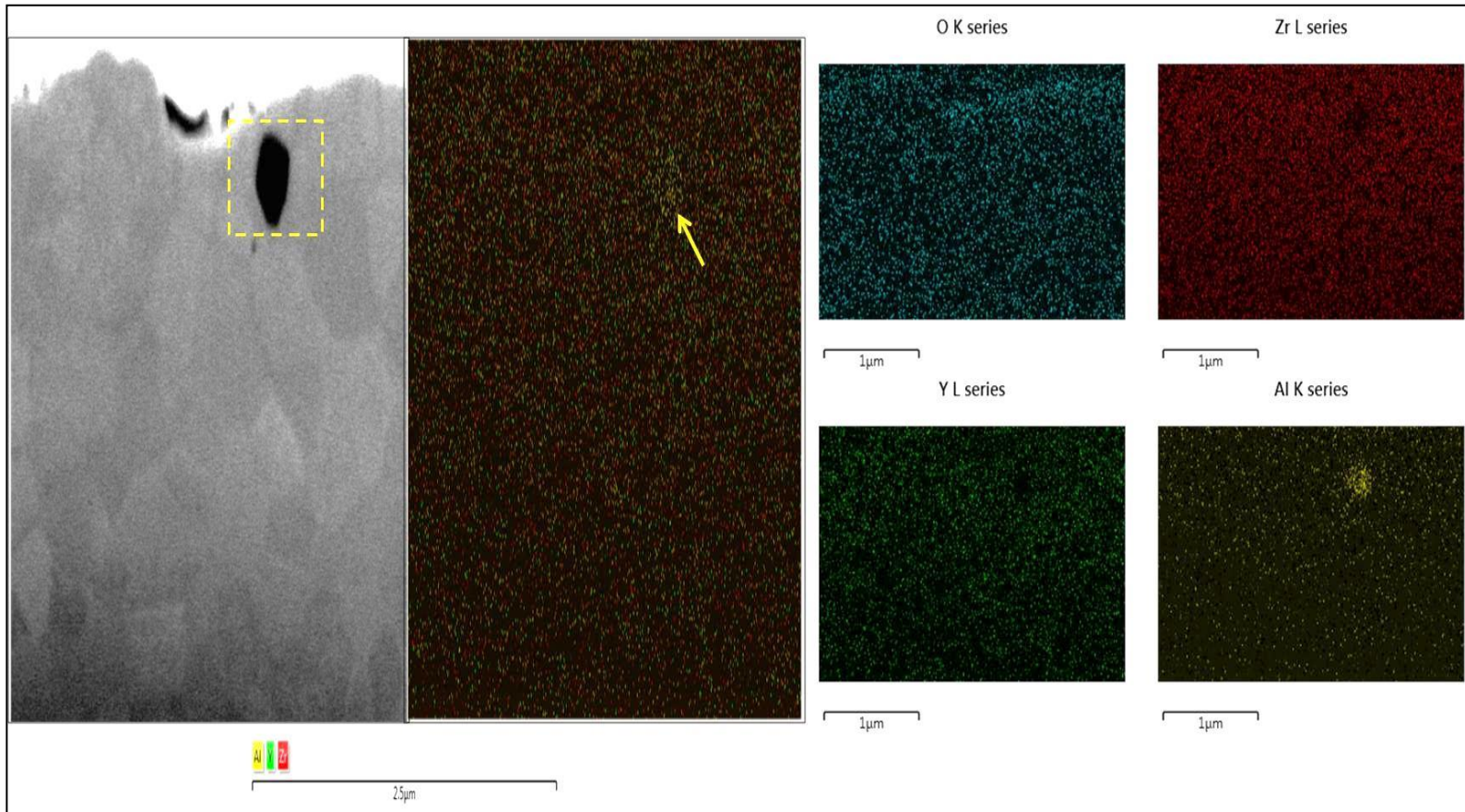


Figure 37. Elemental map for as-received sample obtained using *EDS* coupled *SEM*.

Left, *SEM* field analysed using *EDS*. Middle. Composite elemental map for the studied region of interest showing localised concentration of aluminium (→) in the area corresponds to black particle (yellow dashed square in the left *SEM* image). Right, individual elemental maps for O, Zr, Y and Al.

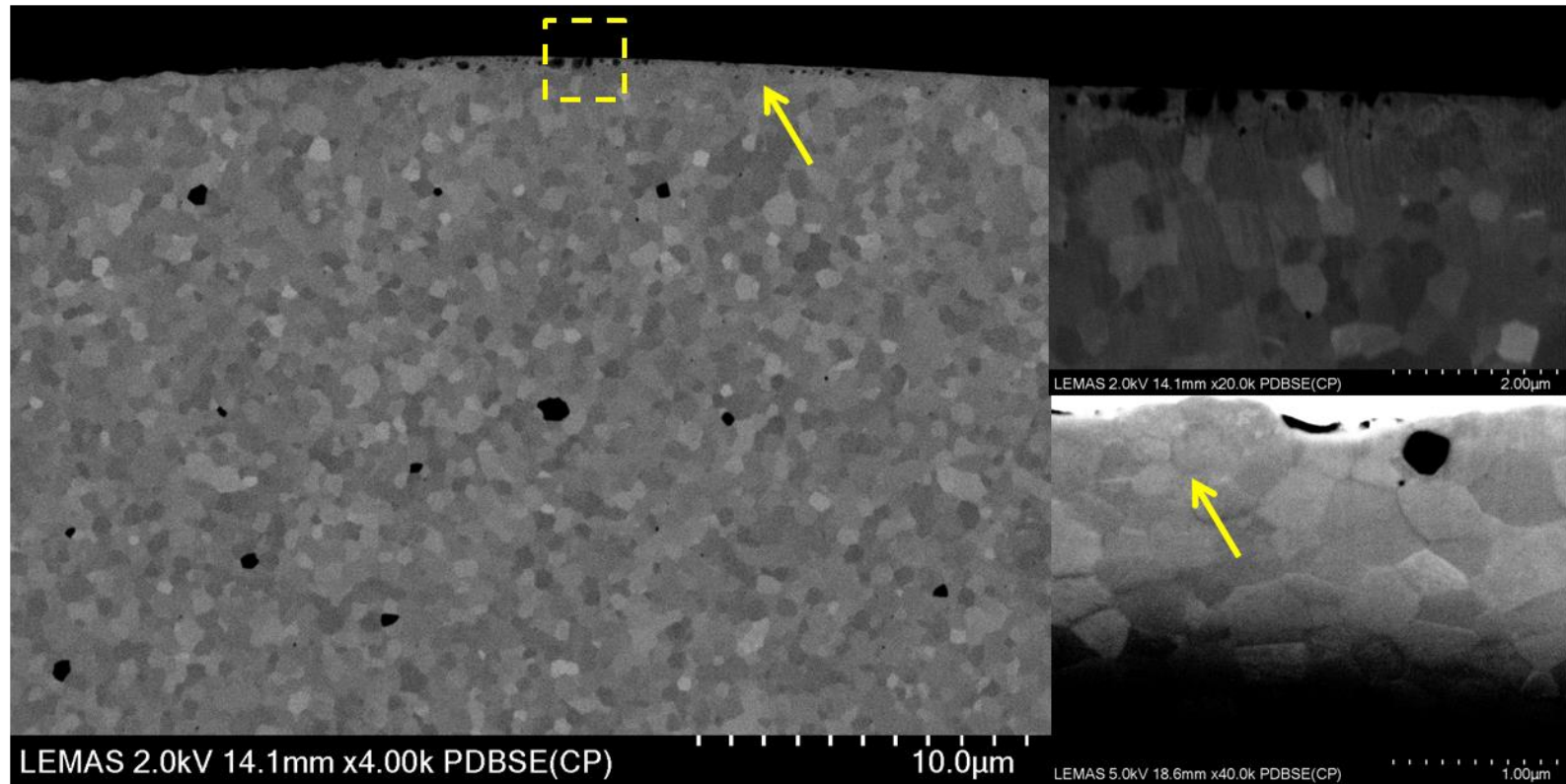


Figure 38. High resolution *SEM* images for ion broad beam polished aged disc sample.

Left, signs of $t \rightarrow m$ could be detected at the most superficial layer of the studied sample. An evidence of significant crystal pull-out can be noticed in the area delineated by yellow dashed square. A higher magnification of this area can be seen in the top right image. Bottom right, zoom in the area annotated with (→) and demonstrating the ill-defined crystal boundaries and possible crystal twinning which are important signs on the $t \rightarrow m$. All images show that $t \rightarrow m$ was localised to the surface as the subsurface and bulk layers recover normal characteristics noticed in as received material.

2.6.4.3 Transmission electron microscopy

Determination of the integrity (lack of *LTD*) depending on homogeneity and border definition of the crystals is a rather subjective and deliberate method. The use of a more objective method was proposed and envisaged. High resolution *TEM* allows imaging of crystals as well as obtaining electron diffraction pattern for single or group of crystals. Each material or phase of material has a unique diffraction pattern determined by the atomic setup. A diffraction pattern provides structural details regarding the sample's orientation, crystallographic structure, symmetry, lattice parameters, various phases if present and whether they are crystalline or amorphous. Such features allow comprehensive analysis of the $t \rightarrow m$ in *Y-TZP* materials.

As the name implies, *TEM* work in transmission mode where a beam of electrons from an electron source travels through a sample and undergoes a series of interactions. The unscattered electrons are then refocused utilising electromagnetic lenses and projected on a fluorescent screen. The resultant image is a shadow image of the sample where dense parts of the sample appear darker. Thus, the samples examined under *TEM* should be ultra-thin in order for the electron beam to be transmitted through. Many techniques have been used in order to achieve adequate *TEM* sample preparation including; electropolishing, broad ion beam milling and most recently, *FIB-SEM* (Langford, 2006).

The latter technique demonstrates superior performance for preparing *TEM* samples which is attributed to; (1) ability to navigate to a region of interest under extremely high magnification utilising the coupled *SEM*, (2) avoiding ion-induced damage for the area of interest, (3) the change in the sample brightness of images acquired with *SE* mode while it is being thinned can be used to monitor its thickness, (4) *TEM* lamellae can be prepared to within 50 nm of a feature of interest which allow studying minute defects and interfaces, (5) the accuracy of positioning a *TEM* lamella utilising *FIB-SEM* is dramatically higher in comparison to other methods, (6) a limited amount of circumferential milling is required as the *FIB* is near perpendicular to the surface of the sample, (7) *TEM* lamellae can be prepared in a relatively short time and (8) *TEM* lamellae can be prepared from samples with irregular or unusual geometries such as screw-shaped dental implants. Utilising this technique, there is no

need for mounting/embedding, plain grinding and polishing (Langford and Clinton, 2004, Langford, 2006).

In this project, the milled/imaged surfaces prepared by **FIB-SEM** (as discussed in Section 2.6.4.2) were converted into electron transparent lamellae $13\ \mu\text{m} \times 5\ \mu\text{m} \times 50\ \text{nm}$. This was achieved utilising the microsampling technique first described by Ohnishi *et al.* (1999) (Ohnishi *et al.*, 1999). The technique was utilised in an *in-situ* lift-out fashion where a thin lamella ($13\ \mu\text{m} \times 5\ \mu\text{m} \times 0.4\ \mu\text{m}$) was prepared by milling away surrounding material apart from an anchor point. A range of voltages, probe sizes and different beam currents were used during this procedure. A platinum needle tip attached to manipulator was inserted in the platinum protective layer deposited earlier and then the anchor point is milled to free the lamella. The Lamella was then mounted to a **TEM** slot by local platinum welding. The needle was then severed and moved away. Finally, the lamella was further thinned using a lower beam current (0.1-0.3 nA) until an electron transparent final thickness was achieved (50 nm).

Lamellae obtained from as-received and aged implants were examined using high resolution field emission gun **TEM** operating at 200 kV (Tecnai, FEI, USA). **TEM** images and electron diffraction patterns were acquired with a CCD camera (SC600A Orius, Gatan, UK) and high-angle annular dark field (**HAADF**) detector. Diffraction patterns were analysed utilising DigitalMicrograph™ software (Gatan Microscopy Suite, UK) as follows; images for electron diffraction patterns obtained from **TEM** were calibrated using the software according to the scale bar embedded in the image. Then, atomic interplanar distance (d-spacing) was calculated for each pattern. Obtained data was matched to crystallographic parameters of reference tetragonal and monoclinic **Y-TZP** material.

Examined crystals within the subsurface of lamellae obtained from as-received and aged implants revealed similar crystalline features as shown in Figure 39 and Figure 40, respectively. Both samples exhibited well defined, sub-micron and densely packed crystals. Spot electron diffraction patterns were obtained for single crystals. Analysis of electron diffraction data revealed D-spacing values similar to those for reference tetragonal **Y-TZP**. Surface crystal could not be investigated as they were lost due to ion beam induced damage.

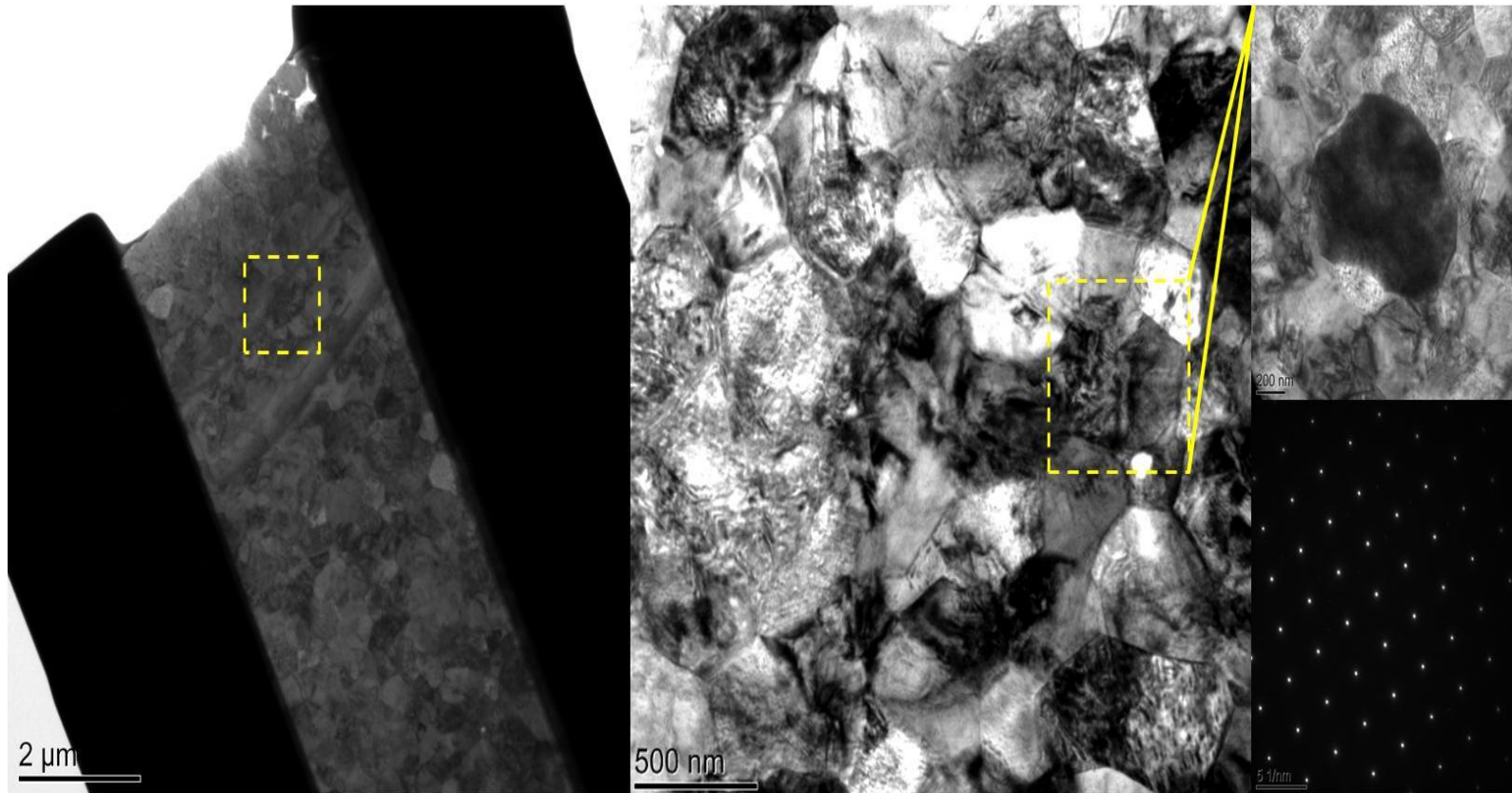


Figure 39. **TEM** analysis of **FIB**-prepared lamella obtained from representative as-received sample.

Left, lamella mounted in **TEM** grid where the ion beam induced surface damage can be seen. Middle, magnification of the area delineated with dashed yellow rectangle. Well-defined crystal boundaries can be seen with no evidence of microcracking. Right top, high magnification of single crystal that was imaged to obtain single crystal diffraction pattern (bottom right). Analysis of interplanar or D-spacing revealed that the examined crystal represent tetragonal phase of **Y-TZP**.

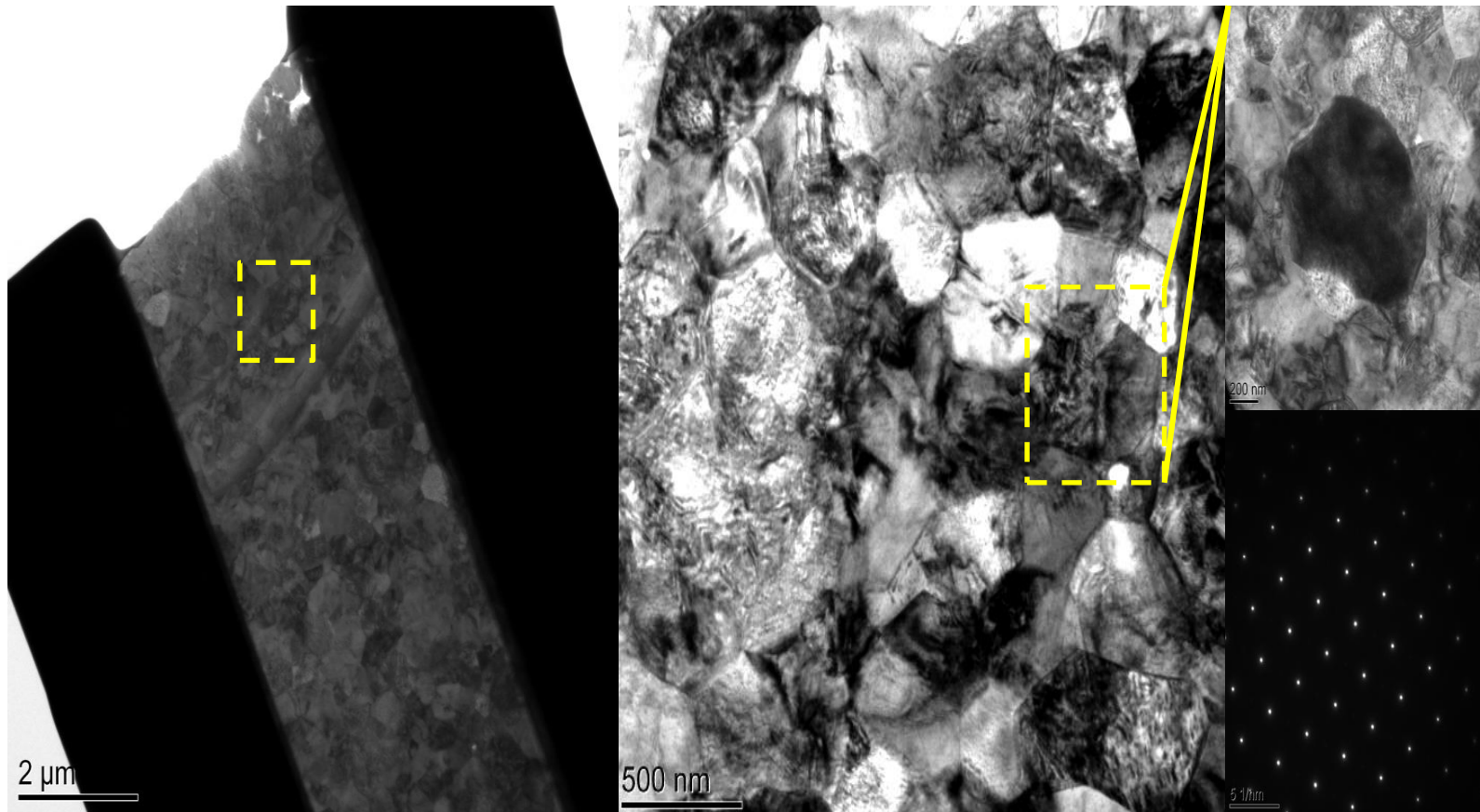


Figure 40. *TEM* analysis of *FIB*-prepared lamella obtained from representative aged sample.

2.7 Discussion

The used ageing cycle in this study (Section 2.4) was chosen to simulate *in vivo LTD* for what is equivalent to a reasonable lifetime for a dental appliance (i.e. at least 10 years). In addition, it was chosen to conform to the ISO standards for testing ceramic surgical implants (ISO 13356, 2008). We assumed that the *LTD* activation energy of the tested material was similar to that calculated by other authors. The assumption was made on the grounds of close resemblance between the two material's chemical composition and microstructural features. Additionally, the authors utilised kinetics-based method and exploited temperature, time and transformation (T-T-T) curves to extrapolate *LTD* rates to body temperatures (Chevalier *et al.*, 2007b, Chevalier *et al.*, 2009). This technique is allegedly reported to be the single most important method to provide a robust lifetime prediction utilising intermediate temperatures (Lughi and Sergo, 2010). Assuming validity of this assumption, the used ageing cycle in this project may mimic 15-20 years of *in vivo LTD*

The rate of *LTD* is highest at temperature range of 200-300 °C (Kobayashi *et al.*, 1981, Cales *et al.*, 1994, Piconi and Maccauro, 1999). *LTD* requires several years in order to take place at *in vivo* or room temperature. It probably requires longer period to have pronounced effect on the crystalline structure and reliability of the material. Long-term, real-time, *in vivo* (body temperature) or room temperature *LTD* or stress-induced $t \rightarrow m$ data on monolithic zirconia ceramics is currently scarce (Sergo and Clarke, 1995, Sergo *et al.*, 1995, Piconi *et al.*, 1998, Lughi and Sergo, 2010). In simple terms, 10-years *LTD* or stress induced $t \rightarrow m$ data require a 10-year study, which is neither feasible nor practical. Therefore, $t \rightarrow m$ rates and thereby *LTD* kinetics and *Y-TZP* lifetime at room temperature have been estimated until now from accelerated, intermediate temperature ageing experiments.

The use of this approach for extrapolating room-temperature predictions may however be subjected to serious imperfections. This problem is twofold, the significant disparity within the reported activation energy for *Y-TZP* materials and the excessive differences between $t \rightarrow m$ rates induced at room temperature in comparison to intermediate temperatures (100-300 °C). Lughi *et al* reviewed published *LTD* activation energy values for various *Y-TZP* materials with a similar composition.

They found that activation energy varied significantly (56-106 kJ/mol) with grain size, density, testing conditions and temperatures (Lughi and Sergio, 2010).

Few studies reported significantly high $t \rightarrow m$ rates despite performing room temperature, *in vitro* ageing. On one hand, such findings may be irrelevant as **LTD** rates in these studies were measured for zirconia thermal barrier coatings. The high porosity of such structures renders them highly susceptible to **LTD** in the first place. On the other hand, if such a high $t \rightarrow m$ rate took place in environment with almost negligible amount of residual stresses, the amount of **LTD** induced by hydrothermal ageing at 134 °C and 2 bar (with significant residual stresses) for 1 hour will be by no means representative of 2-3 years of 37 °C ageing (Lughi and Sergio, 2010).

The validity of accelerated ageing studies at intermediate temperatures received another setback following the very recent striking **LTD** data published by Keuper *et al* (2014). The authors investigated the effects of five years, wet and dry storage at 37 °C on the **LTD** within a commercially available, sintered, white body **Y-TZP** material. They also compared between prolonged 37 °C storage and accelerated ageing using an autoclave at 134 °C. Their findings remarkably indicated that a pronounced linear, surface to bulk progression of **LTD** upon storage at 37 °C and under minimal water pressure. The obtained data at low temperatures exhibited delayed-onset behaviour, where $t \rightarrow m$ started after an incubation period ranged between 0-7 months as opposed to the immediate start of $t \rightarrow m$ in accelerated ageing. More interestingly, the thickness of the **LTD** affected layer after four years of 37 °C storage was similar or larger when compared to accelerated hydrothermal ageing for five hours (which supposedly simulate 10-20 years of *in vivo* **LTD** at 37 °C) as indicated by **FIB-SEM** (Keuper *et al.*, 2014). Additionally, the thickness of the transformed zone was at least triple when compared to our investigation. These findings may cast doubt on the validity of accelerated, short-term hydrothermal ageing studies and long term-alternatives may be required. In fact, some long-term hydrothermal ageing studies on **Y-TZP** materials at intermediate temperatures revealed extensive **LTD** and strength degradation (Binner *et al.*, 2011, Cattani-Lorente *et al.*, 2011, Paul *et al.*, 2011, Kohorst *et al.*, 2012). The work on this project started in 2010 when these findings were not in press yet. Thus, the use of one accelerated **LTD** protocol can be considered as an inevitable downside of the study. A future work with extended, intermediate temperature and 37 °C are required for further verification of **LTD** in this

particular material. This is particularly important given that the above cited work is the first of its type and requires rigorous appraisal.

The macroscopic effect of *LTD* can be significantly catastrophic to an extent that negates the use of zirconia as an implant material. However, several studies showed that *LTD* can be minimised to biologically acceptable levels by optimising manufacturing process, use of optimum crystal size, removal of impurities and embracing the use of various *LTD*-resistant materials such as alumina-zirconia composites and ceria-doped zirconia. Zirconia blanks showed no significant deterioration in mechanical properties after being embedded into the medullary cavity of the tibia of rabbits for a period of 30 months. It was also reported in the latter study that zirconia can be used clinically as it retains a bending strength of over 700 MPa after being immersed in 95°C saline solution for over 3 years (Shimizu *et al.*, 1993). Consistent findings were reported by Cales *et al.* (1994) who concluded that zirconia implants used in hip replacement surgeries maintained sufficient mechanical properties when recovered two years after implantation procedure (Cales *et al.*, 1994). Other studies remarked that conflicting data on the survival and strength of these implants can be attributed to the microstructural design and quality of the ceramic manufacturing (Cales, 2000, Chevalier *et al.*, 2007b, Chevalier *et al.*, 2009, Lughì and Sergo, 2010).

Jerome Chevalier is the brightest name in field of zirconia ageing with numerous, widely cited publications on this subject. In his extensive review on *LTD* of zirconia biomedical implants, he, along with his co-workers, concluded that “*although in the 1990s Y-TZP ceramics were considered very promising materials for biomedical applications, long-term follow-up is needed to address the critical problem of aging in vivo and its negative impact on orthopaedic implant durability. As 600,000 patients to date have been implanted with zirconia hip joint heads, a careful explant analysis must be conducted, with a special emphasis on LTD-microstructure relationships. However, most zirconia implants were processed at a time when ageing was not yet fully understood. Methods to assess a priori the ageing sensitivity of a given zirconia ceramic have been developed and should lead to safer implants. In the meantime, new zirconia or zirconia-based materials that overcome the major drawback of the standard Y-TZP are now available*” (Chevalier *et al.*, 2007b).

Studying $t \rightarrow m$ phenomenon utilising a single technique provides an incomplete picture of **LTD** and its potential effects. This is attributed to the inherent limitations of each individual technique. The effect of hydrothermal ageing and stress induced $t \rightarrow m$ was investigated using several distinct, complementary techniques in Section 2.6. To the knowledge of the author of this work, this is the only project that has studied **LTD** phenomenon in an injection-moulded **Y-TZP** dental implant material. In Section 2.6.1, **XRD** data revealed that the discs and implants exhibited similar crystallographic features. Both samples were comprised of tetragonal and monoclinic phases.

The cubic phase could not be detected in the studied material as opposed to others investigations (Cattani-Lorente *et al.*, 2011). This can be attributed to the close proximity of crystallographic features of the two phases which render them indistinguishable with regard to **XRD** (Argyriou and Howard, 1995). An extreme example on the limited ability of laboratory **XRD** to differentiate between crystallographically similar compounds is presented in Figure 41. Rietveld refinement of diffraction patterns obtained with neutron radiation may have greater potential to differentiate between these two phases owing to the greater sensitivity to; light atoms symmetric peak shape and scattering at higher diffraction angles (Ilavsky and Stalick, 2000).

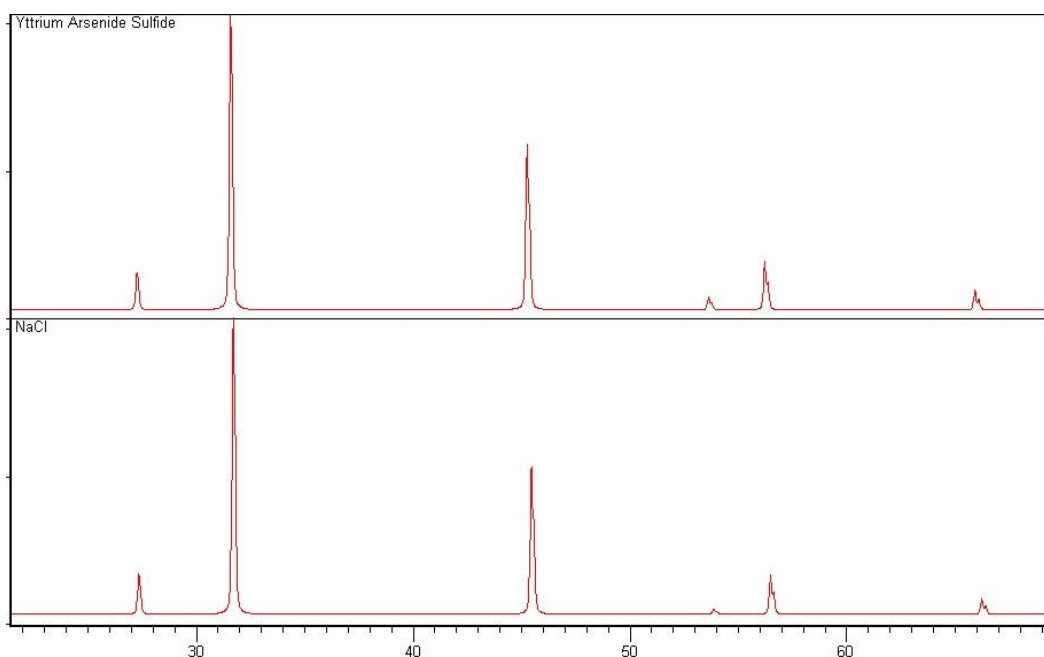


Figure 41. Identical X-ray diffraction patterns for completely different compounds.

Top, **XRD** pattern of Yttrium Arsenide Sulfide, a highly toxic compound. Bottom, **XRD** pattern of table salt. Graph used with permission from Dr. Tim Comyn.

The initial monoclinic phase fraction can be affected by the ethylene oxide sterilisation process. This process involves exposing samples to 40 °C, minimal steam pressure and injections of gases for at least three hours. Despite the low temperatures and pressure, such conditions may induce *LTD* or affect the sensitivity of the material to *LTD* (Keuper *et al.*, 2014). Hydrothermal ageing doubled the amount of monoclinic phase in both discs and implants. The volume fraction was however still below the maximum limit set by the ISO standards for surgical implants (ISO 13356, 2008).

Hydrothermal ageing generated a highly textured monoclinic phase in (111, $\bar{1}11$) directions. This can be an exacerbation of a pre-existing texture as a result of the injection moulding manufacturing. This however cannot be confirmed as the second monoclinic peak was not present in the diffraction data for as-received samples.

Texture or preferred orientation may also be responsible for the significant disparity of the results obtained by the two data analysis methods used to estimate monoclinic phase fraction. The Rietveld refinement method is very effective in adjusting for preferred orientation. However, it could not be used in this study as the diffraction data was obtained over a small 2θ range where only two peaks of monoclinic and a single tetragonal phase peaks are present. A full range diffraction data (2θ : 10-110) analysed by Rietveld refinement can theoretically resolve the problem. However, this solution was precluded as increasing 2θ will increase the depth of X-Ray penetration which thereby changes the area under investigation. Additionally, peak overlap may be notable at high angles of reflections. Such issues can be considered as the major drawback for using Rietveld refinement for studying *XRD* in solid materials.

The use of Toraya's modification of Garvie and Nicholson's equation may also be unreliable as it does not take in consideration the effect of preferred orientation. A preliminary pilot work using *EBSD* confirmed presence of texture or preferred orientation in as-received samples. However, the difference in surface texture prior and after hydrothermal ageing could not be estimated using this technique. This was attributed to the large number of crystals with 'no solution' or unidentifiable orientation in aged samples as shown in Figure 42. The possible cause of this problem is described later in this Section.

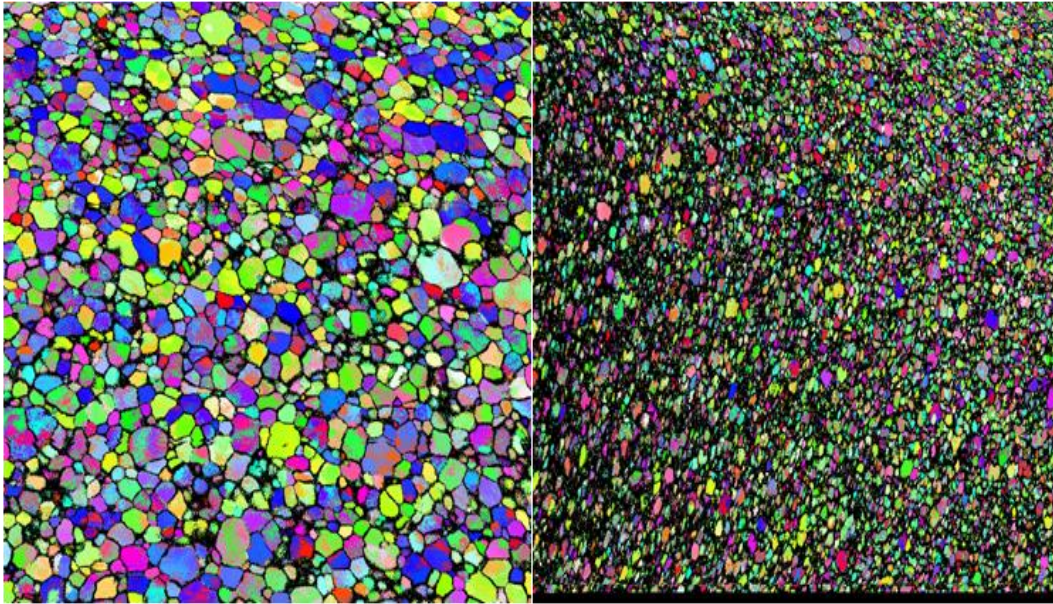


Figure 42. **EBSD-SEM** texture analysis of the injection moulded **Y-TZP**.

EBSD-SEM was used to determine spatial orientation of the crystals on the surface of as-received (left) and aged (right) mirror polished, injection-moulded discs. Crystals with similar colours exhibit the same orientation. The larger the number of 'same orientation' crystals, the greater the magnitude of preferred orientation or surface texture. The as-received sample seemed to exhibit a fair amount of surface texture. Texture analysis was not feasible for aged sample due to the large number of blacked-out crystals which indicate 'no solution' or unidentifiable orientation.

Whether the Rietveld refinement method is underestimating or Toraya's modification is overestimating the monoclinic phase fraction was something that could not be determined. Several attempts were made to study this area of uncertainty utilising known weight percentages of pure monoclinic and tetragonal **Y-TZP** powders. Obtaining a homogenous mixture of the two powders was impossible despite meticulous mixing methods including; long-term trituration or evaporating solvent used to mix small quantities of powders. This is a direct result of the different densities and thus volume of both powders. Tetragonal powder is obtained by sintering as described earlier which increases density to a large extent in comparison to the as-received monoclinic powder. All diffraction data of these mixtures revealed extremely high monoclinic phase fractions despite the fact that the mass percentage of used monoclinic powder did not exceed 20%. These findings indicated that monoclinic powder always topped the tetragonal powder and occupied the majority of the X-Ray interaction volume.

Due to their configurations, the majority of laboratory **XRD** systems negate studying small and confined areas of samples such as an indentation imprint, tip of implant thread or a cross section of a thin fractured surface. The incident X-Ray beam of the used machine in this project was reduced to minimum (2 mm) in order to reduce signal-noise ratio.

XRD coupled computed tomography technique (**ctXRD**) has been recently introduced. Analogous to conventional CT, a sonogram (dataset) in **ctXRD** represents a set of diffraction patterns collected by probing a slice in the sample with a monochromatic pencil-like primary beam at certain projection angles. The technique has high agreement with laboratory **XRD** and allows studying small areas and phase mapping. **ctXRD** has been reported to have poor momentum resolution (Harding *et al.*, 1987, Kleuker *et al.*, 1998).

Laboratory **XRD** has inherent limitations; the limited penetration depth is among the most obvious from this work. X-Rays can provide crystallographic information regarding a 10 crystal deep layer in **Y-TZP** material, X-Ray penetration depth $\approx 5\mu\text{m}$ (Gremillard *et al.*, 2010). Thus, the technique has no use in studying **LTD** in the bulk of the zirconia materials (Chevalier *et al.*, 2007b). **XRD** is a sensitive technique with regard to sample mounting, placement in relation to the X-Ray beam, sample's geometry and flatness. This is particularly important in this project given the irregular shape, and variable head/thread height along the implant length. Such sample geometry compromised signal to noise ratio and the quality of some scans. Whenever Rietveld method was used for data analysis, these variables were refined.

The 'relatively' high penetration depth of X-Rays used in conventional **XRD** reduces the diffracting volume of the surface layer of the studied sample. This in turn, compromises the signal/background ratio and thereby the technique's sensitivity toward the composition of the superficial layers of the material. Additionally, conventional **XRD** delivers crystallographic information limited to the area of maximum diffracting intensity. The **GIAXRD** technique was used to unravel the spatial distribution of the monoclinic phase within the depth accessible by **XRD** according to Gremillard's *et al* (2010) method (Gremillard *et al.*, 2010). The whole principle of this method relies on the use of stationary (fixed) incident beam at small angles which increases; the path length of the X-Ray beam, the diffracted intensity and

signal/background ratio specifically from the superficial layers of the sample (Rau *et al.*, 2011). The authors of this technique exhaustively described the mathematical derivation of their method. They also numerically tested it in theoretical configurations as well as commercially available *Y-TZP* materials. Their findings indicated that the technique is promising with regard to determination of surface fraction and depth of the monoclinic phase within the area accessible by X-Rays. However, there are three caveats with the use of this technique; firstly, extrapolating monoclinic phase fraction beyond the maximum X-Ray penetration depth may be misleading which is related to immediate divergence of fitting functions outside the limits of X-Ray penetration. Secondly, the type of the fitting function may significantly affect the bounds of the monoclinic phase depth profile. The fact that several functions can be fitted adequately to X_m profile, as indicated by goodness of fit parameters, poses a significant challenge to this method. Thirdly, the method was derived assuming that studied materials are composed of monoclinic and tetragonal phases only and disregarded the very likely presence of cubic phase. However, this may be of a little significance given the similarity between tetragonal and cubic phases in terms of crystallographic features.

GIAXRD findings indicated that monoclinic phase fraction within as-received sample was distributed to a very small depth that is less than 0.8 μm (Section 2.6.1). These findings were in line with those reported for a non-aged material that contained 20% alumina content (Gremillard *et al.*, 2010). In the current analysis there was one problem during the fitting and deducting the inverse Laplace transform. The difference in X_m values for as-received sample at incidence angles more than 2° steeply decreased which made F_{m0} approach infinity. The fit was bound to $F_{m0} = 25\%$ which was the maximum monoclinic phase fraction within the aged sample. This however compromised the apparent quality of fit, yet not the goodness of fit parameters. The same issue was present with the other published report (Gremillard *et al.*, 2010).

Hydrothermal ageing increased the monoclinic phase fraction and the $t \rightarrow m$ affected zone which is compatible with the nucleation and growth mechanism of *LTD* (Gremillard *et al.*, 2004b). The use of short ageing cycle resulted in a surface-confined *LTD* affected zone. This is contrary to other reports indicated bulk involvement with *LTD* (Gremillard *et al.*, 2010, Cattani-Lorente *et al.*, 2011). The disparity of the

results can be explained by the differences in hydrothermal treatment periods and *LTD* resistance between different studies and materials, respectively.

Raman spectroscopy was used to investigate hydrothermally induced *t*→*m* as in Section 2.6.2. As-received samples contained negligible amount of monoclinic phase fraction. Hydrothermal treatment resulted in a notable increase of the monoclinic phase fraction. However, the values varied upon the use of point or area scans and were significantly lower in comparison to the *XRD* technique. The contradiction between the estimated monoclinic fraction yielded by *XRD* and Raman spectroscopy is a well-documented issue. As cited by Chevalier *et al* (2007), there was no agreement between the findings of both techniques which could have linear, logarithmic, or power law dependencies. In this study, the disparity can be also attributed to the difference between the examined areas by each technique (Chevalier *et al.*, 2007a). Diameter of the incident laser beam was calculated using Equation 15 (Lewis and Edwards, 2001):

$$\varpi = 1.22 \frac{\lambda}{nA} \quad (15)$$

Where;

ϖ is the theoretical diameter of the Ar^+ laser beam

λ is the laser wavelength (488nm)

nA is the numerical aperture of the focusing objective

The area studied by a Raman point scan ranged between 0.92-4.5 μm^2 while area mapping scans were obtained for a 400 μm^2 areas. *XRD* was used to investigate an area of 20 mm^2 . These findings indicate that the monoclinic phase might not be homogeneously distributed along the surface of the samples

Having a confocal microscope arrangement linked to it, Raman spectroscopy has wide application in studying stress induced *t*→*m* within Vickers indentation imprints and fractured surfaces. Additionally, the effect of hydrothermal treatment on the pattern and quantity of stress-induced *t*→*m* was investigated. The monoclinic phase fraction was quantified and mapped within fractured surfaces and Vicker's indentation imprints in as-received and aged samples. Identification and quantification of cubic phase using Raman spectroscopy can be difficult owing to the closely similar Raman spectra of the tetragonal and cubic phases. The software that was used in this study to

analyse Raman data did not enable the identification and quantification of the cubic phase in contrast some other studies (Pittayachawan, 2008).

Fractured surfaces exhibited a concentration of monoclinic phase in the centre (midway between tension and compression surfaces) as well as the tensile surface but to a lesser extent. There was no difference between the aged and as-received samples. Clarke and Adar (1984) reported that stresses generated during the fracture of zirconia toughened alumina resulted in 3% monoclinic phase fraction when determined by Raman spectroscopy and 8% as per *XRD* (Clarke and Adar, 1984). No emphasis on the distribution of the $t \rightarrow m$ was made.

When examining fractured surfaces of 9 mol% MgO stabilised *PSZ* ceramics with a Raman microprobe, Lee *et al* (2009) reported high concentrations of monoclinic phase near the tension and compression surfaces. Additionally, a steady decrease in monoclinic phase fraction measured from just below the tension surface to within 200 μm of the compression surface was noticed (Lee *et al.*, 2009b). Pittayachawan *et al* (2007) demonstrated concentration of monoclinic phase only around the fracture origin and reported increased concentration of cubic phase on the tension surfaces of the studied samples (Pittayachawan *et al.*, 2007).

Vickers indentation induced significant $t \rightarrow m$ in as-received and aged samples in the present study. Possible tetragonal to cubic phase transformation as a result of indentation process (Kohal *et al.*, 2009b) was not investigated in this study for the same reasons described in Section 2.6.2. Within the imprints of the indenter in the as-received sample, the amount of $t \rightarrow m$ was the lowest in the centre and increased significantly when moving toward the edges. Unsurprisingly, the corners of the imprint exhibited the highest amount of monoclinic phase as the highest amount of stress is expected to be generated in such areas.

The high degree of $t \rightarrow m$ near the corners and the edges of the imprint may be attributed to the type of stress these areas were subjected to. Tensile and shear stresses generated by the sides of the indenter (edges and corners of the imprint) effectively induce $t \rightarrow m$ in comparison to compressive stresses generated by the tip of the indenter (centre of the imprint) (Delgado-Ruíz *et al.*, 2011). The $t \rightarrow m$ was not only confined to the imprint, it also extended but to a lesser extent to areas just outside the imprint

where plastic deformation is expected to occur. Material recovered the pure tetragonal composition in areas unaffected by plastic deformation. Pittayachawan *et al* (2009) reported the level of monoclinic phase exhibited limited variation within the indentation imprint in addition to significant tetragonal to cubic phase transformation at the centre (Pittayachawan *et al*, 2009). Delgado-Ruíz *et al's* (2011) work has showed an almost linear decrease $t \rightarrow m$ of **Y-TZP** with distance from the centre of the indentation imprint (Delgado-Ruíz *et al.*, 2011).

Little difference was however noticed between the centre and the edges of the imprint in aged samples. A decrease of monoclinic phase fraction was noticed along one direction from centre to edge. The area affected by plastic deformation and $t \rightarrow m$ seemed to be larger than for the as-received group. The overall difference in the total monoclinic phase fraction was small and could be equal to difference in baseline content of monoclinic phase in each sample.

The aforementioned techniques have the capability to investigate surface or near surface $t \rightarrow m$. Determining **LTD** occurrence or susceptibility of a 5 mm diameter implant on the basis of studying the superficial 5 μm may not be appropriate. The use of Synchrotron radiation as a comprehensive adjunct technique was envisaged (Section 2.6.3). The energy of the X-Ray beam generated by Synchrotron source is significantly higher than that generated by a laboratory X-Ray tube. This in turn, allows studying the whole sample thickness in a remarkably short time.

Synchrotron X-Rays have been widely utilised for characterisation of zirconia based materials especially those used for thermal barrier coating applications. It has also been used to study time-resolved *in situ* monoclinic phase formation under hydrothermal and pressure conditions (Leoni *et al.*, 1998, Yamashita *et al.*, 2008, Bremholm *et al.*, 2009, Lipkin *et al.*, 2013). To our knowledge, there are currently no research papers that reported the use of Synchrotron for purpose of detecting **LTD** in **Y-TZP** dental implant materials.

The generated diffraction Synchrotron patterns for as-received, machined, aged and machined-aged samples were identical to that for a pure tetragonal powder. The findings indicate that such technique is only appropriate for detection of advanced

LTD that propagated to the bulk of the material. The diffraction patterns of aged samples were expected to exhibit monoclinic phase peaks. However, none of the patterns obtained by Synchrotron X-Ray diffraction did so. This can be attributed to the exceedingly low diffracting volume of the transformed zones (2-4 μm) in comparison to the untransformed counterparts (approximately 5 mm) in the path of X-Ray beam. The likelihood of having porous regions in the bulk of injection moulded implants in comparison to other manufacturing technique is not widely studied. These areas may be affected and/or highly susceptible to **LTD** process. The use of Synchrotron in transmission mode may be considered as an essential measure in order to prevent duplicating the drastic scenario with the ‘went undetected’ porous core of zirconia hip implants.

Extrapolating data regarding **LTD** effects on zirconia implant materials based solely on crystallographic techniques may be risky. An extreme example emphasising this risk is presented in Figure 41 that demonstrates identical **XRD** patterns for a two fundamentally different materials. The concerns regarding the validity and reliability of these techniques may be further in question given the close proximity of crystallographic parameters of different phases of zirconia materials. Direct imaging and characterisation of the consequences of hydrothermally- or stress-induced $t \rightarrow m$ at macroscopic and microscopic scales were used in Section 2.6.4 to obtain a better understanding of the **LTD** sensitivity of the studied material.

Optical interferometry (profilometry) was used in Section 2.6.4.1 to characterise surfaces of polished and polished-aged samples. Martensite reliefs were shown on the topographic maps and increased roughness parameters were demonstrated upon hydrothermal treatment of polished samples. One-way ANOVA revealed significant difference in roughness parameter (S_a , R_a) among aged and as-received samples. The data is of great statistical value as the used optical interferometer was used to study a significantly large area ($\approx 1 \text{ mm}^2$) in comparison to other techniques such as **AFM** or Raman spectroscopy. These findings were in agreement with those published by Kawai *et al* (2011) who reported significant increase in R_a as a result of hydrothermal ageing in **Y-TZP** and alumina toughened zirconia (**ATZ**) (Kawai *et al.*, 2011). In their work, R_a values for aged **Y-TZP** and **ATZ** were in excess of 100 nm in comparison to the current work, 29 nm. This may be attributed to the higher baseline R_a for polished

samples and longer hydrothermal ageing cycle used by the authors. A limitation of this technique is the necessity for an absolutely clean and debris-free sample. Debris can be easily mistaken for surface martensite reliefs. The problem is further complicated by the fact that profilometers are not equipped to study the nature of surface protrusions. Examining of samples under *SEM* prior to interferometry investigation may be helpful to determine the cleanliness of the sample.

The use of *FIB* and broad beam ion polishing ensured non-invasive sample preparation. It also allowed the high quality imaging and comprehensive analysis of microscopic consequences of hydrothermal ageing on the studied *Y-TZP* material (Section 2.6.4.2). Loss of crystalline homogeneity and crystal twinning were among the most prominent signs of *LTD* that could be detected. Intergranular cracks could not be detected in the studied aged samples. This could be attributed to the high depth of field of *SEM* which negates appropriate detection of shallow microcracks. The relatively poor resolution of the transformed zone might further complicate the problem. Another explanation could be that the used short hydrothermal ageing cycle did not allow formation of such cracks. The use of broad beam ion polishing allowed studying the crystalline structure at a larger scale in comparison to *FIB*. Findings obtained from both preparation techniques were very similar. Additionally, disc and implant samples exhibited similar microstructural features when examined under high resolution *SEM*.

High resolution *TEM* was used in Section 2.6.4.3 to examine morphological and crystallographic changes in the crystalline structure as a result of hydrothermal ageing. It is noteworthy that, at the time of writing this thesis, this work was the first to investigate *LTD* phenomenon in zirconia dental implants utilising this method. Imaging of the transformed zone was difficult owing to the notable ion beam-induced damage despite the deposition of platinum protective layer prior to *in situ* lift out procedure. Electron diffraction patterns were obtained for individual crystals in the subsurface area. Diffraction pattern were analysed using a less than robust method were D-spacing and ratio between crystalline lattice parameters matched to a reference *XRD* data for tetragonal and monoclinic phase.

According to this method of data analysis, all the examined crystals of interests were matched to tetragonal phase. However, the reliability of this method may not be

adequate. The use of sophisticated software packages may improve the quality and reliability of extrapolations from this technique. Such software packages however require a specific output file format which was not available on the used system.

EBSD detectors coupled to **SEM** may be valuable for phase determination and mapping of zirconia material (Kawai *et al.*, 2011, Keuper *et al.*, 2014). The technique utilises an electron beam that is incident on an angled sample which diffracts the electrons and a diffraction pattern is generated on a fluorescent screen. Diffraction patterns for each studied crystal is then matched to a reference database and indexed to an acquired **SEM** image. The use of this technique may overcome the subjectivity with direct examination of **LTD** consequences using **SEM** or limited reliability of analysed **TEM** electron diffraction patterns. However, the use of this technique requires a highly polished sample. Thus, when using a conventional **EBS**D-**SEM** setting, the sample should be mounted in resin and mirror polished and 100% flat. Any change in the surface inclination will change the reflection/diffraction angles and thereby compromise the output of the investigation. This can explain the poor indexing and areas of ‘no solutions’ within phase maps obtained from aged samples studied as part of some pilot work in this project (Figure 43).

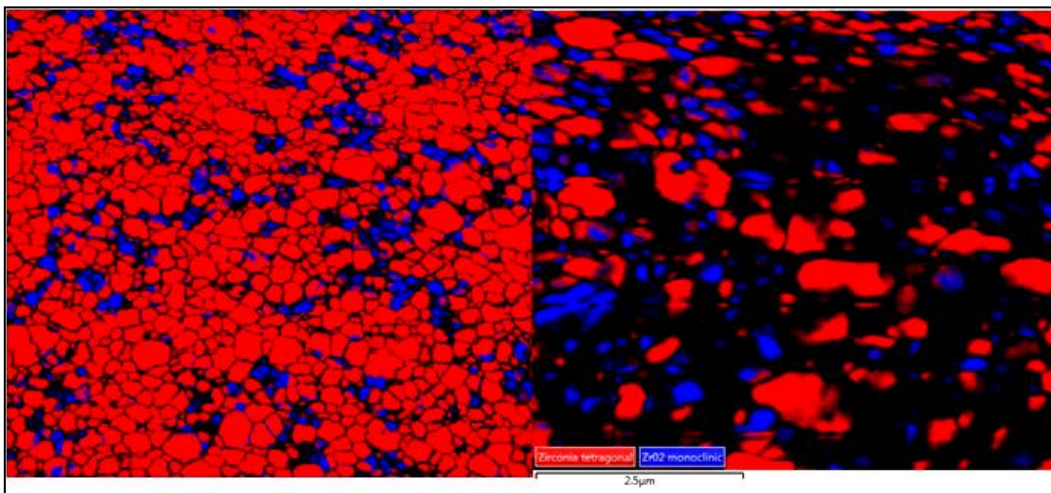


Figure 43. **EBS**D-**SEM** phase map for mirror polished **Y-TZP** samples.

Left, phase map obtained for as-received (left) polished sample where the majority of crystals were indexed as tetragonal (red). Right, **EBS**D-**SEM** map for a mirror-polished sample after hydrothermal ageing. The majority of crystal were un-indexed (black) as software could not match them to any solution based on the reference material data phase.

As received samples were studied adequately using **EBDS-SEM** which may indicate that changes in surface roughness and flatness (also shown by optical profilometry) as a result of hydrothermal treatment may compromise the validity of this technique. A similar problem was reported by Kawi *et al* (2011) who could not obtain any phase map of hydrothermally aged samples (Kawai *et al.*, 2011). Some recent **FIB-SEM** systems have an integrated **EBS**D detector. Effectively, these systems allow *in situ* mapping of a slice milled using **FIB**. Theoretically, this technique may be optimum to study $t \rightarrow m$ as the **FIB** produces a perfectly flat and polished surface. However, the same problem, areas of ‘no solution’, has been reported by a recent **FIB-EBS**D-SEM study (Keuper *et al.*, 2014).

Chapter 3: Mechanical Studies

3.1 Introduction

Zirconia assumes three structurally different crystalline phases; monoclinic, tetragonal and cubic depending on temperature. The tetragonal phase can be partially stabilised at room temperature by addition of small concentration of dopant or stabiliser such as yttrium oxide (Y_2O_3) (Gupta *et al.*, 1977, Hellmann and Stubican, 1983b). **Y-TZP** have a superior potential for clinical use when compared to monoclinic and cubic phases owing to its machinability coupled with high strength and fracture toughness exceeding 1200 MPa and $16 \text{ MPa/m}^{1/2}$, respectively (Piconi and Maccauro, 1999, Vagkopoulou, 2009). When mechanically challenged, for example by a propagating crack, the metastable tetragonal crystals can transform to monoclinic phase ($t \rightarrow m$). This process is accompanied by 3-5% volumetric expansion of the crystals which yields radial compressive stresses that halts the crack propagation. Compared to other ceramics, the unsurpassed strength of **Y-TZP** is due to both the dense, submicron crystalline structure and the unique transformation toughening mechanism or, stress-induced $t \rightarrow m$ transformation (Garvie *et al.*, 1975b, Gupta *et al.*, 1978).

Machined zirconia ceramics and those manufactured by cooling from the cubic phase or direct deposition of tetragonal-prime zirconia powder may exhibit another possible stress-induced toughening mechanism. Ferroelastic domain switching or ferroelastic toughening occurs whereby crack energy can be absorbed and dissipated via rotation of tetragonal crystals around one of the axes to form the so called a twin phase with a different orientation. These changes ultimately increase the material's toughness without notable increase the monoclinic phase ratio (Virkar and Matsumoto, 1986, Chan *et al.*, 1991a)..

Y-TZP can suffer long-term structural deterioration (microcracking and loss of strength) as a result of slow and spontaneous $t \rightarrow m$ transformation process particularly when stored in humid environment or water (Kobayashi *et al.*, 1981). This phenomenon is called low temperature degradation (**LTD**) or ageing. By definition, $t \rightarrow m$ transformation during **LTD** should not be triggered by the local stresses produced

at the tip of an advancing crack as in case of transformation toughening phenomenon (Lughi and Sergo, 2010). Unfortunately, we cannot exploit the remarkable possibility of the former without taking the risks of the latter (Chevalier *et al.*, 2007b).

LTD is a water-mediated martensitic phase transformation that propagates via nucleation-and-growth mechanism. Water is believed to provide free radicles that start the surface corrosive attack and cause lattice shrinkage and build-up of tensile stresses (corrosive-stress process) (Schubert and Frey, 2005). $t \rightarrow m$ starts in the most unstable areas such as grain boundaries where the largest amount of tensile stresses is present (Schmauder and Schubert, 1986a) and then propagates to the centre of the grain as water attack continues (Chevalier *et al.*, 2007b). Tensile stresses resulted from $t \rightarrow m$ cause microcracking at the grain boundaries which in turn, accelerates deeper water penetration and thereby deeper effect of **LTD** (Deville *et al.*, 2004). Nucleation refers to the transformation of a single grain, which can act as a nucleus for further transformation. Growth refers to the preferential extension of $t \rightarrow m$ to the crystals in the vicinity of the nucleus. Growth occurs as a result of the tensile stresses generated from the expanded-transformed grain (Chevalier *et al.*, 1999a).

LTD can have two major macroscopic adverse effects on zirconia dental implants. Firstly, cracking and monoclinic crystals pull-out may cause loss of crystalline coherence and consequently decline in mechanical reliability. Secondly, the released particles can elicit immune response that ultimately cause aseptic bone loss and implant loosening (Chevalier *et al.*, 2007b, Lughi and Sergo, 2010).

The evidence regarding the effect of ageing on the reliability of the **Y-TZP** is equivocal. Several authors reported conflicting findings regarding zirconia ceramics subjected to *in vivo* or *in vitro* induced **LTD**. An *in vitro* experiment has shown that Young's modulus and hardness values of **Y-TZP** bars were reduced by 30% when they were subjected to hydrothermal ageing (Cattani-Lorente *et al.*, 2011). It was also reported that fracture strength of **Y-TZP** was reduced significantly following hydrothermal ageing (Ban *et al.*, 2008, Flinn *et al.*, 2012). The decline in these mechanical parameters was attributed to the increased monoclinic phase fraction which is more susceptible to microcracking.

Several *in vitro* and *in vivo* studies reported that effect of ageing on the durability of **Y-TZP** was negligible (Shimizu *et al.*, 1993, Cales *et al.*, 1994, Ardlin, 2002,

Papanagiotou *et al.*, 2006). This has led to new thinking as to whether the presence of monoclinic phase is detrimental or not. In fact, there is some evidence suggests that $t \rightarrow m$ localised to the surface may lead to the establishment of surface compressive stresses that balance out applied tensile stresses and thereby strengthen the material (Kosmać *et al.*, 1981, Virkar *et al.*, 1987, Tanaka *et al.*, 2003). This has been consolidated by both the fact that medium- to long-term data from clinical studies rarely identified fracture of zirconia as a problem. Additionally, there is no correlation between failures and *LTD* in all studied *Y-TZP* materials used for dental applications (Molin and Karlsson, 2007, Özkurt and Kazazoğlu 2010, Sailer *et al.* 2007).

3.2 Experimental procedures and results: zirconia discs

3.2.1 Accelerated *in vitro* ageing

Injection moulded, acid-etched, ethylene oxide sterilised, 17.85 ± 0.011 mm diameter and 1.03 ± 0.014 mm thick zirconia discs were provided by the manufacturer (Maxon motor GmbH, Germany). Discs were aged in a 1.2 L high pressure hydrothermal reactor (Series 4540 Parr, U.S.A) with 300 ml of distilled water. The ageing cycle lasted for 5 hours at operating temperature and pressure equal to 134 °C and 2 bar, respectively. Samples were left in the hydrothermal reactor upon completing the cycle until 50 °C temperature was reached. The cooling rate was estimated to be 0.011 °C/sec. Samples were dried using air and stored in a desiccator until further testing.

3.2.2 Biaxial flexural strength

Alongside many other superior characteristics, high strength and toughness of *Y-TZP* based ceramics endorsed their use in the dental field. In addition, the unsurpassed advances at the level of manufacturing technologies facilitated the exploitation of such materials. *CAD-CAM* exponentially expanded the use of *Y-TZP* as an aesthetic, and yet a high strength alternative to metal alloy based dental implants and restoratives. Other technologies such as *CIM*, powder coprecipitation and *HIP* were among the assets that enabled the manufacturing of high-precision components required for dental implant systems.

Depending on chemical composition, microstructural features and processing method, *Y-TZP* based ceramics exhibit flexural strength ranging from 750-1310 MPa

(Ruiz and Readey, 1996, Casellas *et al.*, 2001, Ardlin, 2002, Milleding *et al.*, 2003, Guazzato *et al.*, 2005, Curtis *et al.*, 2006, Denry and Holloway, 2006, Ban *et al.*, 2008, Denry and Kelly, 2008, Flinn *et al.*, 2012). Several studies investigated the effect of various *in vitro* and *in vivo* ageing approaches on the flexural strength of **Y-TZP** based ceramics. Several authors reported no detrimental effects of various ageing mechanisms and durations on strength and reliability of this material. In contrast, other studies reported strength degradation of **Y-TZP** materials upon artificial and *in vivo* ageing. The disparity can be attributed to; the different ageing mechanisms and durations used by different investigators, differences in parameters governing the activation barrier of **LTD**, differences in sample geometries and data analysis techniques.

Studying the pure tensile strength of ceramic materials by direct tensile strength tests is a difficult task owing to their brittleness and subsequent difficulties in gripping and aligning the specimens. Thus, direct tensile strength tests have seldom been used to study brittle materials (Bowen and Rodriguez, 1962, Zidan *et al.*, 1980, Brown, 2010). Uniaxial flexural strength tests were introduced as an alternative method. The latter tests may yield highly variable strength values as a result of edge fracture effect. Additionally, they require substantially flat and large samples which may be difficult to achieve in the case of dental ceramics (Ban and Anusavice, 1990).

The biaxial flexure test is a widely used, viable alternative to apply biaxial tension on the surface of a ceramic sample (Wachtman *et al.*, 2009, Callister and Rethwisch, 2012). The flexural strength can be determined using three balls supporting a thin ceramic disc with a centrally applied loading rod, also known as piston-on-3-balls (Kirstein and Woolley, 1967). The use of this setup allows testing warped samples directly after firing which in turn, eliminates the need for machining the samples to a specified geometry and flatness. In the case of zirconia based-ceramics, this is an extremely important aspect as machining itself may alter material's properties. Finally, it disregards the edge effect in areas located outside the supporting balls and thereby enhances the reliability of the test outcome (Wachtman *et al.*, 2009).

A group of technically identical samples can fail at largely variable loads owing to the differences in the size of the major crack or cracks in the area subjected to loading. Therefore, the strength of brittle materials has to be described by a

probability function. The size of the sample is an important factor in the statistical behaviour of reliability of ceramic materials. It follows that under the same stress, the probability of failure of larger samples is higher than a smaller counterparts due to the higher probability of having larger number of major cracks (Wachtman *et al.*, 2009).

The basis of contemporary ceramic manufacturing is largely dependent on the statistical distribution function model proposed by Weibull. Weibull statistics provides a quantitative method to determine strength reliability of brittle materials based on the assumption that failure at any flaw translates as failure of the whole sample. This is a form of extreme statistics applying the weakest link theory or extreme distribution function that offers the advantage that a material in a given system can survive evidently longer than the estimated lifetime by such a model.

The two parameter Weibull distribution function for a brittle sample subjected to uniaxial fracture strength test with a volume (V) and strength (σ) is given by Equation (16) (Weibull, 1951, Danzer *et al.*, 2007):

$$F = 1 - \exp \left[- \frac{V}{V_0} \left(\frac{\sigma - \sigma_u}{\alpha} \right)^\beta \right] \quad (16)$$

Where;

F is the probability of failure,

β is the Weibull modulus,

α is the characteristic strength,

σ_u is the stress level below which the material will not fail (equals 0), and

V_0 is the chosen normalising volume

The value of β measures the variability in the strength of the material and it is inversely related to the scatter of fracture strength data. The higher the β value the narrower scattering to be expected in the fracture strength data. The value of α represents the stress level of fracture strength where probability of failure equals to 63%. Weibull moduli of dental ceramics usually fall in the range of 10-15. Great efforts are however being made to minimise flaws and attain β values equal to 20 (Wachtman *et al.*, 2009).

The biaxial flexural strength (**BFS**) was determined for 60 sterilised discs that were equally divided into two groups; as-received and hydrothermally aged discs. A universal testing machine (LR10K material tester, Lloyd, UK) was used for this purpose according to the ISO standards for dental ceramics (ISO 14704, 2008). Prior to the test, the radius and thickness of each sample were measured three times using a digital micrometer (Mitutoyo Ltd, Hampshire, UK) and an average was obtained. Each disc specimen was placed centrally on three, industry-standard grade, hardened steel, 5 mm diameter ball bearings. Ball bearings were placed 120° apart on a 10 mm diameter support circle.

Discs were loaded using a custom-made, steel, 1.6 mm diameter piston at a cross head speed of 0.5 mm/min until failure point. A load-controlled load cell with 5 kN upper load limit was used. In all tests, a thin polythene sheet was placed between the pushing rod and specimen to ensure even stress distribution while loading. The fracture loads were obtained from load-extension graphs generated by NexygenPlus® software (AMETEK Test & Calibration Instruments, USA). **BFS** values were calculated using Equations 17, 18 and 19:

$$\mathbf{BFS(MPa)} = -0.2387 \frac{\sigma(X - Y)}{d^2} \quad (17)$$

$$X = (1 + \nu) \ln \left(\frac{r_2}{r_3} \right)^2 + \left[\frac{1 - \nu}{2} \right] \left(\frac{r_2}{r_3} \right)^2 \quad (18)$$

$$Y = (1 + \nu) \left[1 + \ln \left(\frac{r_1}{r_3} \right) \right]^2 + (1 - \nu) \left(\frac{r_1}{r_3} \right)^2 \quad (19)$$

Where;

σ : fracture load (N)

d : disc' thickness at loading point (mm)

ν : Poisson's ratio (assumed to be 0.25)

r_1 : radius of support circle (mm)

r_2 : radius of loaded area = radius of pushing rod (mm)

r_3 : radius of the disc (mm)

SPSS statistics, version 19 (IBM, USA) was used to perform one-way analysis of variance (ANOVA) to assess statistical differences between the means of **BFS** of the as-received and aged groups. Statistical software (Weibull ++, version 9.0.10; ReliaSoft Corp, Tucson, Arizona) was used for the determination of the two-parameter Weibull estimates and 95% (2-sided) confidence intervals (**95% CI**) according to the maximum likelihood method. Origin Pro 9.1 (OriginLab, USA) was used to plot all presented data. **SEM** (S-3400N, Hitachi, Japan) was used to examine bulk morphology of representative fractured surfaces from as-received and aged discs.

The mean **BFS** values of the as-received and aged groups were 1003.68 ± 73.05 MPa and 1033.11 ± 102.10 MPa, respectively. Comparison of means was performed using one way ANOVA test at the 5% significance level which showed no significant difference in the mean **BFS** of the two groups ($p > 0.05$). A difference in Weibull modulus (β) (15.9 vs. 10.8) and characteristic strength (α) (1036.88 vs. 1079.74 MPa) was however noticed for as-received and aged samples, respectively. The difference was not significant as the **95% CI** of both parameters overlapped as shown in Table 8.

The **BFS** values were plotted against Weibull percentiles for as received and aged groups separately as shown in Figure 44. R^2 values for both data sets indicate good fit of the data to the assumed linear statistical distribution. Comparative Weibull plot for both groups is shown in Figure 45.

Table 8. Summary of mean (MPa) and Weibull parameters obtained for BFS data

	<i>As-received</i>	<i>Aged</i>
Mean (SD)	1003.68 (73.05)	1033.11 (102.1)
β (95% CI)	12.5- 15.8 -20.5	8.7- 10.8 -14.2
α (95% CI)	1012.3- 1036.9 -1062.1	1042.4- 1079.7 -1118.5
R^2	0.99	0.98

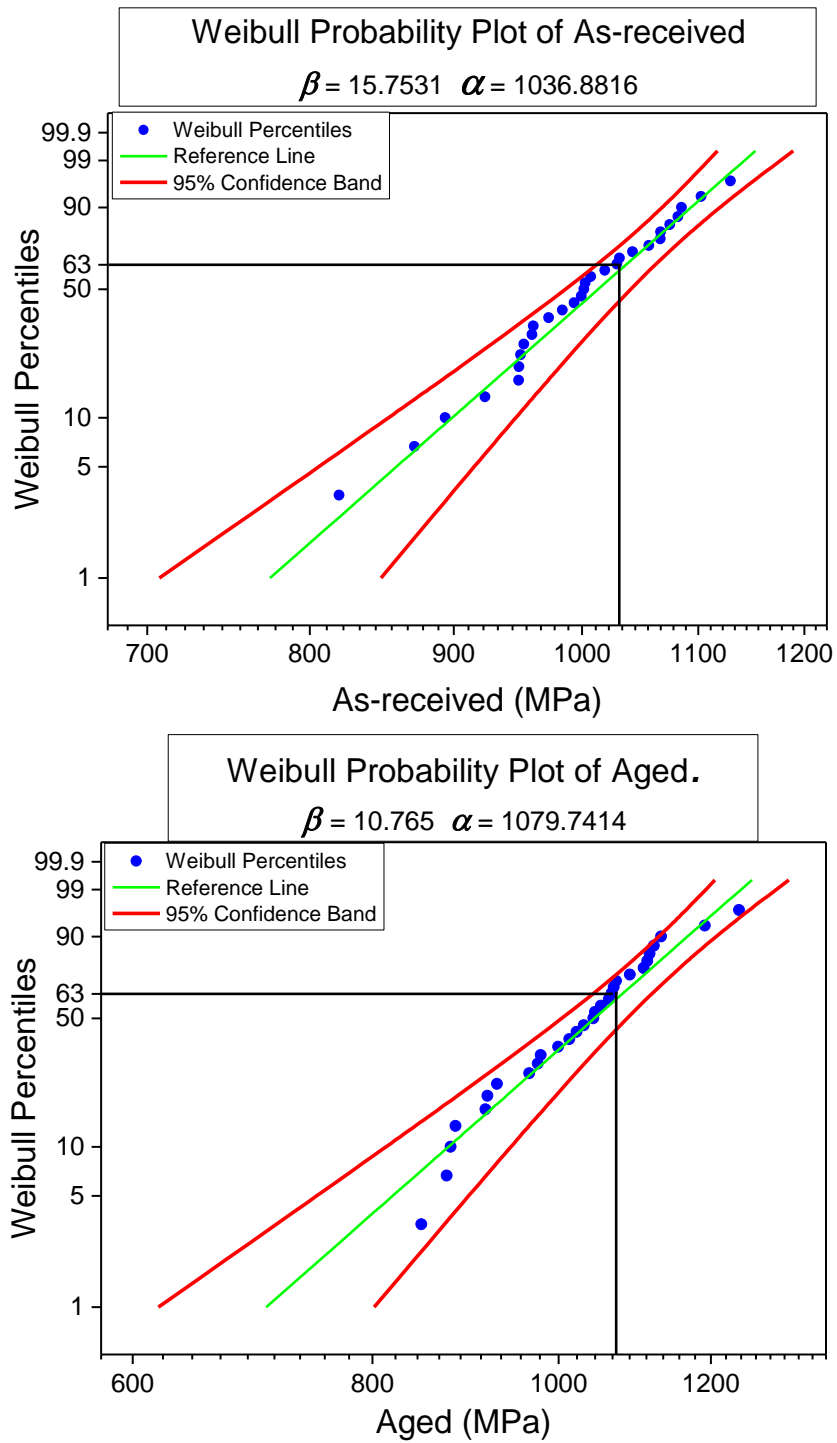


Figure 44. Weibull probability plots for **BFS** data for as-received and aged samples. Blue circles represent **BFS** values plotted against Weibull percentiles. Characteristic strength (α) was calculated as the load where 63% of samples failed. Red lines represent upper and lower **95% CI** bounds.

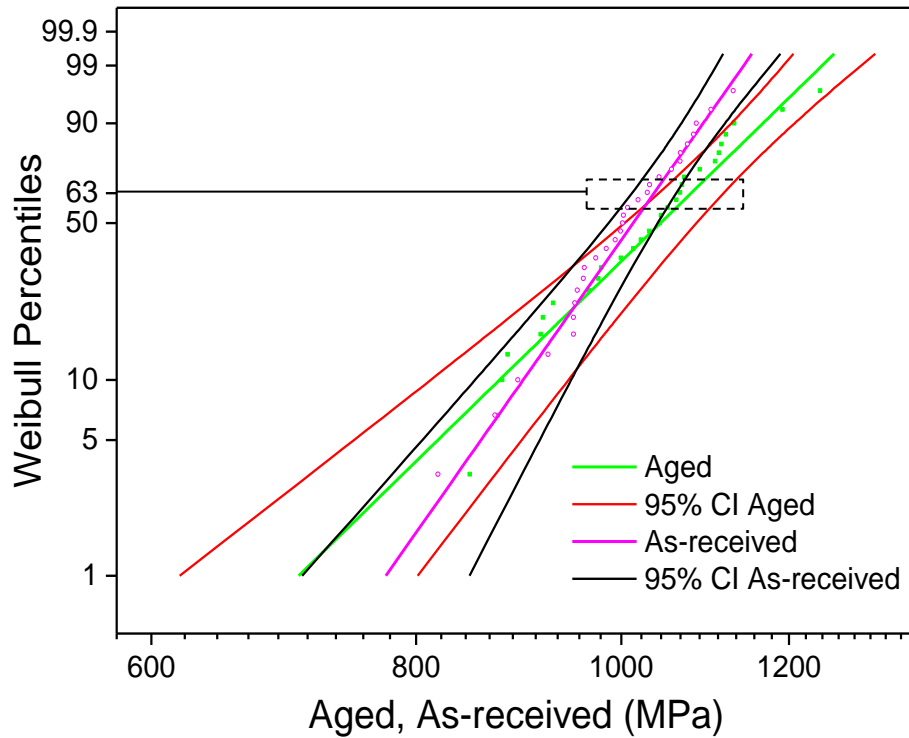


Figure 45. Comparative Weibull plot for *BFS* data.

The intersection between Weibull lines and data points of as-received (amber) and aged (green) samples indicate the similar reliability of both groups. The overlap between **95% CI** of α and β or strength at 63% probability (red lines) of failure for both groups confirm the lack of statistically significant difference between the reliability of both groups.

Examination of fractured surfaces of representative as-received and aged discs under *SEM* revealed similar mode of failure in both groups. The tensile side of samples from both groups exhibited hackles running in the direction of cracking and separating parallel portions of the crack surface. A primary Wallner line was seen in both samples which indicated surface rather than bulk origin of the fracture.

Under low magnifications, neither of the samples showed any sign of porosity, internal defects, pores, pores agglomerates or areas of high contrast that may indicate presence of microcracking as a result of *LTD*. Figure 46 and 47 represent *SEM* fractography of representative as-received and aged samples obtained from *BFS* test.

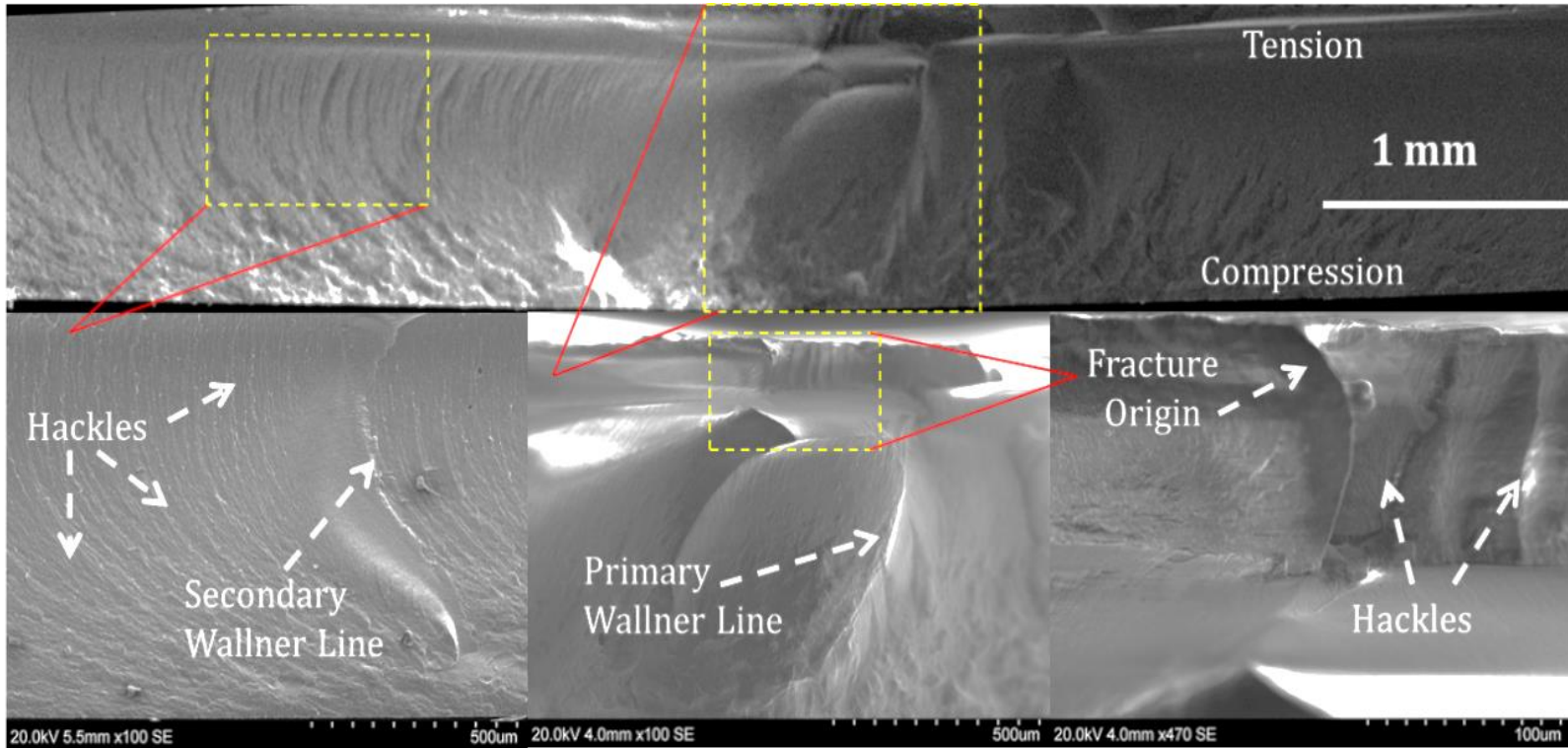


Figure 46. *SEM* fractography of as-received sample.

Fracture origin was identified at the tensile surface where maximum flexure is concentrated at the opposite side of the push rod or piston. The classical manifestations of crack propagation in brittle solid materials are annotated. They include; hackles, primary and secondary Wallnar lines.

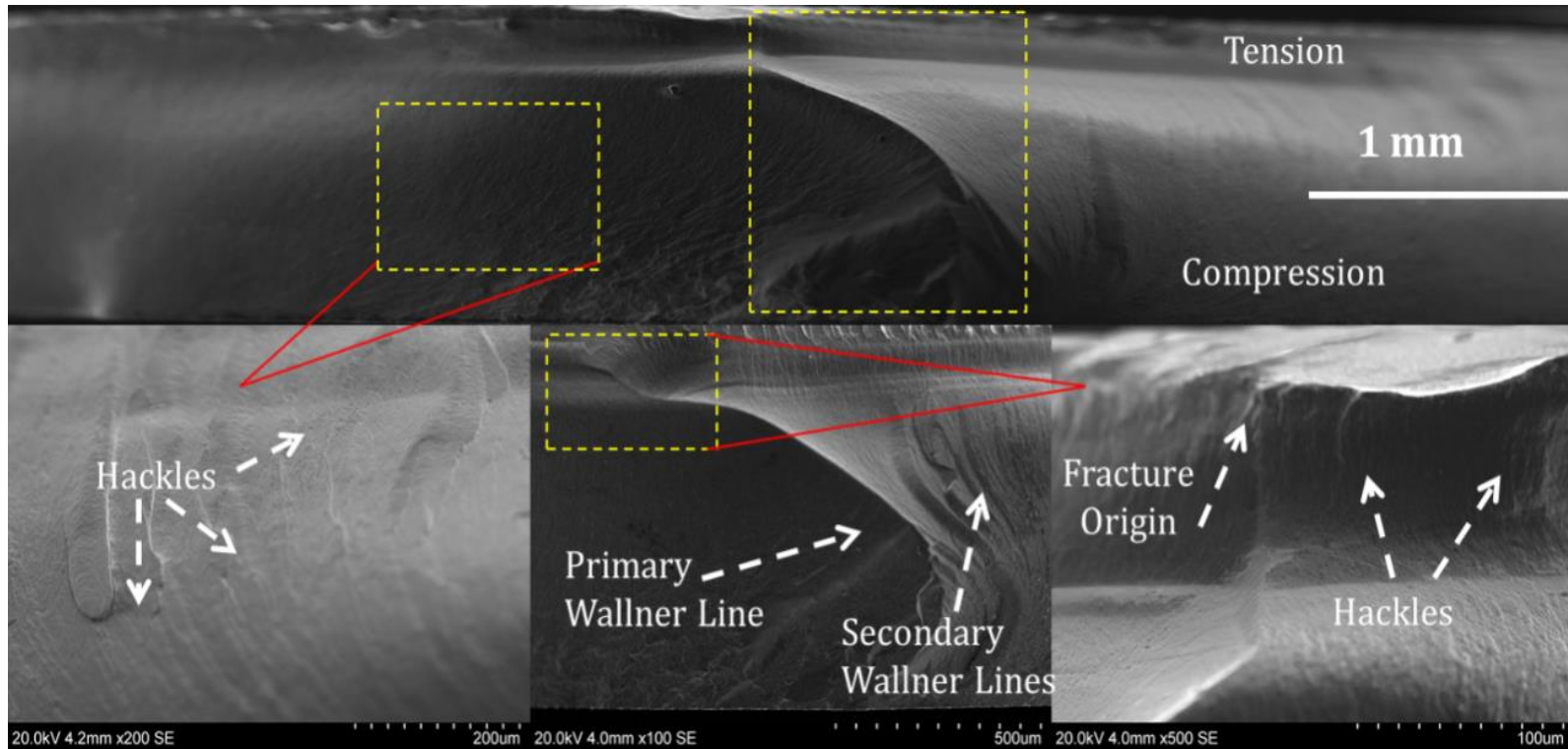


Figure 47. *SEM* fractography of representative aged sample.

The appearance of the fractured surfaces from aged samples was very similar to as-received counterparts.

3.2.3 Edge fracture strength

Edge strength or toughness describe the brittle material's resistance to chipping or flake detachment upon loading. The edge fracture strength test has been widely utilised to assess the durability of brittle materials which have their edges subjected to machining or mechanical loading such as valves and cutting tools made of ceramics or hardened metals (Danzer *et al.*, 1997, Morrell and Gant, 2001). In dentistry, marginal integrity of the dental restoratives is a key factor in their longevity. Marginal chipping is a frequently encountered problem and may lead to aesthetic and biological complications. Studying the edge fracture strength and chipping behaviour of ceramic materials used in dental implantology, in particular, is considered of a high importance. The thin implant threads are susceptible to significant amount of stress during insertion and loading which theoretically can increase the risk of implant fracture. In addition, chipping of the edge of implant's head may compromise marginal adaptation of the crown prosthesis which can lead to plaque retention and subsequent peri-implant soft and hard tissue inflammation.

Edge fracture strength test involves loading the sample vertically at a certain distance from the edge using a hard standard indenter. Upon loading, brittle materials respond by combination of plastic deformation followed by formation of cracks at the corners of the indentation as when using the Vickers diamond indenter. Propagation of the formed cracks, particularly those running parallel to the edge or towards it, is enhanced by the elastic relaxations of the edge face. A completely detached spall or flake will only be formed when the load exceeds the critical limit with subsequent crack propagation outside the edge (Morrell and Gant, 2001). Depending on plasticity and toughness of the material, acoustic detection sensor in the edge fracture strength machine can detect three types of failures namely, localised deformation (indentation), indentation with cracking and complete chipping or spall formation (Watts *et al.*, 2008).

The force (N) required for chipping the specimens at a distance of 0.5 mm from the specimen edge is, by definition, the edge fracture strength (Watts *et al.*, 2008). An experimental work by Morell and Gant (2001) confirmed the previously reported linearity between the chipping load and distance from the edge for a number of fine-grained brittle ceramic materials. However, they reported slight departure from the

linear relationship in Cobalt hardened materials and sintered silicon carbide ceramics which can be attributed to; R-curve effect, internal stresses and surface finish near the edge (Morrell and Gant, 2001). With regard to *Y-TZP* materials, Petit *et al* (2009) reported a unique non-linear relationship between the chip size and the applied load (Petit *et al.*, 2009). Several studies investigated the static edge fracture strength of *Y-TZP* based ceramics. Petit *et al* (2009) reported edge fracture load range between 200-300 N at 0.3 mm distance from the edge (Petit *et al.*, 2009). Others reported lower values but used different indenters (Gogotsi *et al.*, 2007). To the author's best knowledge, there is no data so far regarding the effect of ageing on the edge fracture strength of *Y-TZP* based ceramics.

In this project, sixty discs were equally divided into as-received and aged groups were subjected to edge fracture strength. The test was performed in three well-spaced apart locations within each sample and an average edge fracture strength value was calculated. For this purpose, an edge strength measurement device (CK10, Engineering Systems, UK) was used to determine fracture strength of material at a distance equal to 0.3 mm from the edge. Vickers diamond indenter was used to vertically load samples at crosshead speed of 1 mm/min. The acoustic sensor was disabled and only chipping load was measured for all samples. Statistical analysis, data plotting and *SEM* post-mortem examination was performed as described in Section 3.2.2.

The mean value of edge fracture strength for as-received group (239.86±16.93 N) was slightly lower than the aged group (248.11±12.13 N). There was no significant statistical difference between the mean values as indicated by Welch and Brown-Forsythe tests ($p>0.05$). Weibull modulus and characteristic edge strength were higher for the aged group, no statistically significant difference was however present as indicated by the overlapping **95% CI** of both parameters. Mean fracture edge strength values and Weibull parameters are summarised in Table 9. Edge fracture loads were plotted against Weibull percentiles for both groups as shown in Figure 48.

Table 9. Summary of mean (N) and Weibull parameters obtained for edge fracture strength data.

	<i>As-received</i>	<i>Aged</i>
<i>Mean (SD)</i>	239.8(16.9)	248.1(12.1)
β (95% CI)	11.9- 15.7 -20.2	17.5- 22.2 -29.2
α (95% CI)	241.9- 246.01 -253.4	249.7- 252.1 -257.7
R^2	0.97	0.98

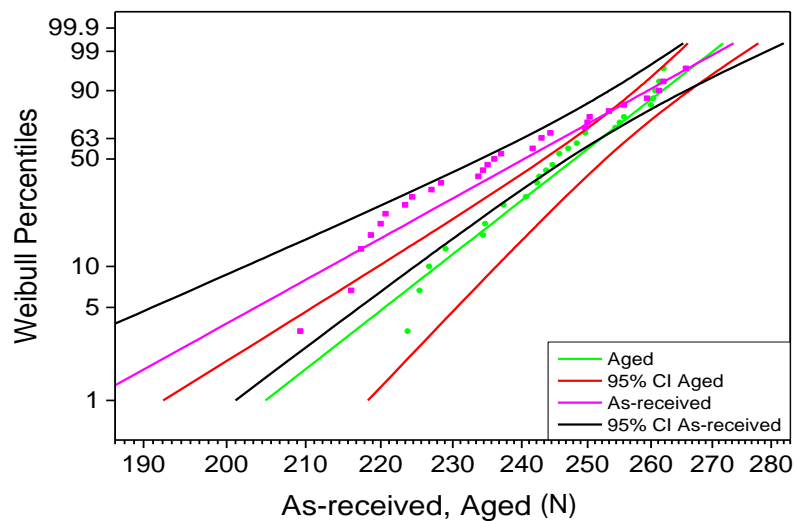
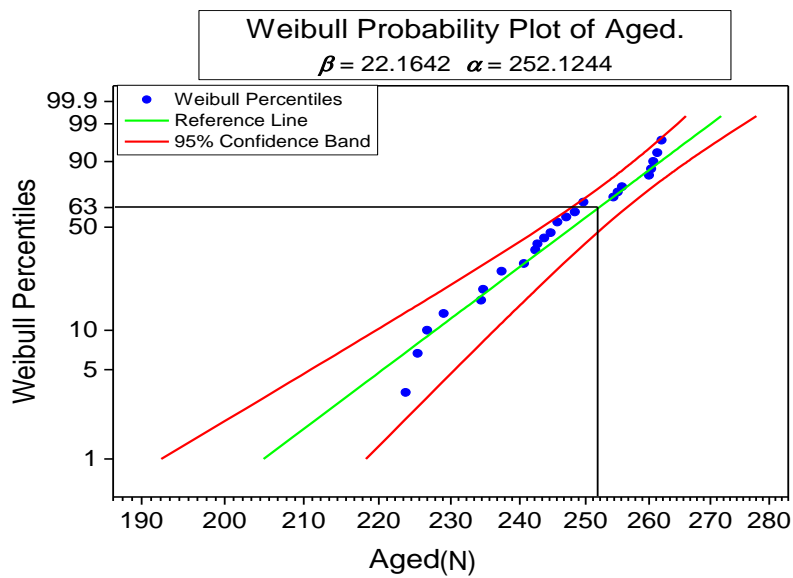
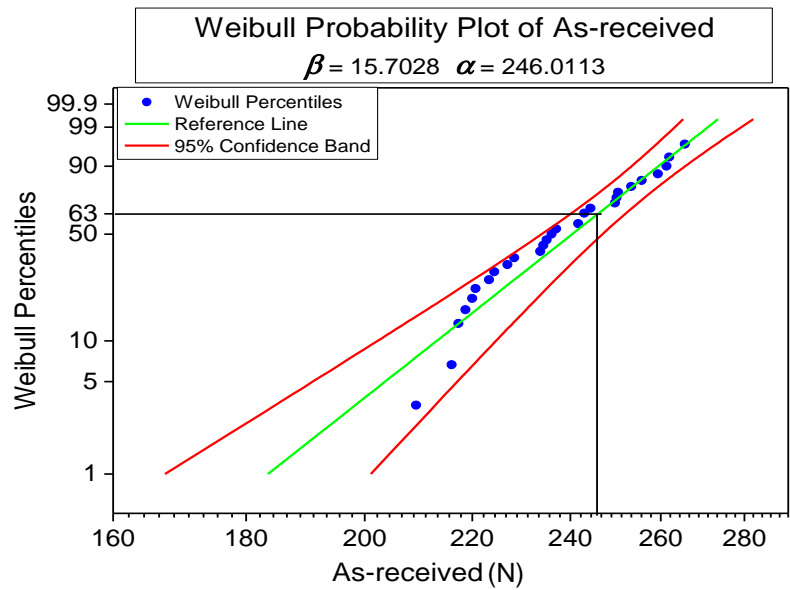


Figure 48 Weibull probability plots for edge fracture strength test. Weibull plots for as-received (top), aged (middle) samples.. Comparative Weibull plot for edge fracture strength data for both groups (bottom).

Post-mortem views of the chipped samples from as-received and aged samples clearly demonstrated fracture origin, loading area or area with elastic deformation and flake fracture lengths. In both groups, the width of the chip scar was approximately double the flake fracture distance and the chipping did not involve the whole thickness of the material (Figure 49 and 50).

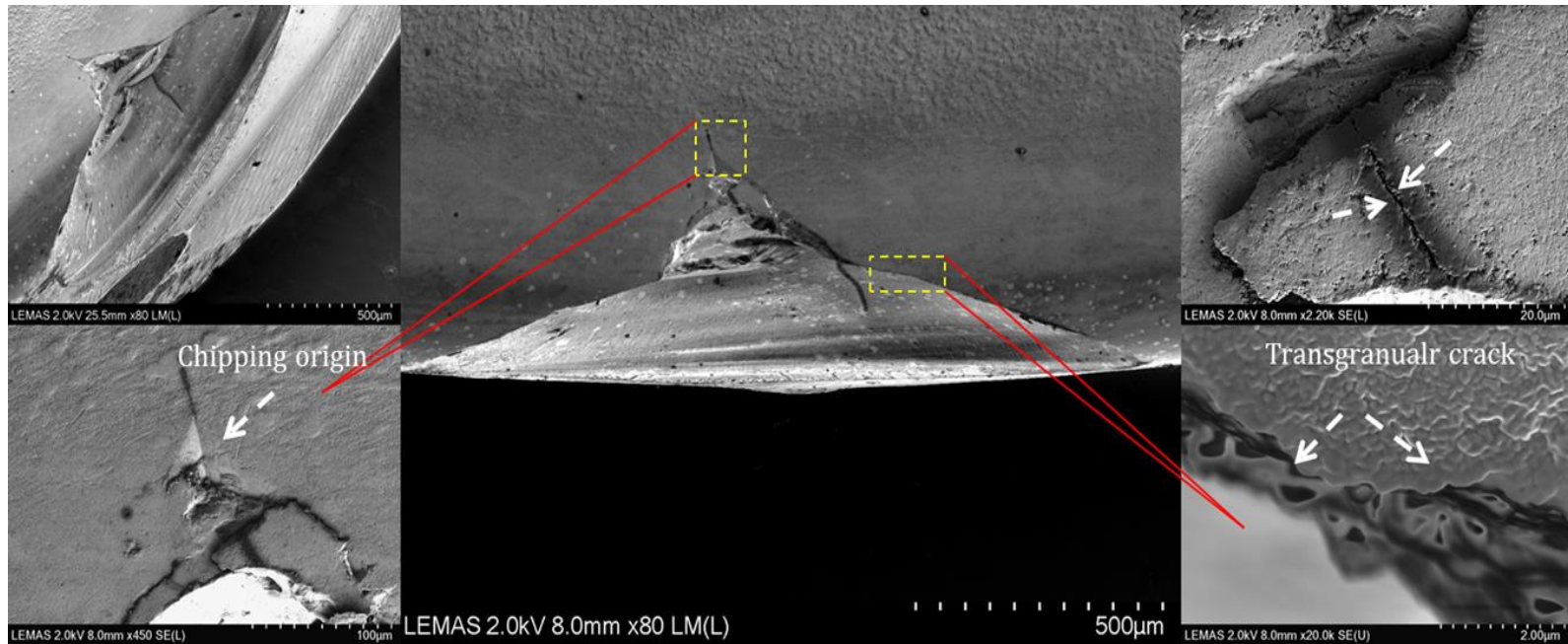


Figure 49. **SEM** post-mortem examination of the fractured edge of a representative as-received sample.

Middle, low magnification of the chip scar where the initial crack developed upon loading can be seen. Bottom left, chipping origin is shown at higher magnification. The imprint of the Vickers indenter used to load the sample can be noticed with subsequent elastic deformation and two cracks originating from the side of the imprint. Top left, image demonstrates that the chip was only confined to partial thickness of the sample. Right, cracks originating toward the periphery (bottom) or the centre (top) of the sample were transgranular in nature. No evidence of crack bridging was detected.

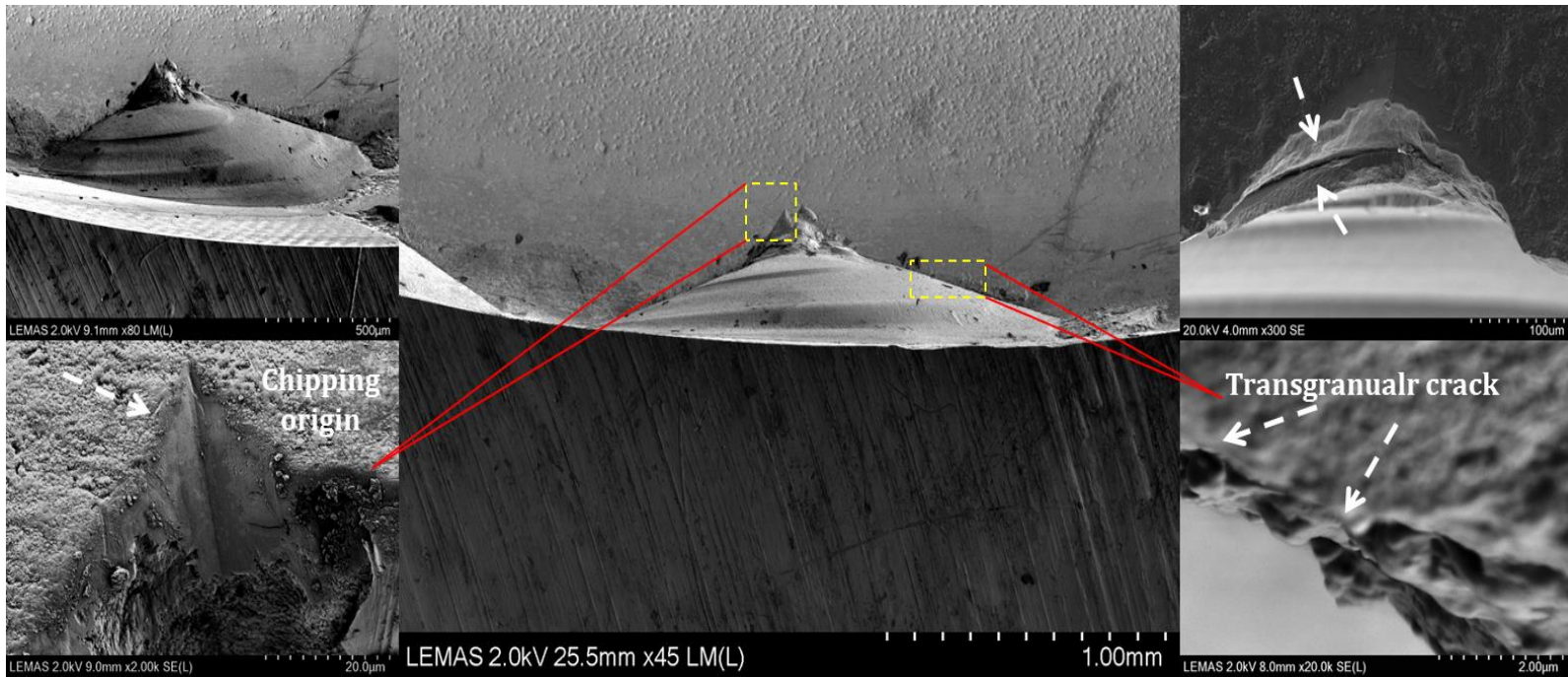


Figure 50. **SEM** post-mortem examination of the fractured edge of a representative aged sample. The appearance of the chipped edges from aged samples was very similar to as-received counterparts.

3.2.4 Microhardness

Hardness of a given brittle material denotes the resistance to plastic deformation and brittle fracture when subjected to penetrating ‘compressive and shear’ loading such as indentation (Herrmann, 2011). Characterisation of this important property can be performed at various scales via using variable loads and indenter sizes and geometries. Brinell, Meyer and Rockwell hardness are considered as macroindentation tests while Knoop and Vickers hardness are regarded as microindentation tests (Yovanovich, 2006). The third type of indentation tests is nanoindentation and it is described in the Section 3.2.5.

Hardness of any material is largely affected by; bonding forces between the atoms and packing density of the grains inside the crystalline lattice, surface and bulk density of the material, presence of surface or bulk porosity, grain size and orientation, microstrain and amount of impurities (Herrmann, 2011). In addition, in transformation toughened materials such as *Y-TZP*, phase composition of the material may largely influence hardness. It has been reported that Vickers hardness of zirconia ceramics decreased with decreasing dopant concentration which indicates an inverse relationship between amount of monoclinic phase formed by $t \rightarrow m$ and hardness values (Lin & Duh, 2003).

Hardness is a crucial parameter for ceramics used in the biomedical field. High hardness values are required for ceramics used as wear- and abrasion-resistant parts such as prosthetic ball and socket hip-joint in addition to dental implants and restoratives. The standard specification for High-Purity Dense *Y-TZP* for Surgical Implant Applications by ASTM (withdrawn in 2007), stipulated that Vickers hardness number (*HV*) shall be no less than 11.8 GPa at a load equal to 1 Kg (ASTMF 1873-98, 1998).

Commercially available, as-received, polished, uncoloured and coloured *Y-TZP* ceramics exhibited Vickers hardness values ranging from 12.9-13.6 GPa (Pittayachawan *et al.*, 2007, Pittayachawan, 2008). In other studies, machined and polished *Y-TZP* samples demonstrated comparable Vickers hardness values between 11-13.70 GPa (Luthardt *et al.*, 2002, Guazzato *et al.*, 2004). Furthermore, it has been concluded that variation in the sintering time from 1.6 hours to 3 hours and thermocycling in distilled water for 20,000 cycles in 5–55 °C had no detrimental effect

on the Vickers hardness values of a commercially available **Y-TZP** based ceramic (Hjerppe *et al.*, 2008).

The Vickers microhardness test is a reliable method for determination of microhardness of ceramics. It utilises a diamond indenter to apply a prescribed load on the surface of the sample for a predetermined period of time. The Vickers indenter has square-based pyramidal geometry with an angle of 136° between opposite faces at the vertex. During the indentation process, brittle materials exhibit two types of deformation, elastic deformation and brittle fracture. Upon the end of the indentation cycle, an optical microscope is used to determine diagonal lengths of the imprint (d_1 and d_2). **HV** (GPa) is given by the relation between the load (F) in Newton (N) and surface area of the imprint (d_v^2 , $d_v=[d_1+d_2]/2$) in (mm²) according to Equation 20 (Yovanovich, 2006, Herrmann, 2011):

$$HV = 0.1891 \left(\frac{F}{d^2} \right) \quad (20)$$

The volume of imprint caused by the indenter depends on the indenter's geometry, load applied to the indenter, duration of loading and the amount of elastic recovery after indentation. The relationship between the average diagonal length (d_v) of the imprint and the penetration depth (t) of the indenter is given as (Yovanovich, 2006):

$$dv = 7t \quad (21)$$

The Vickers contact area (A_v) and indenter's penetration depth are related as (Yovanovich, 2006):

$$A_v = 24.5 t^2 \quad (22)$$

In this project, Vickers hardness values were measured for as-received and aged discs (n=30) according to the ISO standards for testing advanced technical ceramics (ISO 14705, 2008). A microhardness tester (HM-112, Mitutoyo, UK) was used to perform indentation tests on four randomly selected areas of each disc. Average microhardness measurement was calculated for each sample. Indentation testing was performed using 1 Kg loading with loading period of 15 sec. The indentation diagonal lengths were defined using an integral optical microscope under ×50 magnification.

The Vickers hardness values were calculated automatically by the software integrated to the microhardness machine according to Equation (20).

In order to improve the quality of imaging and to achieve better visualisation of cracks resulting from Vickers indentation, four discs were mirror polished using Tegamin preparation system-20 (Struer, UK). Polishing stages and products used are shown in details in Table 7, Section 2.6.4.1. Optical microscopy at $\times 1000$ magnification using Dark Field and Differential Interference Contrast to assess levels of remaining deformation (BXiS, Olympus, UK). Remaining surface roughness was assessed using a 3D optical profilometer (NPFLEX, Bruker, UK). Roughness average (R_a) was less than 20 nm. Two discs were aged according to protocol described in section 3.3.1. Indentation testing was done in several areas following the protocol explained in the previous paragraph.

Statistical analysis and data plotting was performed as described in Section 3.2.2. Assuming that the development of a Vickers indentation as a result of vertical loading can be regarded as failure, statistical software (Weibull++, version 9.0.10; ReliaSoft Corp, Tucson, Arizona) was used for the determination of the 2-parameter Weibull estimates and 95% (2-sided) confidence intervals according to the maximum likelihood method. High resolution *SEM* equipped with cold field emission gun (Series SU8230, Hitachi, Japan) was used to examine the morphology of indentation imprints and the associated cracks developed around the indenter in representative as-received and aged discs.

The mean Vickers hardness of the as-received group (14.06 ± 0.61 GPa) was slightly higher than the aged group (13.81 ± 0.44 GPa). The mean depth of penetration (t) of Vickers indenter was 5.14 ± 0.10 μm and 5.18 ± 0.07 μm for the as-received and aged groups, respectively. One-way ANOVA revealed no statistically significant difference between the two groups ($p > 0.05$) (Table 10). In addition, 2-parameter Weibull estimates were calculated for hardness values for both groups as shown in Figure 51. There was no significant difference in the probability of failure as indicated by overlapping **95% CI** for Weibull modulus and characteristic hardness (Figure 52).

Table 10. Summary of mean HV, penetration depth (t) and Weibull parameters. Mean (SD).

	<i>As-received</i>	<i>Aged</i>
HV (GPa)	14.06(0.61)	13.81(0.44)
β (95% CI)	21.1- <u>25.9</u> -31.9	21.6- <u>27.5</u> -34.9
α (95% CI)	14.1- <u>14.3</u> -14.5	13.8- <u>14.03</u> -14.2
R^2	0.91	0.97
t (μm)	5.14 (0.1)	5.18 (0.07)

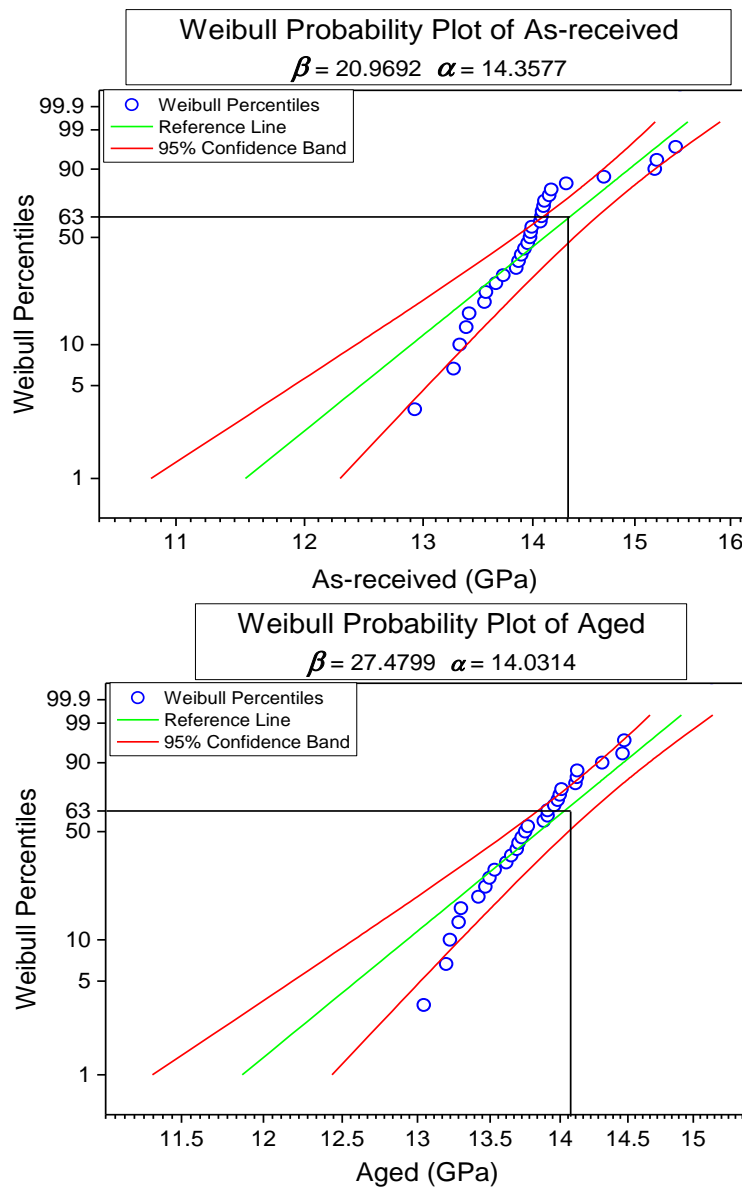


Figure 51. Weibull plots for Vickers hardness data for as-received and aged groups.

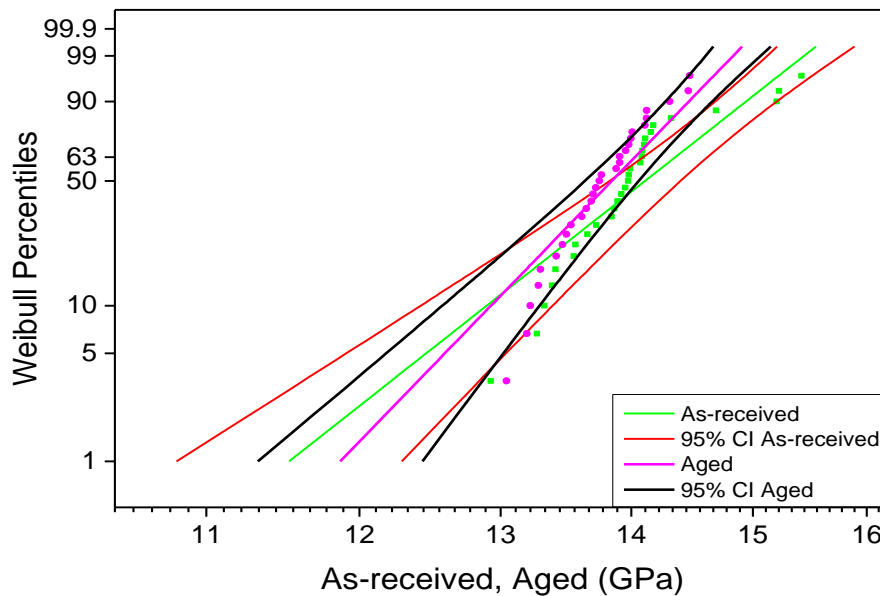


Figure 52. Comparative Weibull plot for Vickers indentation data.

SEM examination of representative, polished and unpolished, as-received samples revealed characteristic Vickers imprints with approximately similar diagonal lengths. Tilting samples at 15° clearly showed the raised edges of the imprints that represent areas of plastic deformation. Cracks were noticed near the corners, sides and inner slopes within the imprints. The major cracks developed mainly outside the imprint's corners and higher magnification revealed the transgranular nature of such cracks as shown in Figure 53 and 54. Smaller cracks occurred in various areas of the imprint and some of them were intragranular in nature. Edges exhibited some roughness due to grain pull-out.

Similar findings were noticed in the imprints made on aged samples (Figure 55). However, a large area exhibited significant change in contrast outside the imprints made on the polished-aged sample that could be an indication on $t \rightarrow m$ phase transformation in the area of plastic deformation (Figure 56). It is very likely that this demonstrates the transformed areas with elastic deformation zone caused by shear stresses of the sides of the indenter.

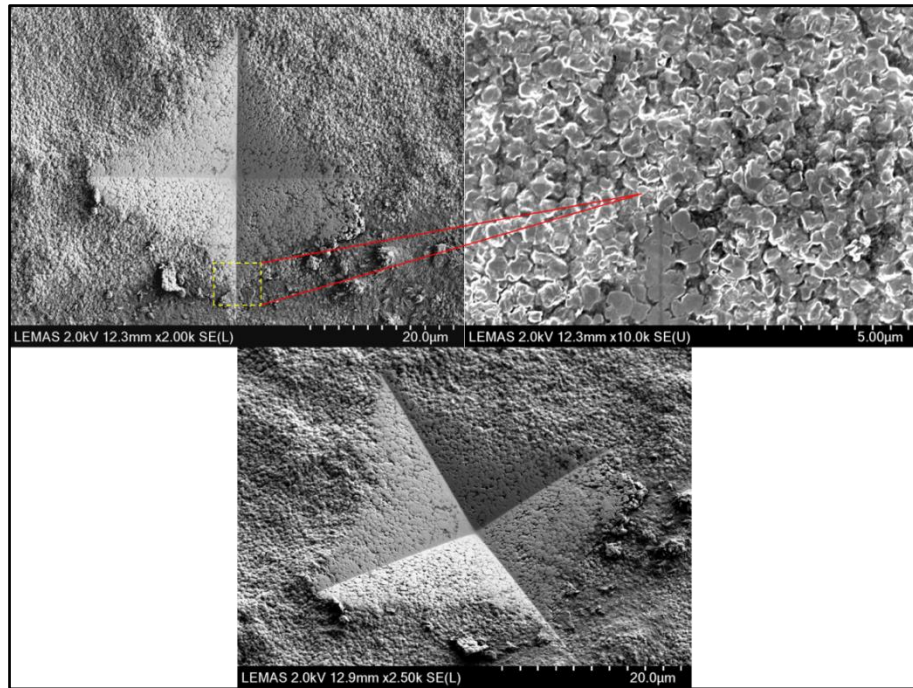


Figure 53. **SEM** examination of Vickers indentation imprint on representative as-received (unpolished) sample.

Characteristic Vickers imprint with approximately similar diagonal lengths is shown in top left image. No major crack development could be detected as a result of surface roughness. Areas of plastic deformation and crystal pull-out can also be seen in the same view. At higher magnification (top right), small, unclear cracks can be seen within the corner and slopes of the imprint. Tilting sample at 15° emphasised the raised edges of the imprint and the area of

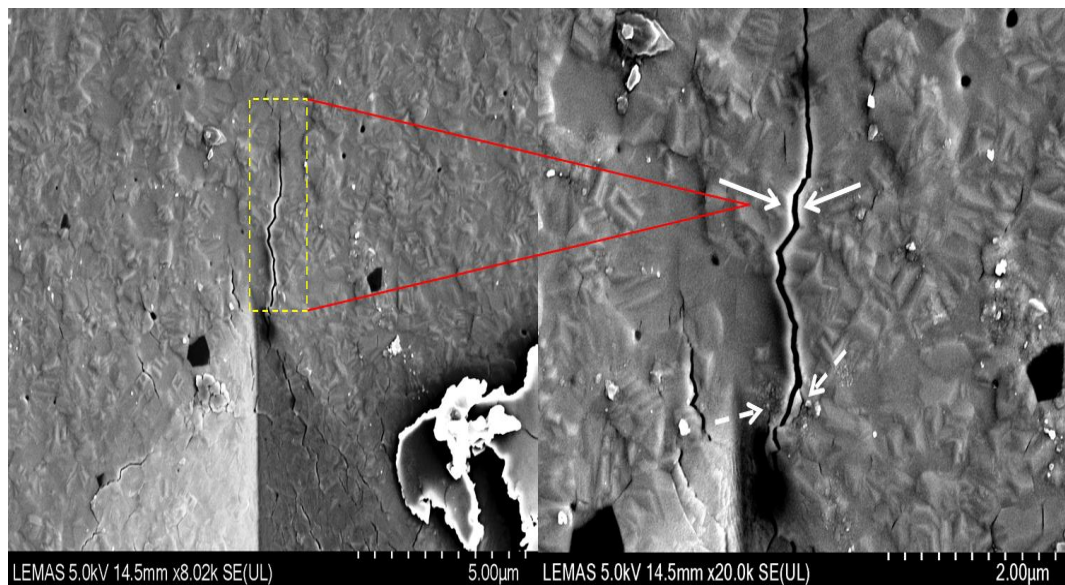


Figure 54. **SEM** examination of cracks associated with Vickers indentation on polished, as-received sample.

Cracks developed around the corners of the indenter made on a representative as-received sample were mixed. The crack shown (left) and magnified (right) started as intragranular (←→) and then propagated in transgranular fashion (→).

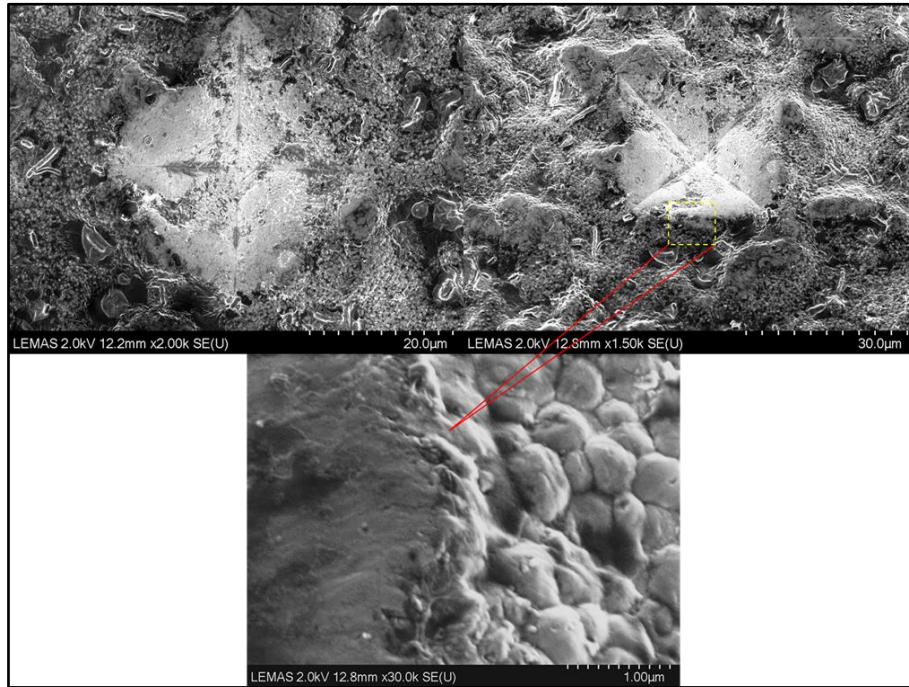


Figure 55. **SEM** examination of Vickers indentation imprint on representative aged (unpolished) sample.

Characteristic Vickers imprint similar to as-received sample. Higher rate of crystal pull-out and plastic deformation can be seen however

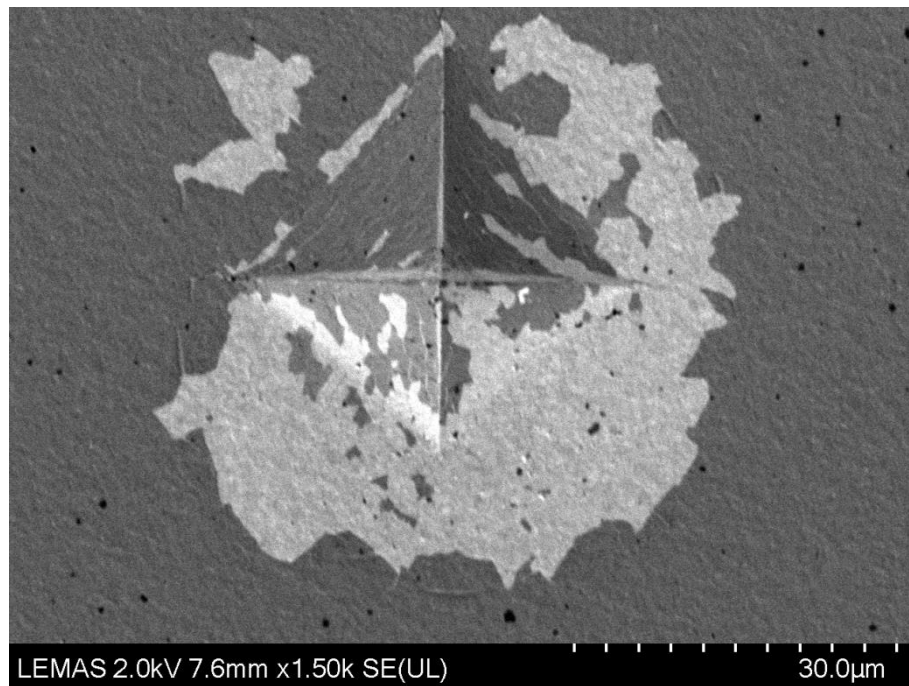


Figure 56. Change in contrast around Vickers indentation made on polished-aged sample. SEM image obtained using secondary electron (UL) detector revealed change in the contrast of areas around the indentation imprint that were subjected to tensile/shear stresses during indentation process. Such changes may be highly indicative of $t \rightarrow m$ process.

3.2.5 Nanoindentation

Nanoindentation or synonymously called instrumented indentation is a widely used, convenient method to examine a material's mechanical properties. It is particularly useful to study small volumes, thin films, microscopic structures and different layers of any given material. This technique is exploited using highly sensitive machinery that can apply loads at very low magnitudes to an indenter and record the resultant penetration depth in high precision and accuracy. Operating the machine in depth sensing mode allows generating load-displacement hysteresis graphs which can be used to calculate hardness and Young's modulus values of a given material. Nanoindentation utilises a Berkovich diamond indenter. It is a triangular pyramid with 65.3° angle between the vertical axis and each of the faces (Yovanovich, 2006, Fischer-Cripps, 2011, Dey and Mukhopadhyay, 2014).

According to this method, hardness (H) is defined as the mean pressure under the indenter at the maximum penetration depth and is calculated according to Equation 21 proposed by Weiler (Weiler, 1989):

$$H = \frac{P_{max}}{26.43t^2} \quad (21)$$

Where;

P_{max} is the maximum load (N), and
 t is the penetration depth (nm) at the maximum load

Reduced modulus (E_r) is calculated by fitting a power function to a portion of the unloading curve (50-100% of maximum load). The calculated slope is applied in Equation (22) originally described by Oliver and Pharr to determine the reduced modulus (E_r) of the sample (Oliver and Pharr, 1992):

$$\frac{dP}{dh} = \beta \frac{2}{\sqrt{\pi}} \sqrt{AE_r} \quad (22)$$

Where;

dP/dh is the slope of the fitted function to the selected portion of the unloading curve,
 β is the empirical indenter shape factor, and
 A is the projected contact area of the indenter as a function of depth

Young's or elastic (E_s) modulus is calculated using Equation 23 (Oliver and Pharr, 1992):

$$\frac{1}{E_r} = \frac{(1 - \nu_s^2)}{E_s} + \frac{(1 - \nu_i^2)}{E_i} \quad (23)$$

Where;

ν_s is the Poisson's ratio for the sample= 0.25,
 ν_i is the Poisson's ratio for the indenter= 0.07, and
 E_i is the Young's modulus of the indenter= 1141 GPa

Nanoindentation is considered as a superior technique to evaluate mechanical properties. In contrary to microhardness tests, nanoindentation can measure Young's modulus values of the material and allows studying small volumes and layers of the material thanks to the depth sensing mechanism. Additionally, the use of this technique negates the need for post-mortem examination of imprints generated by indenter which eliminates a multitude of errors as will be discussed in Section 3.4 (Doerner and Nix, 1986, Pharr and Oliver, 1992).

Nanoindentation is an optimum technique to characterise **LTD** within layers of a wide range of thicknesses of zirconia based ceramics. This is particularly relevant given the difficulty of interpreting data from the commonly used crystallographic techniques as far as the penetration depth and volume of interaction are concerned. In addition, nanoindentation studies provide direct evidence on the extent of **LTD** and allow examination of its effects on mechanical parameters in a spatially-resolved basis (Doerner and Nix, 1986, Pharr and Oliver, 1992, Rho *et al.*, 1997).

In the last decade, several research papers reported hardness and Young's modulus of zirconia based ceramics using nanoindentation techniques. Guicciardi *et al* (2007) reported hardness values ranging from 15-17 GPa and Young's moduli ranging from 220-270 GPa for a partially stabilised **Y-TZP** material with three different grain sizes. They also concluded that the smaller was the grain, the higher were the hardness values and Young's moduli (Guicciardi *et al.*, 2007). On the other hand, Lian *et al* (2007) concluded that coarse- and fine-grained fully yttria stabilised zirconia exhibited similar reduced modulus and hardness, 228 GPa and 19.8 GPa vs. 217.8 GPa and 18.9 GPa, respectively (Lian *et al.*, 2007).

A steady decline in hardness and Young's modulus was noticed in *Y-TZP* as a function of hydrothermal ageing time (Gaillard *et al.*, 2008, Cattani-Lorente *et al.*, 2011). Using a thin-film method, the latter authors determined Young's modulus and hardness of the degraded layer as 185 GPa and 11-13 GPa, respectively (Gaillard *et al.*, 2008). Catledge *et al* (2003) studied the effect of *in vivo* ageing on the hardness of explanted femoral heads. Initial hardness was determined as 17.8 GPa that declined to 12.2 and 10.6 GPa after 60 and 62 months of implantation, respectively (Catledge *et al.*, 2003).

In this project, a Nanoindentation Platform (Micro Material Ltd, Wrexham, UK) was used to perform nanoindentation testing on as-received and aged discs (12 per group). Before testing; the machine was calibrated for load and depth using standardised masses and reference material (fused silica), respectively. Discs were attached to an aluminium custom-made fixture by a thin layer of cyanoacrylate adhesive (RS, UK).

A Berkovich indenter was used to apply a load equal to 40, 100, 150 or 200 mN at a loading rate of 2 mN/sec. The load was held for a period of 5 sec to minimise elastic recovery prior to unloading at the same rate. Each disc received an indentation test in five, 300 μm distant areas. Hardness and reduced modulus values were calculated from the unloading load-displacement hysteresis curves utilising NanoTest Platform III software (Micro Material Ltd, Wrexham, UK). Post-indentation data was used for thermal drift correction at a dwell period of 60 sec.

Typical indentation load-displacement hysteresis curves obtained for as-received and aged samples at 40, 100, 150 and 200 mN loads are presented in Figure 57. Load-displacement hysteresis curves exhibited good continuity and no pop-in or pop-out were noticed. Maximum penetration depth of the indenter was slightly higher for the aged samples when 40 and 150 mN loads were applied. The curves were almost overlapping when 100 and 200 mN loads were applied.

Means and standard deviations of plastic penetration depths were calculated for aged and as-received samples under 40, 100, 150 and 200 mN loads. One-way ANOVA revealed no statistically significant difference in the plastic penetration depths under similar loads among as-received and aged samples ($p > 0.05$). Data of mean plastic penetration depths is presented in Table 11 and Figure 58.

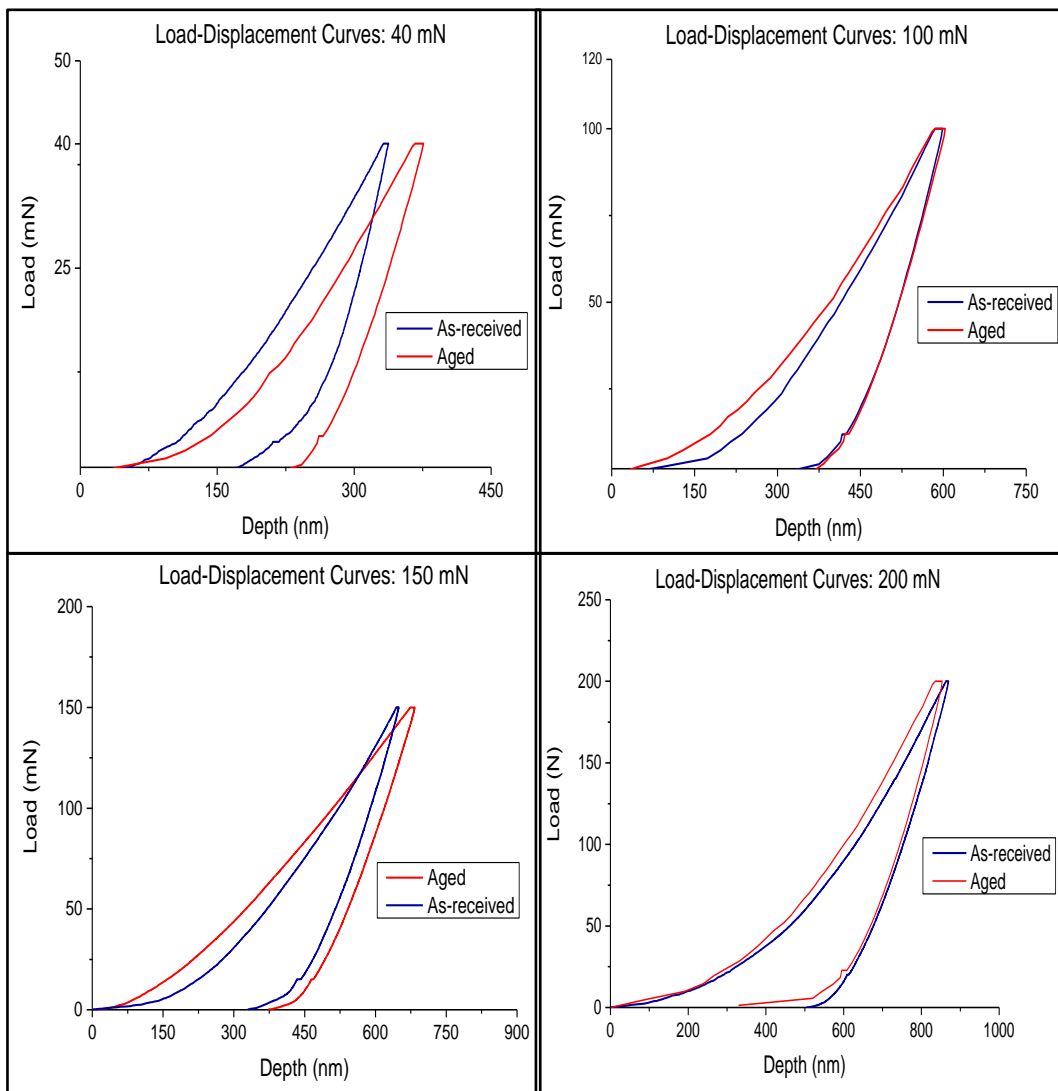


Figure 57. Representative load-displacement (depth) hysteresis curves.

Load-depth hysteresis curve depicts the change in displacement as a result of changing the applied load to the nano-indenter. Each curve is composed of loading (the part closer to y-axis) and unloading (the rear part of the curve) cycles. The two parts are intervened by a plateau where the load is held constant to prevent creep or elastic recovery. Increasing the load clearly increased displacement or investigation depth. The curves for as-received (blue) and aged (red) samples overlapped upon using loads equal to 100 and 200 mN. The use of 40 and 150 mN resulted in slight shift of the curve for some of the aged samples (top left and bottom right). However, mean penetration depth was not statistically different from the as-received group ($p > 0.05$).

Table 11. Summary of mean displacement or plastic depths. (SD)

Load (mN)	Penetration depth (nm)	
	As-received	Aged
40	312.51 (45.85)	316.45 (36.6)
100	501.09 (58.89)	491.07 (57.17)
150	604.98 (77.25)	609.25 (63.26)
200	744.08 (57.03)	727.09 (50.31)

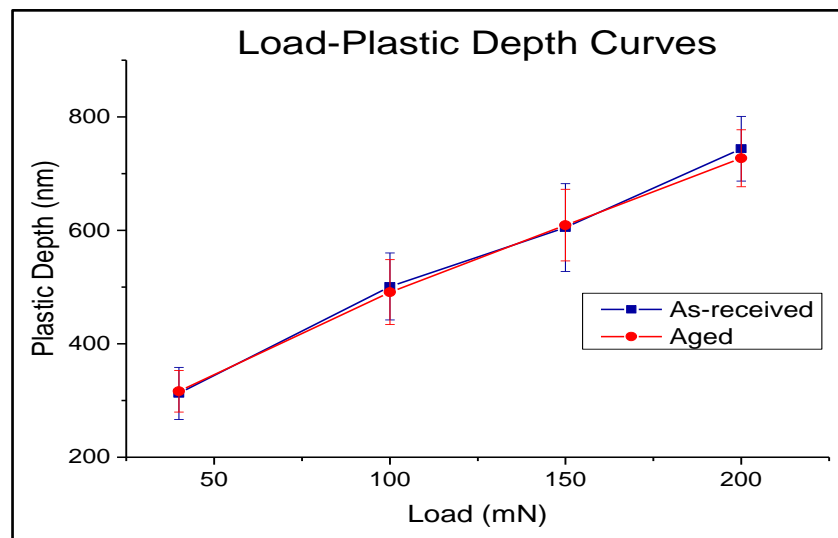


Figure 58. Comparative graph demonstrating the load-displacement relationship for as-received and aged groups.

ANOVA test and post hoc analysis (Fisher's least significant difference, LSD) revealed no statistically significant differences between as-received and aged samples' hardness values and Young's moduli when measured at similar loads and thereby depths ($p > 0.05$). Different layers within the as-received and aged samples exhibited no significant difference in Young's moduli. However, hardness values at depth of 650 nm (tested by 150 mN load) were significantly higher in comparison to other tested layers in the as-received group.

The superficial layer of aged samples (at depth \approx 350 nm, tested by 40 mN load) exhibited marginally significant lower hardness values when compared to values obtained from bulk of sample (depths \approx 500, 650 and 800 nm, tested by 100, 150 and 200 mN loads, respectively) ($p=0.048$). Such findings did not hold true as far as

Young's moduli were concerned. Interestingly, the layer of the material, in aged and as-received groups, intervening between the surface and the bulk of the material (depth \approx 600 nm, load 150 mN) exhibited significantly higher hardness and Young's modulus values in comparison to all other layers. Detailed findings of the nanoindentation tests are presented in Table 12 and Figure 59.

Table 12. Summary of hardness (H) and Young's modulus (E_s) values obtained using nanoindentation

Load	H (GPa)		E_s (GPa)	
	As-received	Aged	As-received	Aged
40 mN	13.65 (3.79)	12.91 (3.13)	306.03 (69.9)	289.54 (91.38)
100 mN	14.09 (2.99)	14.21 (2.93)	302.68 (61.52)	291.69 (57.33)
150 mN	15.211 (3.58)	14.80 (2.95)	304.11 (71.1)	309.77 (82.72)
200 mN	13.69(3.22)	14.16 (3.54)	297.02 (67.02)	302.33 (88.68)

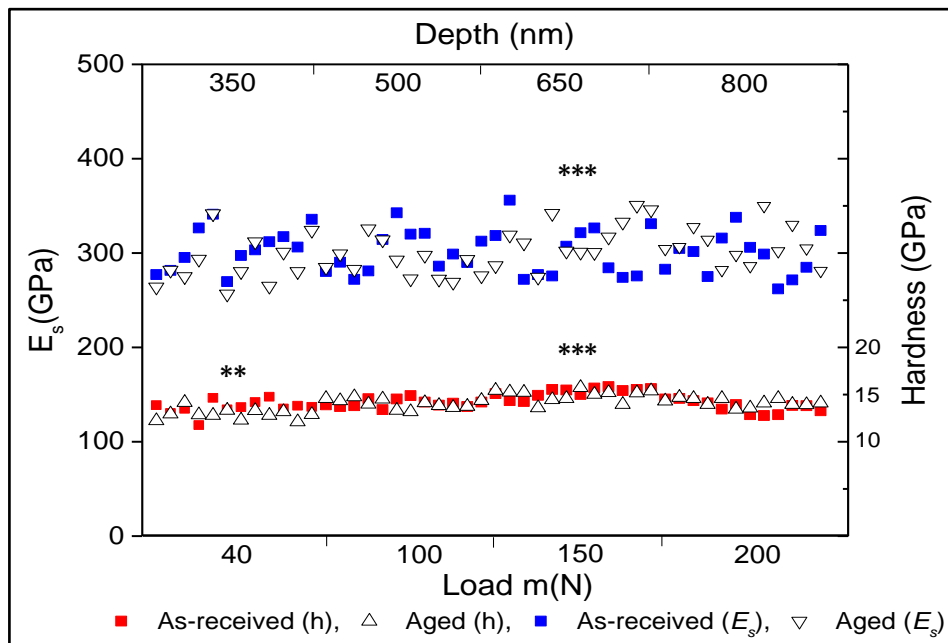


Figure 59. Comparative plot of hardness and Young's moduli.

Each data point represents a mean value obtained from 5 indentation cycles. ** indicate the marginal decrease of hardness of the most superficial layer of the material as a result of hydrothermal ageing ($p=0.048$). *** indicate significantly higher hardness and Young's modulus values of the 600 nm deep layer of the material ($p<0.05$).

3.3 Experimental procedures and results: implant samples

3.3.1 Accelerated *in vitro* ageing

Injection moulded, acid-etched, ethylene oxide sterilised, 5 mm diameter zirconia dental implants (The White Implant Development Corp. The Netherlands) were hydrothermally aged in a 1.2 L high pressure hydrothermal reactor (Series 4540 Parr, U.S.A) with 300 ml of distilled water. The ageing cycle lasted for 5 hours at operating temperature and pressure equal to 134 °C and 2 bar, respectively. Samples were left in the hydrothermal reactor upon completing the cycle until 50 °C temperature was reached. The cooling rate was estimated to be 0.011°C/sec. Samples were dried using air and stored in desiccator until further testing.

3.3.2 Dynamic fatigue

Dental ceramic prostheses are repeatedly challenged by mechanical, chemical and physical stimuli in the oral environment. In one decade, and under physiological conditions, a dental prosthesis can be subjected to more than 2 million chewing cycles, at loads that may exceed 200 N exerted by opposing enamel, dentine or restorative materials (Phillips, 1973, Craig and Ward, 1997, Kelly, 1997, Anusavice, 2014). The exposure to aqueous solutions such as water, which is a major constituent of saliva, is regarded as one of the most important chemical challenges to dental ceramics (Wiederhorn, 1967, Studart *et al.*, 2007b, Kosmać *et al.*, 2008). The rapid fluctuation of the temperature of the oral cavity and the subsequent, repeated episodes of expansion-shrinkage of dental tissues and restorative materials comprise a significant physical challenge to dental prostheses and luting cements (Ritter *et al.*, 1985, Morena *et al.*, 1986, Kern and Wegner, 1998, Blatz *et al.*, 2004, Von Steyern *et al.*, 2006)

Fatigue failure describes the phenomenon of strength degradation as a result of gradual, progressive growth of pre-existing cracks or nucleation of new ones. This process is initiated and exacerbated by cyclic loading, corrosive-stress and temperature changes. These factors collectively; (1) encourage the growth of pre-existing cracks and flaws initially introduced during processing or clinical adjustment, (2) favour development of *de novo* cracks at the area of mechanical loading and (3) result in constant build-up of plastic strain. When any of these flaws ultimately attain the size of a critical crack, failure takes place (Ritter, 1978, Dauskardt and Ritchie, 1991,

Chevalier *et al.*, 1999b, Munz and Fett, 1999). Kinetics of crack growth as part of the fatigue process exhibits a power-law (crack growth exponent, n) dependence on the opening mode stress intensity factor (Morena *et al.*, 1986).

The effect of fatigue phenomena on a material's strength and reliability can be investigated using the dynamic fatigue test (constant stressing method). In this test, samples are subjected to fluctuating stress in the form of a specific number of loading/unloading cycles at a predetermined load and frequency. In the majority of cases, loading is exerted using a blunt spherical indenter made of hardened steel. In order to account for other factors affecting fatigue failure, testing can be made in water or saliva and at different temperatures (Lawn and Wilshaw, 1975, Jung *et al.*, 2000).

In vitro fatigue tests can be conducted either using S-N curve or step-stress methods. The fatigue life of a given material denotes the number of loading/unloading cycles that precedes fatigue failure. Fatigue limit (σ_a) represents the amplitude of cyclic stress that a given material can endure without causing fatigue failure (Ritchie and Dauskardt, 1991, Wachtman *et al.*, 2009). The fatigue life (f_l) of a given material undergoing subcritical crack growth as part of on-going fatigue process can be given by Equation (24) (Pletka and Wiederhorn, 1982):

$$f_l = B\sigma^{n-2}\sigma_a^{-n} \quad (24)$$

Where;

f_l is the fatigue life,

B is the constant dependent on n , crack geometry and the fracture toughness, and

σ is the initial strength.

The fatigue behaviour of zirconia based ceramics has been widely investigated. Several studies reported on the fatigue behaviour of magnesia and ceria stabilised zirconia ceramics. Fatigue behaviour in such materials is however significantly different from **Y-TZP** based ceramics. These materials possess high toughness and modest strength as a result of the extensive plasticity enabled by the stress-induced $t \rightarrow m$ (Liu and Chen, 1991, Liu and Chen, 1994). Stress-induced $t \rightarrow m$ in such materials results in significant, localised shear bands that intersect with grain boundaries. On the other hand, **Y-TZP** exhibits high strength and modest toughness and rather brittle behaviour. The difference in the manifestations of stress-induced $t \rightarrow m$ may account for the differences in failure modes among different types of

zirconia ceramics. For example, **Y-TZP** materials are most likely to sustain catastrophic failure as a result of growth and propagation of a pre-existing flaw as indicated by steep load-extension curves obtained from flexural strength tests. In contrary, MgO stabilised zirconia exhibit large plastic deformation under relatively low loads which allows for *de novo* crack formation and premature failures (Swain, 1985). Using dynamic fatigue test, fractography and fracture statistics, Liu and Chen (1991) confirmed that **Y-TZP** fatigue failure occurs as a result of growth of pre-existing cracks rather than development and nucleation of stress-induced cracks during the dynamic fatigue test (Liu and Chen, 1991).

Several studies demonstrated the essential role of water in crack propagation. It has been proposed that water may mediate the stress-corrosion process and/or exacerbate stress-induced or spontaneous tetragonal zirconia phase destabilisation (stress-induced $t \rightarrow m$ and **LTD**) (Knechtel *et al.*, 1993, Chevalier *et al.*, 1995, Yin *et al.*, 1995). Chevalier *et al.* (1999) studied the fatigue behaviour of a **Y-TZP** material and confirmed that stress corrosion by water molecules can be the key mechanism for slow crack growth in zirconia based ceramics. The authors concluded that both stress-corrosion and cyclic loading are functional and increase the crack growth rates during dynamic fatigue testing. They attributed such finding to diminished transformation toughening and/or crack bridging of the irreversibly transformed tetragonal phase (Chevalier *et al.*, 1999b).

The role of corrosive stress on post-fatigue strength reliability has been investigated. Cyclic loading in water for short period of time, up to 2000 cycles, and at loads up to 800 N did not seem to affect strength reliability of the **Y-TZP** according to one study (Curtis *et al.*, 2006). However, other studies demonstrated 10-20% reduction in strength-survival of **Y-TZP** ceramics when long-term dynamic fatigue tests (Up to one million cycles) were performed in aqueous solutions such as water and artificial saliva (Morena *et al.*, 1986, Kosmać *et al.*, 2008).

The role of the final surface state and hydrothermally-induced **LTD** or ageing in fatigue behaviour of biomedical grade **Y-TZP** based ceramics has been investigated. It was demonstrated that damage induced by sharp indentation and sandblasting drastically affected long-term performance of **Y-TZP** when tested using dynamic fatigue testing (Zhang *et al.*, 2004a, Zhang *et al.*, 2004b, Zhang and Lawn, 2005).

However, Kosmać *et al* (2008) reported different findings concerning the effect of grinding, sandblasting and sandblasting followed by high temperature annealing. In their study, dynamic fatigue was performed for one million cycles with an upper load limit of 850 N. The authors reported survival rate 64% and 50% of the as-sintered **Y-TZP** samples when tested in air and artificial saliva, respectively. After grinding, the survival rate was reduced to 20% and 10% when the test was performed in air and artificial saliva, respectively. Survival rate of sandblasted samples was 100% under both testing conditions. Sandblasting followed by high temperature annealing resulted in a 90% and 60% survival rates when the test was performed in air and artificial saliva, respectively. Sandblasted samples exhibited the highest biaxial flexural strength after dynamic fatigue test while the ground samples have had the lowest. Furthermore, autoclaving for 2 and 24 hours in artificial saliva at 134 °C affected the survival rates and post-fatigue fracture strength. The authors reported survival rate 60% and 50% of the as-sintered **Y-TZP** samples when aged for 2 and 24 hours, respectively. Ground samples have had a survival rate of 10% and 0% when the ageing was performed for 2 and 24 hours, respectively. Survival rate of sandblasted samples was 80% under both ageing periods. Survival rate of the samples that received sandblasting followed by high temperature annealing was the least affected where 90% and 60% of the samples survived the dynamic fatigue test when the ageing was performed for 2 and 24 hours, respectively. Sandblasted samples exhibited the highest biaxial flexural strength after dynamic fatigue test while the ground samples have had the lowest for samples aged for 2 and 24 hours (Kosmać *et al.*, 2008).

Accelerated and prolonged investigations on standardised **Y-TZP** samples demonstrated variable findings regarding fatigue behaviour of the material. Short-term studies reported that commercially available **Y-TZP** materials survived a dynamic fatigue test for half million cycles when using a load equal to 60-70% of the mean biaxial flexural strength (Pittayachawan *et al.*, 2007, Pittayachawan, 2008). Survival rate and post-fatigue fracture strength were however reduced by 10-15% upon loading for 1 million cycles according to Kosmeć *et al* (Kosmać *et al.*, 2008).

While fatigue behaviour of **Y-TZP** material in non-standard geometries has been widely studied, studies reporting failure of monolithic or full contour **Y-TZP** single crowns, fixed partial dentures and transmucosal abutments remain scarce. The majority of such restorations survived dynamic fatigue and retained high fracture

strength after fatigue testing. Full contour crowns with average thickness of 0.5 mm, milled from commercially available pre-sintered zirconia blocks were investigated by Beuer *et al* (2012). All samples survived a total of 120,000 cycles of unidirectional antagonist loading with a frequency of 1.6 Hz and continuous thermocycling (5 °C and 55 °C). In addition, samples retained high fracture strength after cyclic loading that exceeded 10000 N (Beuer *et al.*, 2012). Furthermore, it has been reported that **Y-TZP** bridges may survive severe dynamic fatigue tests in wet conditions under loads typically applied in the molar region. In spite of their susceptibility to subcritical crack growth, the life-time of such bridges was estimated to be in excess of 20 years with the use of proper connector design and dimensions (Stuart *et al.*, 2007).

The fracture resistance and fatigue behaviour of prefabricated and custom-made **Y-TZP** abutments have been investigated by a number of *in vitro* studies. In their chewing simulation study, Butz *et al.* (2005) compared fracture strength of titanium reinforced zirconia, alumina and titanium abutments. Zirconia abutments showed fracture resistance similar to titanium controls and significantly higher than the alumina group. No screw loosening or detectable cracks could be found in the zirconia group after chewing simulation (Butz *et al.*, 2005). These findings were confirmed by Gehrke *et al.* (2006) who concluded that zirconia abutments exceeded the established values for maximum incisal bite forces reported in the literature and maintained a tight fit inside titanium fixtures after five million chewing cycles (Gehrke *et al.*, 2006).

Clinical studies with relatively high sample size reported good short- to medium-term success rate of veneered zirconia single crowns. From all the followed up restorations, one sustained fracture of the zirconia substructure just one month after insertion indicating flawed processing (Cehreli *et al.*, 2009, Ortorp *et al.*, 2012). Framework fracture was more evident in fixed partial denture restorations. Up to five-year follow-up studies reported less than 10% of fixed partial dentures sustained framework fracture (Sailer *et al.*, 2007, Beuer *et al.*, 2009, Schmitter *et al.*, 2009). Long span restorations, inlay-retained design and non-**HIP** soft-milled frameworks were the most susceptible to fracture (Ohlmann *et al.*, 2008).

Zembic *et al.*(2009) published results of their randomised controlled trial in which 18 zirconia and 10 titanium abutments used to restore implants in canine and posterior regions. Results showed 100% survival rate when abutments were followed

up to a mean period of 3 years (Zembic *et al.*, 2009). Additionally, Nothdurft and Pospiech (2009) studied the performance of zirconia abutments for posterior single tooth replacement and found no mechanical or biological signs of failure associated with any reconstruction followed for six months (Nothdurft and Pospiech, 2010).

Fatigue behaviour of zirconia dental implants has been recently investigated. Utilising a step-stress dynamic fatigue approach, Silva *et al.* (2009) demonstrated an insignificant effect of cyclic loading (up to 150,000 cycles) on the fracture strength of a one-piece zirconia dental implant design. They also concluded that implant head preparation to receive a crown restoration using diamond burs fitted in a high-speed handpiece under copious amount of irrigation did not have any drastic effects on the implants' reliability and fatigue resistance (Silva *et al.*, 2009).

Andreiotelli and Kohal (2009) investigated the fatigue resistance of two types of **HIP** one-piece zirconia implants (Sigma[®] implants, Incermed, Lausanne, Switzerland and BIO-HIP[®], Nobel Biocare AB). Sigma[®] implants exhibited poor performance as 50% failed during fatigue testing. However, they had mean fracture strengths of 1337 and 855 MPa before and after fatigue test, respectively. BIO-HIP[®] implants performed better as more than 90% of studied samples (unprepared, prepared, restored and unrestored) survived the fatigue test. However, it was noticed that preparation of the implant head to receive a crown restoration significantly compromised fracture strength (Andreiotelli and Kohal, 2009).

Kohal *et al* (2011) reported that 1 mm chamfer preparation and cyclic loading (1.2 and 5 million cycles) of **HIP**, one-piece zirconia implants (4 mm diameter; 12 mm length, White Sky[®], Germany) significantly decreased the fracture strength but not to an extent to preclude their use as they could still withstand maximum physiological loads after an extended interval of artificial loading (Kohal *et al.*, 2011).

Sanon *et al* (2013) investigated the effect of hydrothermal ageing on fatigue behaviour of one-piece zirconia dental implants with a porous coating. Using a step-stress approach, the authors calculated Weibull moduli and post-fatigue characteristic strengths for non-aged and hydrothermally-aged (20 hours) implants. Weibull moduli were 0.80 and 0.16 for the aged and non-aged groups respectively; indicating that failure of such implants was not time-dependent and may be attributed to random,

atrocious, processing flaws. The characteristic strength values were 1235 N and 826 N for aged and non-aged implants, respectively (Sanon *et al.*, 2013).

Kohal *et al.* (2006) reported 100% survival rate for one-piece zirconia dental implants restored with high density alumina all-ceramic crowns after being exposed to 1.2 million cycles at load of 50 N and constant thermocycling throughout the test. Additionally, the post-fatigue fracture strength values were not significantly different from unfatigued counterparts and similar to fracture strength values of fatigued titanium implants that were restored with porcelain fused to metal (*PFM*) crowns (Kohal *et al.*, 2006).

A prototype two-piece design comprised of zirconia implant and abutment joined by resin cement and restored with all ceramic crowns was subjected to dynamic fatigue testing for 1.2 million cycles at load equals 45 N with constant thermocycling throughout the test. All samples survived the fatigue test. However, the system exhibited low initial and post-fatigue fracture strength values. More importantly, all failures were confined to the implant head (Kohal *et al.*, 2009a). A Swiss dental implant manufacturer (Swiss dental solutions AG, Switzerland) claims in their marketing material that a 3.8 mm diameter zirconia implant, zirconia abutment and associated interface withstand dynamic fatigue testing according for two million cycles at 240 N without fracture. The associated interface or in other words the joining method can be mechanical (utilising gold, titanium or *PEEK* screws) or adhesive (luting cements) or both. The implant is machined from *Y-TZP* blocks and annealed at high temperatures.

3.3.2.1 Sample preparation

Sixty, 5 mm diameter zirconia implants (White Implant System[®], White Implant Development Corp. The Netherlands) were divided into 2 groups; as-received and aged. The latter group received hydrothermal treatment as in the Section 3.2.1. Each group was further equally subdivided into two groups which received different crown materials. Abutments were prototyped to tightly fit within the internal connection of the implant utilising a digital file of the implant design. Abutments were designed with 10° taper, 5.5 mm length and 4 mm diameter as shown in Figure 60. Detailed 2D drawing of the abutment design is presented in Appendix E. Digital (.STL) file was exported in a PDF viewable version and included in the CD submitted with this thesis.

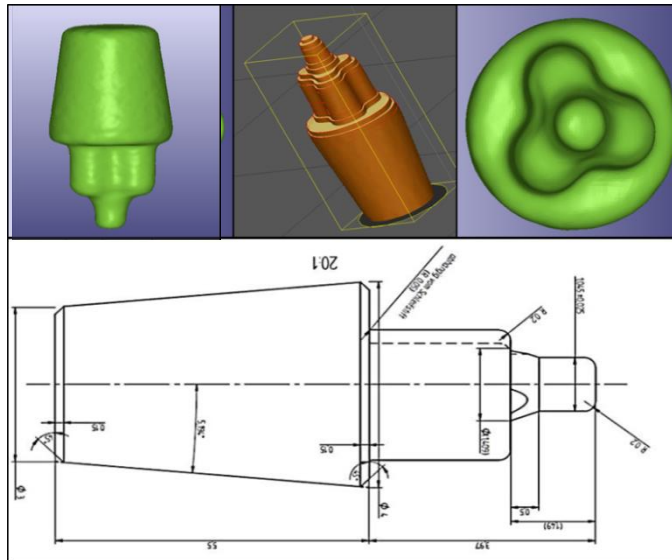


Figure 60. Standardised glass fibre composite (Triflor®) abutment design.

Bottom, 2D drawing of the prototyped abutment. 45° bevels were placed in all line angles to prevent chipping. Top, snapshots from the digital file used to mill the abutments. The 10° taper, the part of the abutment that tightly fits inside the zirconia implant as well as the robust ant-rotation feature can be seen.

Abutments were milled from Triflor® glass fibre raw material (E. Hahnenkratt GmbH, Germany). All abutments were abraded using air-borne Al₂O₃ particles (125 µm, John Winter Dental, UK) for 5 sec at 0.28 MPa pressure from 2 cm distance using pencil microblaster (Renfert GmbH, Germany). Abutments were immersed in 60% acetone and cleaned in ultrasonic cleaner for 3 min.

Following the cleaning process, abutments were washed thoroughly with distilled water and dried using a 3 in 1 syringe. The inner surface of implants and the connecting (submerged) part of *GFC* abutments were primed using methacryloxydecyl phosphate (*MDP*) containing ceramic primer (Clearfil™ Ceramic Primer, Kuraray Dental, Japan). Two layers were used and thinned by air blowing from a 3 in 1 syringe. Components were left to dry at room temperature for at least 2 min.

Abutments were cemented inside implants using a self-adhesive; self-etch; fluoride-releasing, dual-cure resin cement according to manufacturer's instructions (Panavia SA, Kuraray Dental, Japan). Cement was injected inside the implant cavity using a fine tip attached to an automix tube. Primed abutments were placed slowly with slight vibrating movement to prevent air being trapped within the cement layer. While maintaining constant finger pressure on the abutment, excess cement was cured

using halogen light (Demetron® LC™, Kerr, UK) for 5 sec until a slightly thick consistency was achieved. This allows for one-piece excess cement removal. Then, cement was light-cured again for 20 sec and left for 5 min to allow for maximum chemical curing to take place. The coronal 0.5-1.0 mm of the implant head was prepared to 0.5 mm deep chamfer finish line using fine grit, multi-layer gold diamond burs (45 µm, Diatech, Coltene, Switzerland) fitted in a high-speed handpiece (400,000 rpm, Synea®, W&H Dental WerksBürmoos GmbH, Germany) with continuous water cooling. Depth of preparation was continuously checked with the use of periodontal probe and a silicone index made on a non-prepared implant-abutment assemblies.

All samples were sent to an external dental laboratory for construction of all ceramic crowns. The prepared samples were digitally scanned using a blue LED light scanner (Scan ST, Steinbichler, UK). Exocad® DentalCAD software (Exocad GmbH, Germany) was used to design a crown restoration with similar dimensions and morphology to a permanent maxillary central incisor tooth. The cingulum area was overcontoured to provide a flat area for loading. The cingulum area was positioned 4 mm below the incisal edge in the palatal aspect of the restoration. The external surface form of the designed crown was copied to all other restorations. The area of the finish line was customised individually for each crown (Figure 61).

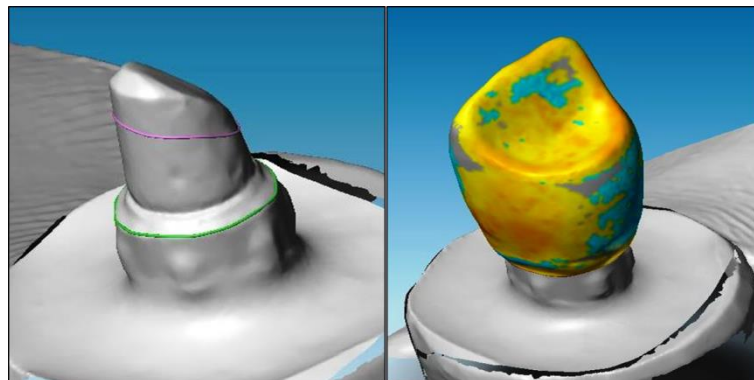


Figure 61. **CAD** of implant supported all ceramic crowns.

Left, a snapshot from the digital file containing the scan for the prepared implant head and cemented abutment. The finish line was identified for each sample to ensure accurate marginal fit. Right, the external surface morphology of the designed crown. Cingulum area was overcontoured to incorporate flat area for loading. This design was used as a bioform that was copied to all other crown restorations.

Thirty implants, 15 as-received and 15 aged, called group 1 and group 3 respectively, were restored using low translucency pressable lithium disilicate glass-ceramic crowns (IPS e.max Press, IvoclarVivadent, UK). Crowns were processed and glazed following the manufacturer instructions using the recommended press furnace (EP5000, IvoclarVivadent, UK). Fitting surfaces of all crowns were etched with 5% hydrofluoric acid (IPS etching gel, IvoclarVivadent, UK) for 20 sec, washed with distilled water and air-dried using 3 in 1 syringe. Internal surfaces of the crowns and restorable part of the implant-abutment assemblies were all primed using ceramic primer (Clearfil™ Ceramic Primer, Kuraray Dental, Japan) as before. Crowns were bonded to implant-abutment assemblies using dual-cure resin cement (Panavia SA, Kuraray Dental, Japan) as described before.

Thirty implants, 15 as-received and 15 aged, called group 2 and group 4 respectively, were restored using monolithic, full contour zirconia crowns (Lava™Plus System, 3M ESPE, UK). Crowns were milled from pre-sintered zirconia blanks, the size of which has been increased to compensate for the sintering shrinkage. Sintering of the milled crowns was performed according to manufacturer’s instructions in a special high-temperature furnace (Lava™Therm, 3M ESPE, UK). Crowns were subsequently polished using standard diamond-loaded rubber polisher set for ceramic materials (Vident™, USA). A high-shine polishing step was performed using a diamond polishing paste and various polishing brushes (Ultradent®, UK). Internal surfaces of the crowns and restorable part of the implant-abutment assemblies were all primed using ceramic primer as before. Crowns were bonded to implant-abutment assemblies using dual-cure resin cement (Panavia SA, Kuraray Dental, Japan) as described before. Flowchart presented in Figure 62 summarises different experimental groups.

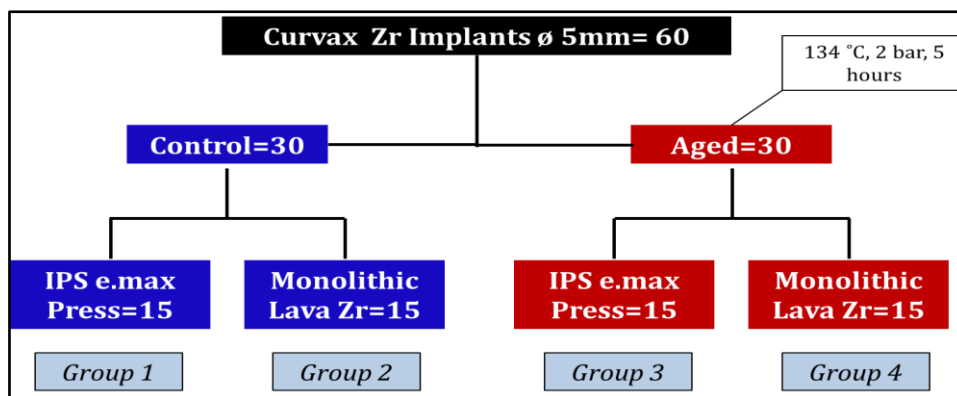


Figure 62. Outline of the study and different experimental groups.

The internal shape of the sample fixture of the dynamic fatigue testing machine (Instron, UK) was recorded using light-bodied silicone impression material (Extrude®, Kerr, UK). The impression was invested with type IV dental stone and replaced with autopolymerising acrylic resin. Negative replicas of the resulting acrylic block were created using silicone duplicating material (Metrosil Plus®, Metrodent, UK). The resulting moulds were used to cast autopolymerizing acrylic resin blocks (Technovit® 4000, HeraeusKulzer, Wehrheim, Germany) that precisely fitted in the sample fixture of the dynamic fatigue machine (Figure 63). Additionally, during the setting process of these blocks, implant-abutment-crown assemblies were embedded centrally and vertically to the level of the first thread of the implant (Figure 64).

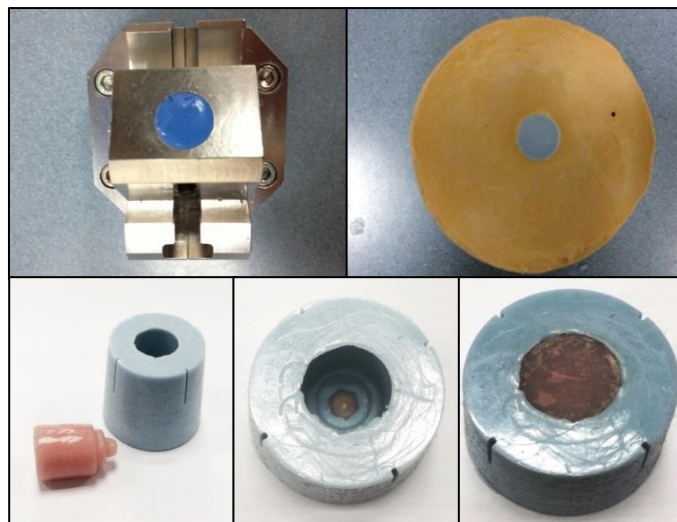


Figure 63. Reproduction of internal surface of the bottom fixture (sample holder) used in dynamic fatigue test.

Stages for creating a mould to be used for mounting implant in resin block that tightly fits to the fixture used to stabilise the sample during dynamic fatigue test. From top left to bottom left, silicon impression of the sample housing, investing with dental stone and subsequent replacement with acrylic., the negative replica of the acrylic pattern using duplicating material, the inside and outside appearance of the final mould used for resin block construction and implant mounting.



Figure 64. . Implant-abutment-crown assembly embedded in resin block

3.3.2.2 Dynamic fatigue test protocol

Dynamic fatigue test was performed in accordance with ISO 14801 for dynamic fatigue testing of dental implants with minor deviations (ISO 14801, 2007). Prepared samples were mounted securely (frictional fit and screw-retained) in the sample holder at 30°. When vertically loaded, the angle between long axis of the sample and the loading apparatus was approximately 120° as shown in Figure 65. This angle falls in the range (110-145°) of inter-incisal angle values in subjects with various types of occlusions (Meneghini and Biondi, 2012).

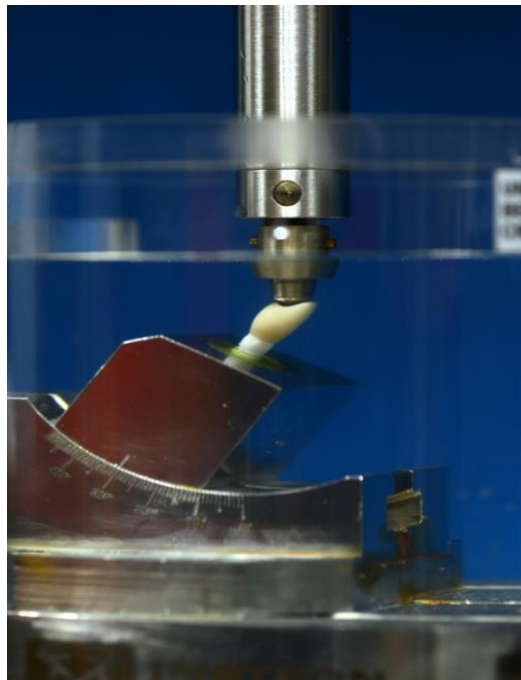


Figure 65. Sample mounted and loaded during dynamic fatigue test.

The effective load range exerted onto the implant–abutment–crown assemblies was 20-200 N. The load was applied using a custom-made loading apparatus with 4 mm diameter hardened steel ball to load the designed flat area incorporated in the palatal surface of the crown. A load cell with maximum capacity of 250 N was used (Dynacell, Instron, UK). Figure 66 demonstrate effective load range delivered to a sample throughout a completed test. A dynamic fatigue testing machine (ElectroPuls E3000, Instron, UK) was used to apply 2.4 million chewing cycles at a frequency of 15 Hz on all samples. The number of cycles was chosen to simulate 10 years of clinical functional loading (DeLong and Douglas, 1983, Krejci and Lutz, 1989). The test was performed whilst all samples were immersed in 37°C distilled water. The water temperature was controlled using a thermal water circulator (Gallenkamp, Germany). WaveMatrix™ Dynamic Test Software (Instron, UK) was used to control the dynamic

fatigue test in reference to digital position of the upper fixture (Figure 67). The test was programmed to stop in the event of displacement of upper loading fixture exceeds 250 μm or load trips the 230 N limit. This allowed detection of fractures, cracks and component debonding. Samples were visually inspected under strong illumination to identify the presence of cracks or hairline fractures in the crown or implant head.

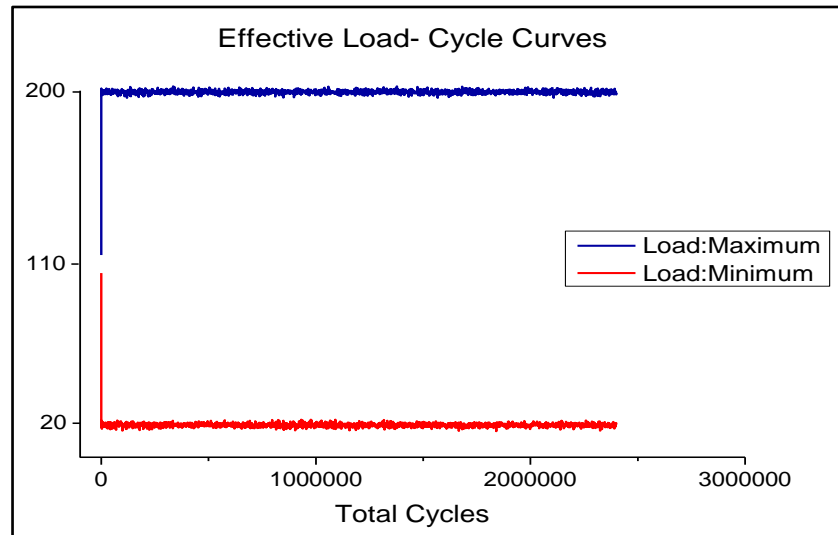


Figure 66. Effective load-cycle curves.

Graph obtained from WaveMatrix™ Dynamic Test Software depicting the effective load delivered to the sample at each cycle during the entire fatigue test.

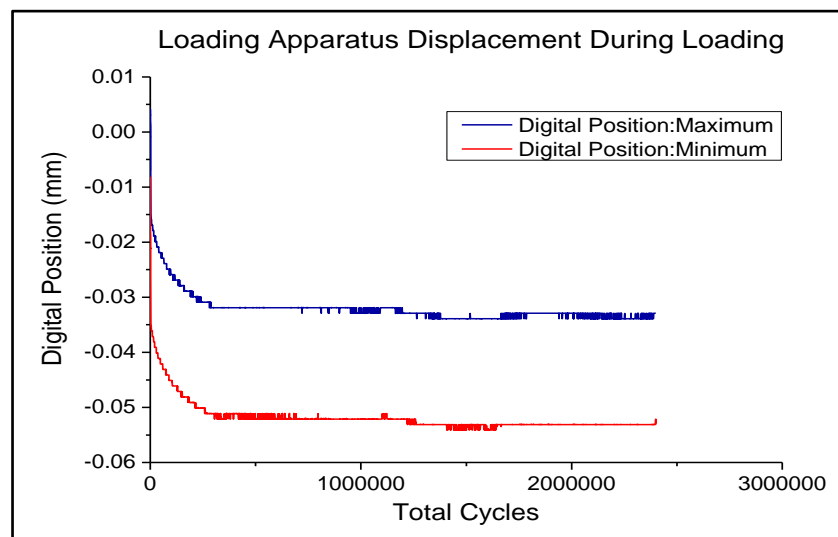


Figure 67. Displacement of upper loading fixture at each loading cycle during the entire dynamic fatigue test.

Displacement of the upper loading fixture is detected by digital position sensors. The maximum amount of displacement in this completed representative dynamic fatigue test did not exceed 55 μm . The test was programmed to stop if the displacement exceeds 250 μm which could be as a result of component cracking, fracture or debonding.

Out of 60 samples, three only failed the dynamic fatigue test (1 sample from each of group 1, group 2 and group 3). All failures occurred after 1.8 million cycles as a result of abutment debonding. None of the failures involved implant head or crown restorations (Figure 68). Such failures caused the machine to stop as the amount of subsequent upper loading fixture displacement was well above 250 μm . A shift in the curve depicting digital position throughout the test was clearly identifiable at the time of failure (Figure 69). Signs of contact abrasion could be seen in both crown materials at the area of loading. No cracks radiating from the loaded areas were however noticed.



Figure 68. Outcome of dynamic fatigue test.

Left, a representative sample debonded after 1.9 M loading cycles. No damage could be detected at the level of implant head or abutment upon examination under strong transillumination and $\times 6$ magnification. Right, loaded area of a crown in a sample from group 1 that survived the dynamic fatigue test. Contact abrasion can be seen in the loaded area but no cracks could be detected in the transilluminated crown.

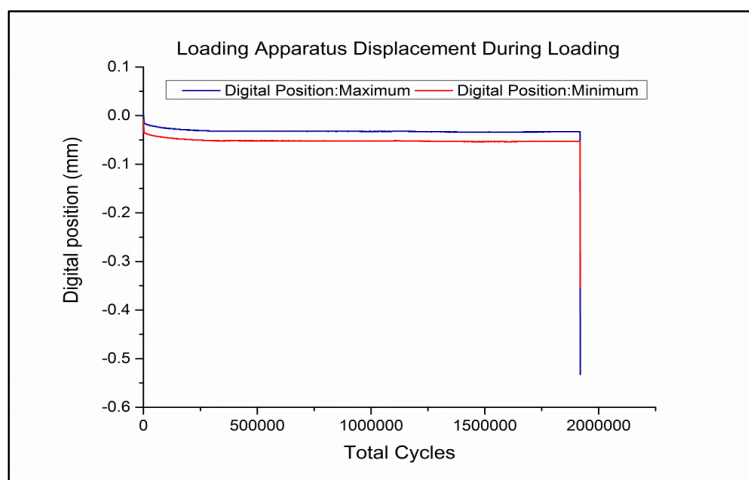


Figure 69. Loading apparatus displacement during fatigue test of a sample that was debonded during loading.

The test was stopped due to tripping the maximum limit of digital position (displacement) of the loading apparatus. The sample was not completely debonded but the movement at the implant abutment interface exceeded 250 μm .

3.3.2.3 Post-fatigue fracture strength

Samples that survived the dynamic fatigue test were loaded to failure to determine post-fatigue fracture strength. The same setup used in the dynamic fatigue test was altered to allow using the machine in static mode. The load cell was changed to 50 kN and the crosshead speed was 0.5mm/min. Testing was performed in distilled water at 37°C. Load-extension curves were generated by WaveMatrix™ Dynamic Test Software (Instron, UK) and used to determine failure loads. Statistical analysis and data plotting were performed as described in Section 3.2.2.

Five failure modes were observed upon loading the 57 samples to failure. Implant head fracture (**H**), fracture at the level of first implant thread (**T**), crown rupture (**R**), abutment-crown bending followed by cervical chipping of the crown (**C**) and a combination of **H** and **R** (**HR**).

H failure mode was characterised with spall formation from the labial side of the implant head. The fracture originated from a crack propagated in the thinnest area confined between the zeniths of the petal shaped internal connection and the inner end of the prepared finish line. In failure mode **T**, the transverse fracture involved the full-thickness of the implant at the level of first thread. The fracture surface was level with the mounting resin. In **R** failure mode, crown fracture involved the labial incisal parts along the sagittal plane of labial aspect of the crown. The fracture originated from cracks developed at the mesio- and disto-labial line angles. The fracture spared the abutment and prepared implant head. In failure mode **C**, failure started as the load caused forward bending of the abutment-crown in the labial direction with subsequent opening of the palatal margin. At higher loads, small ceramic chipping occurred at the cervico-labial aspect of the crown. The chip was delineated by mesial and distal cracks and the finish line on the implant head cervically. A video showing **C** and **H** failures in representative samples from group 1 and 2 is included in the CD submitted with this thesis.

The failure mode **HR** occurred in one sample where the crown rupture did not involve the loading area and the system was able to maintain compressive loading. Then, at a slightly higher load, implant head fractured as described in failure mode **H**. Samples failed following this sequence of events were considered as **H** failure as the interest was in the final outcome of the test as well as to facilitate data analysis

process. Figure 70 demonstrates representative samples sustained each of the aforementioned failure modes.

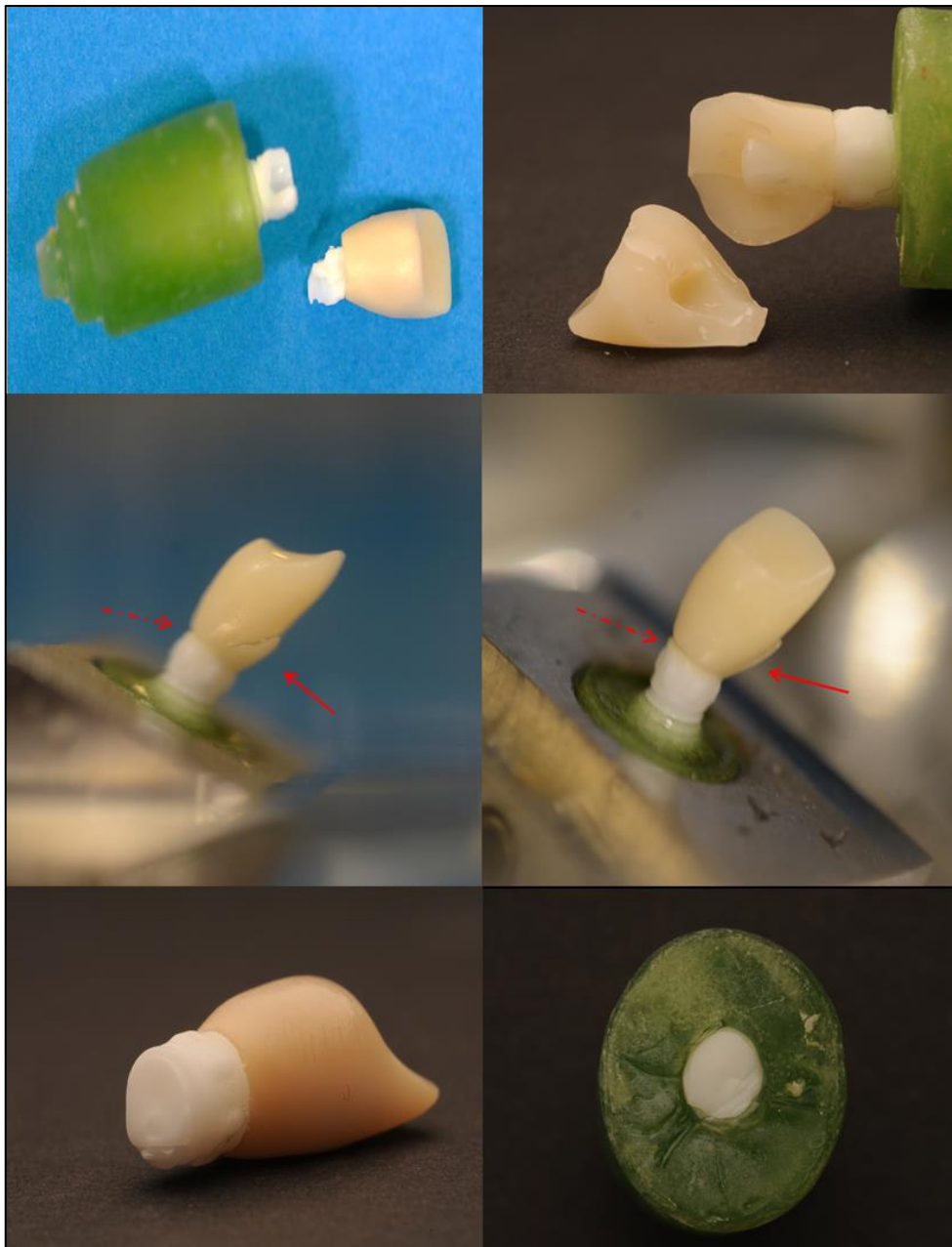


Figure 70. Various failure modes in representative samples during post-fatigue fracture strength test.

Top left, the most common failure mode (**H**) in group 2 & 4. Top right, failure mode (**R**) where the crown ruptured along the frontal plane as a result of cracks originated in the mesial and distal surfaces. Middle, sample failure mode was (**C**). The opened margin between crown and implant indicate bending of the abutment under loading followed by chipping of cervical part of the crown. Bottom, one of the 2 samples that sustained transverse implant fracture at the level of mounting resin or first thread (**T**).

Analysis of failure modes revealed the following findings:

- In group 1, 14 samples were loaded to failure. The failure modes-loads distribution was as the following; 7 samples exhibited **R** as the sole failure mode with mean failure load of 698.61 ± 68.91 N, 4 samples exhibited **C** as the main failure mode with mean failure load of 476.51 ± 46.69 N and 3 samples sustained **H** failure mode with mean fracture load 614.82 ± 51.07 N.
- In group 2, 14 samples were loaded to failure. One sample exhibited **T** failure mode at a load equal to 1070.2 N. Thirteen samples sustained failures from **H** category with mean fracture load of 534.45 ± 138.19 N.
- In group 3, 14 samples were loaded to failure. The failure modes-loads distribution was as the following; 11 samples exhibited **C** as the main failure mode with mean failure load of 345.22 ± 78.31 N and 3 samples sustained **H** failure mode with mean fracture load 490.99 ± 104.16 N.
- In group 4, 15 samples were loaded to failure. One sample exhibited **T** failure mode at load equals to 863.44 N. Fourteen samples sustained failures from **H** category with mean fracture load of 568.65 ± 122.15 N. Table 13 and Figure 71 summarise the results of post-fatigue fracture strength test for all experimental groups.

Table 13. Summary of post-fatigue failure modes and their respective mean loads (N \pm SD) in all experimental groups.

Failure mode	Group 1	Group 2	Group 3	Group 4
Debonding	>2.1 M cycle (1)	>1.8 M cycle (1)	>2.1 M cycle (1)	0
R	698.6 ± 68.91 (7)	0	0	0
C	476.5 ± 46.7 (4)	0	345.2 ± 78.3 (11)	0
H	614.8 ± 51.1 (3)	534.5 ± 138.2 (13)	491.0 ± 104.2 (3)	568.7 ± 122.2 (14)
T	0	1070.2 (1)	0	863.4 (1)

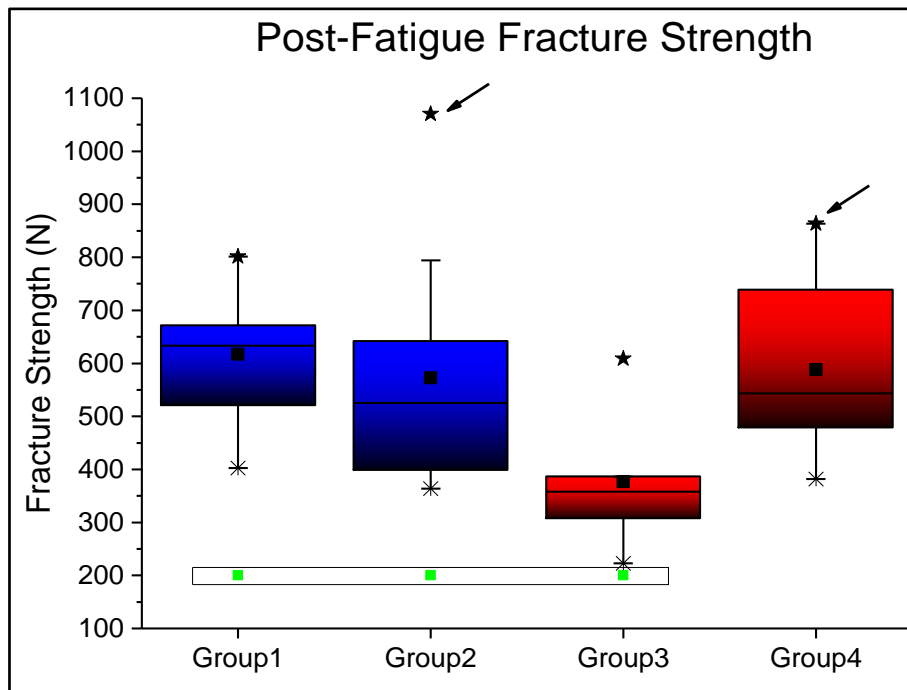


Figure 71. Comparative graph for post-fatigue fracture strength data.

Boxplots represent data from post-fatigue fracture strength tests. Samples debonded during dynamic fatigue test are represented as (■). Outlier values are represented as (★) and when annotated with (→) represent implants that suffered (T) failure mode. Line and square within each boxplot represent mean and median of the dataset, respectively.

The results indicated that the type of crown material largely influenced the failure mode. The use of lithium-disilicate glass ceramic restorations as in group 1 and 3 (IPS e.max Press, Ivoclar Vivadent, UK) to restore implant-abutment assemblies, unsurprisingly resulted in failures sparing the implants in the majority of cases. Crown rupture (R) and crown chipping (C) with abutment deformation were the most dominant failure modes in these groups. As expected, crown rupture occurred at higher loads when compared to crown chipping and abutment deformation (Figure 72). This can explain the higher mean post-fatigue fracture strength of group 1 when compared to group 3 as the former had seven R failures in comparison to none in the latter group.

Weibull parameters were calculated in order to determine differences in the probability of failure among various individual experimental groups. Group 1 exhibited the highest Weibull modulus (β) and characteristic strength (α). Group 2 had the lowest β while group 3 exhibited the lowest α value. The difference between the groups was however not statistically significant as indicated by the overlap in the

95% CI obtained for β and α for all groups. Table 14 summarises Weibull parameters obtained for all experimental groups

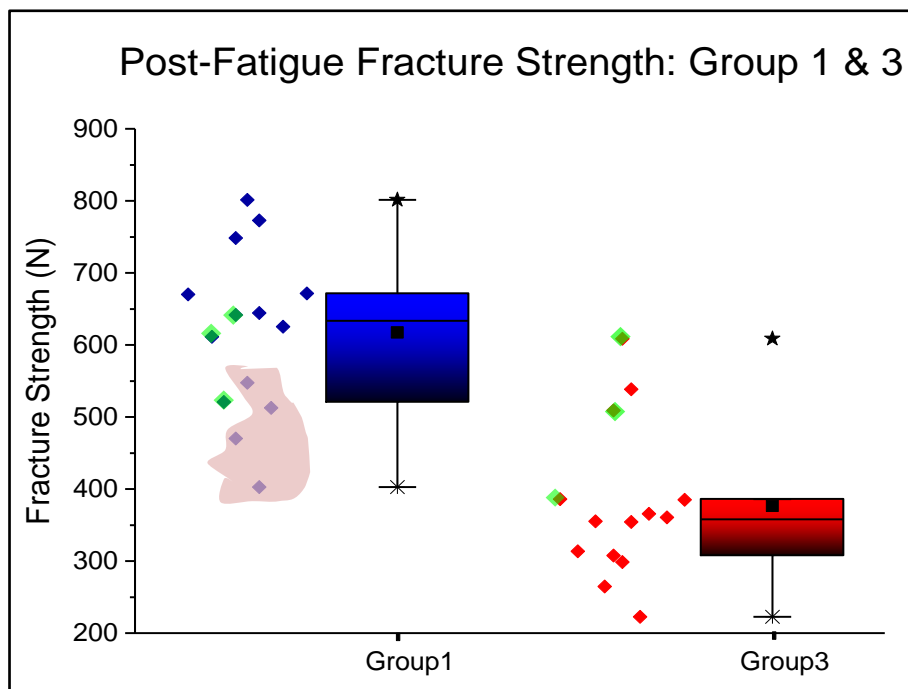


Figure 72. Comparative graph of post-fatigue fracture strength for samples restored with IPS e.max Press crowns.

Boxplots represent data from post-fatigue fracture strength tests. Outlier values are represented as (*). Line and square within each boxplot represent mean and median of the dataset, respectively. Data points are presented beside each boxplot. Data points masked with green represent samples sustained *H* failure mode in group 1 and 3. The 4 points highlighted with faint red represent those samples sustained *C* failure in group 1. The remaining blue points represent samples sustained *R* failure mode. The remaining red points represent samples had *C* failure mode in group 3.

Table 14. Summary of Weibull parameters for post-fatigue fracture strength data (N)

	<i>Mean Failure Strength (SD)</i>	β (95% CI)	α (95% CI)	R^2
Group 1	617.2 (111.9)	4.2- 6.3 -9.6	608.3- 663.7 -724.1	0.95
Group 2	572.7 (191.7)	2.1- 3.1 -4.5	534.1- 640.1 -767.2	0.97
Group 3	376.5 (103.5)	2.6- 3.8 -5.5	358.8- 416 -482.3	0.98
Group 4	588.3 (139)	2.9- 4.4 -6.6	570.1- 646.4 -732.8	0.94

The effect of ageing on the strength of zirconia implants could not be comprehensively verified in groups 1 and 3 as only 3 samples from each group sustained failures involving the implant head. Thus, the values obtained from samples that sustained *H* failure mode were pooled and divided in non-aged implant and aged implant groups. Weibull parameters were calculated and compared for these two groups.

A one-way ANOVA test revealed no significant difference between the mean fracture strength values for samples that had sustained implant head fracture in the pooled non-aged and aged groups ($p > 0.05$). In addition, Weibull moduli were 4.12 (**95% CI**: 2.74-6.21) and 5.02 (**95% CI**: 3.36-7.51) for non-aged and aged groups, respectively. Characteristic strength values of the studied samples were 588.36 N (**95% CI**: 511.55-676.71) for non-aged and 618.97 N (**95% CI**: 554.07-691.49) for aged groups. The overlapping **95% CI** indicated no significant difference between strength reliability of non-aged and aged implants.

Within the limitations of a relatively small sample size, hydrothermal ageing did not seem to have a significant drastic effect on the strength reliability of the studied implants. Figure 73 shows comparative Weibull plots for pooled, non-aged and aged groups.

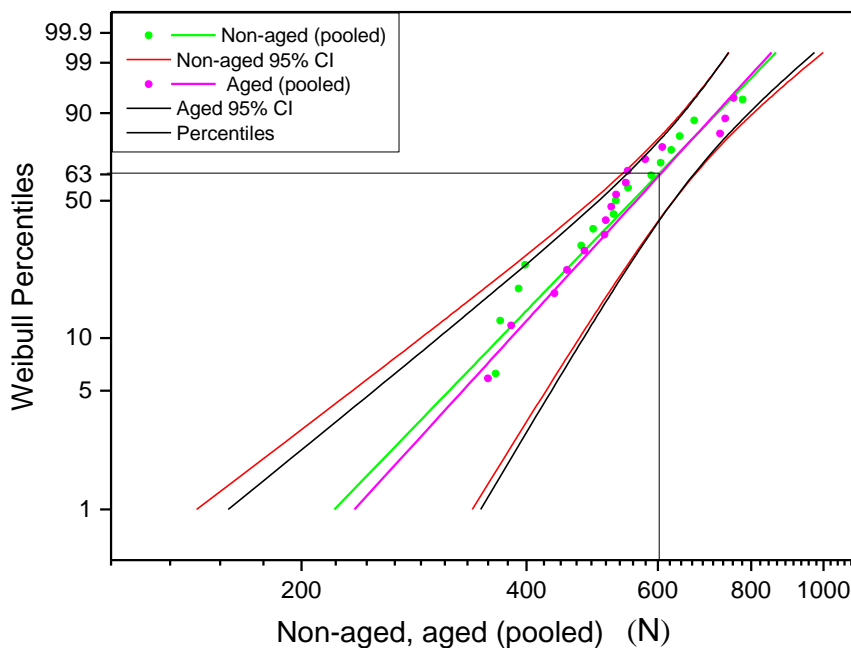


Figure 73. Comparative Weibull plot for pooled post-fatigue fracture strength. data for non-aged and aged implants sustained *H* failure mode.

The load-extension or R-curves were plotted for representative samples that sustained various failure modes in each experimental group. In group 1 and 3, **R** or **HR**, **H** and **C** were the failure modes encountered. During **HR** failure, the crown sustained brittle fracture or rupture as indicated by a sharp symmetric peak. Shortly afterwards, the implant head fractured after limited plastic deformation as indicated by the rounded peak in the R-curve. During **C** failure, abutment bending and margin opening occurred first followed by chipping of the cervical part of the crown. Plastic deformation continued over a wide range due to continuing abutment bending. During **H** failure mode, notable plastic deformation was observed in the R-curve. The failure started with subtle abutment bending followed by implant head fracture. Figure 74 demonstrates R-curves of failure modes of representative samples from group 1 and 3.

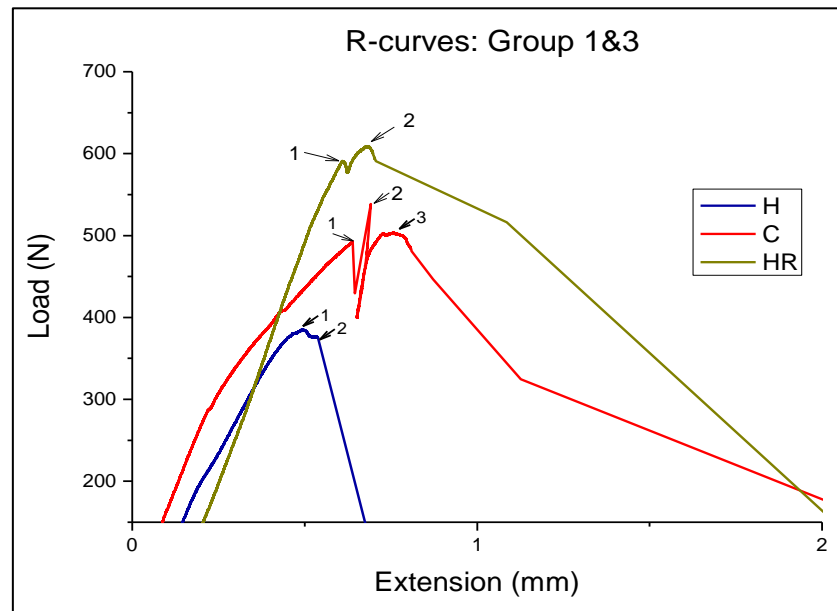


Figure 74. R-Curves for various failure modes in group 1 and 3.

In **HR** (—), crown fractured first (1) followed by implant head (2). In **C** (—) abutment bending started (1), followed by cervical crown chipping (2) and finally prolonged plastic deformation (3) due to continued abutment bending. In **H** (—) Implant head fractured (2) after short period of plastic deformation or abutment bending (1).

In group 2 and 4, **H** and **T** failure modes were encountered. During both modes; implant head (**H**) or body (**T**) fractured after a notable period of plastic deformation. Figure 75 demonstrates R-curves of failure modes of representative samples from group 2 and 4.

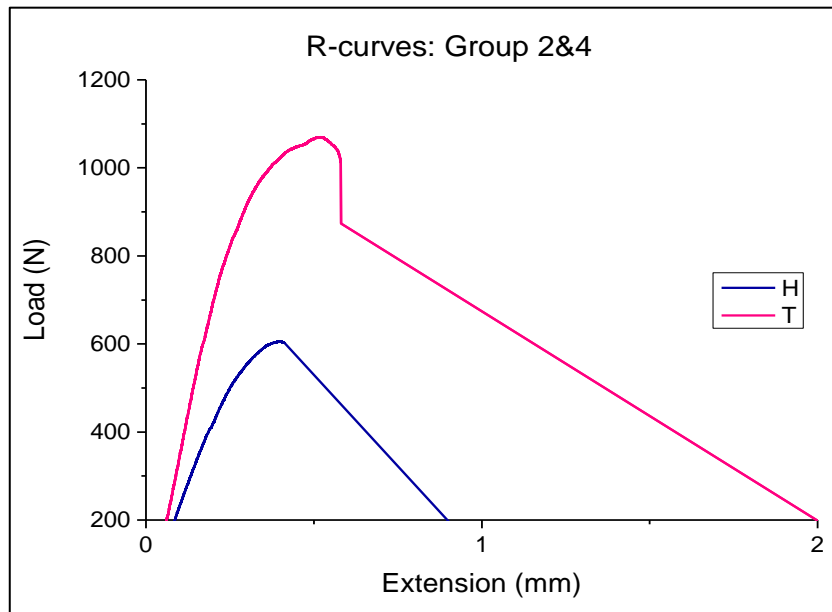


Figure 75. R-Curves for various failure modes in group 2 and 4.

3.4 Discussion

Results of static mechanical tests reported in this chapter are summarised in Table 15. In Section 3.2.2, analysis of variance has shown that there was no statistically significant difference between the mean biaxial flexural strength of the as-received and aged groups. Strength reliability was analysed using Weibull statistics. The assumption that all fracture strength data follows Weibull distribution has been recently and vigorously questioned. It has been shown that the fracture statistics may severely depart from Weibull distribution and such departures can be indiscernible in sample size less than 30 (Danzer *et al.*, 2007). Such problems may be more evident when Weibull parameters are estimated by least squares analytical procedure. However, the use of maximum likelihood method, as in this work, may ameliorate this problem. It was proposed, treated and verified to accurately help with estimation of Weibull parameters (Jayatilaka, 1979, Trustrum and Jayatilaka, 1979). The latter method exploits a series of iterations to solve complex data such as those following a non-linear distribution (Wachtman *et al.*, 2009).

Hydrothermal ageing did not seem to affect flaw distribution as indicated by the lack of significant difference between the Weibull moduli of both groups. In fact, the large values for the Weibull moduli for both groups indicated fewer critical flaws, narrow and homogenous distribution of flaw sizes and presence of flaws in areas subjected to less stress. This in turn enhances the quality of reliability of the material.

In addition, characteristic (Weibull) strength was similar among both groups which points toward that reliability of strength was not affected by the hydrothermal ageing. Piconi *et al* (1998) reported similar findings when they studied strength degradation of a **Y-TZP** material made of yttria coated powder as a result of different ageing condition at different time points. Their material had initial strength and Weibull modulus comparable to the one reported in this study (1035 MPa, 12 vs. 1003.7 MPa, 15.2). When hydrothermal ageing (140 °C, 2 bar) was performed for 6 hours, their material showed comparable behaviour and no strength degradation was noticed (1005 MPa, 17.5 vs. 1033.1 MPa, 10.8). In the same study, exposure of the same material to similar ageing conditions for 120 hours or storage in Ringer's solution at 37 °C for one year had no detrimental effects on strength and reliability (Piconi *et al.*, 1998).

Ardlin (2002), Papanagiotou *et al* (2006) and Borchers *et al* (2010), reported that various prolonged *in vitro* ageing treatments (hydrothermal and chemical) did not adversely affect the flexural strength and reliability of a commercially available **Y-TZP** ceramic. In addition, storage in saline and distilled water at various temperatures and for periods (up to 3 years) did not drastically affect bending strength of **Y-TZP** (Ardlin, 2002, Papanagiotou *et al.*, 2006, Borchers *et al.*, 2010). Maintenance or slight increase in the flexural strength after heat treatment (ageing) may be attributed to the plastic or non-linear deformation exhibited by the heat-treated samples (Swain, 1985).

Other studies however reported strength degradation of **Y-TZP** materials upon artificial and *in vivo* ageing. The majority of these studies performed extremely prolonged ageing which does not correlate to the target survival period of the material when used *in vivo* (Ban *et al.*, 2008, Flinn *et al.*, 2012). One of the studies used very thin **Y-TZP** (0.2 mm) bars which is applicable to crown and bridge dental restorations but not to dental implants which at least have 4 mm diameter (Flinn *et al.*, 2012). In addition, the authors of these studies only compared the mean **BFS** values of different groups using two-way ANOVA test which is reportedly considered inadequate (Wachtman *et al.*, 2009). This is attributed to the fact that flexural strength of ceramics is heavily dependent on the presence and distribution of major flaws as a result of processing or surface treatment. Thus, robust, failure probability based statistical analysis methods should be used for such comparison.

Table 15. Summary of results from static mechanical studies.

	<i>Biaxial Flexural strength (MPa)</i>		<i>Edge Fracture Strength (MPa)</i>		<i>Vicker's Microhardness (GPa)</i>	
	<i>As-received</i>	<i>Aged</i>	<i>As-received</i>	<i>Aged</i>	<i>As-received</i>	<i>Aged</i>
Mean (SD)	1003.7 (73.1)	1033.1 (102.1)	239.8(16.9)	248.1(12.1)	14.06(0.61)	13.81(0.44)
β (95% CI)	15.8 (12.5-20.5)	10.8 (8.7-14.2)	15.7 (11.9-20.2)	22.2 (17.5-29.2)	25.9 (21.1-31.9)	27.5 (21.6-34.9)
α (95% CI)	1036.9 (1012.3-1062.1)	1079.7 (1042.4-1118.5)	246.01 (241.9-253.4)	252.1 (249.7-257.7)	14.3 (14.1-14.5)	14.03 (13.8-14.2)
R2	0.99	0.98	0.97	0.98	0.91	0.97
t	-	-	-	-	5.14 (0.1)	5.18 (0.07)

	<i>Hardness (GPa)</i>		<i>Plastic Depth (nm)</i>		<i>Young's Modulus (GPa)</i>	
<i>Load (mN)</i>	<i>As-received</i>	<i>Aged</i>	<i>As-received</i>	<i>Aged</i>	<i>As-received</i>	<i>Aged</i>
40	13.7 (3.8)	12.9 (3.1)	312.5 (45.9)	316.5 (36.6)	306.0 (69.9)	289.5 (91.4)
100	14.1 (2.9)	14.2 (2.9)	501.1 (58.9)	491.1 (57.2)	302.7 (61.5)	291.7 (57.3)
150	15.2 (3.6)	14.8 (2.9)	604.9(77.2)	609.3 (63.3)	304.1 (71.1)	309.8 (82.7)
200	13.7 (3.2)	14.2 (3.5)	744.1(57.0)	727.1 (50.3)	297.0 (67)	302.3 (88.7)

Analysis of variance has shown that there was no statistically significant difference between the mean edge fracture strength values of the as-received and aged groups as shown in Section 3.2.3. Edge strength reliability was analysed using Weibull statistics. Hydrothermal ageing did not seem to affect flaw distribution as indicated by the lack of significant difference between the Weibull moduli of both groups. In fact, the large values for the Weibull moduli for both groups indicated fewer critical flaws, narrow and homogenous distribution of flaw sizes and presence of flaws in areas subjected to less stress. This in turn enhances the quality of reliability of the material. In addition, characteristic (Weibull) edge strength was similar among both groups which points toward that reliability of strength was not affected by the hydrothermal ageing.

The edge fracture strength (chipping load) was determined at a distance of 0.3 mm from the edge. The very widely used test setup at 0.5 mm distance from the edge was not used in this project because; firstly, pilot testing revealed that the load required to cause chipping was very high and caused displacement of the sample in many instances despite the robust locking device used to stabilise the samples. Secondly, on several occasions, the high loads applied to the indenter caused gross fracture of the samples rather than edge chipping.

The machine used for this test can be operated in load or acoustic sensing modes. In the latter case, the event of formation of an indentation or minor cracking at low loads will be sensed as a failure and cause the test to terminate. In addition, operating the machine in this mode can be difficult as a result of external noise that may interfere with optimum testing. Thus, the machine was operated in load sensing mode where the load cell detects abrupt drop in load as a result of chipping.

Generally, ceramic materials are more susceptible to catastrophic marginal fractures owing to their low edge fracture strength and brittleness. However, thanks to the dense crystalline structure and the transformation toughening mechanism, the studied *Y-TZP* material demonstrated very high edge fracture strength values which exceeded those reported for ductile materials such as resin composites (Watts *et al.*, 2008). The measured edge fracture loads at 0.3 mm distance from the edge in this study were slightly different from those reported in the literature. Gogotsi *et al* (2007) reported edge fracture loads for three different *Y-TZP* materials ranging between

180-220 N (Gogotsi *et al.*, 2007). In addition, Petit *et al* (2009) found that edge fracture load ranged between 150-320 N for two different types of **Y-TZP** (Petit *et al.*, 2009). The incongruence in the reported edge fracture strength may be attributed to several elements including; firstly, the aforementioned studies used a variety of sample preparation techniques such as polishing, machining, and machining followed by high temperature annealing. Secondly, investigators used indenters with different geometries which was reported to have an effect on and the chip size and thereby edge fracture strength values (Gogotsi *et al.*, 2007).

Several investigators utilised the same setup in order to measure the edge fracture strength as a function of distance from the edge and thereby the chip size. There is a consensus that the higher loads are required to produce a larger chip size. However, whether the relationship assumes linear mode or not has still not been exhaustively investigated for **Y-TZP** materials. One study reported significant departure from linear relationship in two different **Y-TZP** materials (Petit *et al.*, 2009). Investigating this aspect was not feasible in this project owing to limited access to the machine required for such testing.

Another testing setup has been used to measure the edge fracture strength of **Y-TZP**. Petit *et al* (2009) reported the use of sliding indentation test utilising a scratch tester at several displacement speeds (0.5-15 mm/min) and loads (20-80 N) (Petit *et al.*, 2009). This technique utilises minimal loading which results in smaller chip sizes. Smaller chips are less likely to be affected by surface flaws in the vicinity of the propagating cracks which in turn, significantly reduce the distortion of the chip geometry and the scattering of the edge fracture strength values. The consistency between the data derived from static and sliding edge fracture strength tests was reported as being high especially when adjustment for differences in friction coefficient values was performed (Petit *et al.*, 2009). Comparison of test results from static and sliding chipping tests at distance of 0.3 mm from the edge is not feasible. This is attributed to the fact that chipping at this distance is impossible to occur under such minimal loads used in the sliding chipping test.

The studied as-received material exhibited a high Vickers hardness number comparable to those reported in the literature for commercially available **Y-TZP** materials as shown in Section 3.2.4 (Luthardt *et al.*, 2002, Guazzato *et al.*, 2004,

Pittayachawan *et al.*, 2007, Pittayachawan, 2008). This can be attributed to highly dense microstructure, submicron crystal size, highly textured surface as a result of injection moulding processing as well as the unique toughening mechanisms possessed by *Y-TZP*. Monoclinic phase exhibits significantly lower hardness values in comparison to tetragonal counterpart (Ingel *et al.*, 1983, Din and Kaleem, 1998). Thus, it is expected that hydrothermal ageing will cause decline in Vickers hardness values of the material. This however was not the case, analysis of variance has shown that there was no statistically significant difference between the mean Vickers hardness values of the as-received and aged groups. This can be related to the minimum amount of monoclinic phase formed after hydrothermal treatment. Additionally, the part of the material was tested is very likely to be at a depth that was beyond *LTD* penetration. The calculated penetration depths of the indenter in both groups were in excess of 5 μm . At this level, *GIAXRD* revealed that the amount of transformation is negligible as mentioned in Section 2.6.1.

The above mentioned findings were in agreement with Swain *et al* (1985) who reported that hydrothermal ageing at 1100 °C for 2, 16 and 40 hours had no significant effect on Vickers hardness values of MgO-stabilised zirconia. However, the same authors reported significant increase of the diameter of area affected by plastic deformation around the imprints as a function of ageing (Swain, 1985). *SEM* investigation revealed that the area of plastic deformation could be significantly larger in the polished-aged samples in comparison to polished counterparts. The notable change in the material's contrast under *SEM* imaging using the electron backscattered detector is a strong indicator that the material with plastic deformation areas sustained significant *t*→*m*. Findings of Raman spectroscopy around Vickers indentations made on polished-ages samples (Section 2.6.2) also points toward such conclusions.. The phase transformation could be attributed to the shear stresses generated at the sides of the penetrating indenter..

Vickers hardness measurements are vulnerable to a multitude of significant errors. Some are related to the optical resolution of the integrated optical microscope and ability of the investigator to precisely determine imprint's diagonal lengths. The use of high loads to create bigger indents is advisable to overcome such problem. However, this may further complicate measurement making by causing crack or spall formation. Additionally, using higher loads may magnify the error introduced by

indentation size effect (*ISE*). The latter is one of the most commonly cited problems with microindentation testing of ceramic materials. *ISE* describes the phenomenon of declining hardness values upon using higher loads (Bull *et al.*, 1989, Farges and Degout, 1989). It is attributed to experimental errors and several structural characteristics of the material and may be clear upon using loads ranging between 1-10 Kgf (Gong *et al.*, 1999). Furthermore, ceramic materials are very likely to undergo elastic relaxation during or after unloading. This process leads to significant changes in the dimensions of the indenter's imprint and thus undermines the validity of hardness values (Tarkanian *et al.*, 1973).

A nanoindentation test was used to assess mechanical properties of different layers of the as-received and aged samples as shown in Section 3.2.5. The use of this technique allows overcoming the issue with elastic recovery as it involves measuring the hardness values automatically prior to unloading and negates the need for direct examination of the indenter's imprint. Additionally, it utilises the unloading curve to calculate reduced modulus and thereby the Young's modulus of the material which cannot be achieved by the conventional microindentation techniques. Furthermore, it allowed systematic investigation of the mechanical properties of the materials at much smaller depths in comparison to Vickers indentation. Investigating the effect of artificial *LTD* at shallower depths is of major importance in this study. This is indicated by *GIAXRD* study in Section 2.6.1 that demonstrated a localised $t \rightarrow m$ that was confined to approximately 1 μm . Vickers microhardness test may be irrelevant in this context as the penetration depth of the indenter was in excess of 5 μm .

Analysis of variance revealed a marginally significant decrease in hardness values for the aged samples when 40 mN load was used at penetration depth up to 300 nm in comparison to 200 mN (850 nm). The decrease in hardness can be ascribed to the increased monoclinic phase after hydrothermal ageing. *GIAXRD* confirmed that the maximum amount of monoclinic phase was located within this layer of the material (~25%). Remarkably, the change in hardness values was only marginal despite the substantial difference in hardness between tetragonal zirconia (12-16 GPa) and monoclinic zirconia (6-7 GPa) phases. None of the studies investigated the effect of ageing on hardness of *Y-TZP* reported hardness values less than 10 GPa regardless ageing time and conditions. Berkovich indenter's diameter is approximately 10 times smaller than the average diameter of a single crystal. Thus, there is a high probability

that several indentations were made in untransformed tetragonal crystals. Alternatively, the crystals in the vicinity of the indent may retain their toughening ability via either, $t \rightarrow m$ or ferroelastic domain switching and resist further brittle fracture and plastic deformation. Furthermore, the localised compressive stresses generated by $t \rightarrow m$ could maintain hardness values comparable to the tetragonal phase.

Our findings were in agreement with a previously published paper which reported approximately 10% reduction of hardness after 10 hours of hydrothermal ageing of a **HIP, Y-TZP** material with an average grain size of 700 nm. However, when using a material with average grain size of 200 nm, the same authors reported a steady hardness value upon using loads from 10-400 mN and ageing time up to 60 hours (Guicciardi *et al.*, 2007). In a different study, Cattani-Lorrente (2011) reported approximately 17% decrease in hardness of the superficial 300 nm layer of a **Y-TZP** material after 24 hours of hydrothermal ageing (Cattani-Lorente *et al.*, 2011).

Beyond the depth of 300 nm, i.e. using loads higher than 40 mN, aged samples recovered hardness values similar to the as-received counterparts. This may suggest that the hydrothermal ageing performed on the injection-moulded **Y-TZP** had an isolated effect on the hardness of the transformed layer without any gradient effect.

In contrast to findings from hardness measurements, hydrothermal ageing caused no reduction in Young's modulus of superficial layers. These findings were in agreement with those reported by Guicciardi *et al* (2007) who demonstrated minor decrease in hardness but not in Young's modulus for a **Y-TZP** material with average grain size of 700 nm upon hydrothermal ageing for 10 hours (Guicciardi *et al.*, 2007). Additionally, in all studies that reported a decline in hardness and Young's modulus as a function of hydrothermal ageing, the decrease in hardness was substantially more notable than for Young's modulus (Catledge *et al.*, 2003, Cattani-Lorente *et al.*, 2011).

Unlike for hardness, a decline in stiffness or Young's modulus of **Y-TZP** is not dependent on the presence of monoclinic phase. This is not surprising in the light of comparable Young's moduli for tetragonal and monoclinic phase of **Y-TZP** (Chan *et al.*, 1991b). In order to cause significant deterioration of stiffness, the hydrothermal ageing should be severe enough not only to induce partial $t \rightarrow m$, but also to manifest structural changes in the crystalline composition. Gillard *et al* (2008) explained this phenomenon in their **FIB-SEM** study. The authors reported that a

network of microcracks was noticed exclusively in aged samples under the indentation imprint. Subsequently, they proposed that the presence of microcracks, and thereby the deterioration of stiffness of the transformed layer, could be a result of one or combination of the following; (1) pre-existing microcracks generated by $t \rightarrow m$ accompanied volumetric expansion during hydrothermal ageing which can be further opened as the indentation is performed, (2) deformation by cracking rather than plastic deformation due to lacking of stress-induced $t \rightarrow m$ and switching of the ferroelastic domains in the irreversibly transformed layer (Gaillard *et al.*, 2008).

Hardness and Young's modulus of different layers within as-received and aged groups were compared using post-hoc analysis. In as-received samples, there were no significant differences between all layers except at 600 nm depth (150 mN load) where hardness and Young's modulus were significantly higher. In aged samples, the hardness values of at 300 nm depth (40 mN load) were marginally lower than other layers. Similar to as-received samples, at 600 nm depth (150 mN load), hardness and Young's modulus were significantly higher than other layers. This could possibly be related to one or more of the followings; firstly, residual stresses and/or crystalline texture as a result of injection moulding process might have formed an energy barrier that strengthens the material at this particular depth. Secondly, this observation may be an indication of *ISE* that starts at 150 mN load. To verify the latter, a series of higher indentation loads should be used and *ISE* will be confirmed if a progressive decrease in hardness values was noticed. The possibility that this might be caused by an experimental/systematic error is remote as measurements using all loads were done at the same time.

Hardness is measured by dividing maximum load by the contact area. Contact area in microindentation testing is defined as the surface area of the tip-faces that are in contact with the sample. In nanoindentation, contact area is the projected area of contact between the sample and tip of the indenter. Berkovich and Vickers indenters have the same projected contact area at similar penetration depth and both produce approximately 8% strain during indentation (Yovanovich, 2006). However, the two indenters differ in geometry, a Vickers indenter is a 4-sided pyramid while the Berkovich indenter is a 3-sided pyramid. Hence, the values for nanohardness can be directly converted to equivalent Vickers hardness by multiplying the former with the projected to face contact area ratio (0.927) given the use of Berkovich indenter with

perfect geometry (Rice and Stoller, 2000). Upon conversion of results from nanoindentation test at all loads, results were comparable to those obtained by Vickers microindentation test for both, as-received and aged groups. The best match however was between Vickers data and nanohardness measurements made at loads of 150 mN.

The average force generated during physiologic chewing cycle in the anterior region of subjects with long span bridges supported by periodontally compromised teeth was determined to be between 12-17 N (Lundgren and Laurell, 1986). Other studies reported bite forces below 50 N during physiologic chewing cycle (De Boever *et al.*, 1978). Chewing load in the posterior region was estimated to be approximately 130 N in dentate subjects (Proffit *et al.*, 1983). The majority of studies that have investigated long-term performance of ceramic restorations and implants in the anterior region used an effective load below 100 N (Libman and Nicholls, 1994, Kheradmandan *et al.*, 2001, Kohal *et al.*, 2006, Kohal *et al.*, 2008, Kohal *et al.*, 2009a, Kohal *et al.*, 2011). The duration of one chewing cycle under physiologic conditions has been estimated to be 0.6-1.1 sec. The frequency of chewing is thereby can be estimated between 0.9-1.7 Hz (Gillings *et al.*, 1973). DeLong *et al.* (1983) recommended a maximum loading frequency of 3-4 Hz for optimum simulation of clinical conditions during *in vitro* fatigue tests performed using their dynamic fatigue device. Kelly (1997) cited that average number of chewing cycles per day is approximately 1400 cycles (Kelly, 1997). It has been determined that 1.2 million loading cycles *in vitro* are equivalent to 5 years of *in vivo* function (DeLong and Douglas, 1983, Krejci and Lutz, 1989). ISO standards for dynamic fatigue testing of dental implants recommends a maximum loading frequency 15 Hz and 2 Hz under dry and wet conditions, respectively (ISO 14801, 2007). Despite detectable water-assisted crack growth, likelihood of failure was similar for samples tested in dry and wet conditions. However, it has been found that failures were more likely to occur under lower loading frequency (2 Vs. 30 Hz). The authors attributed this finding to the low strain rate sensitivity phenomenon where damage accumulation mechanisms are less likely to occur under higher stress rates (Lee *et al.*, 2009a).

The dynamic fatigue test in Section 3.3.2 was performed using a load range (20-200 N) that is significantly higher in comparison to the aforementioned studies. This was done in order to examine the performance of the implant design under extreme conditions and predict 'worst case' application. Furthermore, the number of

cycles used in this test was higher than all other studies that have investigated zirconia dental implants. It was chosen to examine the durability of the implant design for 10 years which is considered as a reasonable lifetime for a dental implant. In addition, tests were performed in water and under relatively high frequency. The high stress rate used may have affected –to unknown extent- the results as it reduced the time when the samples were in contact with water and decreased the likelihood of damage accumulation. Using lower stress rates was not feasible owing to the long time needed to test all samples and limited availability of the machine.

Several studies reported various maximum bite force values for natural and prosthetic teeth utilising various methodologies. It has been concluded that the mean maximum bite force between incisor teeth in dentate subjects can vary between 161-222N. These measurement were made under various experimental conditions utilising a strain gauge device (Hellsing, 1980). Maximum physiological biting force values varies with age and facial morphology and may be as high as 290 N in the incisor teeth region (Kiliaridis *et al.*, 1993). Lyons & Baxendale (1990) determined the maximum bite force range of 11-35 Kg in the canine region when studied 10 dentate subjects using an electromagnetic device. Half of the subjects exhibited signs of advanced tooth wear as a result of bruxism (Lyons and Baxendale, 1990). Körber& Ludwig (1983) reviewed several bite force studies and estimated an average maximum biting force of approximately 200 N (Körber and Ludwig, 1983). A reliable implant-abutment-crown assembly is expected to retain fracture strength higher than the maximum bite force in the anterior region. Assuming that the average maximum bite force in the anterior region is 200 N, Schwickerath (1986) proposed that un-fatigued reconstructions are expected to exhibit fracture strength of 400 N. Such assemblies should retain greater than 200 N post-fatigue fracture strength assuming strength deterioration by 50% as a result of dynamic fatigue process (Schwickerath, 1986, Schwarz *et al.*, 1988).

In this study, the dynamic fatigue test was performed to mimic the clinical environment as much as possible. Implant-abutment-crown assemblies were prepared exactly as for clinical application. The used mounting resin has a modulus of elasticity of approximately 12 GPa, which approximates that of human bone in order to represent clinical conditions in terms of bone remodelling and stress distribution (Kohal *et al.*, 2010). The angle between the vertical upper loading fixture and the long

axis of the implant was in accordance of ISO requirements and resembled the interincisal angle between natural anterior teeth. The test was performed in distilled water at 37 °C to account for the water-assisted crack growth.

The survival of all implants (100%) and debonding of 3 abutments (5%) can be regarded as an optimum performance given the extreme conditions the test was performed in. The use of ceramic primer (Clearfil™ Ceramic Primer, Kuraray Dental, Japan) with the resin cement (Panavia SA, Kuraray Dental, Japan) possibly had significant effect on durability of adhesive bond between various components (Keul *et al.*, 2013). These findings confirm the protective role of using a low-strength *GFC* abutment under cyclic loading. This effect was, to a large extent, maintained upon statically loading implants to failure point after fatigue test whenever relatively low strength crown restorations were used (IPS e.max Press, Ivoclar Vivadent, UK). In group 1 and 3, only 6 samples sustained implant head fracture (20%). However, the use of high strength crown restorations (Monolithic Lava™Plus System, 3M ESPE, UK) negated the protective effect as all samples sustained implant head or body fracture when statically loaded to failure.

The post-fatigue fracture strength values were comparable to those reported for titanium implants restored with *PFM* crown restorations (Kohal *et al.*, 2006). Failures involving implant heads occurred at mean loads exceeding 490 N which is well above the most commonly accepted value of maximum bite force in the anterior region. Failures that involved fracture through the middle of the crowns with a palatal and labial fracture segment (*R*) in IPS e.max groups occurred at significantly higher loads than those reported for samples that sustained a similar failure mode but were tested for half of the cycle number and load (Kohal *et al.*, 2006). The variability of failure modes in supposedly identical samples in group 1 and 3 may be attributed to differences in the dimensions of the prepared finish line in the implant heads. Despite meticulous care taken to ensure consistency of amount of preparation using silicone index and measurements with periodontal probe, it is very likely that preparation was heavier in some samples especially in groups 1 & 3. The discrete implant head fractures in these groups are very likely to be as a result of excessive thinning of the implant head at the zenith of the tri-petal internal connection. This theory is further consolidated as the fracture origin was always located in this area. Mechanical preparation with diamond burs may have caused a reduction in strength. However,

failures occurred at loads higher than those expected to be in the oral environment. These findings were in agreement with previously published data for one- and two-piece zirconia implant systems (Kohal *et al.*, 2006, Kohal *et al.*, 2011, Kohal *et al.*, 2012).

The difference in failure mode and values among group 1 and 3 can be attributed to the difference in thickness of crown material in the area of finish line. Despite identical external surface forms, the thickness of the crown at this area is depicted by the preparation and thereby may vary accordingly. Lower failure loads in group 3 are unsurprising as the amount of force required to rupture the crown along the sagittal plane is higher than chipping a smaller piece of ceramic in the area of maximum tension during bending test. Another explanation could be a difference in the angle between the loading upper fixture and the long axis of the implant despite careful mounting of the samples.

A case can be made against this design on the basis that the crown material is the sole protector against catastrophic failure involving the implant head rather than the engineered weak link introduced in the system. A counter argument can be made as even in the samples restored with high strength crowns (monolithic zirconia), R-curves indicated notable plastic deformation in the system before failure. The R-curve for a sample from group 2 was compared to a counterpart obtained from a one-piece zirconia implant. The latter sample demonstrated a rather brittle failure where the load spiked and abruptly decreased to zero. In contrary, implants restored with a *GFC* abutment and monolithic zirconia crown still exhibited a notable plastic deformation (along a range of ≈ 0.5 mm) prior to implant head fracture (Figure 76).

These findings are of major significance as in the clinical situation, changes in the implant supported crown exceeding 0.25 mm can be easily identified by the patient and the dentist. The plastic deformation may cause changes in the patient's bite and thereby, make the patient seek help regarding pain or discomfort as a result of a 'high spot' for instance. Additionally, plastic deformation can be expressed in the form of an open margin at the implant-crown interface. A defective margin as small as 0.2 mm can be detected and rectified under the magnification provided by dental operative microscope.

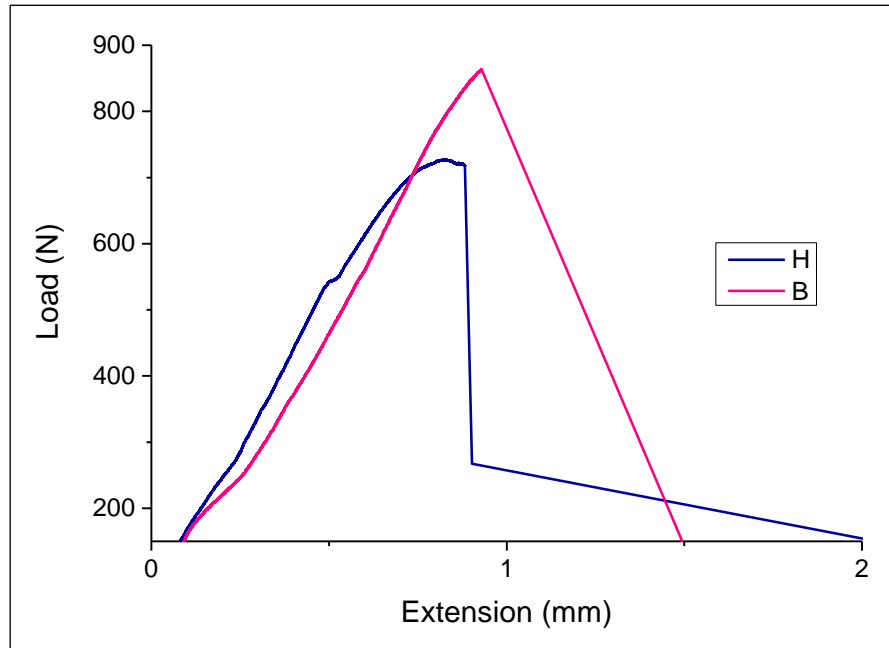


Figure 76. R-curves for zirconia implants restored with GFC abutment (H) and Lava crown compared to one-piece zirconia implant (B).

The effect of hydrothermal ageing on the fracture strength of the implant could not be determined in group 1 & 3 as 20% of failures involved the implant head. In group 2 & 4, there was no significant difference between fracture strength and strength reliability of the aged and as-received implants. This could be attributed to (1) the limited and surface-confined amount of $t \rightarrow m$, (2) the highly dense and packed structure and (3) reduced surface flaws as no mechanical grinding was involved with the manufacturing process. The same findings were reported by Sanon *et al* (2013) who performed a longer hydrothermal ageing on one-piece implants and found no difference in strength reliability between aged and non-aged groups (Sanon *et al.*, 2013).

Chapter 4: **Surface Characterisation and Biological Assessment**

4.1 Introduction

Natural teeth are comprised of highly differentiated and complex hard and soft tissues. Odontogenesis, tooth formation, occurs in tooth germs in the alveolar bone where an intricate cascade of biological events takes place. Morphogenesis, epithelial histogenesis, cell differentiation and matrix mineralisation are among the cornerstone processes in odontogenesis that involve highly orchestrated cell-cell and cell-matrix interactions. The process is normally culminated by the formation of immature tooth that erupts through mucosal tissues and undergoes post-eruptive maturation (Nanci, 2008, Lesot and Brook, 2009).

The roots of natural teeth are covered by an avascular hard tissue called cementum and invested with alveolar bone. Highly ordered periodontal ligament (*PDL*) intervenes and connects the two structures. *PDL* is a highly specialised soft connective tissue that ranges in width between 0.15-0.38 mm depending on location, age and inflammatory status. As with all connective tissue types, *PDL* contains cells and extracellular compartments of collagenous and non-collagenous fibres. Fibroblasts are the most abundant cell type in *PDL*. Osteoblasts, osteoclasts, cementoblasts, epithelial cell rests of Malassez, mesenchymal stem cells and inflammatory cells are among the other cell types within *PDL*.

Principal *PDL* fibres are inserted in the alveolar bone and root cementum and made of collagen type I, III and XII. They can be classified, according to their location and orientation, to; horizontal, oblique, apical, interradicular, and transseptal fibres. The collagenous fibre bundles are embedded in ground substance. Elastic fibres such as oxytalan are also present in *PDL* and form a mesh-like sheath that extends vertically from the cemento-enamel junction to the apical part of the root. Additionally, *PDL* has four types of nerve endings as well as a blood supply system (Nanci, 2008). *PDL* performs highly specialised functions such as; (1) provision of viscoelastic support and protection by linking teeth to the alveolar bone, (2) provision of sensory input to the masticatory system (pressure and proprioception), (3) force distribution and cushioning

effect and (4) playing a dynamic role in controlling bone, cementum and *PDL* fibre remodeling (Beertsen *et al.*, 1997, Palmer, 1999, Nanci, 2008)

In contrast, a dental implant is a metallic or ceramic biocompatible device that is placed in a surgically prepared bony site in the jaw bone. Initial implant stability (known as primary stability) is obtained from the mechanical interlocking of implant screw threads in the cortical and trabecular bone. Long-term stability is achieved by newly formed bone in the vicinity of the implant surface via the process of osseointegration. Unlike natural teeth, osseointegrated implants lack *PDL* and are only separated from the newly formed bone by a thin, afibrillar interfacial zone. This zone is rich in glycosaminoglycans or noncollagenous proteins such as osteopontin and bone sialoprotein as revealed by high resolution *SEM* and immunohistochemistry studies. Thus, the dental implant can be looked at as an ankylosed tooth that is deprived of the above mentioned *PDL* specialised functions. The lack of viscoelastic force dissipation mechanisms may lead to stress concentration around the neck of the implant. This in turn, may be responsible for marginal bone loss encountered with dental implants. Proprioceptive sensory input may though be functional within surrounding bone and oral structures (Palmer, 1999, Puleo and Nanci, 1999).

4.1.1 Osseointegration

A series of highly orchestrated cellular and extracellular matrix biodynamic processes occur at the level of a surgically instrumented bone and bone-implant interface in order to maintain long-term implant stability. The desired outcome of such processes is to lay down the maximum amount of newly formed bone tissue in the vicinity of the inserted implant. This process is referred to as osseointegration and was first described by a Swedish scientific group led by the recently deceased orthopaedic surgeon, Per-Ingvar Brånemark (Puleo and Nanci, 1999, Mavrogenis *et al.*, 2009). In his earliest publication, Brånemark (1959) defined the process of osseointegration as “a direct structural and functional connection between highly differentiated, ordered, living bone and the surface of a load-bearing implant” (Brånemark, 1959, Mavrogenis *et al.*, 2009). This concept originated from experimental studies on the microscopic circulation of bone marrow in the rabbit fibula in the early fifties. The research originally aimed to study bone healing and bone marrow response following various types of bone injuries. A unique type of injury, implantation of titanium chambers of a

screw-shaped design, was further investigated utilising long-term *in vivo* microscopic studies in the early sixties. It was observed that the implanted titanium chambers were inseparably incorporated within the surrounding bone which also infiltrated the thin spaces within the surface of the implanted titanium chamber. These findings were the backbone for current anatomical-histological definition and characterisation of the osseointegration process. Further *in vivo* studies on dogs and then on humans confirmed the possibility of attaining stable, load-bearing dental implants that could be used to replace missing teeth and other oro-facial structures (Adell *et al.*, 1981, Brånemark, 1983, Adell, 1990). These observations formed the basis of a clinical definition of osseointegration, or so called ‘rigid fixation’, which implies an absence of observable, progressive movement of the implant upon applying a force ranging from 1 to 500 g (Adell *et al.*, 1981, Misch, 2008).

The process of osseointegration involves a highly complex cell-cell communication and can be divided into four consecutive phases; haemostasis, inflammation, proliferation and remodelling. Immediately after surgical preparation and implantation, the inflicted mechanical and thermal damage results in localised, superficial necrosis of bone tissue. Additionally, adsorption of proteins from blood and tissue fluids at the wound site to the surface of the implant occurs immediately upon implantation. Furthermore, hematoma formation at the bone-implant interface is a major event that results from severing fine blood capillaries within trabecular bone and subsequent blood perfusion of surgical site. Ions and serum proteins such as albumin, fibrinogen and fibronectin adhere to the implant surface. Haemostasis is then achieved by orchestrated changes in platelet morphology, adhesion, spreading and aggregation that eventually lead to platelet plug formation. Platelets also undergo intracellular biochemical changes that result in the release of various growth factors such as thromboxane which stimulate further platelet aggregation and synthesis of platelet derived growth factor (*PDGF*) that stimulates the cell division of fibroblasts. The latter cells produce fibrin monomers that cross-link and promote blood clot organisation by formation of fibrin networks that adhere to the implant surface. The fibrin network also form a provisional matrix for subsequent bone healing processes. This matrix provides the osteoconductive scaffold where osteogenic cells can migrate and start bone formation (Puleo and Nanci, 1999, Mavrogenis *et al.*, 2009, Zhang, 2014).

During the inflammatory phase, necrotic bone, tissue debris and residual bacteria are eliminated by immune cells such as polymorphonuclear leukocytes (*PMNs*). *PMNs* are chemotactically attracted to the wound site following the release of various pro-inflammatory interleukins and bradykinin that increase post-capillary venules' permeability and promote *PMNs*' attachment to endothelial cells. *PMNs* combat antigenic cells and substances through the release of reactive oxygen species and various highly digestive proteases. At this stage, the wound site is on the verge of uneventful healing or accelerated inflammation and eventual implant loss. The efficiency of the immune response, the remaining bacterial count and toxic by-products are among the major determinants of the outcome at this stage (Mavrogenis *et al.*, 2009, Zhang, 2014).

Monocytes/macrophages are the next immune cells to arrive at the wound site. They are chemotactically attracted by the released monocyte chemotactic protein (*MCP-1*) from *PMNs*. Macrophages can further eliminate bacteria and antigenic substances by the process of phagocytosis. More importantly, phagocytes dominate during the late inflammatory phase where they synthesise and release tissue inhibitor of metalloproteinases (*TIMPs*). *TIMPs* have a major role in preserving growth factors embedded in matrix proteins and proteoglycans via inhibition of the proteases released from *PMNs*. This has a major role in the wound healing process and allows the commencement of the proliferative phase.

Growth factors within the organised blood clot such as *PDGF*, vascular endothelial growth factor (*VEGF*) and fibroblast growth factor (*FGF*) further stimulate fibroblast proliferation and angiogenesis process within few days post implantation. Fibroblasts synthesise and release extracellular matrix components such as collagens, elastins and proteoglycans. Furthermore, the hypoxic conditions within the wound stimulate the expression of hypoxia inducible factor (*HIF*) from endothelial cells and macrophages. *HIF* upregulates expression of angiogenic factors such as *VEGF* which promotes angiogenesis. *VEGF* mainly targets mesenchymal stem cells around the blood vessels, the perivascular cells, and stimulates their migration toward low oxygen concentration areas to form new blood vessels (Mavrogenis *et al.*, 2009, Zhang, 2014).

One week post implantation, a notable decrease in primary stability of the implant demarcates the beginning of the osteoclastic function to resorb necrotic and micro-fractured bone edges. This process results in releasing of important bone growth factors from the resorbed bone matrix such as bone morphogenetic proteins (*BMPs*), transformation growth factor beta (*TGF- β*) and *PDGF*. Under the influence of these factors, especially *BMPs*, perivascular mesenchymal stem cells migrate toward existing bone trabeculae and differentiate to osteoblasts. The attachment of osteoblasts is mediated by adsorbing proteins such as fibronectin. Osteoblasts secrete organic bone matrix from the repaired bone toward implant surface. Matrix is subsequently mineralised to woven bone utilising calcium phosphate molecules. Surprisingly, osteoblasts and mesenchymal stem cells seem to migrate and attach to the implant surface as early as 24 hours post implantation. Attachment is thought to be mediated by the early adsorbed non-collagenous proteins. Osteoblasts start depositing afibrillar layer/matrix on the implant surface and poorly mineralised osteoid, which collectively form a 0.5 mm thick, continuous, layer that is rich in calcium, phosphorus, osteopontin and bone sialoprotein. The early formed matrix promotes further cell attachment, mineralisation and contact osteogenesis. The latter refers to the process of bone formation by osteoblasts on the surface of the implant toward the healing bone (Puleo and Nanci, 1999, Mavrogenis *et al.*, 2009, Zhang, 2014).

Woven bone grows parallel to implant surface through the intramembranous pathway. The newly grown bone in the irregularities at the surface of the implant is a key factor in the long-term, secondary stability of the implant or the so called, biological fixation. However, it is not effectively designed to adapt under cyclic loading transmitted through the implant. Regulated by osteocytes, osteoclast-osteoblast mediated bone remodelling commences weeks after implantation. Osteoclasts resorb the formed woven bone and osteoblasts lay down a new highly mineralised lamellar bone that is structured perpendicular to the implant surface (Mavrogenis *et al.*, 2009, Zhang, 2014). Lamellar bone in contact with the implant surface undergoes morphological remodelling as adaptation to mechanical loading of the implant. The remodelled bone can extend up to 1 mm from the implant surface (Probst and Spiegel, 1997, Franchi *et al.*, 2005, Mavrogenis *et al.*, 2009, Eriksen, 2010).

4.1.1.1 Factors determine the success of osseointegration

During the early nineteen eighties, Brånemark's research group proposed six interrelated factors that directly influenced the success of osseointegration. According to their 15 years of experience and growing number of laboratory and clinical research reports, they stated that the success of osseointegration is heavily dependent on implant related parameters including; implant material, implant design and surface topography. Bone/host related factors as well as surgical placement technique and loading were also considered among the important osseointegration success determinants (Albrektsson *et al.*, 1981). In this section, only implant related factors will be reviewed as the others are beyond the scope of this work.

The process of osseointegration denotes the situation where a non-vital, non-biological device is successfully anchored within living bone without progressive movement under cyclic loading. It however, cannot be considered as a biological property of an implant design or material. In other words, bone integration noticed under the microscope can be attributed to the lack of a local or systemic immune response to the implant. Thus, osseointegration can be seen as a consequence of lacking a rejection reaction mediated by the recipient tissue rather than a positive biological tissue reaction or implant material property (Linder *et al.*, 1983, Stanford and Keller, 1991, Mavrogenis *et al.*, 2009).

4.1.1.1.1 Biocompatibility of the implant material

cpTi and titanium alloys are among the most widely used implant materials owing to their high biocompatibility, corrosion resistance and adequate mechanical and physical properties (Albrektsson *et al.*, 1981). Implant material should be bio-inert and biocompatible in order to minimise or eliminate any adverse immune response that may lead to fibrous encapsulation and eventual loss of the implant. Furthermore, implants may undergo significant changes upon exposure to a physiological environment. It has been cited that the titanium oxide layer has triple the initial thickness upon removal which is a strong indication of significant electrochemical, corrosive oxidation stress (Sundgren *et al.*, 1986, Lausmaa *et al.*, 1988, Puleo and Nanci, 1999).

Corrosion by-products are highly relevant as they can cause a significant, local immune response and/or induce systemic toxicity. Evard *et al.* (2010) concluded that

there was an increase in the prevalence of oral allergies to metals, including supposedly inert materials like gold and titanium especially in patients with history of allergy to other metals. They also maintained that titanium oral implants can induce type I or IV allergic reactions which can be responsible for unexplained failure cases of dental implants in some patients (Pigatto *et al.*, 2009, Evrard *et al.*, 2010). A histological study on retrieved titanium hip implants showed a strong inflammatory response to these implants and was regarded as a contributing factor for failure (Lalor, 1991). In addition, Sicilia *et al.* (2008) reported a 0.6% prevalence of allergy to titanium in patients who received dental implants and recommended allergy tests in some cases (Sicilia *et al.*, 2008).

High concentrations of titanium ions were detected locally, i.e. in bone in the vicinity of implants (Jorgenson *et al.*, 1997). Significant concerns about titanium ion release due to corrosion and wear and subsequent systemic toxicity have been raised recently (Andreiotelli *et al.*, 2009, Koutayas *et al.*, 2009, Evrard *et al.*, 2010). Corrosion by-products have been detected in regional lymph nodes, internal organs, serum and urine (Black *et al.*, 1990, Kazuhisa and Iizuka, 1993, Onodera *et al.*, 1993, Jacobs *et al.*, 1998). Beside other factors mentioned in Section 1.1, concerns regarding titanium toxicity have led to the emergence of some ceramic implant materials as alternative to titanium

Zirconia ceramics were among the most widely studied and used ceramic implant material owing to their high biocompatibility, optimum mechanical and optical properties (Andreiotelli *et al.*, 2009, Hisbergues *et al.*, 2009, Koutayas *et al.*, 2009, Vagkopoulou *et al.*, 2009). Zirconia showed a high level of biocompatibility and safety which allowed its' use as biomedical implant which can be traced back to late nineteen sixties (Helmer and Driskell, 1969). The use of zirconia heads in total hip arthroplasty was reported in the late nineteen eighties (Christel *et al.*, 1988). Before then, zirconia was used to coat base metal alloy implants in an attempt to enhance stability of dental implants in dogs (Cranin *et al.*, 1975).

Zirconia dental implants are placed in contact with bone and oral mucosal tissues. Several studies investigated toxic effects of the material in the most abundant cells within these tissues. Raffaelli and co-workers demonstrated low cytotoxicity, strong adhesion capacity and increased cellular growth rate of fibroblasts upon

exposure to zirconia ceramics (Raffaelli *et al.*, 2008). The effect of zirconia on osteoblasts was among the most attractive topics for researchers as was the case with titanium. The most fundamental and widely cited work in this field was performed by Josset *et al.* (2010) who found that zirconia did not induce cellular or deoxyribonucleic acid (*DNA*) toxicity and can favourably interact with osteoblasts *in vitro*. In addition, the same group reported that zirconia did not hinder or interfere with physiological mechanisms of protein and extracellular matrix production (Josset *et al.*, 1999). Furthermore, Sterner *et al.* (2004) found that alumina and titanium induced reactivity of human monocytes to a greater extent when compared with zirconia (Sterner *et al.*, 2004). Other *in vitro* studies showed no difference between the effect of zirconia, alumina and/or titanium on macrophages and lymphocytes (Piantelli *et al.*, 1992, Catelas *et al.*, 1999).

Analogous to corrosion in titanium implant materials, zirconia may suffer structural deterioration as a result of $t \rightarrow m$ process. The monoclinic phase resulting from such a process is more prone for pull-out and thereby, zirconia particle release may be an issue with this material. However, this phenomenon was only reported with polyethylene cup-zirconia head, hip implants where both materials sustained a high rate of contact wear (Chevalier *et al.*, 1997, Chevalier *et al.*, 2007b, Chevalier *et al.*, 2009). Zirconia dental implants are however used in a different arrangement. It is the restoration supported by the implant that is subjected to cyclic loading rather than the implant itself making the problem of contact wear of a less concern. Yet, spontaneous $t \rightarrow m$ as a result of *LTD* process may be an issue. To the knowledge of the author of this thesis, there are no research studies on local or systemic particle release from zirconia dental implants.

4.1.1.1.2 Implant design

‘Implant design’ has been presented as a comprehensive term to describe the 3D structure, configuration, external outline, form, shape, surface macrostructure and macro-irregularities of a particular implant. Configuration and location of prosthetic interface, presence of threads or other special features such as grooves, vents, flutes or porosity are all important implant characteristics that can be underpinned under the term ‘implant design’ (Sykaras *et al.*, 1999, Steigenga *et al.*, 2003). A plethora of

implant designs have been introduced throughout the evolution of dental implant practice.

Generally, implants can be categorised according to the following important features; threaded and non-threaded, cylindrical and tapered, one- and two-piece, internal or external connections and soft tissue or bone level. The earliest, probably most fundamental, long-term research work published in the area of clinical dental implantology was in 1981 (Adell *et al.*, 1981, Albrektsson *et al.*, 1981). The authors reported their 15 years follow-up data on thousands of cylindrical, threaded, two-piece, soft-tissue level *cpTi* dental implants placed in several hundreds of patients. Both groups had very high success rate, implant and prosthesis stability, over the whole follow-up period and concluded that such design is highly recommended for clinical use. The use of such a design enhanced long-term osseointegration owing to the following reasons:

(1) Threads maximise primary stability via actively engaging bone and thereby reducing mobility which is detrimental to osseointegration (Frandsen *et al.*, 1984, Sennerby *et al.*, 1991, Ivanoff *et al.*, 1997). In addition, incorporation of threads increases the surface area available for new bone formation and stimulates bone deposition by adequate stress distribution (Albrektsson *et al.*, 1981, Carlsson *et al.*, 1986, Siegele and Soltesz, 1988).

(2) Cylindrical design ensures intimate contact between implant surface along the whole osteotomy length and reduces the bone-implant gap (Carlsson *et al.*, 1988, Sykaras *et al.*, 1999).

(3) The use of a soft tissue level implant confines the microgap and micromovement between the prosthetic part and implant well above the bone level. This in turn, reduces the possibility of marginal bone loss and enhances long-term success of osseointegration (Hermann *et al.*, 2001b).

The above mentioned findings on the effect of implant design on the success of osseointegration were derived from studies exclusively performed on *cpTi* or titanium alloys. The amount of published data on various zirconia implant designs is significantly lower and for shorter follow-up periods. In a radically different approach, the use of a truly anatomical one-piece zirconia implant was recently reported. The

implant can be custom made for each extraction socket via laser scanning of the extracted roots. An anatomic, root-analogue zirconia implant is then milled using *CAM* technology to replace extracted teeth with high adaptation to the bony walls. The authors claimed good performance of these implants after 30 months (Pirker and Kocher, 2008, Pirker *et al.*, 2011).

The one-piece zirconia implant design is the most widely available for clinical use. In titanium implants, such a design has superior osseointegration potential owing to the absence of a microgap and micromovement (Hermann *et al.*, 2001b). However, one-piece zirconia dental implants exhibited a fairly high early failure rate (during healing phase) which ranged between 2-26% after follow-up periods up to 2 years (Mellinghoff, 2006, Oliva *et al.*, 2007, Lambrich and Iglhaut, 2008, Depprich *et al.*, 2012).

Payer *et al.* (2012) published their results after two years follow-up of 19 immediately loaded zirconia implants. They reported 95% two-year survival according to the clinical and radiographic parameters they examined (Payer *et al.*, 2012). In contrary, Kohal *et al.* (2012) found that immediately restored one-piece zirconia implants had one-year cumulative survival rate comparable to titanium counterparts. However, they remarked that the incidence of bone loss was considerably higher than that for titanium implants. Thus, the studied implants could not be recommended for clinical use (Kohal *et al.*, 2012). These findings were in line with those reported by Cannizzaro *et al.* (2010) who demonstrated high failure rate due to significant bone resorption in the healing phase around one-piece zirconia implants especially when placed in fresh extraction sockets and immediately provisionalised (Cannizzaro *et al.*, 2010).

The number of two-piece zirconia implant designs is very scarce. One clinical study reported the outcome of a single centre, two-year longitudinal case series. Forty nine implants were placed in the posterior region of the jaw in 32 patients. Zirconia abutments were bonded to implants with adhesive resin cement. Five implants were lost due to aseptic loosening during the healing phase. The authors concluded that the one-year cumulative survival rate after loading was 87% (Cionca *et al.*, 2014).

4.1.1.1.3 Surface topography

Implant surface topography is among the most widely studied areas in dental implantology. Surface topography depicts the orientation and roughness of the surface which is highly dependent on manufacturing processes and further surface modification if present. Manufacturing implants by milling or turning yields an anisotropic surface i.e., surface with distinct surface orientation. Original Brånemark implants are an example of anisotropic, machined implants produced by turning process (Wennerberg and Albrektsson, 2009).

Osseointegration and osseointegration processes are largely dependent on the free surface energy, hydrophilicity and wettability of the implant surface. Various surface treatments were used in order to improve such parameters and thereby, increase the osseointegration of the implants (Kieswetter *et al.*, 1996, Yahyapour *et al.*, 2004, Rupp *et al.*, 2006). Surface roughening is one of the most commonly used surface treatments. It increases the area available for new bone formation, improves the attachment of cells and proteins involved in the process of osseointegration and modifies surface composition, free energy, wettability and hydrophilicity. It can be performed by subtractive techniques (sandblasting and/or acid etching) or additive methods (plasma, hydroxyapatite or fluoroapatite coating) (Rupp *et al.*, 2006, Wennerberg and Albrektsson, 2009).

Several *in vitro* studies on osteoblasts or osteoblast-like cells demonstrated that microstructured, roughened titanium surfaces exhibited enhanced cellular attachment, adsorption of major proteins required for bone formation (fibronectin), expression of genes encoding for proteins essential for osteoblast function, cellular proliferation and differentiation in comparison to machined and smooth surfaces (Martin *et al.*, 1995, Degasne *et al.*, 1999, Mustafa *et al.*, 2001). Furthermore, large numbers of *in vivo* animal studies reported a stronger biofunctional bone response to roughened titanium implants when compared to machined counterparts. This was indicated by higher bone-to-implant contact (**BIC**), histomorphometric analysis, push-out/pull-out strength, bone-to-implant retention tensile strength and removal torque (Buser *et al.*, 1991, Suzuki *et al.*, 1997, Rønold and Ellingsen, 2002, Shalabi *et al.*, 2006, Wennerberg and Albrektsson, 2009).

Various surface treatments, especially those of a mechanical nature, may increase the susceptibility of zirconia to *LTD*. Thus, surface modification of zirconia is more challenging in comparison to titanium. Sintering powders to the dental implant surface, nano-structuring using nanotechnologies, microstructuring using sandblasting and/or acid-etching, laser, plasma and *UV* light treatment have all been used to produce a roughened zirconia surface (Kohal *et al.*, 2013).

A limited amount of data is currently available regarding the effect of surface topography of zirconia implant materials on the *in vitro* behaviour of osteoblast and osteoblast-like cells. Osteoblast-like cells had a significantly higher early proliferation rate when cultured on sandblasted and acid-etched *Y-TZP* discs in comparison to turned *Y-TZP* controls (Bächle *et al.*, 2007). Additionally, acid-etched *Y-TZP* material had higher early osteoblast proliferation rate in comparison to acid-etched titanium (Depprich *et al.*, 2008). Micro- and nano-structured *Y-TZP* (sandblasted and etched) demonstrated higher wettability, enhanced proliferation, greater alkaline phosphatase activity and higher expression of osteogenic markers when compared to polished or micro-structured (sandblasted) *Y-TZP* materials (Ito *et al.*, 2013).

Several *in vivo* animal studies demonstrated superior osseointegration with roughened *Y-TZP* material when compared to control, smooth *Y-TZP* implant materials (Sennerby *et al.*, 2005, Gahlert *et al.*, 2007). Powder injection moulded *Y-TZP* implants manufactured using a roughened mould exhibited significantly higher *BIC* and removal torque values than the turned titanium implants and zirconia implants manufactured using a smooth mould (Park *et al.*, 2012). Furthermore, *Y-TZP* implants roughened using selective infiltration-etching technique demonstrated significantly higher *BIC* in rabbit femur heads in comparison to as sintered *Y-TZP* and turned titanium implants (Aboushelib *et al.*, 2013b).

A multitude of clinical studies reported higher success rates, more stable crestal bone levels and higher implant retention rates when comparing roughened to turned (smooth) dental implants (Fröberg *et al.*, 2006, Albrektsson *et al.*, 2012). A recent Cochrane systematic review with meta-analysis on seven clinical trials revealed significantly higher early failure with turned implants when compared to roughened counterparts (Esposito *et al.*, 2014). With regard to clinical studies investigated the

effect of surface roughness on zirconia implant survival, one study reported higher success rate of acid-etched one-piece *Y-TZP* implants in comparison to coated or turned *Y-TZP* implants (Oliva *et al.*, 2010).

4.1.2 Soft tissue integration (Periointegration)

The oral masticatory mucosa, is composed of keratinised epithelium that is tightly bound to underlying bone via a dense fibrous connective tissue (lamina propria). Teeth have an exclusive anatomic feature as they are the only structure that perforates through mucosal tissues during tooth eruption process. Oral mucosa surrounding erupting/erupted teeth is called gingiva. Gingivae can be classified into, marginal, attached and interdental. The attached gingiva is separated from lining mucosa by the mucogingival line. It is firmly bound to the underlying cementum and bone. Marginal gingiva surrounds teeth and creates a scalloped collar. It is separated from tooth structure by the so called, gingival sulcus which is lined with non-keratinised sulcular epithelium. Interdental gingiva has similar histological features to marginal gingiva, but has a different outline (Nanci, 2008).

The region where the gingiva meets tooth surface is called the dentogingival complex. It is a unique arrangement as it is the only possible ingress portal for bacteria and toxins from oral environment to the underlying tissues. The floor of the gingival sulcus is lined by stratified squamous non-keratinised epithelium cells and is known as the junctional epithelium (*JE*). It is created by the fusion of reduced enamel epithelium and oral mucosa during the process of tooth eruption. *JE* is attached to tooth enamel or cementum by the internal basal lamina (*IBL*), the constituents of which are laminin-5 and amelotin. Such proteins leave the *IBL* with a high attachment capacity to mineralised tissues. *IBL* is attached to *JE* by means of hemidesmosomes. *JE* is attached to the supporting connective tissue via external basal lamina (*EBL*) (Nanci, 2008).

JE is supported by structurally and functionally different lamina propria of other oral mucosal tissues. The lamina propria contains low grade inflammation even in clinically healthy gingiva. Inflammatory cells migrate through the permeable *JE* and eventually appear in the gingival crevicular fluid. Lamina propria supporting *JE* provides 'permissive' growth, i.e. the proliferation of immature, undifferentiated epithelium cells. This is believed to have crucial role in healing and regeneration of

the dentogingival complex after periodontal disease or surgery. In contrast, lamina propria supporting sulcular and oral epithelium has instructive growth role and induces the proliferation of highly differentiated and matured epithelium (Nanci, 2008).

Gingiva is attached to tooth surfaces by a group of highly organised collagenous fibre bundles. Such fibres are inserted in root cementum and alveolar bone and/or lamina propria. Depending on their orientation and insertion, they can be classified to; dentogingival, alveologingival, circular, dentoperiosteal and transseptal fibre groups (Nanci, 2008). In natural teeth, **JE** has a fundamental function to maintain the integrity of periodontal ligament and underlying bone. The dynamic, unique architectural integrity coupled with high turnover rate of **JE** play a crucial role in the immune response to pathologic chemical and bacterial substances. **JE** cells; (1) secrete antimicrobial substances, (2) are able to express proinflammatory cytokines that can elicit a specialised immune defence mechanism and (3) allow permeation of inflammatory cells from the underlying connective tissue (Ji *et al.*, 2007).

The **JE** and connective tissue attachment are lost during tooth extraction. In the case of dental implants, the re-establishment of soft tissue attachment around the inserted implant at early stages of wound healing is a major determinant in implant success. The formation of a long-lasting, effective barrier, also known as the biologic width, shortly after implant insertion, protects supporting bone against bacterial penetration which could eventually lead to the loss of the implant (Donley and Gillette, 1991, Rompen *et al.*, 2006).

The newly formed soft tissue barrier or interface is composed of epithelial and connective tissue layers. Both layers are interfaced with a non-living implant material rather than biological tissues as in the case of natural teeth. The histogenesis, morphogenesis, macroscopic and microscopic features of such interface have been widely studied in the literature.

The formation of **JE** at the surface of the transmucosal component of the implant commences shortly after implantation when epithelium at the borders of traumatised soft tissues migrate across the formed blood clot and granulation tissue. Once reaching the surface, a series of interactions between oral epithelium and the implanted surface takes place. They result in apical proliferation with morphological and functional alterations of the oral epithelium in contact with the implant (component). Eventually,

a peri-implant sulcus lined with sulcular epithelium, two mm long **JE** will form around the implant (component) in a very close analogy to natural teeth (Donley and Gillette, 1991, Buser *et al.*, 1992, Abrahamsson *et al.*, 1997, Cochran *et al.*, 1997, Rompen *et al.*, 2006).

Despite the differences in their origin, it has been substantially concluded that anatomical features and histochemical characteristics of the implant-soft tissue interface are very similar to dentogingival complex in natural teeth. Additionally, many structural and ultrastructural features, patterns of differentiation and function were very similar in peri-implant soft tissues and gingivae. Additionally, the attachment mechanism of **JE** to titanium surfaces was consistently reported to be similar to natural teeth. Basal lamina and hemidesmosomes formation was detected as early as three days postoperative and considered as the major attachment mechanism between epithelial cells and implanted titanium by several animal and human studies (Donley and Gillette, 1991, Mackenzie and Tonetti, 1995, Listgarten, 1996, Lindhe and Berglundh, 1998, Rompen *et al.*, 2006).

Despite the high migration and proliferation capacity of oral epithelium, apical migration at the implant (component) surface is a limited and confined to a certain dimension. Three interplaying factors have demonstrated a significant role in controlling the down growth process of oral epithelium including; the presence, quality and stability of fibrin clot/granulation tissue in contact with the implanted surface, interactions with the titanium oxide layer and the signalling mechanism from the underlying connective tissue (Berglundh *et al.*, 1991, Chehroudi *et al.*, 1992, Listgarten, 1996, Rompen *et al.*, 2006).

The healing of the connective tissue underlying oral epithelium (lamina propria) after the surgical placement of an implant (component) is a key factor in the formation of the biologic width and soft tissue integration around the dental implant. Connective tissue wound healing commences with fibrin clot formation and adhesion at the incision/extraction site followed by adsorption of extracellular matrix proteins. The organisation of the clot into granulation tissue and further transformation of the latter to mature connective tissue demarcates a successful connective tissue wound healing process (Rompen *et al.*, 2006).

Mature connective tissue within peri-implant soft tissues is located between the marginal bone and *JE*. It has two distinct zones; the inner, fibre-rich, fibroblast-poor, zone which is located in the vicinity of the implant surface. This part of connective tissue resembles scar tissue and it is separated from the implant surface by a thin layer of proteoglycans. The outer zone however, is a highly vascularised and cellular with fibroblast as the most dominant cell type (Hansson *et al.*, 1983, Buser *et al.*, 1992, Abrahamsson *et al.*, 1997, Cochran *et al.*, 1997, Rompen *et al.*, 2006).

The inner zone of connective attachment plays a significant role in the long-term success of dental implants. It forms an important part of the biological barrier that protects the underlying bone against chemical and bacterial toxins. It is however different from natural teeth in two aspects; the fibres are not inserted in the implant material and run mostly parallel to the implant surface. Effectively, these fibres form a cuff around the implant but lack the physical interdigitation that is seen between fibres, cementum and alveolar bone in the dentogingival complex. For these reasons, connective tissue-implant interface can hardly be qualified as attachment and may exhibit inferior mechanical resistance as compared to that of natural teeth (Buser *et al.*, 1992, Listgarten, 1996, Hermann *et al.*, 2001a, Rompen *et al.*, 2006).

4.1.2.1 Factors determine the success of periointegration

The most fundamental function of the soft tissue, biologic width around implants is to maintain effective and stable barrier against bacterial invasion through the peri-implant sulcus. Additionally, stable soft tissue levels are essential from an aesthetic point of view especially in the areas of high aesthetic demands such as anterior maxilla. Several factors may affect the outcome of the periointegration process. These factors can be categorised in three groups; host, surgical technique and material related factors. The latter are of a significant importance and underpin material characteristics, surface topography and configuration of the prosthetic platform. These factors may individually or collectively affect the behaviour of cells and components within epithelium and connective tissue and eventually determine the nature and quality of the biologic width (Donley and Gillette, 1991, Rompen *et al.*, 2006).

4.1.2.1.1 Biocompatibility of the transmucosal material

The use of a biocompatible substrate in the transmucosal component of the implant system is of great importance in order to maintain cell viability, eliminate

host-rejection reactions and promote biological functions. Several studies reported the superiority of titanium and zirconia ceramics as transmucosal components owing to the high biocompatibility toward most dominant cell types in biologic width components namely, oral epithelium and connective tissue.

In an *in vitro* investigation, it has been demonstrated that human oral keratinocytes had similar viability and initial attachment when cultured on mirror-polished *cpTi* and *Y-TZP* surfaces for 48 hours (Kimura *et al.*, 2012). Additionally, gingival epithelial cells exhibited comparable viability and morphology when seeded on both *cpTi* and *Y-TZP* surfaces with similar surface roughness for 1 and 24 hours (Rigolin, 2014). Titanium and zirconia surfaces also exerted low cytotoxicity, strongly induced adhesion capacity, increased cellular growth rate and greater viability of fibroblasts (Raffaelli *et al.*, 2008, Pae *et al.*, 2009).

Whether zirconia surfaces have a superior effect on the proliferation, attachment and differentiation potential of cell types within soft tissues in comparison to titanium is controversial and difficult to extrapolate. This is attributed to the heterogeneity of the studied cells and different surface characteristics of the studied materials. Größner-Schreiber *et al* (2006) found significant improvement in human fibroblast adhesion to titanium discs when coated with zirconium nitride in comparison to control (Größner-Schreiber *et al.*, 2006). This study however utilised a zirconium compound that is different from those used in implant systems and thereby, undermines the validity of the comparison.

Several *in vivo* studies investigated the anatomical and histological features as well as predictability of peri-implant soft tissue integration with transmucosal implants/components. Animal studies indicated that the use of zirconia and titanium resulted in comparable dimensions (*JE* and connective tissue), quality and stability of biologic width (Kohal *et al.*, 2004, Welander *et al.*, 2008, Stadlinger *et al.*, 2010, Piattelli *et al.*, 2011). Long-term clinical studies revealed that the response of peri-implant soft tissues and health were optimum around zirconia transmucosal abutments (Brodbeck, 2003, Zembic *et al.*, 2014, Ferrari *et al.*, 2015). Moreover, zirconia and titanium transmucosal abutments have been clinically compared and found to produce statistically comparable survival rates, biological and technical complications (Van Brakel *et al.*, 2011, Zembic *et al.*, 2013). However, zirconia abutments were

associated with shallower sulcus depths after three months in this study (Van Brakel *et al.*, 2011). In the clinical trial by Bianchi *et al.* (2004), it was found that the hybrid implant system (titanium endosseous part and *Y-TZP* soft tissue collar) performed better than titanium controls in terms of probing depth, bleeding on probing and plaque index. Also, rapid stabilisation of peri-implant tissues was documented in the first year and survival rate after two years found to be 100% (Bianchi *et al.*, 2004). However, this clinical trial seemed to be at a high risk of bias as there was not enough information about randomisation and allocation concealment, a small sample size and no information about assessors' blinding.

4.1.2.1.2 Inflammatory status within biologic width

The second important pillar of periosteal integration is an inflammation-free environment as the inflammatory process may collaterally damage soft tissue attachment to dental implants by releasing various proteases in an attempt to combat bacterial infections. Angiogenesis (new blood vessel formation) is believed to be a strong indicator of the inflammatory status in soft tissues. Presence of angiogenic factors and the enzymes they express such as *VEGF* and Nitric Oxide Synthases I & II are indicative of inflammatory processes as they are released by neutrophils in response to bacterial infection (Hisbergues *et al.*, 2009).

In their split mouth clinical trial, Degidi *et al.* (2006) demonstrated significantly higher inflammatory infiltrate with connective tissue surrounding titanium healing caps when compared to zirconia counterparts. Additionally, the authors confirmed the lower inflammatory status around zirconia by studying various angiogenic markers in biopsies from peri-implant soft tissues surrounding the two materials in human subjects (Degidi *et al.*, 2006).

4.1.2.1.3 Surface topography of the transmucosal component

Surface topography has an essential impact on the formation of the implant-soft tissue interface. Early research concluded that “*alteration of the titanium surface morphology may selectively enhance the attachment of either epithelial cells or fibroblasts, theoretically enhancing the formation of a biologic seal between the implanted titanium surface and its adjacent tissue*” (Donley and Gillette, 1991). This conclusion was made on the basis of research studies investigated connective tissue and epithelial attachment on porous surfaces. Despite sounding reasonable, especially

in the light of substantial evidence supporting such a statement in the case of osseointegration, current evidence is not fully compatible with such effect.

In vitro research findings suggested that the effect of surface roughness on the attachment and proliferation of epithelial cells may be variable (Piattelli *et al.*, 2011). A comparative study investigated the effect of surface topography on the attachment and proliferation of osteoblasts and gingival keratinocytes cells. The findings indicated a fundamental difference in the response of the two cell types to various surface topographies. It was shown that attachment of epithelial cells was significantly better to polished titanium in comparison to a micro-textured counterpart (Hormia *et al.*, 1991, Lauer *et al.*, 2001).

On the other hand, a study by Carmine *et al* (2003) indicated that roughened titanium surfaces (sandblasted) enabled superior epithelial cell adhesion and spreading when compared to smoother (turned) surfaces (Carmine *et al.*, 2003). The authors of the latter paper extrapolated their findings on the grounds of filopodia (cytoplasmic extensions) exhibited by the epithelial cells. However, this conclusion may lack accuracy as other authors commented that morphological appearance of filopodia does not necessarily indicate higher adhesion capacity. Additionally, upon careful inspection of the *SEM* images presented in the original publication, it appeared that epithelial cells are bridging over, rather than adhering to valleys of the roughened titanium surface (Rompen *et al.*, 2006). Additionally, it has been demonstrated that roughened titanium surfaces (etched and sandblasted/etched) reduced the growth rate and spreading of epithelial cells when compared to polished titanium surfaces in cultures up to 28 days (Baharloo *et al.*, 2005).

Similar findings were reported upon studying fibroblasts behaviour when seeded on titanium or zirconia surfaces with different surface characteristics (Hormia and Könönen, 1994, Mustafa *et al.*, 1998, Takamori *et al.*, 2008). An inverse relationship has also been cited between surface roughness and the adsorption and production of proteins pivotal to soft tissue attachment such as fibronectin and vinculin (François *et al.*, 1997, Baharloo *et al.*, 2005).

Several animal studies compared the effect of surface topography of titanium and zirconia transmucosal components on the characteristics of the implant-soft tissue interface. The majority of the studies indicated no significant difference between the

features and dimensions of the mucosal barrier around transmucosal components made from titanium or zirconia with different surface roughness (Abrahamsson *et al.*, 2002, Rompen *et al.*, 2006, Piattelli *et al.*, 2011). Clinical studies on human subjects comparing the effect of surface roughness of zirconia or titanium transmucosal components on the mucosal barrier are still lacking.

4.1.3 Commercially available modified implant surfaces

Subtractive surface modification techniques are widely used to provide macro- and/or micro-structured implant surfaces. Sandblasting and/or acid etching is one of the most researched techniques for this purpose. SLA[®] topography (Straumann, Switzerland) (SLA stands for sandblasted, large-grit, acid-etched) is one of the most well-documented surfaces that has been verified rigorously in the literature (Kim *et al.*, 2008, Buser *et al.*, 2012). However, research findings indicated that micro-structured titanium surfaces may be rendered hydrophobic as a result of air being entrapped within smaller roughness cavities. This in turn, results in heterogeneous surface with low wettability and free surface energy. Additionally, interaction between CO₂ in the air and the titanium oxide layer may result in the formation of hydrocarbons and carbonated contaminants which further degrade the free surface energy (Rupp *et al.*, 2006).

Hydrophilicity and free surface energy are major determinants in the essential process of protein adsorption and cell attachment during the early stages of osseointegration and periosteal integration. Thus, surface roughness may have an overall effect of retarding tissue integration processes initially and thereby, elongate the period required for healing. Application of hydrophilic coatings may be not appropriate as they may conceal the surface microstructure and negate its positive effect on tissue integration processes (Rupp *et al.*, 2006).

A novel hydrophilisation technique was utilised to ameliorate the aforementioned issues with microstructured surfaces. The original SLA[®] implant surface was treated and processed according to this hydrophilisation method and introduced to the market as SLActive[®] surface. The technique relies on maintaining surface reactivity of the titanium oxide layer by eliminating air contamination as described in Section 4.2.1.

An *in vitro* study demonstrated that using such a processing method, the amount of carbon contamination could be reduced in the order of three times. Additionally, the amount of oxygen and titanium can be doubled hence the nomenclature, chemical surface modification. Free surface energy was significantly higher in SLActive[®] surfaces when compared to original SLA[®] counterpart. These findings may indicate improved hydrophilicity and wettability of the surface upon using such processing conditions (Rupp *et al.*, 2006).

Research findings indicated superior performance of SLActive[®] surface in comparison to SLA[®] predecessor (Wennerberg *et al.*, 2011). It has been demonstrated that SLActive[®] surface significantly enhanced osteoblast proliferation, attachment and osteogenic differentiation when compared to SLA[®] surface (Masaki *et al.*, 2005, Klein *et al.*, 2010, Lai *et al.*, 2010, Mamalis and Silvestros, 2011, DU *et al.*, 2012, Gu *et al.*, 2013). Animal studies indicated that SLActive[®] surface induced superior osseointegration and bone regeneration capacity when compared to SLA[®] surface (Buser *et al.*, 2004, Schwarz *et al.*, 2007b, Mardas *et al.*, 2011). Clinical studies demonstrated superior and faster initial healing which allowed safe and predictable use of SLActive[®] implants for immediate and early loading procedures even with poor quality bony sites (Ganeles *et al.*, 2008, Zöllner *et al.*, 2008, Chambrone *et al.*, 2014).

Conventional mechanical or chemical methods may be less effective with zirconia owing to the high hardness of the material. Additionally, roughening zirconia surface may be detrimental to the durability of the material beside the possible increase in *LTD* sensitivity (Kohal *et al.*, 2004, Gahlert *et al.*, 2007, Schliephake *et al.*, 2010, Aboushelib *et al.*, 2013b). A non-invasive manufacturing technique to produce a *de novo* rough surface was proposed to ameliorate the issues with subtractive surface treatment, i.e. implants were manufactured using *CIM* process. Here, a roughened inner surface of the mould produced a zirconia surface that exhibited higher osseointegration capacity when compared to smooth zirconia and machined titanium implants (Park *et al.*, 2012a).

Injection-moulded zirconia implants that are further treated with a novel, patented acid etching technique (*MDS*) have been recently introduced (Maxon Dental Surface, Maxon Motors GmbH, Germany). Viability of fibroblasts increased by 1.3 folds with zirconia implants that received *MDS* treatment when compared to machined titanium and zirconia implants (Christiane *et al.*, 2012). Additionally, an animal study revealed a high level of osseointegration and soft tissue integration when compared to machined titanium and zirconia implants (Mai *et al.*, 2012, Gredes *et al.*, 2014).

The present study aims to compare the surface characteristics of a *SLActive-like* titanium and *MDS* zirconia surfaces as well as the biofunctional response of fibroblasts and osteoblasts toward these surfaces.

4.2 Experimental Procedures and Results

4.2.1 Sample preparation

The topography and chemistry of *cpTi* (grade II) was altered to produce a surface comparable to the commercially available SLActive[®] surface. An 18 mm diameter grade II *cpTi* rod was supplied from a metal manufacturer (Schröder Plating Service, The Netherlands). The rod was milled to a 15.6 mm diameter which is a similar diameter to the bottom of a well in a 24-well cell culture plate. The rod was sliced to produce 1.5 mm thick discs using tungsten carbide points (J.S. Precision Engineering Ltd, UK).

Discs were mounted to custom plastic holders using double-sided adhesive tape (Struer, UK). Discs were mirror polished using Tegamin preparation system-20 (Struer, UK). The process comprised of 4 stages, plain grinding, fine grinding, polishing and oxide polishing. Various stages and products used are shown in details in Table 16. Optical microscopy at ×1000 magnification using Dark Field and Differential Interference Contrast was used to assess levels of remaining deformation (BXiS, Olympus, UK). Figure 77 shows a representative mirror-polished sample.

Table 16.. Polishing stages and sequence used prior mechanical and chemical titanium surface treatment

<i>Stage</i>	<i>Cloth</i>	<i>Speed</i>	<i>Suspension</i>	<i>Suspension pre-dosing</i>	<i>Suspension dosing</i>	<i>Lubricant</i>	<i>Force</i>	<i>Time</i>
<i>Plain grinding</i>	<i>Silicon Carbide 320</i>	<i>150</i>	<i>-</i>	<i>-</i>	<i>-</i>	<i>Water</i>	<i>25</i>	<i>Until flat</i>
<i>Fine grinding</i>	<i>MD-Largo</i>	<i>150</i>	<i>DiaPro Allegro/Largo 9μm</i>	<i>1</i>	<i>10</i>	<i>-</i>	<i>20</i>	<i>7.5</i>
	<i>Allergo-Largo</i>	<i>150</i>	<i>DiaPro Largo 3μm</i>	<i>1</i>	<i>10</i>	<i>-</i>	<i>20</i>	<i>4</i>
<i>Polishing</i>	<i>MD-Plan</i>	<i>150</i>	<i>DiaProPlan 3mm</i>	<i>1</i>	<i>9</i>	<i>-</i>	<i>15</i>	<i>3</i>
	<i>DP-Plan</i>	<i>150</i>	<i>DiaProDur 1μm</i>	<i>1</i>	<i>9</i>	<i>-</i>	<i>15</i>	<i>3</i>
<i>Oxide polishing</i>	<i>MD-OP</i>	<i>150</i>	<i>OP-S 0.04 mm</i>	<i>-</i>	<i>-</i>	<i>5% H₂O₂</i>	<i>35</i>	<i>10</i>



Figure 77. Mirror polished grade II *cpTi* discs.

Mechanical and chemical modification to produce *SLActive-like* surface was done according to the following procedure:

- Polished discs were thoroughly washed with concentrated acetone and then cleaned with distilled water in ultrasonic bath.
- Discs were then dried and pickled in a solution of 10% HNO₃, 2% HF and 2% NH₄F (1:1:1) for 30 sec at 55 °C. Discs were then washed with distilled water and pickled again in a solution of 10% HNO₃, 2% HF (1:1) for 30 sec at room temperature. Appearance of representative discs at this stage is shown in Figure 78.
- Discs were sandblasted with grade 60, 250 μm diameter aluminium oxide abrasive particles at a 5 cm distance and pressure equal to 2 bar until their surfaces appeared consistently grey as shown in Figure 79 (John Winter Foundry, UK).
- Discs were cleaned in concentrated acetone using ultrasonic bath for 30 min.
- Discs were placed in a Pyrex[®] beaker and topped with a solution of distilled water, fully concentrated HCl and H₂SO₄ (1:2:1). The beaker was heated to 100 °C and the temperature was maintained for 5 min. The whole procedure was performed in a fume hood.
- Discs were retrieved and placed in a CaOH solution and then cleaned thoroughly with distilled water in ultrasonic bath for an hour. Discs were placed in fresh ultrapure water and kept in anaerobic cabinet purged with N₂

gas for 3 hours along with open test tubes containing isotonic NaCl solution to extract any remaining oxygen or CO₂ in the liquids (Concept 1000, Russkin, UK).

- Discs were then cleaned in the ultrasonic bath using the degassed ultrapure water for an hour. Discs were retrieved and left to dry then placed in test tubes containing NaCl. Tubes were sealed using an air-tight screw lid.
- Samples were sent for an outreach facility to receive gamma radiation sterilisation with dose range of 25-40 kGrey for 12 hours (Xiros, UK).



Figure 78. Grade II *cpTi* discs after two acid pickling cycles .



Figure 79. Sandblasted *cpTi* discs with Alumina abrasive particles (250-500µm).

Injection moulded zirconia samples used in this project had two different surface topographies; one was as rough as the inner surface of the mould used for manufacturing ‘*Zr-M*’ and the other was further chemically roughened using a patented acid etching technique ‘*MDS*’. The samples were supplied by the manufacturer in the form of 15.41 ± 0.02 mm diameter and 1.01 ± 0.016 mm thick discs

(Maxon motor GmbH, Germany). All discs were ethylene oxide sterilised and stored in sealed plastic bags until they were used.

4.2.2 SEM characterisation

High performance cold field emission **SEM** was used to examine surface topography of representative samples from **Zr-M**, **MDS** and **SLActive-like** surfaces (SU8230, Hitachi, Japan). Additionally, **EDS** was used to characterise elemental composition of the three surfaces (Aztec Energy, Oxford Instruments, UK). The system is equipped with silicone drift detector (X-Max[®]) and pulse processor (X-Stream-2) (Oxford Instruments, UK). Data was analysed using sophisticated elemental analysis software (AztecEnergy, Oxford Instruments, UK).

EDS analysis of injection moulded zirconia samples (**Zr-M**) surface revealed weight percentage of 73.37%, 23.72%, 1.95%, 0.61% and 0.35% of the following atoms; Zr, O, Y, Hf, and Al, respectively (Figure 80).

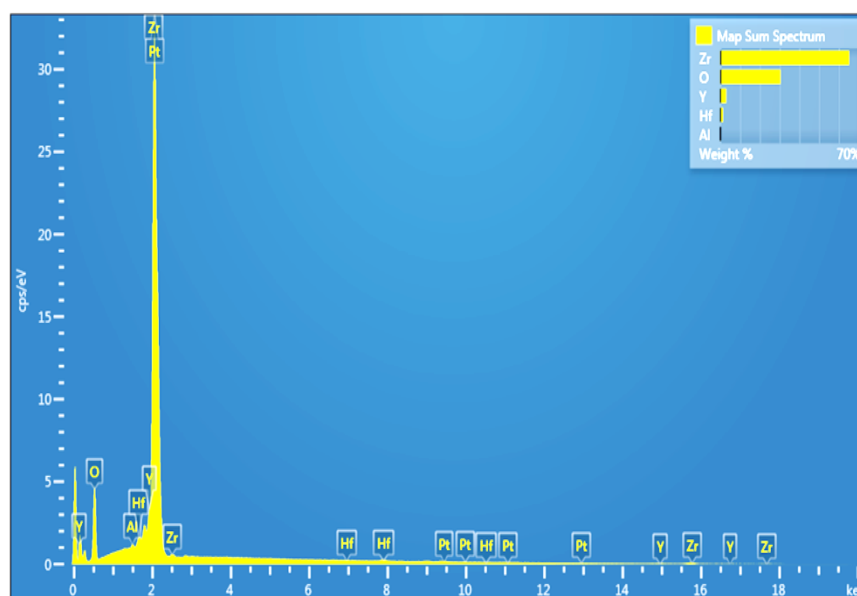


Figure 80. **EDS** spectrum of **ZR-M** zirconia surface.

SEM analysis revealed that the (**Zr-M** group) had slightly microstructured surface. Grooves and 10-15 μm diameter micropores could be detected under lower magnifications. At higher magnifications, the material exhibited a homogenous appearance with fine crystalline structure with clear crystal boundaries and tightly closed inter-crystal spaces (Figure 81).

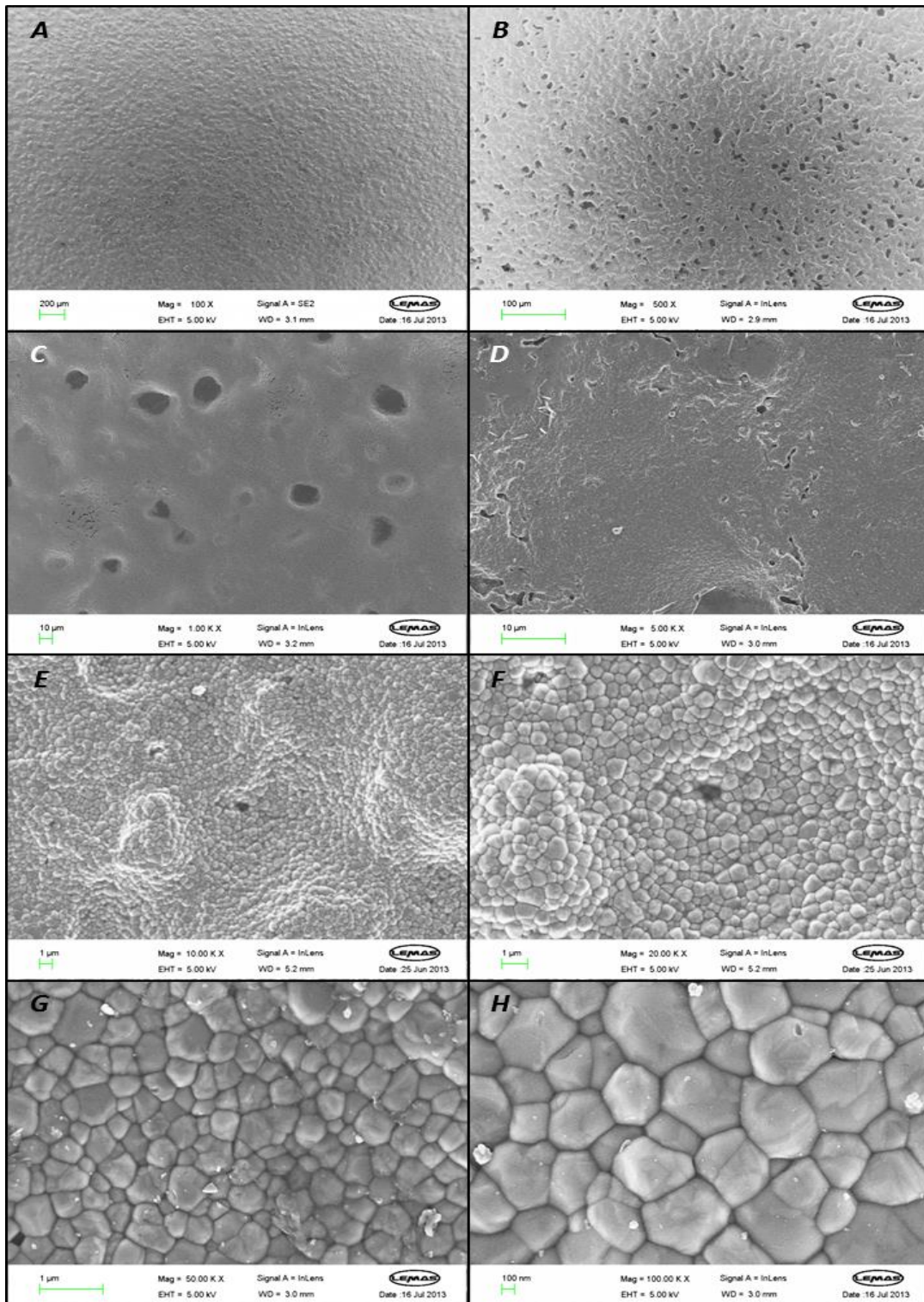


Figure 81. **SEM** examination of **Zr-M** disc surface.

Low magnification revealed minimally rough surface (A) with limited surface micropores (B). Medium magnifications demonstrated 10-15 μm diameter micropores (C). Higher magnification revealed waviness of the **Zr-M** surface (D, E & F) as well as homogenous and highly compacted equiaxial crystals (G&H).

Acid etching of the studied zirconia material (*MDS* group) was very effective in altering surface topography of zirconia discs and implants. Microscopically, the size and density of micropores grooves. However, the effect of acid etching was more significant at the crystalline level or nano-scale where; (1) significant dislodgment of superficial crystals was noticed, (2) loss of the homogenous crystal outline, (3) notable decrease in grain size and (4) subsequent and enlargement of the inter-crystal distant in comparison to *Zr-M* group (Figure 82 and 83).

Surface topography of *MDS* discs was compared to that for the commercially available implants and both specimens had highly similar topographies (Figure 84). Acid etching treatment did not induce any noticeable change in the elemental composition of the studied sample as indicated by the *EDS* analysis. *EDS* spectrum of *MDS* surface was identical to that for *Zr-M* presented in Figure 80.

In *SLActive-like* surface, *EDS* elemental analysis revealed weight percentage of 80.61%, 12.46%, 6.27% and 0.65% for Ti, O, C and Al respectively. The traces of Al were very likely to be sandblasting particles that cleaning in ultrasonic bath failed to dissociate from the titanium disc surface. The detected signal from C atoms indicated CO₂ adsorption and organic contamination with subsequent formation of various carbonate or hydrocarbon compounds as a result of exposure to air while the sample was transferred to the microscope (Figure 85).

The studied *SLActive-like* surface appeared significantly rougher than *Zr-M* and *MDS* groups. Large-grit sandblasting rendered the *cpTi* surface very irregular. The effect of the sandblasting was noticed as deep, large craters with very sharp and elevated boundaries. Furthermore, warm acid-etching produced smaller micropits (~1µm in diameter) within the craters (Figure 86).

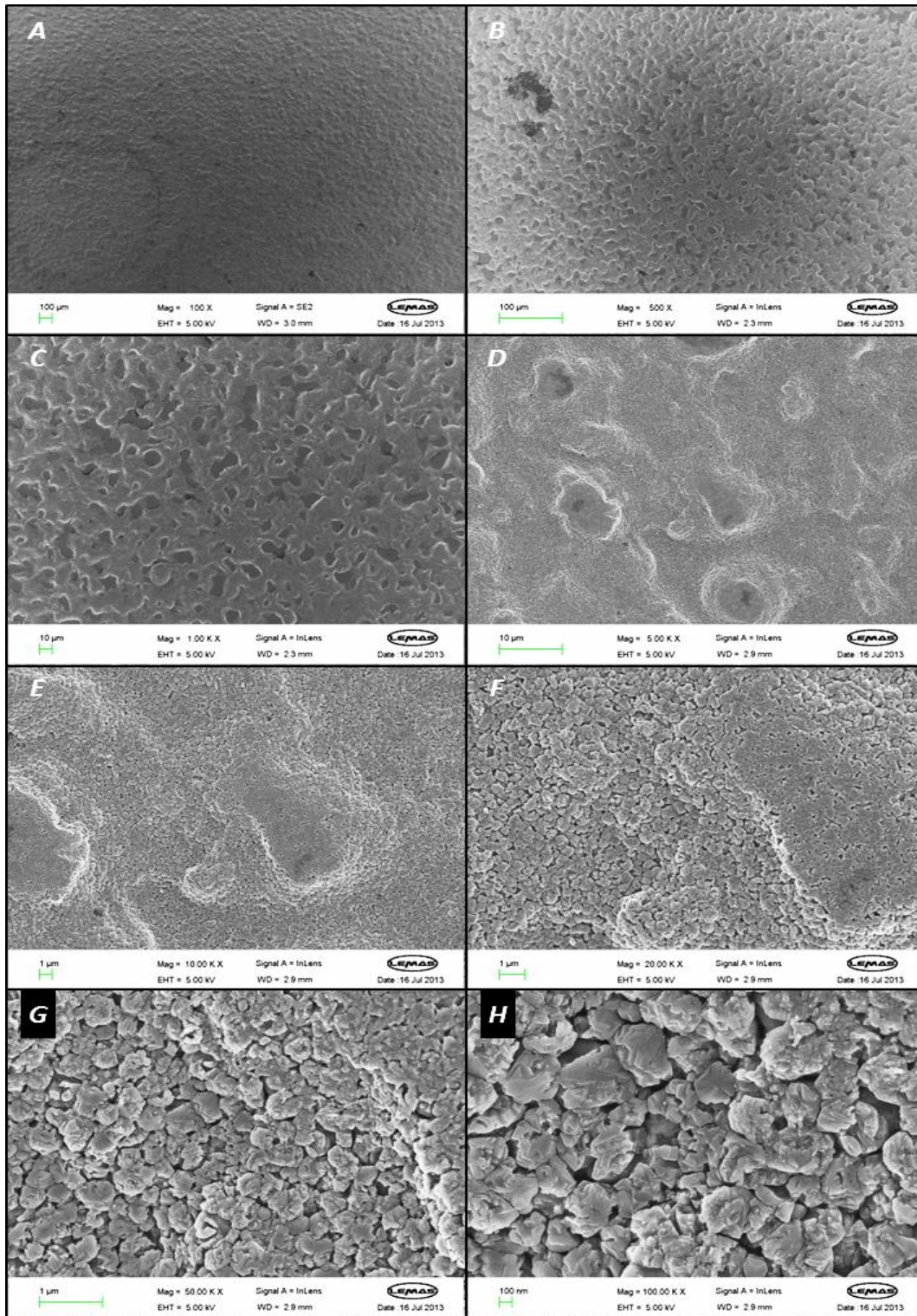


Figure 82. **SEM** examination of **MDS** disc surface.

Low magnification revealed highly rough surface (A) with abundant surface micropores (B). Medium magnifications demonstrated 20-25 μm diameter, hour-glass like surface irregularities (C). Higher magnification revealed significant peak and valley surface texture (D, E & F). High magnification images revealed significant alteration of crystal outline and increase of inter-crystal spaces as a result of acid etching process (G&H).

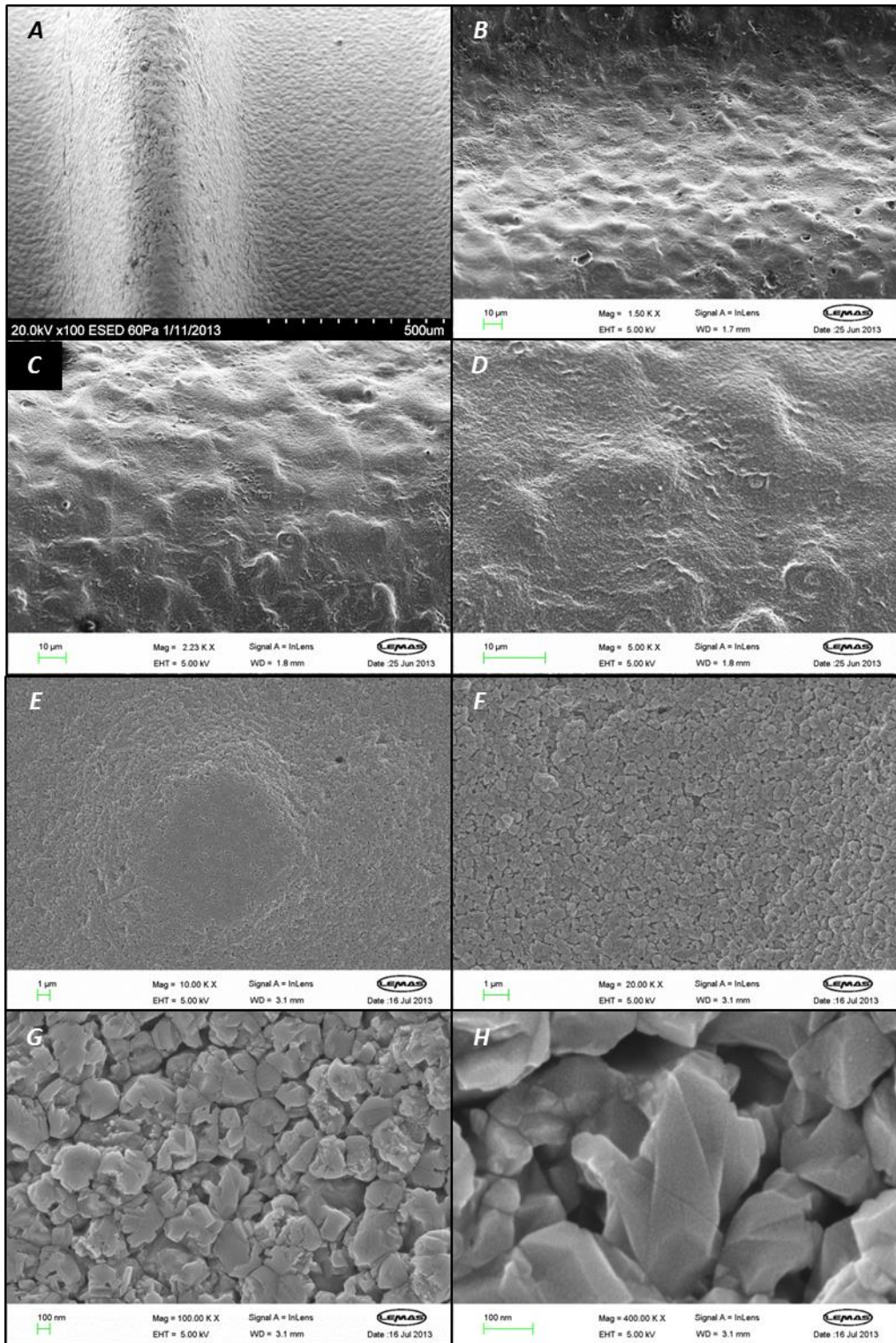


Figure 83. **SEM** examination of Zirconia implant surface.

Surface of the studied implant exhibited similar topographical features to the **MDS** discs. The difference in the surface appearance under medium magnifications (B, C & D) can be attributed to the difference in the orientation of the surface between implant thread and flat **MDS** disc.

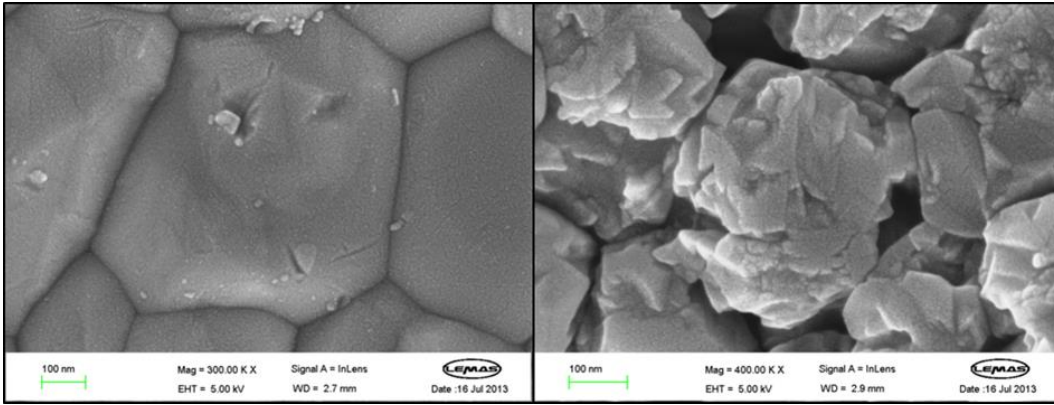


Figure 84. Comparative *SEM* views for *Zr-M* and *MDS* surfaces.

Single crystal, high magnification *SEM* image for *Zr-M* surface (*left*) and *MDS* surface (*right*) demonstrating the significant effect of the acid etching treatment on crystal shape and outline

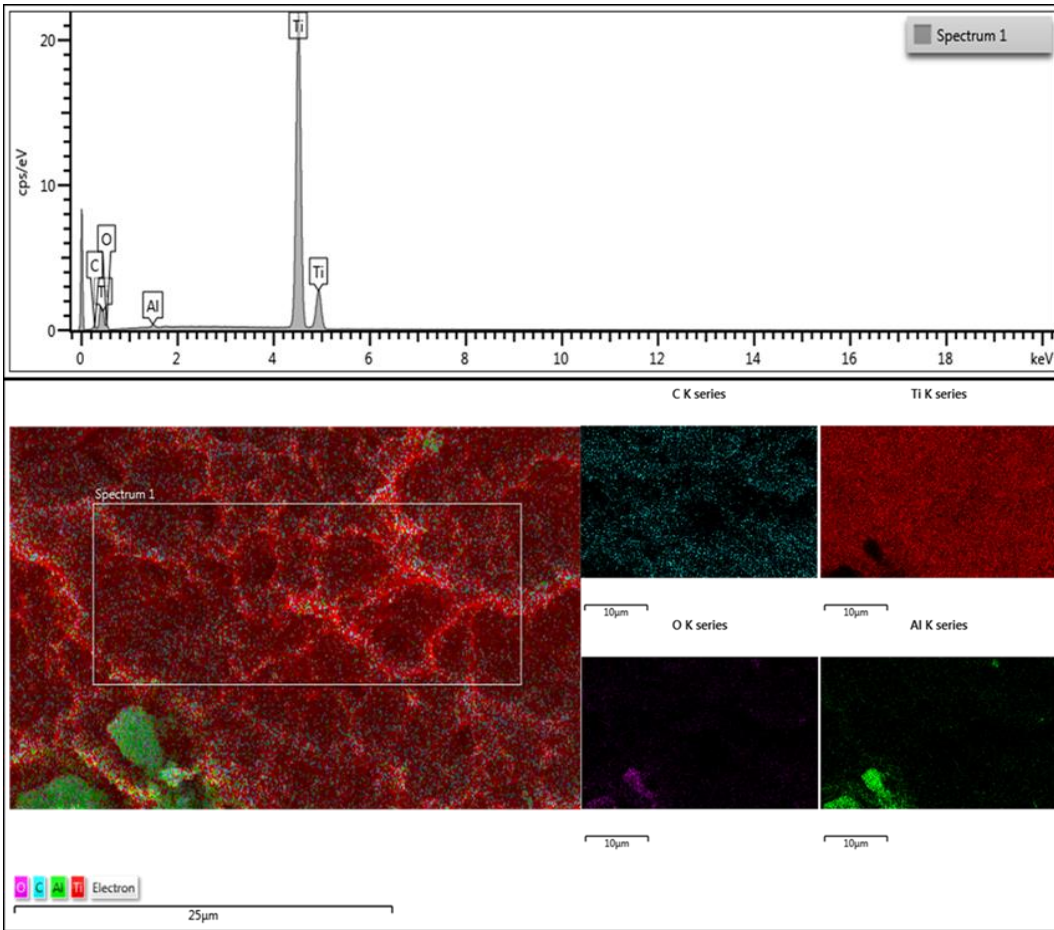


Figure 85. *EDS* analysis of *SLActive-like* surface.

Top, *EDS* spectrum for *SLActive-like* surface with strongest titanium peak. *Bottom*, elemental map of representative area within *SLActive-like* surface. The isolated cluster of Al_2O_3 is very likely attributed to alumina sandblasting particle that was not dissociated despite rigorous cleaning method.

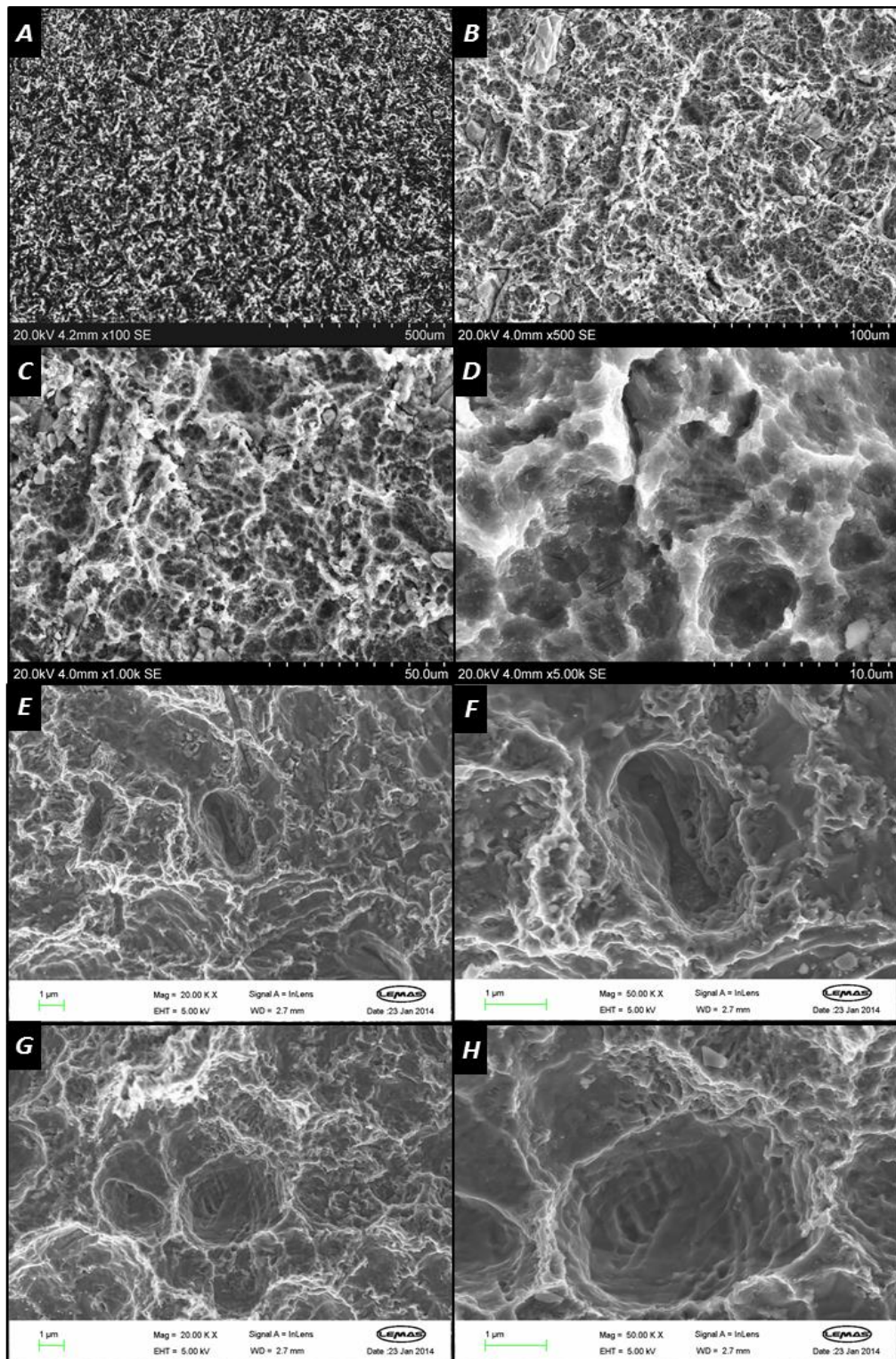


Figure 86. *SLActive-like* titanium surface topography under *SEM*

Highly rough surface under low magnification (A, B & C). Hierarchically, several level, ordered structure where larger concavities created by sandblasting (D) embraced smaller round micropits created by the warm acid attack (E-F & G-H).

4.2.3 Surface roughness analysis: Confocal laser scanning microscopy

Confocal laser scanning microscopy (*CLSM*) has become a widely utilised tool for 3D surface topography characterisation and analysis. The wide application of *CLSM* in this field was parallel with the development of computer-based image processing systems. The basic principle of *CLSM* can be briefly described as follows; a laser beam from a laser source travels through an aperture or illumination pinhole and then focused using the microscope objective lens into a diffraction limited laser beam on the focal plane (surface) of an opaque sample. The depth (slice) of sample that is in focus produces the maximum reflection of light through the detector pinhole. However, the light scattered from defocused depths or areas is suppressed by reducing the pinhole size while imaging the defocused slices. This is in simple terms the basis of optical sectioning or the so called, depth-discriminated signal detection. Optical sectioning effectively enhances lateral resolution and enables acquisition of high-resolution optical images along the sample's z coordinate. The series of optical images are then reconstructed using the appropriate algorithms in order to create a topographical image (Jordan *et al.*, 1998).

In the present study, 3D topographic maps were obtained from five regions of interest widely distributed at the surface of each disc from *Zr-m*, *MDS* and *SLActive-like* groups (n=10 per group). Discs were individually placed on glass slides and mounted at the stage of a *CLSM* with the treated surface facing upward (TCS SP II, Leica, Germany). A 100 mW Argon laser source was used in reflection mode to acquire x-y scans along z coordinate of the sample (488 nm blue, 568 nm green, 647 nm red). The laser beam was focused on the surface of the sample using $\times 10$ microscope objective and the numerical aperture was set at 0.3 (10/0.3NA). Scan velocity was adjusted to 400 Hz and the window format was set to 512 \times 512 pixels. The vertical acquisition was performed at 1 μm step size by moving the stage in the z direction between the positions where brightest and darkest images were obtained (40-150 μm studied thickness, 40-150 optical sections).

Topographical image was reconstructed from the obtained optical sections. Roughness parameters were measured for 1 mm^2 region of interest at five different positions at the surface of each sample (Leica Confocal Software, Germany). Table 17 summarises the studied roughness parameters and their respective definitions.

Table 17. Roughness parameters and their definitions (Feng *et al.*, 2002)

Parameter	Abbreviation	Definition
Average (Swedish) height	H_{avg}	The roughness between two predefined reference lines. The upper line exposes 5% of the data, and the lower line exposes 90%
Arithmetical mean deviation.	R_a	The average roughness or deviation of all points from a plane fit to the test part surface. Available for profile and areal data.
Root-mean-square (RMS) roughness	R_q	The average of the measured height deviations taken within the evaluation length or area and measured from the mean linear surface. R_q is the RMS parameter corresponding to R_a
Maximum depth of valley	R_v	The maximum distance between the mean line and the lowest point within the sample. It is the maximum data point height below the mean line through the entire data set.
Maximum peak height	R_p	The maximum distance between the mean line and the highest point within the sample. It is the maximum data point height above the mean line through the entire data set.
Fold increase in surface area	S_a/S	Ratio between profiled surface area and the evaluated surface area

In the present study, the injection moulded (**Zr-M**) samples resulted in a moderately rough surface owing to the micro-textured inner surface of the used mould. Acid etching (**MDS**) unreservedly increased all surface roughness parameters. **SLActive-like** samples demonstrated highly rough and microtextured surfaces. Tables 18 summarises the mean values and standard deviations obtained for roughness parameters and S_a/S ratio for all experimental groups.

Table 18. Mean and standard deviation values of measure roughness parameters (μm) for all experimental groups

Parameter	Zr-M	MDS	SLActive-Like
H_{avg}	31.71 (4.24)	40.27 (6.51)	37.71 (5.49)
R_a	1.09 (0.09)	2.19 (0.22)	2.49 (0.34)
R_q	1.41 (0.11)	2.94 (0.27)	3.27 (.43)
R_v	4.08 (0.41)	7.15 (0.79)	6.72 (0.78)
R_p	12.94 (2.16)	24.92 (1.59)	30.71 (9.03)
S_a/S	1.31 (0.02)	1.56 (0.07)	1.48 (0.18)

Data from all parameters were assessed for normal distribution using Shapiro-Wilk normality test. Data points from all studied roughness parameters were normally distributed ($p>0.05$). However, test for homogeneity of variances (Levene's test) revealed significant difference in the variance of R_a , R_q , R_p and S_a/S ($p<0.05$). The means of these parameters were compared among different groups using non-parametric independent samples Kruskal-Wallis test. Post-hoc analysis was performed using Games-Howell test. H_{avg} and R_v were normally distributed and had equal variances (Shapiro-Wilk and Levene's tests; $p>0.05$). Comparison of means was performed using ANOVA and post-hoc Tukey HSD test.

Statistical analysis revealed the following findings:

- There was no significant difference in the H_{avg} , R_a and R_q values between *MDS* and *SLActive-like* surfaces ($p>0.05$). However, these parameters were significantly higher in comparison to *Zr-M* group ($p<0.05$).
- *SLActive-like* surface demonstrated the highest mean maximum peak height (R_p) followed by *MDS* and *Zr-M* groups. The difference was statistically significant between all groups ($p<0.05$).
- *MDS* group demonstrated the highest mean maximum valley depth (R_v) followed by *SLActive-like* and *Zr-M* groups. The difference was statistically significant between all groups ($p<0.05$).
- *MDS* and *SLActive-like* surfaces resulted in significant increase in the S_a/S in comparison to *Zr-M* ($p<0.05$).

Representative, reconstructed, 3D images from regions of interest in two experimental surfaces are shown in Figure 87. The reconstructed images showed similar findings to those observed using *SEM*. *Zr-M* exhibited moderately rough surface with scarce distribution of micropores. *MDS* treatment resulted in a significantly rougher surface with increased density and diameter of the micropores and valleys. The reconstructed images for *SLActive-like* samples were very dark and could not be printed properly and thus, not included in the report.

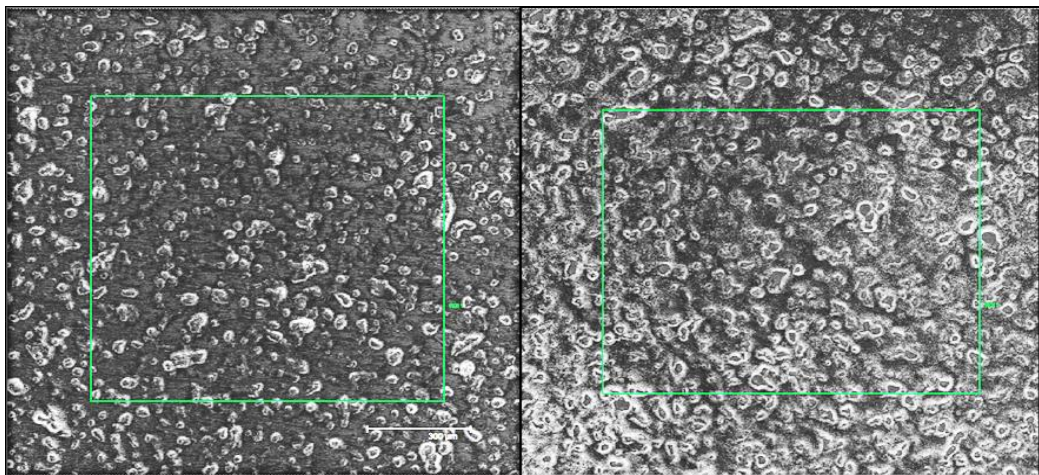


Figure 87. Representative 3D reconstructed topographical images for *Zr-M* (left) and *MDS* (right).

4.2.4 Water contact angle measurements

Once the implant is in contact with body fluids and tissues, a series of dynamic physico-chemical changes occurs at the implant surface. The formation or the increase of the already existing, oxide layer is the hallmark of chemical changes that take place immediately after implantation. The adsorption of body fluids and proteins to the implant surface is a key factor on the biological response around the implant and has a major role in the formation of cell–biomaterial interface (Anselme *et al.*, 2000, Rupp *et al.*, 2004).

Surface wettability is a major determinant in protein adsorption, cell attachment and migration processes (Rupp *et al.*, 2004). It describes the ability of a liquid to spread on a solid surface. Wettability is a result of interactions between the cohesive forces between the molecules of the liquid in air or liquid-air surface tension (σ_l), critical surface energy at the solid-air interface (σ_s) and solid/liquid interfacial tension (σ_{sl}) (Bico *et al.*, 2002, Sobczak *et al.*, 2007, Van Noort, 2014). Wettability can be evaluated by the angle formed between a given surface and liquid drop which is known as, the contact angle (θ). It is given for a flat homogeneous solid by Equation (25), originally described by Young (Young, 1805);

$$\cos \theta = \frac{\sigma_s - \sigma_{sl}}{\sigma_l} \quad (25)$$

Alteration of surface topography may efficiently reduce the contact angle and allow penetration of a liquid front into the micro-textured surface to fill all the roughness cavities (Bico *et al.*, 2002).

In the present study, distilled water contact angles on **Zr-M**, **MDS** and dried **SLActive-like** surfaces were measured at room temperature (22 °C). A CAM200 goniometer (KSV Instruments, Finland) was used perform equilibrium contact angle measurements ($\pm 0.1^\circ$ precision) in a closed glass chamber to reduce evaporation. Computer-controlled, motorised syringe was used to dispense 5 μ l sessile droplets on the surface of the sample. The needle was removed from the droplet and the equilibrium contact angle measurement was performed 2 sec after the release of the needle. The measurement was performed four times on 10 different discs from each group. Images were processed using CAM 200 software (KSV Instruments, Finland).

The mean equilibrium contact angle measurements were not obtained for *SLActive-like* surface as the distilled water droplet radially spread over the surface as demonstrated in a Video included in the CD. The equilibrium contact angle was assumed to be 0°. *Zr-M* exhibited moderately high equilibrium contact angles ranging from 76.16-90.99° with a mean value of 83.62±4.53°. *MDS* group exhibited significantly lower equilibrium contact angle ranging from 32.66-52.81° with mean value of 44.43±4.85° (Independent Samples Mann-Whitney test: p<0.05).

Figure 88 show representative equilibrium contact angle measurements in *Zr-M* and *MDS* groups. In both groups, contact angles measurements seemed to be widely dispersed as can be seen from the relatively large standard deviation. This may indicate lack of surface homogeneity within each disc and among the discs from the same group.

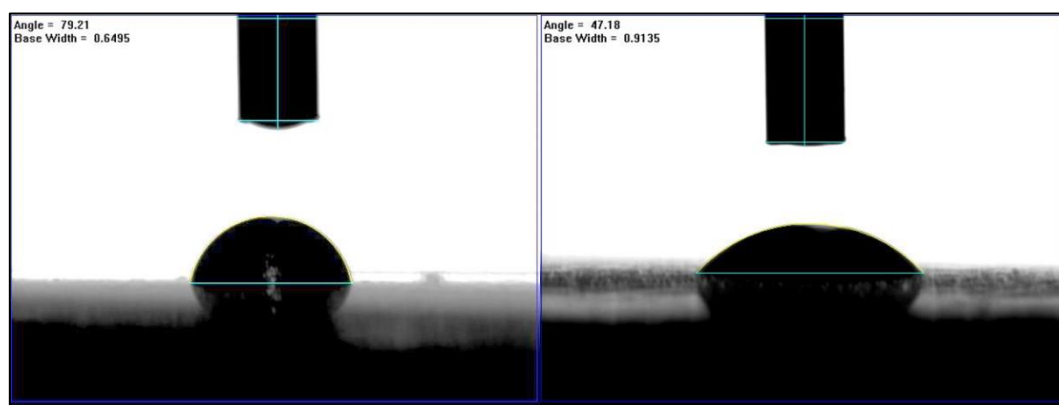


Figure 88. Contact angle measurements for *Zr-M* (left) and *MDS* (right).

4.2.5 Cell proliferation and viability studies

Biocompatibility is a widely used generic term in biomaterials sciences. The success of biomedical implants is extensively dependent on the biocompatibility of used materials (Hanker and Giammara, 1988). The term describes the ability of the material to maintain the host response within the tolerance of the biologic tissue without possessing toxic or injurious effects upon implantation in biological systems (Williams, 1999). This can be ensured by testing all materials intended for biomedical use *in vitro* and *in vivo* to demonstrate that they are unable to provoke or initiate inflammatory, allergic, immune, toxic or neoplastic processes (Hisbergues *et al.*, 2009).

The technical or procedural definition of biocompatibility of implant materials encompasses the ability of the material to prove biological safety through several biological tests (ISO10993-1, 1992). *In vitro* cytotoxicity is among the most important studies in this field. The integration of an implant with its surrounding tissues is highly dependent on the cells in the vicinity of the implant. Thus, viability and optimum biological function of cells in the vicinity of biomedical implants are the most fundamental pre-requisites for success of any implantation procedure. For dental implants, fibroblasts, osteoblasts and immune cells within blood are of concern as they are the most abundant cell types in peri-implant soft and hard tissues (Hisbergues *et al.*, 2009).

ISO 10993 describes direct and/or indirect cell contact tests for *in vitro* cytotoxicity (ISO 10993, 1992). Such techniques can provide quantitative and qualitative analytical techniques to study the biocompatibility of implant materials. Such tests can provide information regarding cell number, proliferation potential, migration capacity and cell viability. These tests are considered as initial screening methods and should be followed by more comprehensive and sophisticated *in vivo* animal studies prior proved suitable for clinical application.

The present study evaluated the proliferation capacity and viability of primary human gingival fibroblasts and human osteosarcoma cells upon the direct incubation on zirconia, titanium and tissue culture plastic surfaces for various periods of time.

4.2.5.1 Cell culture procedures

Human gingival fibroblasts (*HGF*) were purchased from Biological Products and Solutions (Innoport, Spain). Cells were cryopreserved, harvested from a single donor and were delivered at passage 1 (5×10^5 cells, batch # 5846). The second cell type used in this study was human osteosarcoma cells from *G-292* cell line. Cells at passage 4 were obtained from the School of Dentistry, University of Leeds cell line reserve. Both cell types were amplified, serially passaged up to passage 6 and a sufficient cell number was preserved in liquid nitrogen from each passage number for future use.

Cell culture procedures were performed in a disinfected, class II tissue culture cabinet with sterile reagents. All cell cultures and cells seeded on experimental samples were incubated at 37°C, 5% CO₂ and at 95% humidity. T175 Corning plastic

cell culture flasks with gas exchange/filtered screw-type lids were used for cell amplification (Corning[®] Costar[®], The Netherlands). Cell culture medium, Dulbecco's modified eagle medium (*DMEM*), was mixed with 10 % fetal bovine serum (*FBS*) and 1 % penicillin/streptomycin antibiotics combination (Sigma-Aldrich, Poole, UK). This type of media already contained 2 mM of L-glutamate.

Cleavage of attached cells from tissue culture plastic or the experimental samples was performed using 0.25% trypsin 0.02% ethylene diamine-tetraacetic-acid (trypsin-*EDTA*) (Sigma-Aldrich, Poole, UK). Prior to application of trypsin/*EDTA*, culture medium was aspirated and adherent cells washed twice with 0.1 M phosphate buffer solution (*PBS*) (Lonza, Slough, UK) to eliminate any traces of *FBS* that might suppress trypsin/*EDTA* activity.

A suitable amount of trypsin/*EDTA* (5 ml) was applied for 5 min whilst the cells were kept in a tissue culture incubator at 37°C, 5% CO₂ and at 95% humidity. Trypsin/*EDTA* was inactivated by addition of *FBS*-containing culture medium; mixture was pipetted out to a 20 ml universal tube and then centrifuged at 200 ×g for 5 min to obtain a cell pellet for splitting (passaging) and freezing.

1×10⁴ cells were used for subsequent passages in each T175 flask. The remaining cells were frozen by mixing them with 10% Dimethyl sulfoxide (*DMSO*), 50% *FBS* and 40% *DMEM* (Sigma-Aldrich, Poole, UK). The cell suspension was pipetted out to 1.8 ml tubes that were placed in a sealed box containing isopropanol. The box was kept at -80 °C for 12 hours; cells were then transferred to liquid nitrogen. Cell growth, attachment or detachment as a result of trypsin/*EDTA* application was checked using a phase contrast microscope (AX 80, Olympus, UK). Cells were passaged as they approached 70-80% confluence.

The studied *HGF* cells appeared to have sharp, bipolar, elongated spindle shape when examined under light microscopy. *HGF* cells seemed to grow in parallel clusters at the stage of 70-80% confluence. In contrast, *G-292* cells were significantly smaller in size. They exhibited multipolar, stellate appearance. Figure 89 demonstrates representative *HGF* and *G-292* appearance under light microscopy at 70-80% confluence stage.

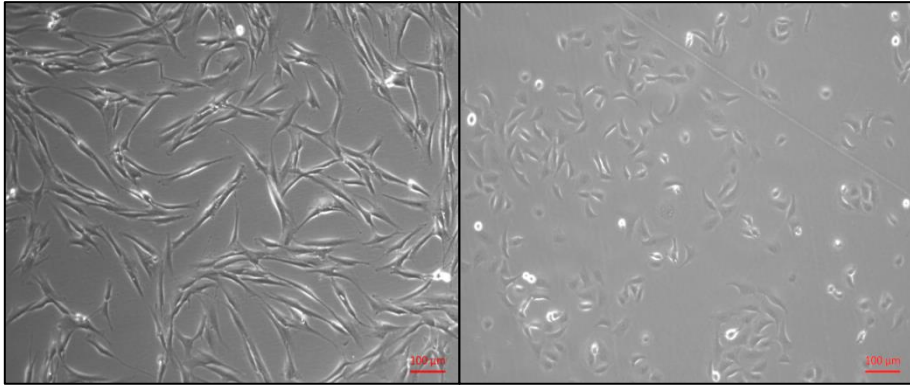


Figure 89. *HGF* (left) and *G-292* (right) cells used in this study at 70-80% confluence stage.

Zr-M, *MDS* and *SLActive-like* discs were snugly fitted in the bottom of 24 cell culture well plates (Corning® Costar®, The Netherlands) in a cell culture cabinet (while wearing surgical sterile gloves and using sterile forceps). The efficiency of the seal between the disc borders and the walls of the well plate was checked by adding 1 ml of *DMEM* on top of the disc and checking the bottom side of the 24 well plate for any leakage. Samples with no leakage were used to seed cells on in order to prevent any cell loss or confounding effect from tissue culture plastic. *HGF* and *G-292* cells were seeded on three discs from each group with seeding density equals to 5×10^4 cell/well. Tissue culture plastic was used as a control as shown in Figure 90. A total amount of 2 ml of *DMEM* was added to each well. The cells were incubated for 24 hours, 1 week, 2 weeks and 3 weeks periods. Cells were harvested using three trypsinisation cycles with 5 min duration for each.

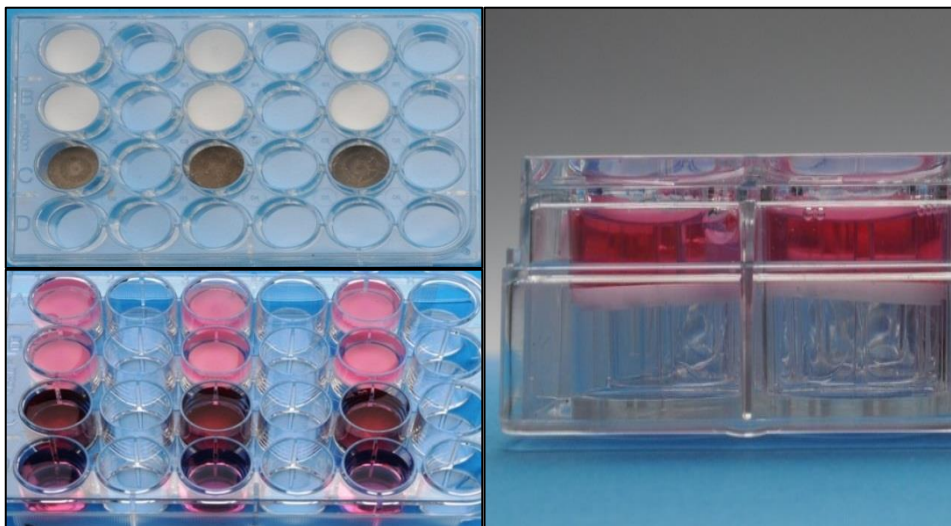


Figure 90. Setup of the tissue culture procedures. Top left, *Zr-M*, *MDS* and *SLActive-like* discs inserted in 24 well plates. Bottom left, Cells (*HGF*) seeded on the discs and control. Right, demonstration of the tight seal between the discs and walls of each well.

4.2.5.2 Assessment of cell proliferation

Proliferation refers to the increase of cell number as a result of cell growth and replication. Biocompatible materials are not supposed to adversely affect the cell proliferation. Rather, implantable materials should provide a platform for cells from adjacent tissues to proliferate and differentiate in order to achieve successful tissue integration. At the level of bone tissue, this feature is known as osteoconductivity. Both zirconia and *cpTi* materials have osteoconductive properties which can be further modified by alteration of surface topography (Al-Nawas *et al.*, 2008).

After each incubation period, the total number of cells was calculated by counting the floating cells in the culture medium as well as the trypsinised cells. Scepter™ 2.0 hand held automated cell counter fitted with 40 µl Scepter sensors was used for cell counting (Merck Millipore, UK). Total cell counts were obtained for five samples from each group and a mean total cell number was calculated. Cell doubling time was calculated using an online tool (Roth, 2006).

After 24 hours incubation period, *HGF* cells exhibited the highest proliferation capacity in *MDS* and control groups. One way ANOVA and Tukey HDS post-hoc analysis revealed no significant difference in the mean total *HGF* count between these groups ($p>0.05$). Total *HGF* count in *MDS* and control was significantly higher in comparison to *SLActive-like* and *Zr-M* ($p<0.05$). There was no statistically significant difference in the mean total *HGF* count between *SLActive-like* and *Zr-M* groups ($p>0.05$). With regard to *G-292* cells, *MDS* group exhibited the highest proliferation rate when compared to all other groups ($p<0.05$). Control group had the second highest mean total *G-292* count which was significantly higher than *Zr-M* and *SLActive-like* groups. *Zr-M* exhibited higher mean total *G-292* count when compared to *SLActive-like* counterpart, however this difference was not statistically significant ($p>0.05$).

After 1 week incubation period, the *MDS* group had a similar mean total *HGF* count to the control groups ($p>0.05$). Both groups had significantly higher mean total *HGF* count when compared to *Zr-M* and *SLActive-like* ($p<0.05$). With regard to *G-292* cells, the control group exhibited the highest proliferation rate followed by *MDS*. The difference was not statistically significant ($p>0.05$) between the two groups. However, difference reached significance level when comparing control and

MDS with *SLActive-like* and *Zr-M* groups ($p < 0.05$). *SLActive-like* exhibited higher mean total *G-292* count when compared to *Zr-M* counterpart, the difference was not statistically significant, however ($p > 0.05$).

After 2 weeks incubation period, control group exhibited the highest proliferation rate ($p < 0.05$). Mean total *HGF* count for *MDS* group was not significantly different from *SLActive-like* and *Zr-M* ($p > 0.05$). However, *SLActive-like* group had significantly higher mean total *HGF* count when compared to *Zr-M* ($p < 0.05$). With regard to *G-292* cells, control group exhibited the highest proliferation rate when compared to all other groups ($p < 0.05$). *SLActive-like* group had the second highest mean total *G-292* count which was comparable to *MDS* (third) and *Zr-M* (lowest) groups ($p > 0.05$).

After 3 weeks incubation period, *MDS*, *SLActive-like* and control groups had comparable total *HGF* count ($p > 0.05$). *Zr-M* group exhibited the lowest mean total *HGF* count ($p < 0.05$). With regard to *G-292* cells, control group exhibited the highest proliferation rate followed by *MDS*, *SLActive-like* and *Zr-M*, respectively. There were statistically significant differences between the mean total *G-292* counts among all experimental groups ($p < 0.05$). Figure 91 summarises the mean total *HGF* and *G-292* cell counts at different incubation periods.

The mean doubling time of *HGF* and *G-292* cells was not significantly different when calculated for cells seeded on control for 24 hours ($p > 0.05$). *HGF* cultured on tissue culture plastic had the lowest doubling time followed by *MDS*, *Zr-M* and *SLActive-like* groups respectively. The difference was statistically significant between all the groups except *MDS* and *Zr-M* as well as *MDS* and control ($p > 0.05$). *G-292* cultured on *MDS* had the lowest doubling time followed by tissue culture plastic, *Zr-M* and *SLActive-like* groups respectively. The difference was statistically significant between all the groups except *SLActive-like* and *Zr-M* as well as *MDS* and control. Figure 92 summarises *HGF* and *G-292* mean doubling times for all experimental groups.

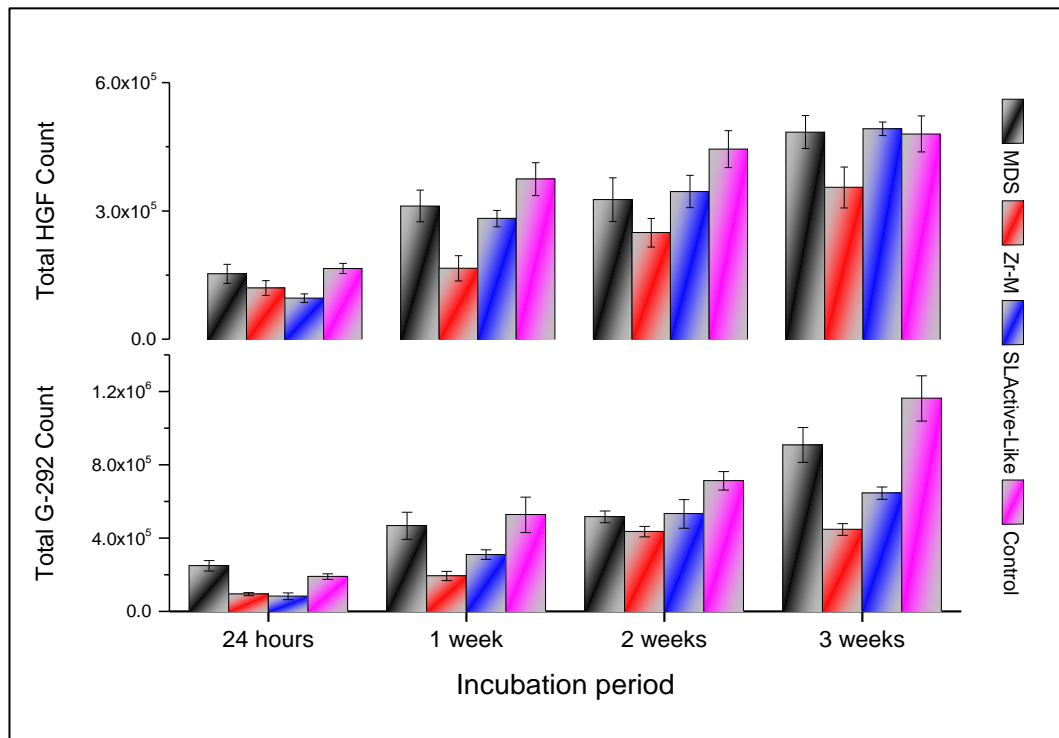


Figure 91. Total **HGF** and **G-292** counts.

Bar chart represents means and standard deviation of total **HGF** (top) and **G-292** (bottom) counts upon incubation on **MDS**, **Zr-M**, **SLActive-like** and **control** surfaces for 24 hours, 1 week, 2 weeks and 3 weeks (n=5). Initial seeding density was 5×10^4 cell/surface.

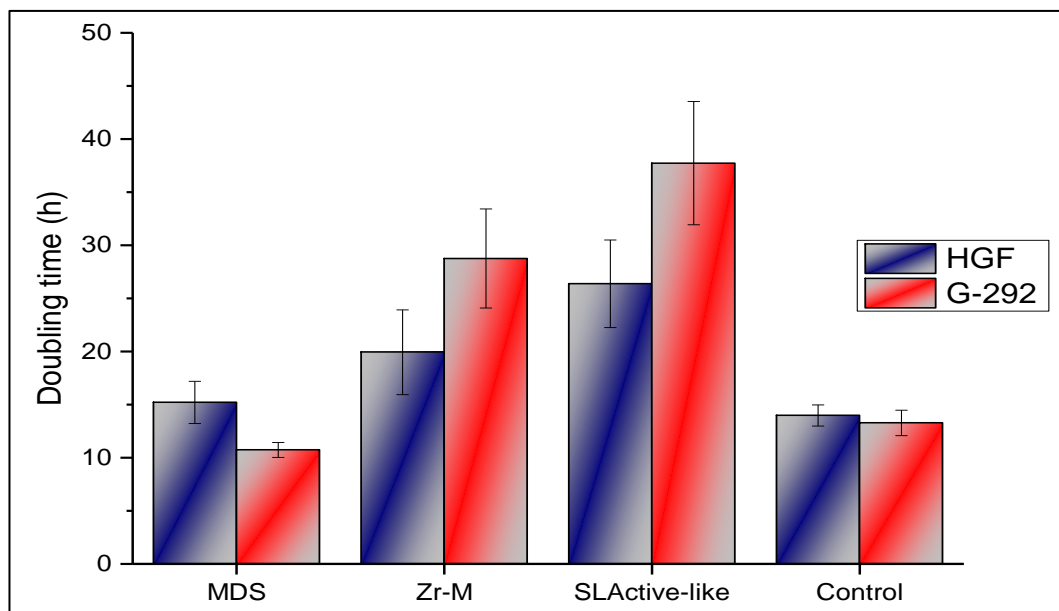


Figure 92. **HGF** and **G-292** doubling times.

Bar chart represents means and standard deviation of total **HGF** (blue) and **G-292** (red) doubling times upon incubation on **MDS**, **Zr-M**, **SLActive-like** and control surfaces for 24 hours (n=5). Initial seeding density was 5×10^4 cell/surface

4.2.5.3 Assessment of cell viability using flow cytometry

Flow cytometry is a versatile analytical platform that is used to perform quantitative, multiparametric analysis of physical and biochemical characteristics of cells including size, granularity, internal complexity and fluorescence intensity. A flow cytometer is comprised of fluidics, optics and electronics systems. The fluidics system acts as a vehicle to transport cells in a stream to the optics system. The latter is comprised of a laser beam that illuminates the cells in the sample stream. The scattered and fluorescent light signals are subsequently collected by lenses and then directed to the appropriate detectors by a series of beam filters and splitters. The electronics system converts the detected light signals into electronic signals according to how the cell scatters incident laser light and the intensity of the resulting fluorescence (BD Biosciences, 2000).

In the present study, a BD Biosciences LSRFortessa flow cytometer was used for cell viability analysis of various experimental groups (BD Biosciences, San Jose, CA). Flowing software version 2.5.1 was used to perform the throughput analysis (Turku Centre for Biotechnology, Finland). The aim of this experiment was to quantify the percentage of viable, pre-apoptotic, apoptotic and dead cells as a result of necrosis. The first step was to establish flow cytometry standards (*FCSs*) for these four cell conditions. In order to achieve the latter three conditions, *HGF* and *G-292* cells at a concentration of 5×10^4 cells/ml were treated as follows;

- To induce pre-apoptosis, cells were deprived of glucose by culturing them in *PBS* overnight.
- To induce apoptosis, cells were *UV* irradiated for 30 min.
- To induce necrosis, cells were incubated in a water bath at 60°C for 60 min.

Following these treatments, the dead cells (heated) were labelled with 10 μ l propidium iodide (*PI*) (Miltenyi Biotec GmbH, Bergisch Gladbach, Germany) from 1 μ g/ml *PI* solution. *PI* is a fluorescent molecule that binds to *DNA*. It is cell membrane impermeant and thus, can only stain cells with a disrupted cell membrane (dead cells as a result of necrosis or apoptosis). The apoptotic cells (*UV* irradiated) were washed with *PBS* and resuspended in 1 ml of Annexin V Binding Buffer (BioLegend, San Diego, CA), of which 100 μ L was transferred to a fresh microtube

before the addition of 5 µl Alexa Fluor[®] 647 conjugated Annexin V (BioLegend, San Diego, CA). Annexin V selectively binds to phosphatidylserine, a protein externalised to the surface of cytoplasmic cell membrane during apoptosis (pre-apoptosis). Additionally, 100 µL of apoptotic cell suspension was dual labelled with both Annexin V and *PI* (dead due to apoptosis). Samples were incubated in the dark at room temperature for 15 min prior to washing and resuspension in *PBS* or Annexin V Binding Buffer. These samples, in addition to an unlabelled negative control and single labelled viable cells were analysed. Unlabelled, single labelled and dual labelled samples were used to set acquisition parameters to reduce autofluorescence and potential channel crossover.

HGF and *G-292* cells cultured on *MDS*, *Zr-M*, *SLActive-like* and tissue culture plastic surfaces for 24 hours, 1 week, 2 weeks and 3 weeks were studied (n=3 per group). Floating and attached cells were harvested from various surfaces by aspirating the *DMEM* and 3 cycles of trypsinisation, respectively. Samples were centrifuged at 200×g for 5 min, washed with *PBS*, centrifuged again at 200 ×g for 5 min and resuspended in 1 ml Annexin V Binding Buffer to which 10 µl of *PI* was added. 100 µl of cell suspension was transferred to a fresh microtube to which 5 µl of Alexa Fluor[®] 647 conjugated Annexin V was added.

Samples were incubated in the dark at room temperature for 15 min before the addition of 400 µl of Annexin V Binding Buffer. Samples were then centrifuged at 200×g for 5 min before resuspension in 500 µl of Annexin V Binding Buffer prior to analysis in the flow cytometer.

Samples were gated based on forward and side scatter to exclude cellular debris from the analysis and were analysed for expression of *PI*, Annexin V and Alexa Fluor[®] 647. Measurements were made in triplicates for each experimental group. A minimum of 1×10^4 gated events were acquired for each sample. Figure 93 and 94 shows representative dot plots for *HGF* and *G-292* cells cultured on the four studied surfaces after 24 hours incubation period.

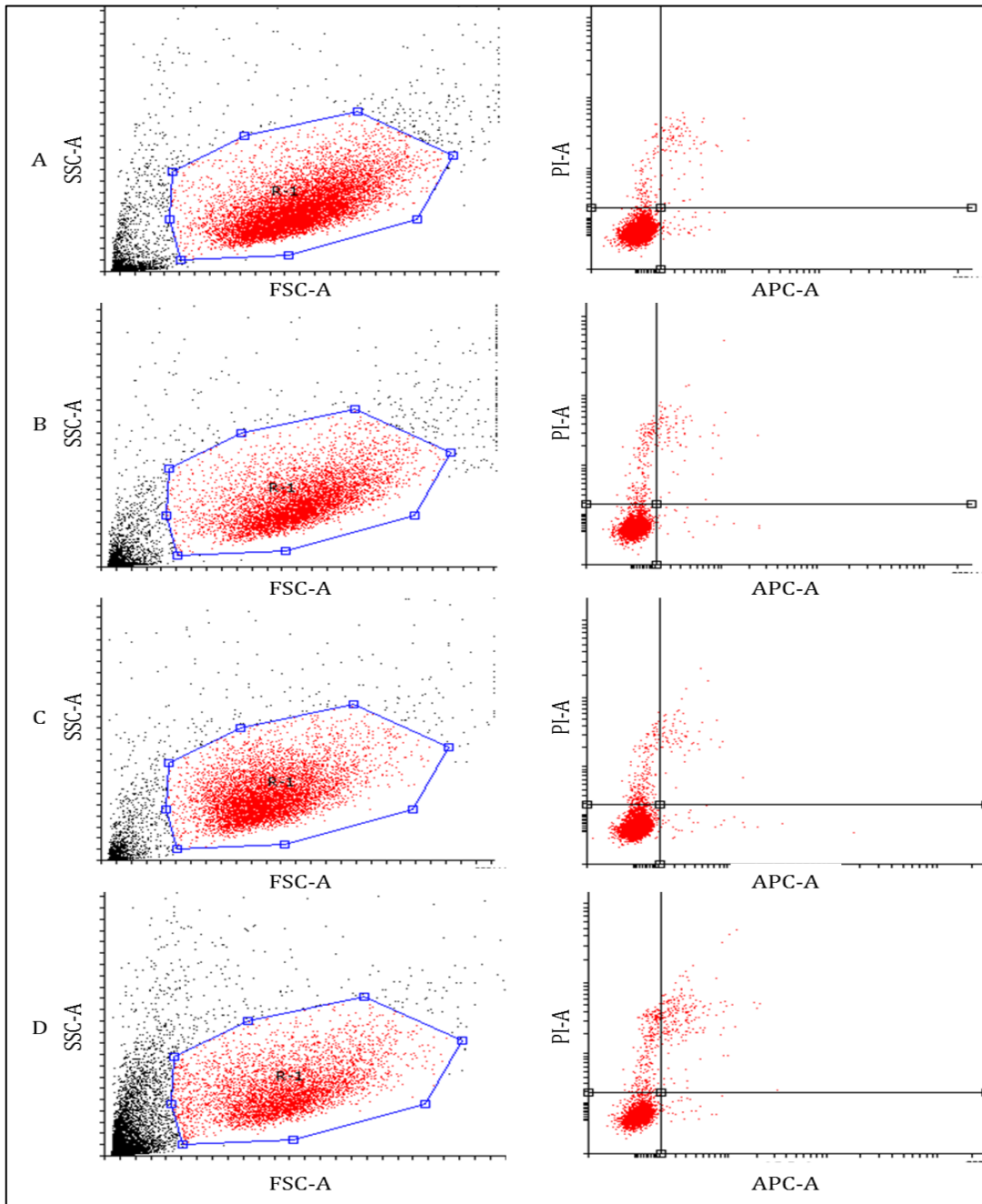


Figure 93. Representative flow cytometry output for *HGF* cells.

A, control, B, *MDS*, C, *Zr-M* and D *SLActive-like* surfaces after 24 hours incubation period. Within each row, dot plot at the left represents the total number of gated cells and particles. R1 is the region of interest contains the events that are more consistent with cell size (red dots). R1 was selected to exclude debris from analysis (black dots). Dot plots at the right represent data analysis. Top quadrants represent dead cells (*PI* positive) and bottom quadrants represent live cells (*PI* negative). Top left represents cells that died due to necrosis, top right represents apoptotic cells (*PI* and Annexin V positive), bottom right represent pre-apoptotic cells (Annexin V positive and *PI* negative) and bottom left represent viable cells (*PI* and Annexin negative).

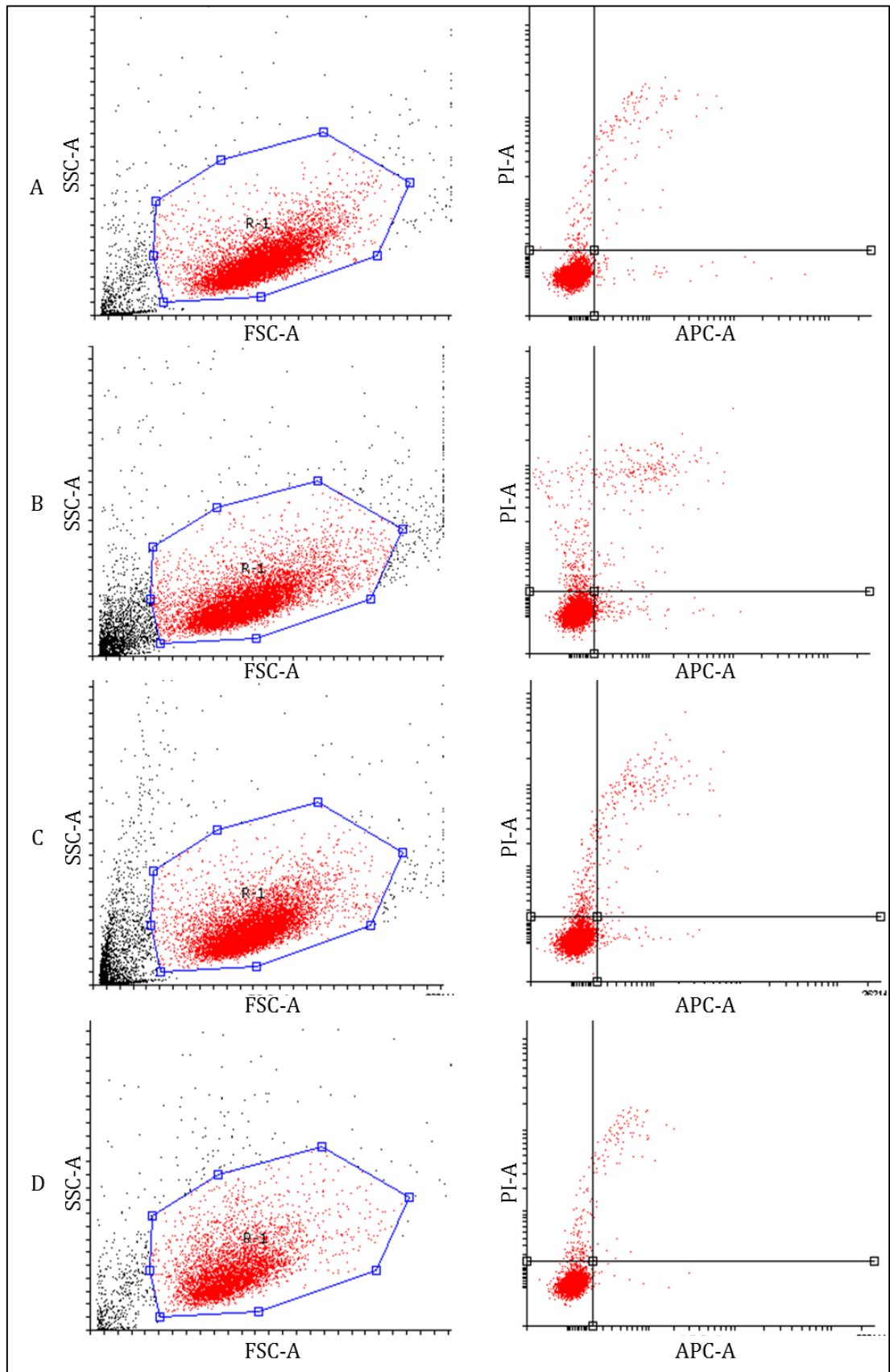


Figure 94. Representative flow cytometry output for *G-292* cells.

A, control, B, *MDS*, C, *Zr-M* and D, *SLActive-like* surfaces after 24 hours incubation period.

Several tests were used to perform statistical analysis on the flow cytometry data. Some of the data sets were not normally distributed and others did not have equal variances. Thus, a combination of tests was used including; independent sample Mann–Whitney U test, one-way ANOVA, Tukey HSD and Games-Howell post-hoc tests. Results from flow cytometry are summarised and presented in Figure 95 and Table 19.

All studied surfaces exhibited high cytocompatibility after all incubation periods (>87% viability). As far as *HGF* cells were concerned, *MDS* surface seemed to induce the least amount of cell necrosis. There were no statistically significant differences in viability percentage of all studied surfaces apart from marginal increase in *MDS* group after 3 weeks incubation period. With regard to *G-292* cells, roughness of zirconia had a notable impact on the percentage of viable and apoptotic cells at early stages. *MDS* was more biocompatible than smoother *Zr-M* counterpart. Moreover, *SLActive-like* surface had significantly higher viability percentage and lower pre-apoptosis, apoptosis and necrosis only at 2 weeks incubation period in comparison to other groups.

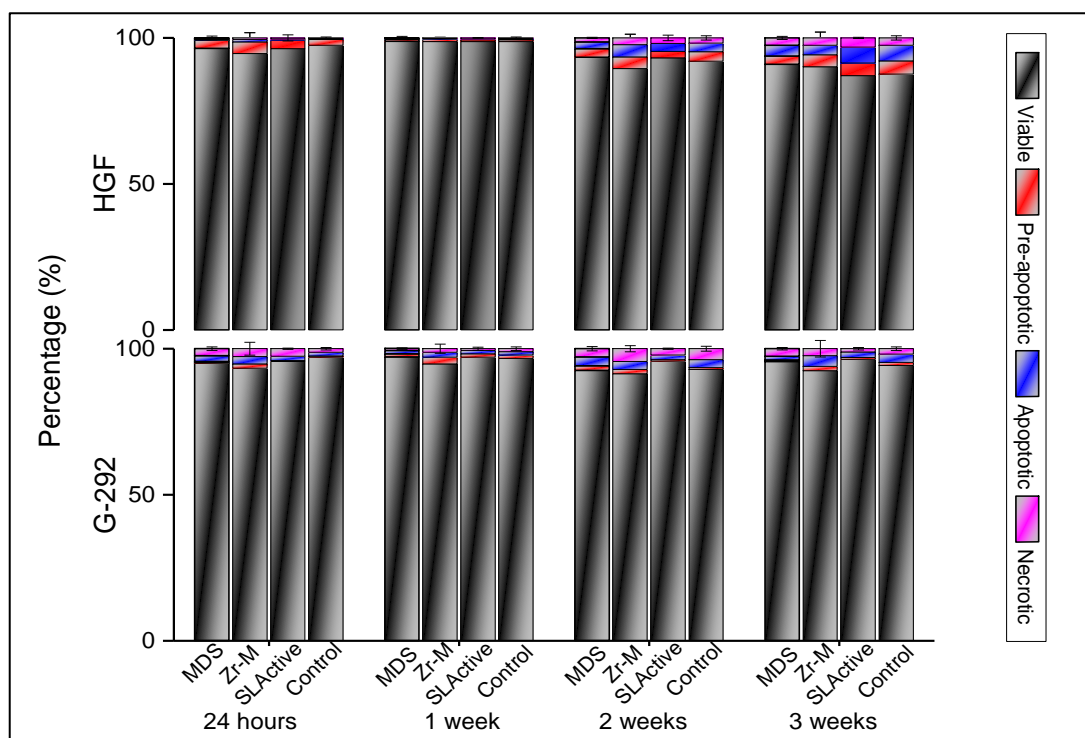


Figure 95. Biocompatibility of implant surfaces as per flow cytometry

Stacked bar chart represents the mean and standard deviation of percentage of viable, pre-apoptotic, apoptotic and necrotic *HGF* (top) and *G-292*(bottom) when cultured on *MDS*, *Zr-M*, *SLActive-like* and control surfaces for 24 hours, 1 week, 2 weeks and 3 weeks.

Table 19. Summary of flow cytometry data

Mean percentages (SD) of viable, pre-apoptotic, apoptotic and necrotic *HGF* and *G-292* cells upon exposure to various materials in comparison to control. Grey and black shaded values indicate $p=0.05$ and $p<0.05$, respectively..

<i>Viable</i>				<i>Pre-apoptotic</i>				<i>Apoptotic</i>				<i>Necrotic</i>				
<i>HGF</i>																
	<i>MDS</i>	<i>Zr-M</i>	<i>SLActive-Like</i>	<i>TCP</i>	<i>MDS</i>	<i>Zr-M</i>	<i>SLActive-Like</i>	<i>TCP</i>	<i>MDS</i>	<i>Zr-M</i>	<i>SLActive-Like</i>	<i>TCP</i>	<i>MDS</i>	<i>Zr-M</i>	<i>SLActive-Like</i>	<i>TCP</i>
<i>24 hours</i>	96.42 (0.60)	94.60 (1.81)	96.32 (1.06)	97.50 (0.27)	2.82 (0.09)	4.01 (0.61)	2.94 (0.12)	1.93 (0.09)	0.58 (0.09)	0.88 (0.61)	0.36 (0.12)	0.28 (0.09)	0.19 (0.05)	0.49 (0.09)	0.38 (0.04)	0.29 (0.03)
<i>1 week</i>	98.84 (0.10)	98.71 (0.25)	98.69 (0.15)	98.76 (0.27)	0.69 (0.03)	0.89 (0.08)	0.67 (0.06)	0.64 (0.14)	0.21 (0.03)	0.22 (0.08)	0.24 (0.06)	0.27 (0.14)	0.18 (0.01)	0.25 (0.05)	0.40 (0.04)	0.34 (0.08)
<i>2 weeks</i>	93.36 (0.39)	89.53 (1.23)	93.20 (0.96)	91.97 (0.78)	2.95 (0.35)	3.95 (0.51)	2.14 (0.60)	3.30 (0.25)	2.35 (0.35)	4.17 (0.51)	2.75 (0.60)	2.92 (0.25)	1.34 (0.28)	2.36 (0.12)	1.92 (0.28)	1.82 (0.45)
<i>3 weeks</i>	91.00 (1.24)	90.11 (1.99)	87.09 (0.18)	87.59 (0.72)	2.83 (0.64)	4.10 (0.71)	4.25 (0.22)	4.57 (0.51)	3.64 (0.64)	3.31 (0.71)	5.53 (0.22)	5.31 (0.51)	2.53 (0.43)	2.48 (0.43)	3.13 (0.39)	2.53 (0.31)
<i>G-292</i>																
<i>24 hours</i>	95.02 (0.64)	93.23 (2.16)	95.55 (0.26)	97.07 (0.44)	0.58 (0.15)	1.48 (0.22)	0.35 (0.03)	0.39 (0.10)	1.93 (0.17)	2.57 (1.08)	1.49 (0.27)	1.30 (0.24)	2.47 (0.40)	2.71 (1.83)	2.61 (0.20)	1.24 (0.32)
<i>1 week</i>	97.14 (0.27)	94.72 (1.55)	97.09 (0.48)	96.63 (0.62)	1.13 (0.13)	2.30 (0.80)	1.18 (0.43)	1.17 (0.41)	1.09 (0.14)	1.68 (0.54)	1.13 (0.15)	1.12 (0.16)	0.72 (0.26)	1.30 (0.25)	0.61 (0.10)	1.08 (0.16)
<i>2 weeks</i>	92.51 (0.73)	91.41 (1.03)	95.70 (0.25)	92.84 (0.84)	1.59 (0.14)	1.42 (0.21)	0.50 (0.17)	0.67 (0.10)	3.08 (0.61)	2.73 (0.34)	1.58 (0.23)	2.72 (0.49)	2.82 (0.21)	4.44 (1.10)	2.22 (0.18)	3.77 (0.35)
<i>3 weeks</i>	95.54 (0.46)	92.47 (2.79)	96.32 (0.44)	94.20 (0.59)	0.61 (0.14)	1.42 (0.43)	0.67 (0.22)	1.06 (0.04)	1.21 (0.40)	3.70 (2.13)	1.83 (0.36)	2.81 (0.10)	2.65 (0.87)	2.41 (0.58)	1.18 (0.15)	1.93 (0.46)

4.2.5.4 Expression profile of genes controlling osseointegration and periosteal integration

Osteoblasts play a key role in the osseointegration process where they are responsible for new bone formation. Several transcription factors orchestrate osteogenic differentiation and stimulate osteogenesis. Runt-related transcription factor 2 (***RUNX-2***) initiates the transcription and subsequent translation of many other genes responsible for extracellular matrix deposition during the early phases of osteogenesis. It is essential for proper execution of the osteogenic program (Drissi *et al.*, 2000). Bone morphogenetic protein 2 (***BMP-2***) is a transformation growth factor that potently induces osteogenic differentiation at early stages of osteogenesis (Chen *et al.*, 2004). Alkaline phosphatase (***ALP***) is an enzyme that is responsible for hydrolysing phosphate groups from proteins to provide inorganic phosphate to be used for bone mineralisation (Orimo, 2010). Osteocalcin (***OSCN***) is a non-collagenous extracellular matrix protein that is expressed during late stages of osteogenesis. Its expression is regulated by ***RUNX-2***, ***BMP-2*** and vitamin D₃. It regulates the calcium ion haemostasis and plays a major role in bone mineralisation (Ducy and Karsenty, 1995).

Fibroblasts are the most abundant cells in the connective tissue part of the peri-implant soft tissues. They are largely responsible for the soft tissue response to implanted biomaterials and long-term success of the implant. Initial attachment of fibroblasts during connective tissue healing has an essential role in this process. Focal adhesion contacts (***FACs***) are the anchorage structures involved in fibroblast adhesion and attachment to the implanted material. ***FACs*** are confined areas of extremely tight contact between the basal cell membrane and the implanted material located at the distal ends of microfilament bundles. ***FACs*** provide sites of mechanical attachment to the extracellular matrix. They also act as foci where adhesion-associated signal transduction is initiated (Singer, 1982, Burridge and Chrzanowska-Wodnicka, 1996, Größner-Schreiber *et al.*, 2006).

The ultrastructural analysis of the ***FACs*** revealed two major components; fibronectin and vinculin. The former is a peri-cellular glycoprotein that apparently mediates the adhesion of fibroblasts to the underlying substrate. The latter is an actin-binding protein that is located within ***FACs*** at the end of actin microfilaments bundles. ***FACs*** can be thus identified by the presence of these components. The abundance of

such components is a reflection and indicator of the efficiency of cell adhesion (Yamada *et al.*, 1976, Geiger *et al.*, 1980, Singer, 1982, Größner-Schreiber *et al.*, 2006).

Several other proteins are involved in fibroblast adhesion such as integrins and vimentins (Gómez-Florit *et al.*, 2014). Furthermore, the durability and strength of soft tissue attachment relies heavily on the density and abundance of collagenous fibres within the connective tissue around the transmucosal part of the dental implant. Ultrastructural immunolabeling of biopsies from soft tissues surrounding dental implants in human mandibles revealed that the connective tissue located under the junctional epithelium and above crestal bone were comprised of several types of collagen fibres. However, type I collagen was in common in all studied parts of connective tissue and was the most dominant fibre in the supracrestal part (Chavrier and Couble, 1998).

Quantitative real time polymerase chain reaction (*qRT-PCR*) is a widely used technique to study the expression profile of specific genes in a single stranded *DNA*. The technique involves amplification of single stranded *DNA* and quantification of the target oligonucleotide sequence utilising specific probes and dye-based detection. The present study used a Taq-Man[®] *qRT-PCR* assay to investigate the effects of various surfaces on the gene expression profile of osteogenic markers (*RUNX-2*, *BMP-2*, *ALP* and *OSCN*) and genes encoding for proteins involved in periosteal integration such as fibronectin (*FNI*), vinculin (*VCL*), integrin- α 2 (*ITGA-2*) and collagen type I α 1 (*COL1A1*). Tissue culture procedures and incubation conditions were similar to those used in proliferation and viability studies described in Section 4.2.5.1. One exception was the seeding density of *HGF* and *G-292* cells for 24 hours incubation period. The number of cells was increased to 1×10^5 cell/well in order to obtain sufficient *RNA* for *qRT-PCR* experiments.

4.2.5.4.1 RNA extraction, quantitative and qualitative analysis

HGF and *G-292* cells were harvested at the end of each incubation period. Cell pellets were washed with *PBS* in order to remove any traces of *DMEM*, centrifuged again and *PBS* was aspirated. Total *RNA* was extracted and purified immediately after harvesting using RNeasy Mini Kit[®] (QIAGEN, UK). In brief, complete disruption of plasma membranes of cells and organelles was achieved using 350 μ l of

β -Mercaptoethanol and RLT lysis buffer (1:100). The mixture was pipetted up and down until the cell pellet was completely dissolved. The resultant lysate was homogenised by vortexing for 1 min. 70% ethanol was added to the homogenised lysate to enhance binding of **RNA** and mixed by pipetting. The mixture and any precipitate was pipetted out to an RNeasy spin column placed in a 2 ml collection tube and centrifuged for 15 sec at 10,000 rpm. The flow through was discarded and 350 μ l of RW1 buffer were added to the column, centrifuged for 15 sec and the flow-through was discarded. On-column DNase digestion was performed to eliminate genomic **DNA** contamination using RNase-Free DNase set (Qiagen, UK). RW1 buffer was used again to wash the spin column's membrane for a several times to eliminate ethanol contamination. 500 μ l of RPE buffer were used twice to wash the spin column's membrane to ensure alcohol elimination. Finally, the **RNA** elution was achieved by addition of 30 μ l of RNase-free water to the spin column and further centrifugation for 1 min at 10,000 rpm. The eluted **RNA** was kept in sterile 1.5 ml plastic tubes and immediately placed on ice. The concentration of the eluted **RNA** was measured using NanoDropTM 1000 spectrophotometer (Thermo Scientific, UK). Measurements were repeated three times and an average concentration was calculated for each sample.

The quality of **RNA** was checked using several criteria obtained from NanoDropTM measurements. **RNA** sample with; an absorbance peak at 260 nm, 260/280 absorbance ratio between 1.8-2.4 and 260/230 absorbance ratio more than 2.0 was deemed as acceptable quality. Integrity of **RNA** was further analysed by agarose gel electrophoresis. The agarose gel (1.2% w/v) was prepared by dissolving the required weight of agarose powder in 100 ml of 1 \times tris acetate /**EDTA** buffer (TAE buffer, Sigma-Aldrich, UK). The gel was heated in the microwave at 75 °C for 1 min until completely dissolved. The gel was allowed to cool down at room temperature for 5 min before addition of 0.5 μ l ethidium bromide dye. The gel was swirled gently to mix the contents, a comb was inserted and the gel allowed to set. A gel tray was placed in the gel tank filled with 250 ml of 1 \times TAE buffer and the comb was removed. A mixture of 2 μ l loading buffer, 8 μ l of RNase-free water containing 1 μ g **RNA** was loaded into the gel. The electrophoresis was performed for 55 min at 100 V. After the completion of the run the gel was viewed under transilluminator **UV** light (Syngene, UK). A run of intact total eukaryotic **RNA** on a denaturing agarose gel should exhibit

ribosomal peaks (bands) at 18S and 28S sedimentation coefficient (*S*). The latter is an indication of molecular size of the *RNA*. The ratio of band intensity (28S/18S) can be used as indication on the integrity of total *RNA*. A 28S/18S ratio of 2 is an indication of intact, high quality *RNA*.

The majority of samples in this study demonstrated high quality, integrity and purity of the extracted total *RNA* according to the studied criteria. The total *RNA* extracted from some *HGF* and *G-292* cells incubated for 24 hours exhibited 260/280 absorbance ratios marginally outside the cited acceptable range for intact *RNA*. This may point toward the presence of *UV* absorbing contaminants such as proteins, genomic *DNA* or traces of the reagents used in the *RNA* extraction process. Such findings are reportedly not considered as a reason to preclude the use of the samples for *qRT-PCR* studies. Further analysis of *RNA* integrity using agarose denaturing gel revealed two distinct bands at 18S and 28S. The 28S bands were larger and of higher densities which is consistent with highly intact total eukaryotic *RNA* samples. Figure 96 illustrates a representative denaturing agarose gel of *RNA* samples extracted from *HGF* and *G-292* cells incubated on *Zr-M*, *MDS*, *SLActive-Like* and control surfaces for 24 hours.

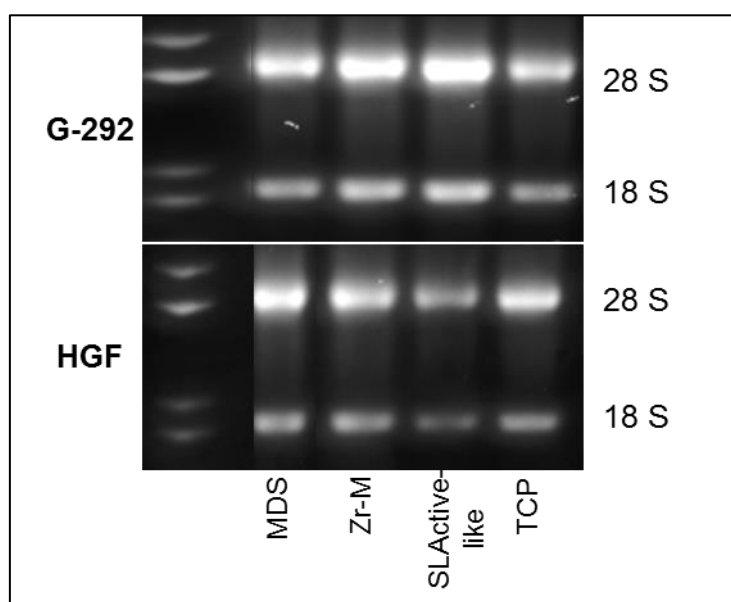


Figure 96. Representative *RNA* electrophoresis gels.

Electrophoresis gel for *RNA* samples extracted from *G-292* (*top*) and *HGF* cells (*bottom*) incubated on *MDS*, *Zr-M*, *SLActive-like* and control surfaces for 24 hours.

4.2.5.4.2 Complementary DNA (cDNA) synthesis

Total *RNA* (200 ng) was reversed transcribed to single stranded *cDNA* using SuperScript® VILO™ MasterMix *cDNA* Synthesis Kit (Invitrogen, Life technologies, UK). *cDNA* reactions were prepared from 4 µl master mix, *RNA* volume containing 200 ng *RNA* and RNase-free water for a final mix of 20 µl. Components were mixed gently by pipetting and then spun down for 25 sec in micro-centrifuge. *cDNA* reactions were incubated at 25 °C for 10 min, 42 °C for 5 min and finally at 85 °C for 5 min. Thermal cycling was performed using Peltier Gradient Thermal Cycler (GMI, USA). At the end of the thermal cycling protocol, *cDNA* was diluted by adding 80 µl RNase-free water. Diluted *cDNA* was stored at -20 °C for further use.

4.2.5.4.3 *qRT-PCR* analysis of *HGF* and *G-292* cells

Taq-Man® *qRT-PCR* assay was used to study the expression profile of the following genes; *RUNX-2*, *BMP-2*, *ALP*, *OSCN*, *FNI*, *VCL*, *ITGA-2* and *COL1A1*. B-actin (*ACTB*) and Glyceraldehyde 3-phosphate dehydrogenase (*GAPDH*) were used as reference or housekeeping genes.

Taq-Man® primers/probes for all studied genes were custom designed and evaluated for priming specificity and amplification efficiency by Primerdesign Ltd., UK. Appendix F contains a copy of the data sheet for one of the studied genes. *qRT-PCR* reactions were made in triplicates for each gene of interest. Each reaction was prepared from; 1 µl of the custom human real-time *PCR* primer with double dye probe (Taqman style) for the studied gene, 10 µl of PrecisionPlus™ MasterMix, 4 µl of RNase/DNase free water (Primerdesign Ltd., UK) and 5 µl of *cDNA*. No template control (*NTC*) reactions were prepared for each used primer to exclude genomic *DNA* contamination of any of the used reagents. *NTC* reactions were prepared exactly as for experimental reaction with the exception that *cDNA* was substituted with RNase/DNase free water. All reactions were loaded to white 96 well plates. A LightCycler 1536 Real-Time *PCR* system was used for the *qRT-PCR* analysis (Roche, UK). The operational software used for data (cycle threshold, *Ct* values) acquisition was ABI 7000 system (Applied Biosystems, UK). Thermal cycling conditions were set according to the manufacturer's instructions which are summarised in Table 20.

Table 20. *qRT-PCR* amplification protocol.

<i>Stage</i>	<i>Repetition</i>	<i>Step</i>	<i>Time</i>	<i>Temperature</i>
1	1	<i>Enzyme activation-Hot start</i>	10 min	95°C
		<i>Denaturation</i>	15s	95°C
2	50	<i>Data collection</i>	60s	60°C

The *Ct* value is an indication on the number of amplification cycles required for the fluorescent signal from the *PCR* products to exceed background level. It is inversely proportional to the amount of target nucleotide sequence of the gene of interest within the *cDNA*. Quantification of expression of gene of interest can be performed relative to an endogenous reference gene (housekeeping gene that is usually expressed constitutively in cell type under various conditions). For data analysis purposes, *Ct* values for *ACTB* were used in this study as it was more constitutively expressed under all conditions in comparison to *GAPDH*. Relative expression of the target gene using the normalised fold change method was assessed according to the following Equations:

$$\Delta Ct_{\text{Sample or Control}} = Ct_{\text{Target Gene}} - Ct_{\text{ACTB}} \quad (26)$$

$$\Delta\Delta Ct = Ct_{\text{Sample}} - Ct_{\text{Control}} \quad (27)$$

$$RQ = 2^{-\Delta\Delta Ct} \quad (28)$$

Where;

Sample refers to *MDS*, *Zr-M* and *SLActive-like* surfaces,

Control refers to tissue culture plastic surface, and

RQ is the relative quantity which refers to the normalised fold change in gene expression

The expression profiles of genes responsible for the synthesis of *FAC* proteins (vinculin and fibronectin) revealed slight upregulation of such genes in the *HGFs* cultured on *MDS* surface in comparison to *SLActive-Like* surface. Subtle differences in the expression profile of these genes were seen in *Zr-M* and *MDS* groups. The highest upregulation of *VCL* and *FNI* was identified in the *MDS* group after 1 week incubation period.

ITGA-2 was highly upregulated in *HGFs* cultured on *Zr-M* and *MDS* for 24 hours and 3 weeks in comparison to control and *SLActive-like* groups. After 1 and 2 week incubation periods, *MDS* group induced the highest upregulation of *ITGA-2* in comparison to all other groups. *COL1A1* was highly upregulated in *Zr-M* and *MDS* groups after 24 hours incubation and only in *MDS* group after 1 week incubation period. Subtle differences were seen in the expression profile of *COL1A1* between all the groups after 2 and 3 weeks incubation period of the *HGFs*. Figure 97 demonstrates the expression profile of *VCL*, *FNI*, *ITGA-2* and *COL1A1* genes as indicated by *RQ* values.

After 24 hours incubation period, early osteogenesis markers (*BMP-2* and *RUNX-2*) were significantly upregulated in *G-292* cells cultured on *MDS* surfaces and to a lesser extent, in *G-292* cultured on *SLActive-like* surfaces. *Zr-M* demonstrated the lowest expression of *BMP-2* and *RUNX-2*. There was no notable upregulation of *OSCN* and *ALP*.

With increasing incubation period, late osteogenesis markers (*OSCN* and *ALP*) started to be upregulated. The greatest upregulation of *OSCN* was noticed in *MDS* group after 3 weeks incubation time followed by *SLActive-like*, *Zr-M* and control groups. The difference in *RQ* seemed to be significant as the relative expression of *OSCN* almost doubled. Similarly, the expression of *ALP* was highest in *MDS* group after 2 and 3 weeks incubation period. However, *Zr-M* exhibited higher expression of *ALP* during at these periods when compared to *SLActive-like* surface. The interesting finding was at incubation period of 1 week where *Zr-M* exhibited greatest upregulation of *OSCN* in comparison to after 2 and 3 weeks incubation periods and other experimental groups at all incubation periods. Figure 98 summarises the expression profiles of the aforementioned osteogenic markers in *G-292* cells.

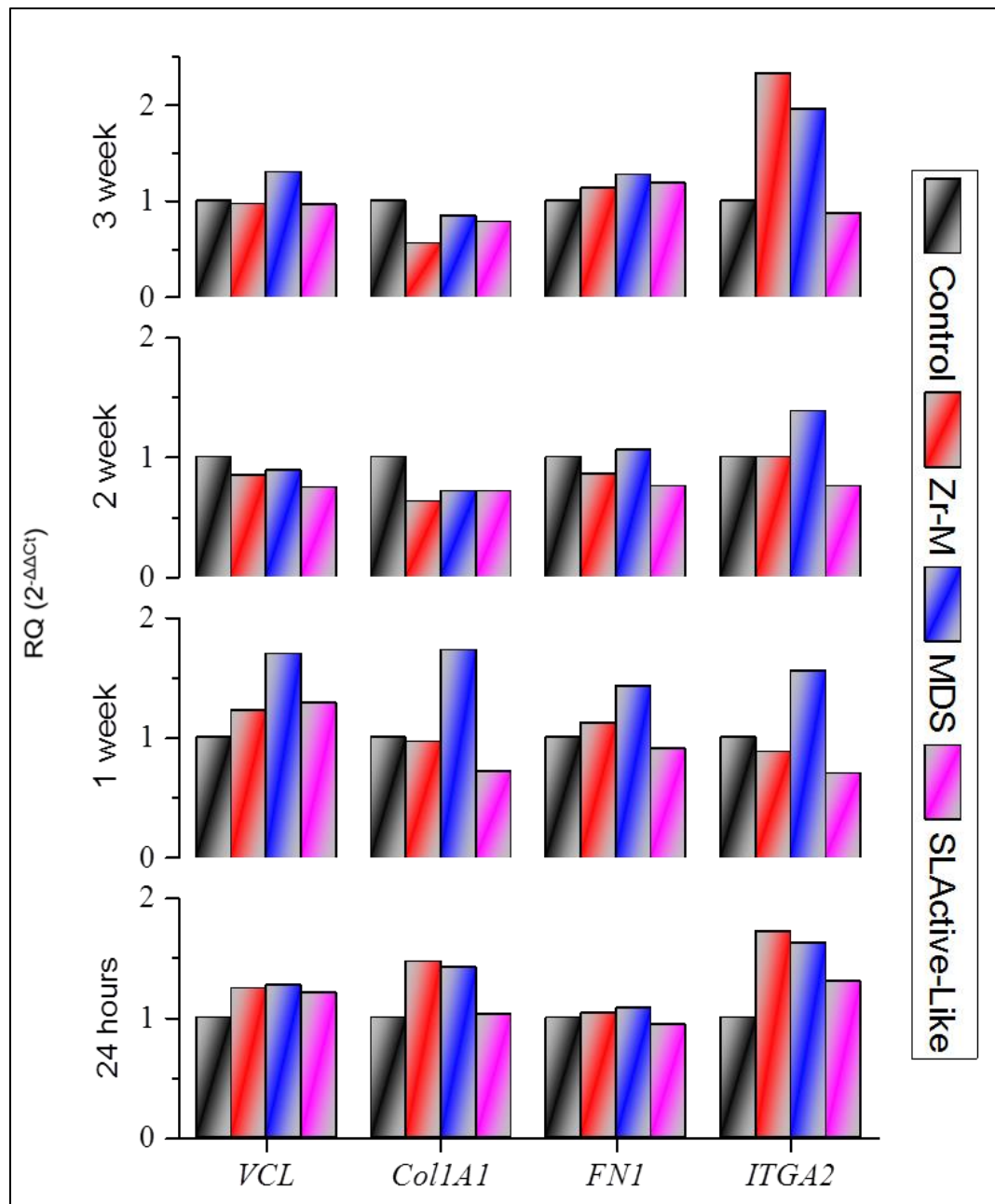


Figure 97. Expression profile of *VCL*, *Col1A1*, *FN1* and *ITGA2* in *HGF* cells.

Bar chart represents changes in the gene expression profile in *HGF* cells when incubated on *MDS*, *Zr-M*, *SLActive-like* and control surfaces for 24 hours, 1 week, 2 weeks and 3 weeks. Mean relative quantity of fold change (**RQ**) was calculated from $2^{-\Delta\Delta C_t}$.

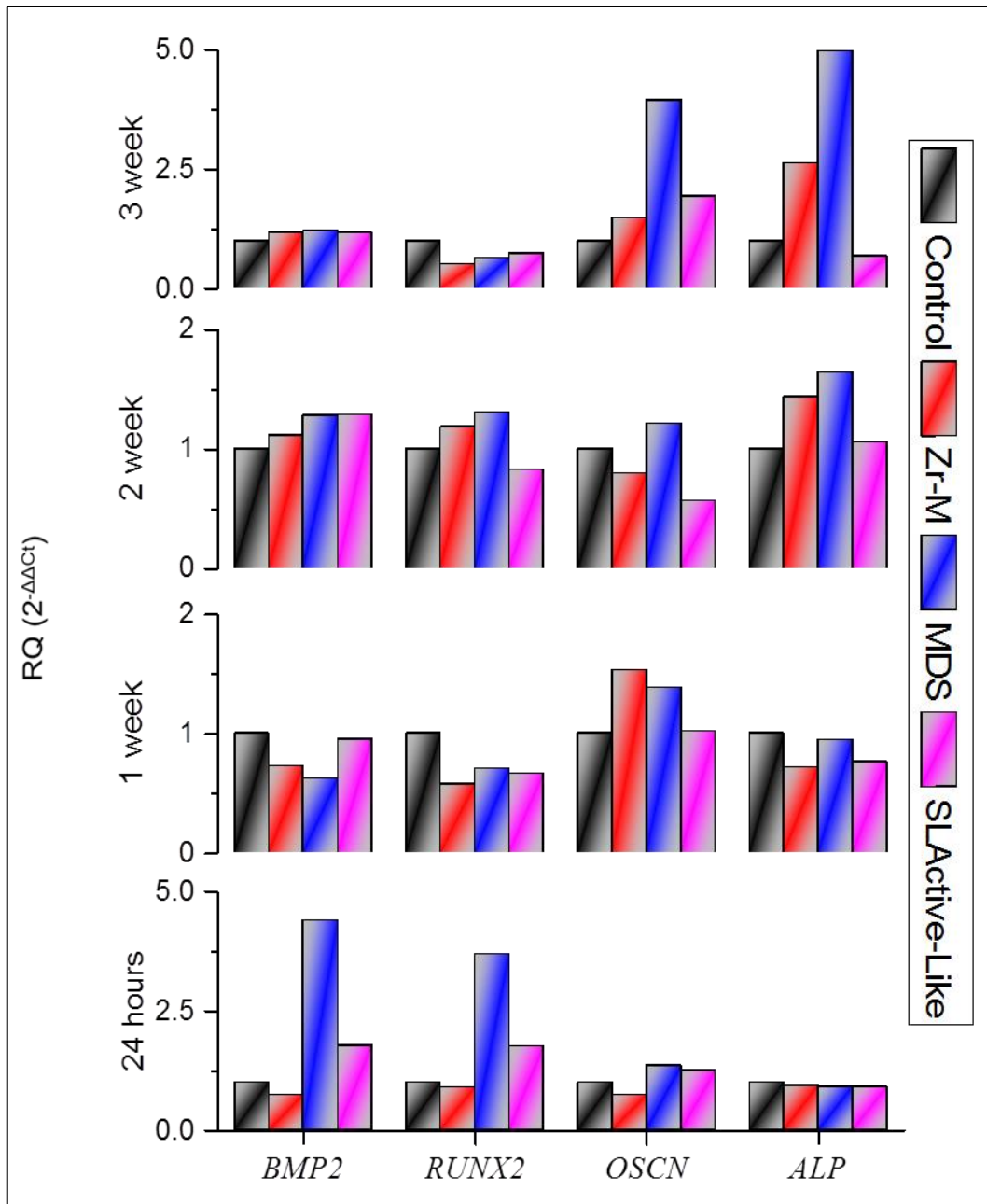


Figure 98. Expression profile of *BMP-2*, *RUNX-2*, *OSCN* and *ALP* in *G-292* cells.

4.3 Discussion

The description of implant surface topography lacks consensus as to what is deemed smooth or rough. Many studies described implant surfaces based on dubious surface characterisation techniques that lack quantitative abilities especially in the era that witnessed the long-term findings on machined Brånemark implants (Wennerberg and Albrektsson, 2009). Additionally, machined implants were deemed smooth despite the fact that some machining techniques may result in roughened implant surfaces. The introduction of *CLSM* and various types of optical profilometers enabled more sophisticated characterisation of surface topographies and quantification of various surface roughness parameters. The height-descriptive line or aerial profiles are commonly reported for implant surfaces in the literature. A classification for implant surface roughness utilised R_a parameter as follow; smooth ($R_a < 0.5 \mu\text{m}$), minimally rough ($R_a 0.5\text{--}1 \mu\text{m}$), moderately rough ($R_a 1\text{--}2 \mu\text{m}$) and rough surfaces ($R_a > 2 \mu\text{m}$) (Albrektsson and Wennerberg, 2004).

In the present study, *CLSM* was used in the present study to calculate the two dimensional aerial parameters for various experimental surfaces (Section 4.2.3). The findings indicated that *CIM* can produce a minimally rough zirconia surfaces by using moulds with roughened inner surfaces ($R_a \approx 1 \mu\text{m}$). Further alteration of surface topography was achieved utilising the proprietary *MDS* acid etching techniques. The R_a value ($2.19 \mu\text{m}$) for the *MDS* surface was just above the range for moderately rough surfaces. The *MDS* acid etching technique did not only result in alteration of texture and waviness of the surface, it also caused notable material removal as indicated by the increased number and density of the surface micropores. Furthermore, acid etching caused significant changes at the crystalline level where it significantly reduced crystal size and rendered the crystals highly irregular as opposed to the initial homogenous, equiaxial outline.

Alteration of surface topography utilising mould roughness and *MDS* treatment can be of a substantial importance in the light of limited ability to achieve such effect with conventional surface treatment. Mechanical surface treatments such as sandblasting and grinding may be ineffective to induce notable alteration of surface topography owing to the very high hardness of zirconia. Additionally, such treatment may have detrimental effects on the mechanical properties and can potentially increase

the risk of material ageing (Zhang *et al.*, 2004a, Zhang *et al.*, 2004b, Zhang and Lawn, 2005). Several studies investigated the effect of sandblasting utilising corundum or alumina particles with different grain sizes. The use of both materials failed to produce surface roughness parameter (R_a) above 1 μm (Gahlert *et al.*, 2007, Schliephake *et al.*, 2010, Saulacic *et al.*, 2014). In contrast, sandblasting grade II *cpTi* with 250-500 μm alumina particles resulted in very rough surface with $R_a \approx 3.15 \mu\text{m}$ (unreported findings in this study). These findings clearly demonstrate the poor efficacy of sandblasting when used with zirconia ceramics.

Zirconia exhibited significantly higher resistance to erosion-corrosion induced by various types of acid attacks when compared to titanium and other ceramic materials (Bermúdez *et al.*, 2005, Chaiyabutr *et al.*, 2008). Sandblasting and etching of *Y-TZP* implants in an alkaline bath (hot solution of sodium hydroxide and potassium hydroxide for 24 hours) resulted in minimally rough implant surface ($R_a = 1.1 \mu\text{m}$) (Ferguson *et al.*, 2008, Schliephake *et al.*, 2010, Saulacic *et al.*, 2014). Proprietary acid etching techniques were also investigated for their effectiveness to roughen zirconia implant surfaces. Some of these techniques utilised warm hydrofluoric acid solutions and produced minimally rough surface with R_a 0.55-0.63 μm (Gahlert *et al.*, 2007, Gahlert *et al.*, 2012, Saulacic *et al.*, 2014). Additionally, a widely marketed one-piece zirconia implant system is claimed to exhibit a moderately rough acid-etched implant surface (ICE[®] surface, $R_a = 1.16 \mu\text{m}$) according to some studies and by the manufacturer (Oliva *et al.*, 2007, Oliva *et al.*, 2010). Sandblasted and acid-etched zirconia surface was investigated and found to have mean R_a value of 0.93 μm (Bächle *et al.*, 2007). Details on the acid etching protocol or type of the used acid could not be found. Furthermore, zirconia surface modification was performed by sandblasting with alumina particles (grain size 30–130 μm) followed by acid-etching with hydrofluoric acid, nitric acid and sulfuric acid with subsequent heat treatment (1200–1400 °C) in order to smoothen the sharp edges as a result of the etching procedure. This patented surface modification resulted in R_a value of 0.94 μm .

An experimental coated zirconia surface, ZiUnite™, was introduced by Nobel Biocare. The implant is produced by sintering dried slurry, sprayed on one-piece zirconia implant and the resulting R_a was estimated to be 1.0 μm . Further modification of this surface was achieved by coating the implant with <50 nm calcium phosphate layer or < 200 nm hydroxyapatite nanoparticles (R_a : 0.94-1.24 μm) (Sennerby *et al.*,

2005, Lee *et al.*, 2009b). A novel selective infiltration-etching technique was recently used to roughen zirconia implant surfaces ($R_a=0.8\mu\text{m}$). The technique utilises molten glass to infiltrate and diffuse between the grain boundaries of zirconia. The glass exerts surface tension and capillary forces to induce sliding, splitting, and rearrangement of the surface zirconia crystals. The glass is subsequently dissolved in an acidic bath in order to expose the created nanoscale inter-crystalline spaces (Aboushelib *et al.*, 2013b). CO_2 laser treatment was also used to create micro-textured zirconia implant surface with R_a values ranging from 0.4-0.9 μm depending on the used laser energy (Hao *et al.*, 2005, Stübinger *et al.*, 2008, Hoffmann *et al.*, 2011).

R_a is the most commonly height-descriptive parameter for implant surface roughness in the literature (Wennerberg and Albrektsson, 2009). R_a is a center line average measurement that is obtained from mean absolute deviation of roughness irregularities (peaks and valleys) from a reference line along the studied area (Gadelmawla *et al.*, 2002). However, the use of this parameter as sole determinant for surface topography may be misleading. This can be attributed to several reasons including; (1) R_a parameter does not distinguish peaks from valleys which render this parameter of no use to estimate surface flaws introduced by the surface treatments which can be expressed as valleys, (2) it does not distinguish roughness from an undulating surface, and (3) it is not sensitive to minimal changes in the roughness profile as well as very high peaks and low valleys. The latter point is very important as large-grit sandblasting and roughness as a result using roughened mould may result in high peaks that can be underestimated if R_a was solely used. For these reasons, R_a values were supplemented with several other parameters such as R_v and R_p that differentiate peaks from valleys and R_q which are more sensitive to large deviations from the mean line as in the case of high peaks and low valleys. The increase of surface area was also determined as a result of surface roughening technique (Gadelmawla *et al.*, 2002, Al-Shammery *et al.*, 2007, Wennerberg and Albrektsson, 2009).

The aim of producing a *SLActive-like* surface in this study was to provide a widely studied and used implant surface that serves as control. The process and concentration of chemicals used to produce the original, commercially available SLActive[®] surface are patent confidentials and were not available. The method followed in in Section 4.2.1 was collated from dispersed information in several studies

and patents (Martin *et al.*, 1995, Simpson and Steinemann, 2002, Zinger *et al.*, 2003, Zhao *et al.*, 2005, Schwarz *et al.*, 2007a). The appearance of the **SLActive-like** surface under **SEM** was very similar to that reported in other studies and by the manufacturer which can be best described as a hierarchically, several level, ordered structure where larger concavities created by sandblasting embraced smaller round micropits created by the warm acid attack (Martin *et al.*, 1995, Rupp *et al.*, 2004, Kang *et al.*, 2009, Schmidilin *et al.*, 2013).

The chemical composition of the surface was significantly different from that reported for commercially available SLActive[®] surface. In particular, oxygen concentration was three times higher than titanium which is an indication on the formation of oxide layer within SLActive[®] (Rupp *et al.*, 2006). Whereas in the **SLActive-like** surface, **EDS** analysis revealed seven times higher titanium concentration when compared to oxygen which may indicate that the surface is largely un-oxidised. This finding could be attributed to the fact that the surface was examined straight after preparation which did not allow enough interaction between the normal saline and/or air for the oxidation reaction to take place.

A superior characteristic of **SLActive-like** surface over SLActive[®] was that the amount of carbon contamination was reduced to less than half in the former surface. It is also worthwhile to stress that surface chemistry analysis performed by Rupp *et al.* (2006) utilised X-Ray photoelectron spectroscopy which could be significantly superior to **EDS** used in the current study (Rupp *et al.*, 2006).

The roughness parameters obtained for the **SLActive-like** surface was in the range of those reported for commercially available SLActive[®]. It has been reported that SLActive[®] surface has R_a ranging between 2-4 μm with a mean value of 2.94 μm (Sammons *et al.*, 2005, Rupp *et al.*, 2006). Another study reported R_a of 3.0 μm and R_q of 3.74 μm which were comparable to those calculated for **SLActive-like** surface produced in this study (Kunzler *et al.*, 2007).

The present study calculated unfiltered, 2D height-descriptive or amplitude parameters in Section 4.2.3. The use of 3D height descriptive counterparts in conjunction with spatial, spacing, hybrid or functional parameters may provide a much better characterisation for all modern implant surfaces. This is becoming a more relevant aspect as the recently introduced surface treatments may alter the surface

topography at the macro-, micro- and nano-scales (Gadelmawla *et al.*, 2002, Wennerberg and Albrektsson, 2009). However, the available software operating *CLSM* used in this study did not support the calculation of such parameters.

Tactile or mechanical stylus surface profilometers, optical profilometers and *CLSMs* are among the most widely used instruments to quantify surface roughness. A study reported high agreement between these techniques when used to measure the same sample (Conroy and Armstrong, 2005). Conversely, other studies reported poor correlation between roughness parameters when measured using tactile and other methods which was attributed to limitation related to size of the stylus, the used sampling rate, force of the tactile profilometers and the hardness of the material (Whitehead *et al.*, 1995, Wennerberg *et al.*, 1996). There is however lack of evidence on the good correlation between roughness parameters measured using various non-contact techniques.

The present study used optical profilometry to measure roughness parameters of representative samples of *MDS* and *SLActive-like* surfaces (data unreported). The 3D height-descriptive parameters S_a , S_q , S_p and S_v were significantly lower in comparison to the 2D counterparts R_a , R_q , R_p and R_v , respectively. The mean S_a for *MDS* was measured as 1.29 μm in comparison to R_a value calculated by *CLSM* (2.19 μm). With regard to *SLActive-like* surface, S_a value was 1.79 μm as opposed to R_a value of 2.49 μm (Figure 99).

Similar observation was reported in another study where *CLSM* had a tendency to overestimate the surface roughness parameters due to the formation of spikes on surfaces with deep roughness irregularities (Al-Shammery *et al.*, 2007). Additionally, *CLSM* may have higher resolution than optical profilometers and is always used at higher magnifications with lower dimensions for regions of interest and thereby yields surface parameters higher than those measured using optical profilometers (Wennerberg *et al.*, 1996).

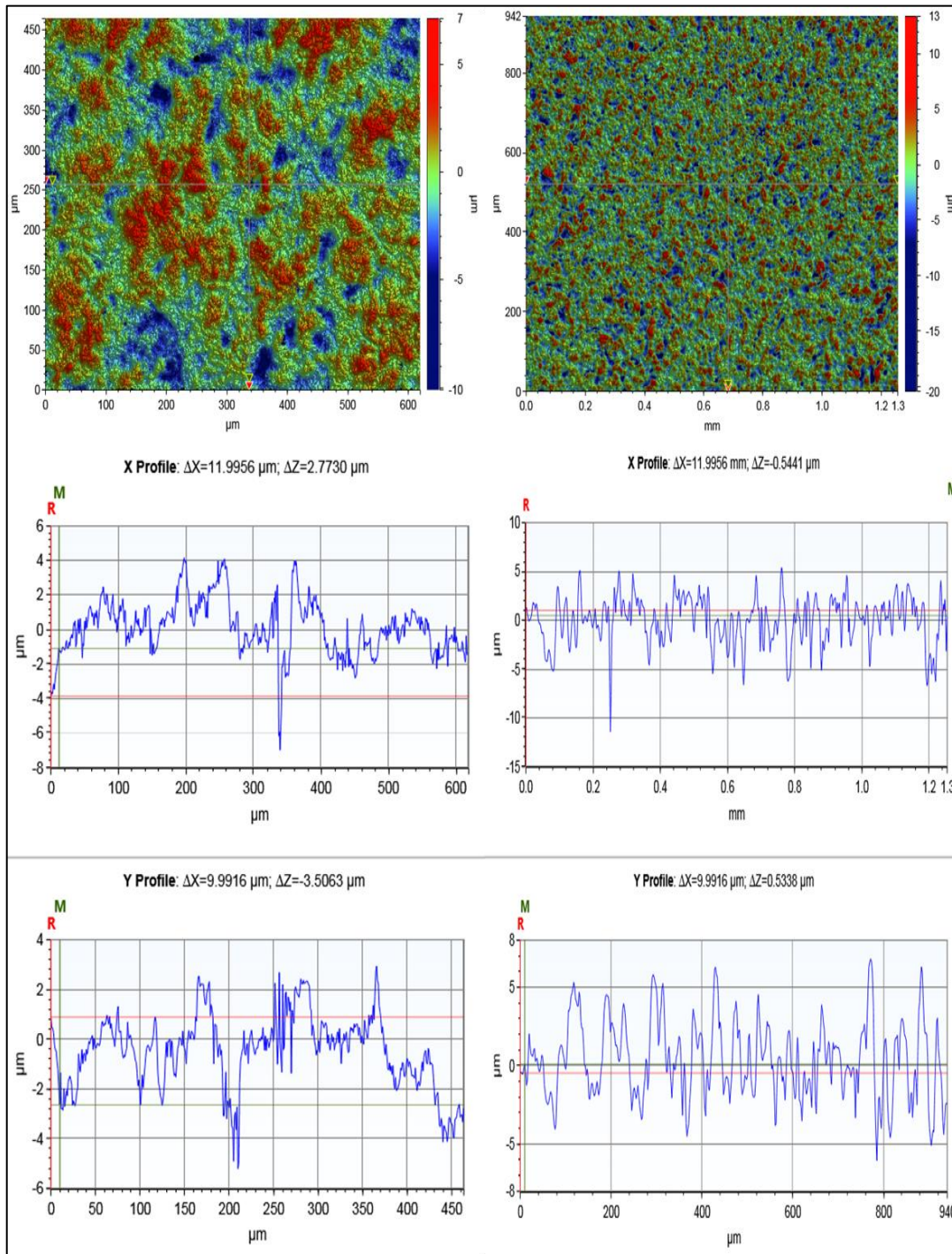


Figure 99. Optical profilometry of *MDS* and *SLActive-like* surfaces.

Left, *MDS* sample and *right*, *SLActive-like* surface. *Top*, topographical image, *middle*, height profile along the *x*-axis and *bottom* is the height profile along *y*-axis.

The findings of this study revealed that there was no significant difference between R_a and R_q for *SLActive-like* and *MDS* surfaces. Both surface treatments exhibited higher roughness parameters than *Zr-M* surface. *SLActive-like* surface exhibited significantly higher mean peak height which can be caused by the large-grit sandblasting. Conversely, *MDS* surface exhibited deeper valleys which can be attributed to material removal as a result of acid attack between the irregularities initially created by the roughened mould. These valleys could be progenitors for critical flaws that may contribute to material failure. However, it is worthwhile to mention that all mechanical studies in Chapter 2 were conducted on zirconia samples that received similar *MDS* treatment. The increase of surface area in *MDS* and *SLActive-like* surfaces was comparable whilst significantly higher in comparison to *Zr-M* surface

Performing *in vitro* biological studies on non-flat surfaces such as implants may be unfeasible. Thus, flat discs with standard geometry were used in Section 4.2.5. However, it is of great importance that the surface topography and chemistry of the experimental are similar to those for implant surface. Therefore, *MDS* treated and commercially available implants (White Implant Development Corp. The Netherland) were studied using *SEM*, *EDS* and *CLSM* and optical profilometry and compared to the studied *MDS* discs. Both samples demonstrated comparable appearance and chemical composition when studied using *SEM* and *EDS* (Figure 100).

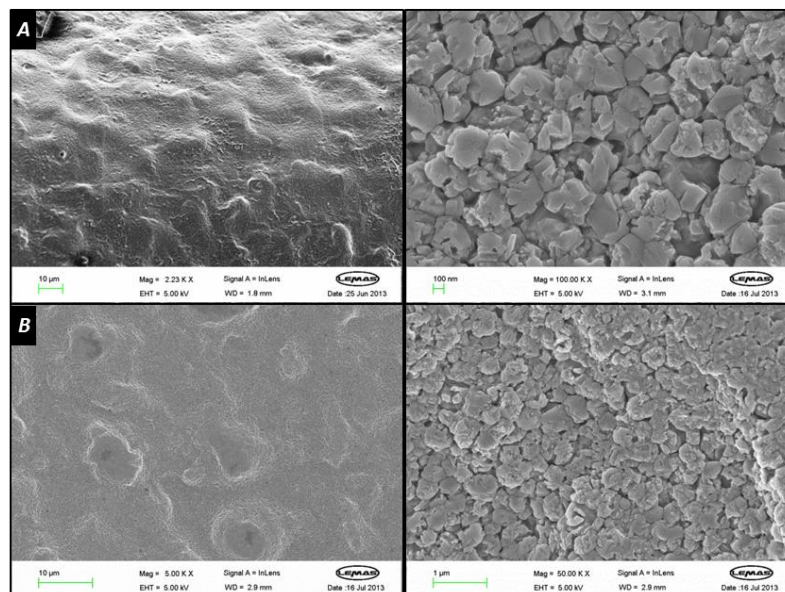


Figure 100. Comparative *SEM* views for implant (A) and disc (B) samples.

Surface roughness parameters obtained for *MDS* discs and implants using *CLSM* and optical profilometer were highly correlated except with R_v parameter (Table 21, Figure 101). However, this parameter is very variable according to the studied region. Overall, these findings may indicate that data obtained from the biological testing can be used to make extrapolations regarding the possible effect of surface topography in implant-cells interaction *in vitro*.

Table 21. Comparison of roughness parameters (μm) of implants versus *MDS* discs. Optical profilometer (OP).

<i>Sample</i>	<i>MDS disc</i>		<i>MDS implant</i>	
	<i>CLSM</i>	<i>OP</i>	<i>CLSM</i>	<i>OP</i>
R_a	2.190667	1.29	2.102	1.21
R_q	2.936	1.63	2.634	1.42
R_p	24.916	7.13	25.498	5.95
R_v	7.15	10.12	11.38	5.56

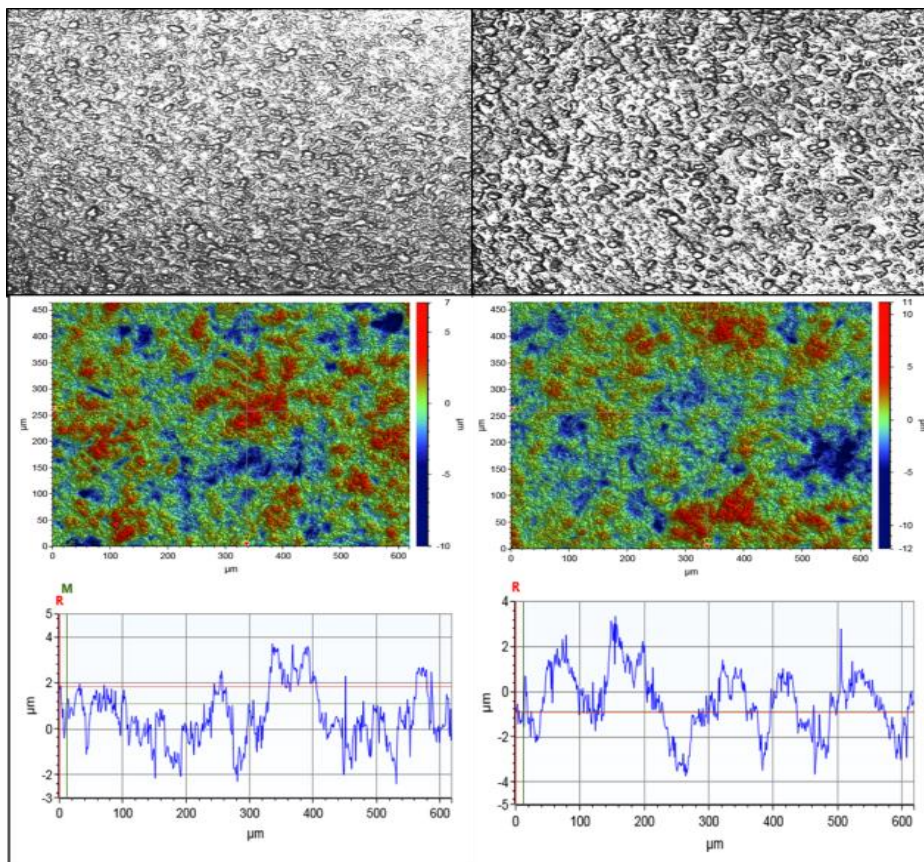


Figure 101. Comparative analysis of surface topography of *MDS* discs and implants.

Left, *MDS* discs and *right*, implants. *Top*, 3D reconstructed *CLSM* topographical image, *middle*, OP topographical map and *bottom*, height profile along Y axis.

The present study demonstrated high wettability of the *SLActive-like* surface (Section 4.2.4). Such finding was in agreement with other several studies that attributed such effect to surface roughness, high surface energy and hydrophilicity of a commercially available, similar surface (Rupp *et al.*, 2006). Additionally, *MDS* surface demonstrated significantly higher wettability as indicated by the low water contact angle ($\theta = 44.43^\circ$) when compared to *Zr-M* ($\theta = 83.62^\circ$). There is a scarce amount of studies investigating the water contact angle of zirconia with various surface topographies. A study reported that smooth surface *Y-TZP* material had θ of 66.4° . No quantitative data analysis was provided for surface roughness however (González-Martín *et al.*, 1999). Furthermore, surface micro-texturing of MgO stabilised zirconia utilising CO₂ laser ($R_a = 0.71 \mu\text{m}$) resulted in 50% reduction of contact angle (Hao and Lawrence, 2003).

The contact angle measurements were performed after two seconds of drop disposal on the zirconia surface. The two seconds period was deliberately considered as the time required for equilibrium where a stable sessile drop can form and a static or equilibrium or Young's θ can be measured. However, interpreting such contact angle measurement can be misleading as the Young's equation was hypothesised for flat, homogenous and uniform solids and it fails to account for surfaces with irregularities. In rough surfaces however, liquid moves to expose fresh surface within the drop in order to wet the fresh surfaces of the solid. The contact angle produced is called a dynamic contact angle. The clearly discernible contact angles formed by expanding of the liquid drop is called advancing angle while the smallest angle formed by contraction of the liquid drop is called the receding angle. The difference between the two angles is known as contact angle hysteresis, which is essentially a reflection of the effect of surface roughness on wettability (Hao and Lawrence, 2003, Yuan and Lee, 2013). Therefore, the presented measurements may not reflect the actual surface wetting characteristics of the studied materials and should be supplemented with further dynamic contact angle measurements. Furthermore, surface free energy was not calculated for various surfaces as the used system did not allow the use of different liquids as a result of complicated tubing system of the available machine.

The biofunctional response of *HGF* and *G-292* cells to various implant surfaces was investigated in Section 4.2.5. The used cells were never allowed to overgrow or reach 100% confluence state in order to ensure that they are healthy and functional to

an optimum level. Additionally, cells from early passage number were used (passage 2 and 4) in order to avoid degradation of biological functions such as proliferation and differentiation capacities which can be caused by cell ageing or replicative senescence phenomenon in serially passaged cells (Hayflick, 1974, Huang *et al.*, 2006).

HGF and *G-292* cells were incubated on the studied implant surfaces using a robust tissue culture technique. Implant surfaces were reproduced on discs with standard geometry that fits tightly in the bottom of cell culture well plates. Such a technique ensured localisation of the majority of seeded cells on the surface of interest. It also eliminated the possible confounding effects that may originate from growth of cells on tissue culture plastic. This method may be superior to other experimental setups used for similar purposes. For example, hang-drop culture is a technique where cells are seeded in small volume of culture medium aiming to maintain the cells on the surface utilising surface tension between the cell suspension and implant material. Cells are then left to attach for two hours and then culture medium is then added (Hempel *et al.*, 2010, Wang *et al.*, 2010). Such technique may be highly susceptible to confounding effect from tissue culture plastic on the cells. The risk of disturbance of cell attachment and functions due to movement of samples in the oversized well plates is significantly high. Moreover, seeding such high number of cells in small volume of culture medium may cause significant cell death and retard the growth as a result of contact inhibition process.

The use of *HGF* from one donor could limit the validity and generalisability of the findings of this study. Additionally, despite the fact that majority of studies use osteoblast-like (osteosarcoma) cells, there are still concerns regarding the similarity of osteogenic features among primary osteoblasts and osteosarcoma cells *in vitro* (Meyer *et al.*, 2005).

The effects of direct contact of the three different implant surfaces on proliferation, viability and differentiation of *HGF* and *G-292* cells was investigated. As reported in Section 4.2.5.2, *MDS* surface exhibited significantly higher proliferative characteristics when compared to smoother *Zr-M* or *SLActive-like* surfaces. This effect was more pronounced on *G-292* cells and at incubation periods for 24 hours and 1 week. These findings may indicate that the roughened (*MDS*) zirconia surface can stimulate growth and proliferation of fibroblasts and osteoblasts

immediately after implantation which in turn, can accelerate bone and soft tissue healing around this particular implant material. Additionally, such an effect is of a great clinical relevance where currently there is an increased patient demand to provide immediate provisional restorations and reduce the time required for healing before provision of permanent implant supported prosthesis.

Flow cytometry was used in the present study to compare the biocompatibility of various implant surfaces (Section 4.2.5.3). In this technique, quantification of viable cells is performed by exclusion of dead or dying cells. Flow cytometry may be considered superior to other commonly used counterparts such as trypan blue exclusion or Methylthiazol Tetrazolium (*MTT*) assays. This is attributed to the former's ability to differentiate between and quantify cells that died due to apoptosis (*PI* and Annexin V positive) or necrosis (*PI* positive). Additionally, flow cytometry allows the quantification of cells undergoing apoptosis at the time of investigation (Annexin V positive). However, it is worthwhile to mention that the percentage of necrosis given by such assay may be not correlated to the material's cytotoxic effect. Rather, it may be as a result of cell rupture caused by shear forces during pipetting. Every attempt was made during the processing of samples not to over-pipette cells and such effect can be considered consistent across all groups.

The current study demonstrated high biocompatibility of the three studied implant surfaces. *HGF* exhibited comparable viability percentage when cultured on all studied implant surfaces as well as tissue culture plastic for 24 hours. However, the percentage of cells that died by necrosis was significantly lower in *MDS* group in comparison to *SLActive-like*. Similar viability findings applied to *G-292* cells at the same incubation period. However, the percentage of cells undergoing apoptosis was significantly higher in *SLActive-like* group when compared *MDS* group. Furthermore, *MDS* surface exhibited marginally higher biocompatible effect on *HGF* when cultured for longer periods (3 weeks) in comparison to *SLActive-like* surface. The latter surface induced significantly higher degree of apoptosis on *HGFs* when compared to *MDS* or *Zr-M*. Such long-term differences were less perceptible with *G-292* cells.

Surface topography, wettability, energy and chemical composition have been identified among the major modulators of fibroblast and osteoblast function *in vitro* and *in vivo*. However, there seem to be a significant amount of contradictions

regarding the role of surface topography in fibroblast and osteoblast functions. This issue is a direct result of the lack of comprehensive understanding of the exact molecular basis of cell-implant material interaction. Additionally, it is very difficult to compare findings from various studies due to; (1) the poor correlation between the different surface roughness quantification methods, (2) different cell types and characteristics and (3) the use of different techniques to determine material's effect on viability and proliferation. The findings of the current study were in agreement of several others which reported that roughened zirconia surfaces increased osteoblast or osteoblast-like cell proliferation in comparison to smooth zirconia or roughened titanium. Nanoporous zirconia surfaces prepared by selective acid etching technique significantly induced proliferation of osteoblasts in comparison to polished zirconia and titanium. The cell counts were higher for the roughened zirconia in this study when compared to SLA[®] but the difference did not reach the statistical significance level (Aboushelib *et al.*, 2013a). In another study, an acid-etched zirconia implant surface was compared to an acid-etched titanium surface. The former demonstrated higher proliferation capacity of primary osteoblasts when compared to titanium counterpart (Depprich *et al.*, 2008). Sandblasted and acid-etched zirconia surfaces exhibited significantly higher pro-proliferative effect on osteoblast-like cells in comparison to SLA[®] titanium surface after 3 days incubation period (Bächle *et al.*, 2007). Conversely, our findings were in disagreement with those reported by Kohal *et al.* (2013) who reported that a minimally rough zirconia surface ($R_a=0.94\ \mu\text{m}$) induced higher osteoblast proliferation rate than rougher titanium counterpart (Kohal *et al.*, 2013). Similarly, roughened titanium and zirconia surfaces impaired human foetal osteoblasts proliferation at early phases after seeding (Setzer *et al.*, 2009).

With regards to fibroblasts, the effect of surface roughness on cell proliferation is rather less predictable. A study identified that smooth zirconia surfaces significantly stimulated fibroblast proliferation when compared to rough zirconia, rough and smooth titanium surfaces (Yamano *et al.*, 2010). Conversely, modified zirconia surface by means of micro-grooves increased proliferation rate of human gingival fibroblasts when compared to smooth zirconia (Pae *et al.*, 2009). Unpolished zirconia surfaces stimulated higher proliferation than acid-etched or sandblasted titanium surfaces but the difference did not reach the significance level (Peššková *et al.*, 2007). However, no comments could be found regarding the surface topography of the used zirconia

surface. Another study reported highest fibroblast proliferation on sandblasted zirconia followed by machined zirconia, SLA[®] titanium and machined titanium, in order. No statistical analysis has been provided in the study, however (Payer *et al.*, 2010)

Studying the effect of implant surface topography on osseointegration process can be investigated by biofunctional response of cells at the genetic level as in Section 4.2.4.5. The current study investigated the effect of various implant surfaces on the expression profile of genes regulating osteoblast metabolism and mineralisation. The early transcription factors that play a major role in osteoblast function and differentiation ***RUNX-2*** and ***BMP-2*** were highly upregulated with the ***MDS*** implant surface when compared to rough ***SLActive-like*** and smoother ***Zr-M*** surfaces after 24 hours incubation period. The early upregulation of ***RUNX-2*** and ***BMP-2*** genes was also reported in roughened titanium and zirconia surfaces in comparison to smooth counterparts (Setzer *et al.*, 2009). The induction of such transcription factors is an indicative of greater proliferation in response to ***MDS*** implant surface which highly correlates to our findings from proliferation and viability studies (Section 4.2.5.3).

After prolonged incubation periods (3 weeks), ***MDS*** implant surface induced greater upregulation of ***OSCN*** and ***ALP*** which are involved in later stages of osteogenesis. Induction of ***OSCN*** was observed after 3 weeks of incubation of human fetal osteoblasts on roughened zirconia surface in comparison to roughened and smooth titanium as well as smooth zirconia (Setzer *et al.*, 2009). In contrary, alkaline phosphatase activity was higher in smooth zirconia surface after 1 week incubation in comparison to roughened titanium surface (Ko *et al.*, 2007). Additionally, etched titanium surfaces induced higher alkaline phosphatase activity in osteoblast-like cells after 2 weeks incubation period in comparison to etched and sandblasted zirconia (Hempel *et al.*, 2010). No significant differences were noticed in the expression profile of ***ALP*** gene was found in fetal human osteoblasts upon incubation for three days and three weeks (Setzer *et al.*, 2009).

The changes in expression profile of osteogenic markers with time and when cultured on ***MDS*** surface was very compatible with the reported osteogenic pathway. Studies have shown that ***BMP-2*** regulates osteoblast differentiation via ***RUNX-2***. The process takes place via *Atf 6* expression that is mediated by ***RUNX-2***. *Atf 6* in turn,

was found to increase *ALP* and *OSCN* expression by directly binding to *OSCN* promoter gene. Additionally, it has been reported that *OSCN* upregulation is accompanied by downregulation of *RUNX-2* and *BMP-2* (Jang *et al.*, 2012). This particular change in the expression profile was clearly evident especially at three weeks incubation period where highest expression of *OSCN* with simultaneous downregulation of *BMP-2* and *RUNX-2* was noticed.

The development of anchorage apparatus for cell attachment and adhesion is the hallmark of initiation of cell–implant surface interaction and can be used to assess the biofunctional response of fibroblasts to the implant material (Grinnell, 1978, Setzer *et al.*, 2009). The present study investigated changes in expression profile of genes encoding for proteins and protein subunits involved in cell attachment and adhesion to the implant material. The findings indicated notable upregulation of genes encoding for components involved in connective tissue attachment was detected for the *MDS* or *Zr-M* groups. After 1 week incubation period, *MDS* demonstrated the highest expression of *VCN*, *COIA1*, *FNI* and *ITGA-2*.

Similar observations were confirmed in studies investigated this aspect at gene and protein levels. For instance, roughened zirconia surface significantly upregulated early expression of *ITGA-2* of *HGF* cells. Additionally, smooth and roughened zirconia surfaces induced the expression of *COIA1* in *HGF* upon incubation for 48 and 72 hours respectively (Yamano *et al.*, 2010). Roughened zirconia surfaces resulted in higher expression of vinculin protein in fibroblasts when compared to smooth zirconia and titanium as well as sandblasted titanium (Nothdurft *et al.*, 2014). Significant increase in the *FACs* containing fibronectin and vinculin was reported upon coating titanium surface with zirconium nitride (Größner-Schreiber *et al.*, 2006). However, the comparison may be invalid the studied material in this project was *Y-TZP*.

Chapter 5: **Clinical Relevance, Conclusions and Future Work**

5.1 Clinical relevance

Conventional methods of replacing missing teeth always come with what can be regarded as a high biological cost in the era of minimally invasive dentistry. The use of dental implants has revolutionised this aspect of dental treatment. They have been utilised widely and successfully for several decades. The developments of highly osseointegrating implant surfaces reduced the time for healing and allowed the adoption of immediate replacement and provisionalisation techniques.

Just recently, the reported high survival rates for *cpTi* implants have been put in question. Survival, as judged by radiographic bone levels and loss of restoration, did not hold valid with the emergence of excessive aesthetic demands by the patients, particularly, who received immediate replacement and/or provisionalisation in the aesthetic zone. This has been largely attributed to the high rate of aesthetic complications due to labial bone plate resorption and subsequent mucosal soft tissue recession.

In the name of prevention and treatment of such aesthetic complications, dentists and patients are continuously exposed to an excessive burden. As far as clinicians are concerned, they are obliged to incur the large cost of the armamentarium and training required for performing advanced surgical grafting procedures. Additionally, legal liability of dental practices has significantly increased as a result of potential complications of such procedures. This in turn, restricted what is supposed to be a standard treatment, to a limited number of clinicians who can afford such burdens.

On the patient's side, the standard grafting procedure requires harvesting a large soft tissue pedicle from the hard palate. The morbidity to the donor side may be significant as a result of possible iatrogenic damage to the greater palatine neurovascular bundle that may result in fatal bleeding. More frequently, pain and discomfort following the procedure are overly troublesome. Furthermore, the cost of the implant treatment increases in order of few thousands of pounds. If for argument's sake all the complications were put aside, interestingly enough, there is not currently

any evidence to suggest that this form of treatment can predictably provide a long-term solution for such aesthetically compromised patients.

The use of tooth-coloured ceramic implants can be regarded as the way forward to ameliorate such problems. In the very likely event of mucosal soft tissue remodelling/recession, the aesthetic sequelae will be far from perceptible around ceramic implants in comparison to their grey, *cpTi* counterparts (Figure 102).



Figure 102. Peri-implant mucosal soft tissue remodelling around various implants in the aesthetic zone.

Left, soft tissue recession around white zirconia implant (→) that caused no concern for the patient at 18 months post-op review (Jum'ah *et al.*, 2011). Right, cervical margin of the crown and 2-3 mm of implant head were exposed creating significant aesthetic concern for the patient 18 months after implant placement. Used with permission from Dr. Howard Gluckman.

Additionally, the use of bioceramics that mediate strong soft tissue attachment such as zirconia may maintain stable soft tissue levels despite the inevitable labial bone plate resorption. Thereby, such an approach may negate the need for complex grafting procedures, negate the need for advanced surgical skills to perform standard implant treatment, reduce overall cost of the treatment and increase patient acceptance.

Figure 103 demonstrates a clinical case scenario where the studied zirconia implant design has been used to immediately replace a poor prognosis central incisor tooth. The implant was restored with an immediate provisional crown. Optimum soft tissue health shortly after surgery can be noticed. Additionally, five-year follow-up assessment reveals significant collapse of labial bone plate and yet, the facial/labial soft tissue level was maintained around the implant head.

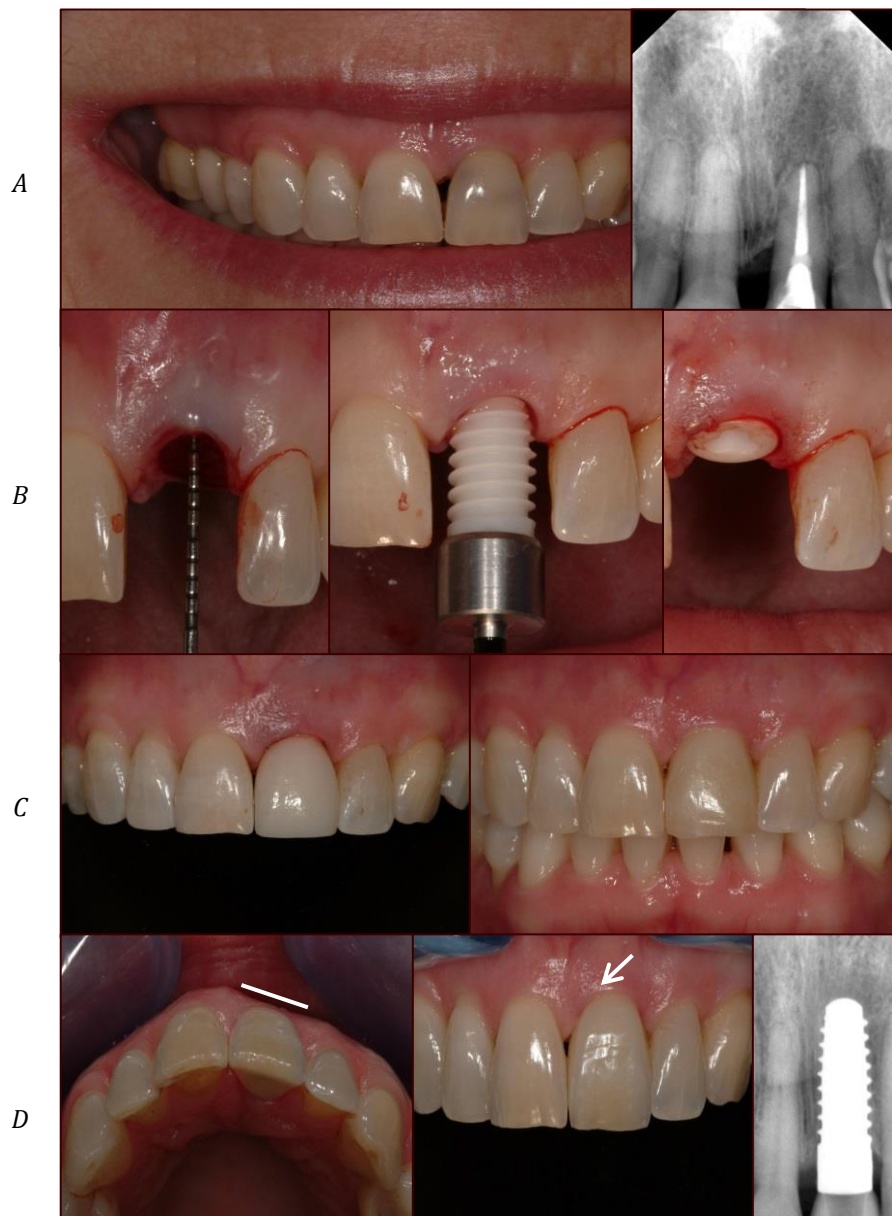


Figure 103. Treatment sequence and outcome of extracted upper left central incisor tooth using zirconia dental implant.

A, Clinical and radiographic demonstration of initial situation of a poor prognosis upper left central incisor. B, Extraction and immediate placement of soft tissue level zirconia implant. The thin tissue biotype is evident as the probe is showing through soft tissues. C, Temporary crown immediately after surgery (left) and 3 months later. Healthy and stable soft tissues can be clearly seen in this case. D, Five years follow-up of the same case reveals stable labial tissue contours (middle: white arrow) despite significant resorption of labial bone plate (left: white line). Stable interproximal bone levels are demonstrated in the radiograph (right). (Jum'ah *et al.*, 2012)

Research on zirconia dental implants is not a new topic. Zirconia dental implants have been widely used and investigated during the last two decades. However, this study is the first to comprehensively analyse crystallographic, mechanical and biological properties of a novel injection-moulded, acid-etched *Y-TZP* material. Additionally, it is the first to investigate the use of a novel hybrid design to overcome design-related shortcomings encountered with conventional one- and two-piece zirconia dental implant systems. Our findings from all studies pointed toward promising performance of the material and the design. Moreover, this piece of work alleviated, at least partially, concerns over *LTD* of zirconia implants and its possible drastic effects on material integrity and reliability.

The elements of the larger translational aim of this project seemed to be mostly fulfilled. Our findings can be regarded as a comprehensive pre-clinical validation of the proposed design. As a matter of fact, these findings were used as the basis of the report submitted for conformity assessment & rules for *CE* marking of medical devices in European Union.

In vitro testing demonstrated that the engineered weak connection exhibited a protective role against catastrophic failures. Such an effect was also noticed in a clinical case treated using this design. The patient sustained an impact trauma on the anterior area of the mouth where an implant was used to replace a missing central incisor tooth. The damage was confined to the crown which could be easily rectified in a clinical setting (Figure 105).



Figure 104. The protective role of the engineered weak link in the implant system.

Left, successful implant replacing upper right central incisor. Right, integrity of implant and abutment preserved following traumatic injury 14 months post-op. Fractured crown was simply remade without any further complications involving the implant or bone. (Jum'ah *et al.*, 2012)

Beside reduction of aesthetic complications and catastrophic mechanical failures, the use of this design may have further advantages clinically. The design moves the connection level to a non-critical, coronal position which is less likely to cause marginal bone loss. Additionally, the prosthesis used to restore the implant is a standard single crown restoration rather than an implant-supported prosthesis. This in turn, simplifies the restorative part of the implant treatment, negates the need for sophisticated impression techniques and several implant accessories such as impression pick-ups and implant analogues. This in turn, can significantly cut down the laboratory cost of the restoration and the overall cost of the treatment.

Work is currently in progress to further refine and optimise this system for better clinical outcomes. Blood contaminating the surface of the internal connection can be detrimental to resin bond strength between abutment and implant. A resilient, polymeric, open-ended tube that snugly fits on the implant head is currently being designed. Such accessory will allow fixation of rubber dam and the use of high concentration acetone that allows decontamination of zirconia surface from saliva and blood and thereby, enhance bonding capacity. Additionally, it allows the control against seepage of cement below soft tissues during abutment bonding. This is of paramount importance to protect against cement-induced high grade inflammatory response and ultimate loss of the implant. Further improvement is being investigated by designing a locator abutment that can inserted tightly in the freshly installed implant. Scanning such locator using intra-oral scanner can be utilised to determine the 3D, spatial position of the implant and the orientation of the internal connection. The generated digital file can be then used to immediately design and manufacture anatomic abutments that are ready for bonding using *CAD-CAM* or 3D printing technologies.

Finally, there are several limitations associated with the proposed design; firstly, the least reliable implant diameter is 4 mm, which can be unfeasible to use in several cases. For instance, bone necking associated with developmental agenesis of teeth (hypodontia) or cases where roots of adjacent teeth converging in the direction of the area of residual space. Secondly, the application of this design may be limited to cases where immediate replacement of extracted teeth is instigated with a pre-requisite that the bony socket is completely intact. This may be important as little is known regarding the behaviour of zirconia implants in augmented (grafted) recipient sites.

5.2 Conclusions

The current work investigated the use of injection moulded *Y-TZP* material as an aesthetic, minimally invasive alternative to conventional dental implant materials. The majority of the studies conducted as part of this project were devoted to investigate the effects of *LTD* or ageing phenomenon on the ultrastructure of the material using crystallographic and imaging techniques. The effects of *LTD* on mechanical properties and reliability of the material were also exhaustively studied at the macro, micro and nano levels. The performance of this material when used as part of a novel implant-abutment-crown assembly was thoroughly investigated under simulated clinical conditions. The biological properties of the proprietary ‘*MDS*’ surface used with this material were investigated with respect to its biocompatibility, ability to promote growth and differentiation of key performers in the osseointegration and connective tissue attachment processes namely, osteoblasts and gingival fibroblasts.

The findings from crystallographic studies (Chapter 2) indicated that the simulated *LTD* using hydrothermal treatment induced localised phase transformation that was confined to the most superficial layer of the material. The resultant monoclinic phase attained highest concentration on the shallowest layer of the material and decreased exponentially toward the bulk. The depth of the transformed zone increased by less than 0.5 μm as a result of the hydrothermal ageing. The integrity of the bulk of the material (*LTD*-free) was confirmed using high energy Synchrotron radiation. The direct imaging of the *LTD*-affected zone indicated that the consequences of phase transformation were limited to moderate crystal pull-out and loss of homogeneity of grain boundaries with no evidence of microcracking.

The current study demonstrated significant variation and inconsistency upon studying the *LTD* phenomenon using different techniques or more interestingly, using different data analysis methods for data obtained using the same technique. These findings cast doubts on the validity of setting a fixed percentage of monoclinic phase as a sole determinant for the fitness for clinical use, as per ISO recommendations for testing zirconia implants. Alternatively, we propose the use of multiple, complementary techniques to quantify and profile the monoclinic phase along the thickness of the material. Additionally, the effect of *LTD* should be directly characterised with respect to its effects on the material using imaging and mechanical

techniques to analyse the consequences of the formation of monoclinic phase rather than strictly identifying it.

Investigation of mechanical properties (Chapter 3) of the transformed zone was performed. The findings indicated that the used hydrothermal treatment did not adversely affect the studied mechanical properties of the material apart from marginal decrease in the hardness of the most superficial layer of the material. An interesting finding was the abrupt, significant increase in hardness and Young's modulus values of the layer of the material intervening between the layer with highest (surface) and lowest (bulk) phase transformation in as-received and aged groups. The injection moulding manufacturing technique could be partly responsible for this toughening mechanism via the strong texture or preferred orientation of the crystals. Additionally, the presence of low level of phase transformation could induce compressive stresses on the crystalline system and induce such a toughening effect.

The studied material exhibited high mechanical properties that were not adversely affected by the hydrothermal treatment. Static mechanical testing revealed that the studied, relevant basic mechanical properties of samples with standard geometry were maintained in the aged group. The material retained high strength and hardness reliability in as-received and aged groups.

The use of the studied material as part of a dental implant system with a novel design was investigated. Dynamic fatigue tests revealed that the proposed design may fulfil the requirements for implant reconstructions used in the aesthetic zone. Samples, prepared exactly as to be used in clinical situation, survived extreme, long-term, simulated clinical conditions. Additionally, samples retained high post-fatigue failure loads, well above the accepted strength level for anterior reconstructions. Furthermore, the potential protective effect of the engineered weak link in the design, using of adhesively cemented low strength *GFC* abutment, was proved to be effective. The use of such a design reduced the catastrophic failures involving the implant head and introduced notable plastic behaviour in a supposedly rather brittle system. This effect was more pronounced when the assembly was restored with a glass ceramic crown restoration. The failures were confined to the abutment and/or crown which can be easily rectified in the clinical situation.

The use of a roughened mould and the proprietary acid etching technique successfully induced alteration in surface topography of the studied zirconia material (Chapter 4). The surface roughness was very comparable to that of a highly micro-textured *cpTi* surface. The studied material demonstrated a highly biocompatible effect on osteoblast-like cells and human gingival fibroblasts. When compared to a ‘gold standard’ *cpTi* surface, the studied zirconia (*MDS*) surface resulted in higher proliferation rates of both cell types at earlier stages of incubation. There were no notable differences on the viability of both cell types however.

In conclusion, the studied implant material/design may fulfil basic aesthetic, mechanical and biological requirements for dental implants placed in the aesthetic zone. The material may exhibit ageing-resistance properties when used *in vivo*. The studied design may overcome shortcomings with other zirconia dental implant systems. The use of this material may negate the need for invasive grafting procedures required to prevent or treat aesthetic complications associated with conventional titanium based implant materials.

5.3 Future Work

5.3.1 Ageing and crystallographic studies

The fact that this study is the first to investigate a ceramic injection moulded *Y-TZP* implants provides a large scope of future work. This is particularly relevant amid the area of *LTD* or ageing. The current findings of this study need further verification using different ageing techniques and protocols. First and foremost, the validity of the prediction of *LTD* utilising standard high temperature and pressure treatments should be further verified by calculating the $t \rightarrow m$ activation energy of this particular material using T-T-T graphs. Additionally, prolongation of the treatment cycle, using different mediums such as saliva and utilisation of chemical elements in the ageing treatments such as acidic or alkaline compounds may provide better understanding to the material’s susceptibility to *LTD*.

Estimating *LTD* of this material under low temperature and a pressure-free environment may be urgently needed especially in the light of new studies that cast doubts on the true representation of intermediate temperature ageing techniques of the *in vivo* situation. Prolonged soaking of zirconia samples at 37 °C in blood, serum or

saliva followed by through assessment of *LTD* and its effects on the material should be instigated. *In vivo LTD* studies should be performed on implanted material in animals' jaws.

The virtue of using complimentary techniques that detect and quantify $t \rightarrow m$ as well as the effects of this process on the material was highly emphasised in this piece of work. There remains the option of utilising further advanced crystallographic techniques such as *AFM*, *Ct-XRD* and *in situ EBSD-SEM* on *FIB* prepared samples. This is highly important in order to accurately map the areas that sustain $t \rightarrow m$ and further examine the morphological changes associated with such process. Furthermore, depth analysis of $t \rightarrow m$ using the *GIAXRD* technique utilised in this project may need further corroboration using other techniques such as high energy neutron diffraction and high energy Raman Spectroscopy. Lastly, comparison of *LTD* rates for this particular material and other zirconia materials manufactured using different techniques should be investigated to determine vital differences, if any, and rectify possible shortcomings.

5.3.2 System's reliability and performance

The current piece of work comprehensively investigated the basic mechanical properties of the studied *Y-TZP* material. However, impact strength, fracture toughness, scratch resistance and rotational fracture strength resistance may be among the other important mechanical properties to visit. Additionally, edge fracture strength can be further verified in both as-received and aged groups using different testing setups to ensure that the obtained findings in the current work are not merely due to the use of a static edge fracture strength test.

Dynamic fatigue testing was carried out at high loads and frequency. It may be worthwhile repeating this test using lower loads and a very low frequency in order to account for the time-dependent water assisted crack growth and improve the test's representation of clinical conditions. Thermocycling during the dynamic fatigue test may also be beneficial for the same latter reason. The use of different abutment and crown materials may be advisable in order to identify the best material combination that serves the ethos of engineered weak link and the concept of retrievable failures.

From the clinical point of view, testing resin nano-ceramic composites such as Lava™ Ultimate and Vita Enamic® or high density biocompatible polymers such as *PEEK* is of great importance. These may potentially outperform the currently used *GFC* (Triflor®) as an abutment material owing to their ease of manufacture (chair-side custom-design and milling ability), high strength and plasticity and good bond strength with various resin luting cements. Similarly, micro-tensile and shear bond strength as well as abutment pull-out strength studies can be performed using various commercially available cements. This is particularly important to identify the most appropriate candidate that ensures long-term durability and at the same time, maintain the system's plastic behaviour that fulfils the aim of the engineered weak link and retrievable failure concept. Finite Element Analysis can be a valuable tool to identify the most favourable cements/materials combination that ensures optimum stress distribution patterns along the implant-abutment-crown assembly.

Several post-fatigue investigations can be further performed. For example, crown marginal integrity or gap can be compared before and after cyclic loading using high magnification imaging techniques such as *SEM*. Micro-CT scanning can be performed also to detect changes or distortion within the implant-abutment connection that could be a result due to micro-movement. The latter is a very important aspect to investigate as micro-movement significantly affects the short- and long-term success of soft and hard tissue integration.

The current study revealed that implant head preparation was a very likely initiator for implant head failure. Preparation led to thinner material between the internal connection and the crown margins where all critical cracks propagated and caused catastrophic implant head failure. These findings have been already conveyed to the manufacturer with recommendations for rectifying such issues. The dimensions of internal connection have been reduced by 1 mm at the expense of the dimensions of the abutment. We predict no drastic effects on the abutment strength as none of the failures involved the abutment. In addition, smaller abutments survived fatigue tests when used with 4 mm diameter implants. Additionally, the need to prepare a finish line on the implant head was reduced by introducing a knife-edge bevel on the circumference of the implant head in the modified design. Comparing the initial and post-fatigue failure modes and loads of implants with prepared and genuine finish lines

may be an important future project. Appendix G shows a comparative drawing of the two designs.

Work is also in progress to design an implant head with anatomical finish line to completely negate the need for implant head preparation. Furthermore, a reverse 4° taper (from head to neck) was also recommended to increase the thickness of attached connective tissue. The survival of those designs needs to be tested. It would also be interesting to compare dynamic fatigue results with titanium implants restored with zirconia abutment and all-ceramic crowns. Zirconia–resin-abutment adhesive bond strength tests, abutment pull test, are required to assess performance of re-bonded abutments.

5.3.3 Biological Studies

The biological studies in Chapter 4 is the least comprehensive one. The intricate process of osseointegration and periointegration coupled with complex host tissue response to implanted materials necessitate further rigorous biological studies. A multitude of *in vitro* tests can be further performed to characterise the biofunctional response of the various tissue components to the studied implant material. Studying the effect of the material on undifferentiated mesenchymal cells can be performed. This can be achieved by investigating the expression of certain surface markers using different techniques such as flow cytometry. **qRT-PCR** can be repeated using primary osteoblasts isolated from healthy human jaw bone. This can be more relevant to dental implant related research. Additionally, a larger spectrum of genes can be investigated that can be more representative of various stages of bone healing and formation. Protein adsorption studies using various techniques such as fluorescence emission spectroscopy can be vital to improve our understanding of the alleged superior soft tissue integration capacity of zirconia. Furthermore, studying the effect of this material on osteoblasts and fibroblasts at protein level is essential to substantiate the data from **qRT-PCR** studies. This can be performed using quantitative proteomics and other qualitative/quantitative techniques such as Western Blot.

Studying the response of human oral keratinocytes to this material should be evaluated. Additionally, to attain better comparison between the studied material and other **cpTi** implant systems in terms of soft tissue attachment. Our experiments should be repeated using smoother titanium surfaces as most of implant systems tend to

reduce the surface roughness of the implant part contacting soft tissues. Furthermore, immunohistochemistry studies can be of a great value to assess morphological changes at the level of cytoskeleton of cells and thereby cell attachment. Additionally, such studies may demonstrate the scarcity/abundance of *FACs* by staining and visualising their protein building blocks such as fibronectin and vinculin.

The use of full-thickness tissue engineered human oral mucosal model to assess soft tissue response to the studied material is recommended. It can overcome some of the shortcomings associated with the use of standard monolayer tissue culture procedures and provide a better insight into the biofunctional response to the implanted materials. However, both techniques fail to simulate the multifaceted *in vivo* processes at the level of bone and soft tissues. Ultimately, assessment of the osseointegration and periosteal integration capacities of the material should be performed using *in vivo* animal studies. A multitude of studies can be used for this purpose including; (1) assessment of clinical parameters such as mobility and probing depth, (2) histological assessment of *BIC* ratio and morphological characteristics of the biologic width, (3) immunohistochemical analysis such as *ALP* staining, detection of inflammatory markers and (4) mechanical tests such as removal torque, push-in and pull-out studies.

It is worthwhile to mention that such studies are currently being conducted by our research collaborators overseas. Finally, long-term randomised controlled trials are currently being planned to validate the use of such a design as a replacement or an adjunct to conventional *cpTi* implant systems.

Chapter 6: References

- ABOUSHELIB, M. N., OSMAN, E., JANSEN, I., EVERTS, V. & FEILZER, A. J. 2013a. Influence of a nanoporous zirconia implant surface of on cell viability of human osteoblasts. *Journal of Prosthodontics*, 22, 190-195.
- ABOUSHELIB, M. N., SALEM, N. A., TALEB, A. L. A. & EL MONIEM, N. M. A. 2013b. Influence of Surface Nano-Roughness on Osseointegration of Zirconia Implants in Rabbit Femur Heads Using Selective Infiltration Etching Technique. *Journal of Oral Implantology*, 39, 583-590.
- ABRAHAMSSON, I., BERGLUNDH, T. & LINDHE, J. 1997. The mucosal barrier following abutment dis/reconnection. *Journal of Clinical Periodontology*, 24, 568-572.
- ABRAHAMSSON, I. & CARDAROPOLI, G. 2007. Peri-implant hard and soft tissue integration to dental implants made of titanium and gold. *Clinical Oral Implants Research*, 18, 269-274.
- ABRAHAMSSON, I., ZITZMANN, N. U., BERGLUNDH, T., LINDER, E., WENNERBERG, A. & LINDHE, J. 2002. The mucosal attachment to titanium implants with different surface characteristics: an experimental study in dogs. *Journal of Clinical Periodontology*, 29, 448-455.
- ADELL, R., ERIKSSON, B., LEKHOLM, U., BRÅNEMARK, P. I. & JEMT, T. 1990. Long-term follow-up study of osseointegrated implants in the treatment of totally edentulous jaw. *International Journal of Oral & Maxillofacial Implants* 5, 347-359.
- ADELL, R., LEKHOLM, U., ROCKIER, B. & BRÅNEMARK, P. I. 1981. A 15years study of osseointegrated implants in the treatment of the edentulous jaw. *Int. J. Oral Surg.*, 10, 387-416.
- AKAGAWA, Y. & ABE, Y. 2003. Titanium: the ultimate solution or an evolutionary step? *Int J Prosthodont*, 16.
- AL-NAWAS, B., GROETZ, K. A., GOETZ, H., DUSCHNER, H. & WAGNER, W. 2008. Comparative histomorphometry and resonance frequency analysis of implants with moderately rough surfaces in a loaded animal model. *Clinical Oral Implants Research*, 19, 1-8.
- AL-SHAMMERY, H. A., BUBB, N. L., YOUNGSON, C. C., FASBINDER, D. J. & WOOD, D. J. 2007. The use of confocal microscopy to assess surface roughness of two milled CAD–CAM ceramics following two polishing techniques. *dental materials*, 23, 736-741.
- ALBREKTSSON, T., BRÅNEMARK, P. I., HANSSON, H. A. & LINDSTRÖM, J. 1981. Osseointegrated titanium implants: requirements for ensuring a long-lasting, direct bone-to-implant anchorage in man. *Acta Orthopaedica*, 52, 155-170.
- ALBREKTSSON, T., BUSER, D. & SENNERBY, L. 2012. Crestal Bone Loss and Oral Implants. *Clinical Implant Dentistry and Related Research*, 14, 783-791.

- ALBREKTSSON, T., DAHL, EVERT, ENBOM, LARS, ENGEVALL, SIGFRID, ENGQUIST, BO , ERIKSSON, ANDERS R., FELDMANN, GÜNTHER, FREIBERG, NILS, GLANTZ, PER-OLOF , KJELLMAN, OLOF, KRISTERSSON, LARS, KVINT, SVEN, KÖNDELL, PER-ÅKE, PALMQUIST, JAN, WERNDAHL, LARS, ÅSTRAND, PER 1988. Osseointegrated Oral Implants *Journal of Periodontology*, 59, 287-296.
- ALBREKTSSON, T. & WENNERBERG, A. 2004. Oral implant surfaces: Part 1-- review focusing on topographic and chemical properties of different surfaces and *in vivo* responses to them. *Int J Prosthodont*, 17, 536-43.
- ALLAIN, J., LE MOUEL, S., GOUTALLIER, D. & VOISIN, M. C. 1999. Poor eight-year survival of cemented zirconia-polyethylene total hip replacements. *Journal of Bone & Joint Surgery, British Volume*, 81, 835-842.
- ALMER, J., LIENERT, U., PENG, R. L., SCHLAUER, C. & OĐEN, M. 2003. Strain and texture analysis of coatings using high-energy X-Rays. *Journal of applied physics*, 94, 697-702.
- ANDERSSON, B., GLAUSER, R., MAGLIONE, M. & TAYLOR, A. 2003. Ceramic implant abutments for shortspan FPDs: a prospective 5-year multicenter study. *The International Journal of Prosthodontics*, 16, 640-646.
- ANDREIOTELLI, M. & KOHAL, R.-J. 2009. Fracture Strength of Zirconia Implants after Artificial Aging. *Clinical Implant Dentistry and Related Research*, 11, 158-166.
- ANDREIOTELLI, M., WENZ, H. J. & KOHAL, R.-J. 2009. Are ceramic implants a viable alternative to titanium implants? A systematic literature review. *Clinical Oral Implants Research*, 20, 32-47.
- ANGELA, D., GIUSEPPA, V., SEBASTIANO, L., ROSANNA, M., BARBARA, B., GIOVANNI, M., LUCIANO, C. & MARIA, E. 2008. Biomonitoring of DNA damage in peripheral blood lymphocytes of subjects with dental restorative fillings. *Mutation Research/Genetic Toxicology and Environmental Mutagenesis*, 650, 115-122.
- ANSELME, K., BIGERELLE, M., NOEL, B., DUFRESNE, E., JUDAS, D., IOST, A. & HARDOUIN, P. 2000. Qualitative and quantitative study of human osteoblast adhesion on materials with various surface roughnesses. *J Biomed Mater Res*, 49, 155-66.
- ANUSAVICE, K. J. 2014. *Phillips' Science of Dental Materials*, Elsevier Health Sciences.
- ARDLIN, B. I. 2002. Transformation-toughened zirconia for dental inlays, crowns and bridges: chemical stability and effect of low-temperature aging on flexural strength and surface structure. *Dental Materials*, 18, 590-595.
- ARGYRIOU, D. N. & HOWARD, C. J. 1995. Re-investigation of Ytria-tetragonal Zirconia Polycrystal (Y-TZP) by neutron powder diffraction-a cautionary tale. *Journal of applied crystallography*, 28, 206-208.
- ASTMF1873-98 1998. Standard Specification for High-Purity Dense Ytria Tetragonal Zirconium Oxide Polycrystal (Y-TZP) for Surgical Implant Applications (Withdrawn 2007), ASTM International, West Conshohocken, PA.

- BÄCHLE, M., BUTZ, F., HÜBNER, U., BAKALINIS, E. & KOHAL, R. J. 2007. Behavior of CAL72 osteoblast-like cells cultured on zirconia ceramics with different surface topographies. *Clinical oral implants research*, 18, 53-59.
- BÅGEDAHL-STRINDLUND, M., HIE, M., FURHOTF, A. K., TOMSON, Y., LARSSON, K. S., SANDBORGH-ENGLUND, G., TORSTENSON, B. & WRETLIND, K. 1997. A multidisciplinary clinical study of patients suffering from illness associated with mercury release from dental restorations: psychiatric aspects. *Acta Psychiatrica Scandinavica*, 96, 475-482.
- BAHARLOO, B., TEXTOR, M. & BRUNETTE, D. M. 2005. Substratum roughness alters the growth, area, and focal adhesions of epithelial cells, and their proximity to titanium surfaces. *Journal of Biomedical Materials Research Part A*, 74A, 12-22.
- BAN, S. & ANUSAVICE, K. J. 1990. Influence of test method on failure stress of brittle dental materials. *Journal of Dental Research*, 69, 1791-1799.
- BAN, S., SATO, H., SUEHIRO, Y., NAKANISHI, H. & NAWA, M. 2008. Biaxial flexure strength and low temperature degradation of Ce-TZP/Al₂O₃ nanocomposite and Y-TZP as dental restoratives. *Journal of Biomedical Materials Research Part B: Applied Biomaterials*, 87B, 492-498.
- BANNISTER, M. 1993. *Science and Technology of Zirconia V*, Taylor & Francis.
- BD BIOSCIENCES 2006. Introduction to Flow Cytometry: A Learning Guide. Available from: www.d.umn.edu/~biomed/flowcytometry/introflowcytometry.pdf. [Last accessed, 28 February 2015].
- BEERTSEN, W., MCCULLOCH, C. A. G. & SODEK, J. 1997. The periodontal ligament: a unique, multifunctional connective tissue. *Periodontology 2000*, 13, 20-40.
- BERGLUNDH, T., LINDHE, J., ERICSSON, I., MARINELLO, C. P., LILJENBERG, B. & THORNSSEN, P. 1991. The soft tissue barrier at implants and teeth. *Clinical oral implants research*, 2, 81-90.
- BERMÚDEZ, M.-D., CARRIÓN, F. J., MARTÍNEZ-NICOLÁS, G. & LÓPEZ, R. 2005. Erosion–corrosion of stainless steels, titanium, tantalum and zirconium. *Wear*, 258, 693-700.
- BEST, S. M., PORTER, A. E., THIAN, E. S. & HUANG, J. 2008. Bioceramics: Past, present and for the future. *Journal of the European Ceramic Society*, 28, 1319-1327.
- BEUER, F., EDELHOFF, D., GERNET, W. & SORENSEN, J. 2009. Three-year clinical prospective evaluation of zirconia-based posterior fixed dental prostheses (FDPs). *Clinical Oral Investigations*, 13, 445-451.
- BEUER, F., STIMMELMAYR, M., GUETH, J.-F., EDELHOFF, D. & NAUMANN, M. 2012. *In vitro* performance of full-contour zirconia single crowns. *Dental Materials*, 28, 449-456.
- BIANCHI, A., BOSETTI, M., DOLCI, G., SBERNA, M., SANFILIPPO, F. & M., C. 2004. *In vitro* and *in vivo* follow-up of titanium transmucosal implants with zirconia collar. *J Appl Biomater Biomech.*, 2, 143-150.
- BICO, J., THIELE, U. & QUÉRÉ, D. 2002. Wetting of textured surfaces. *Colloids and Surfaces A: Physicochemical and Engineering Aspects*, 206, 41-46.

- BINNER, J., VAIDHYANATHAN, B., PAUL, A., ANNAPORANI, K. & RAGHUPATHY, B. 2011. Compositional effects in nanostructured yttria partially stabilised zirconia. *International Journal of Applied Ceramic Technology*, 8, 766-782.
- BLACK, J., SHERK H, BONINI J, ROSTOKER WR, SCHAJOWICZ F & JO., G. 1990. Metallosis associated with a stable titanium-alloy femoral component in total hip replacement: A case report. *J Bone Jt Surg Am*, 72, 126-130.
- BLATZ, M. B., SADAN, A., MARTIN, J. & LANG, B. 2004. *In vitro* evaluation of shear bond strengths of resin to densely-sintered high-purity zirconium-oxide ceramic after long-term storage and thermal cycling. *The Journal of Prosthetic Dentistry*, 91, 356-362.
- BORCHERS, L., STIESCH, M., BACH, F.-W., BUHL, J.-C., HÜBSCH, C., KELLNER, T., KOHORST, P. & JENDRAS, M. 2010. Influence of hydrothermal and mechanical conditions on the strength of zirconia. *Acta Biomaterialia*, 6, 4547-4552.
- BOWDEN, M., DICKSON, G. D., GARDINER, D. J. & WOOD, D. J. 1993. Patterns of stress-induced phase transformation in MgO-stabilised zirconia ceramic revealed using micro-Raman imaging. *Journal of Materials Science*, 28, 1031-1036.
- BOWEN, R. L. & RODRIGUEZ, M. S. 1962. Tensile strength and modulus of elasticity of tooth structure and several restorative materials. *Journal of the American Dental Association (1939)*, 64, 378-387.
- BRÅNEMARK, P.-I. 1959. Vital microscopy of bone marrow in rabbit. *Scandinavian journal of clinical and laboratory investigation*, 11, 1.
- BRÅNEMARK, P.-I. 1983. Osseointegration and its experimental background. *The Journal of Prosthetic Dentistry*, 50, 399-410.
- BRÅNEMARK, P. I., HANSSON, B. O., ADELL, R., BREINE, U., LINDSTRÚM, J., HALLÖN, O. & OHMAN, A. 1977. Osseointegrated implants in the treatment of the edentulous jaw. Experience from a 10-year period. *Scandinavian journal of plastic and reconstructive surgery. Supplementum*, 16, 1-132.
- BREMHOLM, M., BECKER-CHRISTENSEN, J. & IVERSEN, B. B. 2009. High-Pressure, High-Temperature Formation of Phase-Pure Monoclinic Zirconia Nanocrystals Studied by Time-Resolved *in situ* Synchrotron X-Ray Diffraction. *Advanced Materials*, 21, 3572-3575.
- BRESSAN, E., PANIZ, G., LOPS, D., CORAZZA, B., ROMEO, E. & FAVERO, G. 2011. Influence of abutment material on the gingival color of implant-supported all-ceramic restorations: a prospective multicenter study. *Clinical oral implants research*, 22, 631-637.
- BRODBECK, U. 2003. The ZiReal Post: a new ceramic implant abutment. *Journal of Esthetic and Restorative Dentistry*, 15, 10-23.
- BROWN, L. 2010. *Limited Edition Vertebrae ZTA, ready to ship* [Online]. Available: <http://www.vertebr.ae/news/vertebrae-zta-limited-edition/> [Accessed 30 July 2012].
- BULL, S. J., PAGE, T. F. & YOFFE, E. H. 1989. An explanation of the indentation size effect in ceramics. *Philosophical magazine letters*, 59, 281-288.

- BURRIDGE, K. & CHRZANOWSKA-WODNICKA, M. 1996. Focal adhesions, contractility, and signaling. *Annual review of cell and developmental biology*, 12, 463-519.
- BUSER, D., BROGGINI, N., WIELAND, M., SCHENK, R. K., DENZER, A. J., COCHRAN, D. L., HOFFMANN, B., LUSSI, A. & STEINEMANN, S. G. 2004. Enhanced bone apposition to a chemically modified SLA titanium surface. *J Dent Res*, 83, 529-33.
- BUSER, D., JANNER, S. F. M., WITTNEBEN, J.-G., BRÄGGER, U., RAMSEIER, C. A. & SALVI, G. E. 2012. 10-Year Survival and Success Rates of 511 Titanium Implants with a Sandblasted and Acid-Etched Surface: A Retrospective Study in 303 Partially Edentulous Patients. *Clinical Implant Dentistry and Related Research*, 14, 839-851.
- BUSER, D., SCHENK, R. K., STEINEMANN, S., FIORELLINI, J. P., FOX, C. H. & STICH, H. 1991. Influence of surface characteristics on bone integration of titanium implants. A histomorphometric study in miniature pigs. *Journal of Biomedical Materials Research*, 25, 889-902.
- BUSER, D., WEBER, H. P., DONATH, K., FIORELLINI, J. P., PAQUETTE, D. W. & WILLIAMS, R. C. 1992. Soft Tissue Reactions to Non-Submerged Unloaded Titanium Implants in Beagle Dogs. *Journal of Periodontology*, 63, 225-235.
- BUTZ, F., HEYDECKE, G., OKUTAN, M. & STRUB, J. R. 2005. Survival rate, fracture strength and failure mode of ceramic implant abutments after chewing simulation. *Journal of Oral Rehabilitation*, 32, 838-843.
- CALES, B. 2000. Zirconia as a sliding material: histologic, laboratory, and clinical data. *Clinical orthopaedics and related research*, 379, 94-112.
- CALES, B., STEFANI, Y. & LILLEY, E. 1994. Long-term *in vivo* and *in vivo* aging of a zirconia ceramic used in orthopaedy. *Journal of Biomedical Materials Research*, 28, 619-624.
- CALLISTER, W. D. & RETHWISCH, D. G. 2012. *Fundamentals of Materials Science and Engineering: An Integrated Approach*, Wiley.
- CANNIZZARO, G., TORCHIO, C., FELICE, P., LEONE, M. & ESPOSITO, M. 2010. Immediate occlusal versus non-occlusal loading of single zirconia implants. A multicentre pragmatic randomised clinical trial. *Eur J Oral Implantol*, 3, 111-120.
- CANULLO, L. 2006. Clinical outcome study of customised zirconia abutments for single-implant restorations. *The International journal of prosthodontics*, 20, 489-493.
- CARLSSON, L., RÖSTLUND, T., ALBREKTSSON, B. R. & ALBREKTSSON, T. 1988. Implant fixation improved by close fit Cylindrical implant-bone interface studied in rabbits. *Acta Orthopaedica*, 59, 272-275.
- CARLSSON, L., RÖTLUND, T., ALBREKTSSON, B. R., ALBREKTSSON, T. & BRÅNEMARK, P.-I. 1986. Osseointegration of titanium implants. *Acta Orthopaedica*, 57, 285-289.
- CARMINE, M. D., TOTO, P., FELICIANI, C., SCARANO, A., TULLI, A., STROCCHI, R. & PIATTELLI, A. 2003. Spreading of epithelial cells on

- machined and sandblasted titanium surfaces: an *in vitro* study. *Journal of Periodontology*, 74, 289-295.
- CASELLAS, D., FEDER, A., LLANES, L. & ANGLADA, M. 2001. Fracture toughness and mechanical strength of *Y-TZP/PSZ* ceramics. *Scripta Materialia*, 45, 213-220.
- CATELAS, I., PETIT, A., ZUKOR, D., MARCHAND, R., YAHIA, L. & HUK, O. 1999. Induction of macrophage apoptosis by ceramic and polyethylene particles *in vitro*. *Biomaterials*, 20, 625-630.
- CATLEDGE, S. A., COOK, M., VOHRA, Y. K., SANTOS, E. M., MCCLENNY, M. D. & MOORE, K. D. 2003. Surface crystalline phases and nanoindentation hardness of explanted zirconia femoral heads. *Journal of Materials Science: Materials in Medicine*, 14, 863-867.
- CATTANI-LORENTE, M., SCHERRER, S., AMMANN, P., JOBIN, M. & WISKOTT, A. 2011. Low temperature degradation of a *Y-TZP* dental ceramic. *Acta Biomaterialia*, 7, 858-865.
- ÇEHRELI, M. C., KÖKAT, A. M., & AKÇA, K. 2009. CAD/CAM Zirconia vs. slip-cast glass-infiltrated Alumina/Zirconia all-ceramic crowns: 2-year results of a randomized controlled clinical trial. *Journal of Applied Oral Science*, 17, 49-55.
- CHAIYABUTR, Y., MCGOWAN, S., PHILLIPS, K. M., KOIS, J. C. & GIORDANO, R. A. 2008. The effect of hydrofluoric acid surface treatment and bond strength of a zirconia veneering ceramic. *The Journal of Prosthetic Dentistry*, 100, 194-202.
- CHAMBRONE, L., SHIBLI, J. A., MERCÚRIO, C. E., CARDOSO, B. & PRESHAW, P. M. 2014. Efficacy of standard (SLA) and modified sandblasted and acid-etched (SLActive) dental implants in promoting immediate and/or early occlusal loading protocols: a systematic review of prospective studies. *Clinical Oral Implants Research*, .
- CHAN, C. J., LANGE, F. F., RÜHLE, M., JUE, J. F. & VIRKAR, A. V. 1991a. Ferroelastic domain switching in tetragonal zirconia single crystals-microstructural aspects. *Journal of the American Ceramic Society*, 74, 807-813.
- CHAN, S.-K., FANG, Y., GRIMSDITCH, M., LI, Z., NEVITT, M. V., ROBERTSON, W. M. & ZOUBOULIS, E. S. 1991b. Temperature Dependence of the Elastic Moduli of Monoclinic Zirconia. *Journal of the American Ceramic Society*, 74, 1742-1744.
- CHAVRIER, C. A. & COUBLE, M. L. 1998. Ultrastructural immunohistochemical study of interstitial collagenous components of the healthy human keratinized mucosa surrounding implants. *The International journal of oral & maxillofacial implants*, 14, 108-112.
- CHEHROUDI, B., GOULD, T. R. L. & BRUNETTE, D. M. 1992. The role of connective tissue in inhibiting epithelial downgrowth on titanium-coated percutaneous implants. *Journal of Biomedical Materials Research*, 26, 493-515.
- CHEN, D., ZHAO, M. & MUNDY, G. R. 2004. Bone morphogenetic proteins. *Growth factors*, 22, 233-241.

- CHEVALIER, J., CALES, B. & DROUIN, J. M. 1999a. Low-Temperature Aging of *Y-TZP* Ceramics. *Journal of the American Ceramic Society*, 82, 2150-2154.
- CHEVALIER, J., DROUIN, J. M. & CALES, B. 1997. Low temperature ageing behaviour of zirconia hip joint heads. *Bioceramics*, 10, 135-138.
- CHEVALIER, J., GREMILLARD, L. & DEVILLE, S. 2007a. Low-temperature degradation of zirconia and implications for biomedical implants. *Annu. Rev. Mater. Res.*, 37, 1-32.
- CHEVALIER, J., GREMILLARD, L., VIRKAR, A. V. & CLARKE, D. R. 2009. The Tetragonal-Monoclinic Transformation in Zirconia: Lessons Learned and Future Trends. *Journal of the American Ceramic Society*, 92, 1901-1920.
- CHEVALIER, J., LAURENT GREMILLARD & DEVILLE, S. 2007b. Low-Temperature Degradation of Zirconia and Implications for Biomedical Implants. *Annu. Rev. Mater. Res.*, 37, 1-32.
- CHEVALIER, J., OLAGNON, C. & FANTOZZI, G. 1999b. Subcritical Crack Propagation in 3Y-TZP Ceramics: Static and Cyclic Fatigue. *Journal of the American Ceramic Society*, 82, 3129-3138.
- CHEVALIER, J., OLAGNON, C., FANTOZZI, G. & GALÃS, B. 1995. Crack Propagation Behavior of Y-TZP Ceramics. *Journal of the American Ceramic Society*, 78, 1889-1894.
- CHEVALIER, J. R. M., DEVILLE, S., MÜNCH, E., JULLIAN, R. & LAIR, F. D. R. 2004. Critical effect of cubic phase on aging in 3-mol% yttria-stabilised zirconia ceramics for hip replacement prosthesis. *Biomaterials*, 25, 5539-5545.
- CHRISTEL, P., MEUNIER, A., DORLOT, J.-M., CROLET, J.-M., WITVOET, J., SEDEL, L. & BOUTIN, P. 1988. Biochemical compatibility and design of ceramic implants for orthopaedic surgery. *Bioceramics: material characteristics versus in vivo behaviour. Ann NY Acad Sci*, 523, 234-256.
- CHRISTIANE, K.-K., TOMASZ, G., DAGMAR-ULRIKE, R., MARIUSZ, S., MARZENA, D. & TOMASZ, G. 2012. The survival and proliferation of fibroblasts on ceramic implants: an *in vitro* study. *Biomed Tech*, 57, 11-15.
- CHRISTIE, T. & BRATHWAITE, B. 1999. Mineral commodity report 19: Beryllium, Gallium, Lithium, Magnesium, Iridium and Zirconium. *New Zealand Mining. Institute of geological and nuclear sciences.*
- CIONCA, N., MULLER, N. & MOMBELLI, A. 2014. Two-piece zirconia implants supporting all-ceramic crowns: A prospective clinical study. *Clinical oral implants research.*
- CLARKE, D. R. & ADAR, F. 1982. Measurement of the Crystallographically Transformed Zone Produced by Fracture in Ceramics Containing Tetragonal Zirconia. *Journal of the American Ceramic Society*, 65, 284-288.
- COCHRAN, D. L., HERMANN, J. S., SCHENK, R. K., HIGGINBOTTOM, F. L. & BUSER, D. 1997. Biologic Width Around Titanium Implants. A Histometric Analysis of the Implant-Gingival Junction Around Unloaded and Loaded Nonsubmerged Implants in the Canine Mandible. *Journal of Periodontology*, 68, 186-197.

- COLTHUP, N. B., DALY, L. H. & WIBERLEY, S. E. 1990. *Introduction to infrared and Raman spectroscopy*, Elsevier.
- COSYN, J., DE BRUYN, H. & CLEYMAET, R. 2012. Soft Tissue Preservation and Pink Aesthetics around Single Immediate Implant Restorations: A 1-Year Prospective Study. *Clinical Implant Dentistry and Related Research*, no-no.
- COSYN, J., HOOGHE, N. & DE BRUYN, H. 2008. A systematic review on the frequency of advanced recession following single immediate implant treatment. *Journal of Clinical Periodontology*, 39, 582-589.
- CRAIG, R. G. & WARD, M. L. 1997. *Restorative Dental Materials*, Mosby.
- CRANIN, A., SCHNITMAN, P., RABKIN, S. & ONESTO, E. 1975. Alumina and zirconia coated vitallium oral endosteal implants in beagles. *J Biomed Mater Res*, 9, 257-262.
- CURTIS, A. R., WRIGHT, A. J. & FLEMING, G. J. P. 2006. The influence of simulated masticatory loading regimes on the bi-axial flexure strength and reliability of a *Y-TZP* dental ceramic. *Journal of Dentistry*, 34, 317-325.
- DANZER, R., HANGL, M. & PAAR, R. How to design with brittle materials against edge flaking. 6th International Symposium on Ceramic Materials and Components for Engines, 1997.
- DANZER, R., SUPANCIC, P., PASCUAL, J. & LUBE, T. 2007. Fracture statistics of ceramics Weibull statistics and deviations from Weibull statistics. *Engineering Fracture Mechanics*, 74, 2919-2932.
- DAUSKARDT, R. H. & RITCHIE, R. O. 1991. Cyclic fatigue of ceramics. *Fatigue of Advanced Materials*, 133-151.
- DE BOEVER, J. A., MCCALL, W. D., JR., HOLDEN, S. & ASH, M. M., JR. 1978. Functional occlusal forces: An investigation by telemetry. *Journal of Prosthetic Dentistry*, 40, 326-333.
- DE S. JAYATILAKA, A. 1979. *Fracture of engineering brittle materials*, Applied Science Publishers.
- DEGASNE, I., BASLÉ M. F., DEMAIS, V., HURE, G., LESOURD, M., GROLLEAU, B., MERCIER, L. & CHAPPARD, D. 1999. Effects of Roughness, Fibronectin and Vitronectin on Attachment, Spreading, and Proliferation of Human Osteoblast-Like Cells (Saos-2) on Titanium Surfaces. *Calcified Tissue International*, 64, 499-507.
- DEGIDI, M., ARTESE, L., SCARANO, A., PERROTTI, V., GEHRKE, P. & PIATTELLI, A. 2006. Inflammatory infiltrate, microvessel density, nitric oxide synthase expression, vascular endothelial growth factor expression, and proliferative activity in peri-implant soft tissues around titanium and zirconium oxide healing caps. *J Periodontology*, 77, 73-80.
- DELGADO-RUIZ, R. A., CALVO-GUIRADO, J. L., MORENO, P., GUARDIA, J., GOMEZ-MORENO, G., MATE-SÁNCHEZ, J. E., RAMIREZ-FERNÁNDEZ, P. & CHIVA, F. 2011. Femtosecond laser microstructuring of zirconia dental implants. *Journal of Biomedical Materials Research Part B: Applied Biomaterials*, 96B, 91-100.

- DELONG, R. & DOUGLAS, W. H. 1983. Development of an artificial oral environment for the testing of dental restoratives: bi-axial force and movement control. *Journal of Dental Research*, 62, 32-36.
- DEN HARTOG, L., HUDDLESTON SLATER, J. J. R., VISSINK, A., MEIJER, H. J. A. & RAGHOEBAR, G. M. 2008. Treatment outcome of immediate, early and conventional single-tooth implants in the aesthetic zone: a systematic review to survival, bone level, soft-tissue, aesthetics and patient satisfaction. *Journal of Clinical Periodontology*, 35, 1073-1086.
- DENRY, I. & KELLY, J. R. 2008. State of the art of zirconia for dental applications. *Dental Materials*, 24, 299-307.
- DENRY, I. L. & HOLLOWAY, J. A. 2006. Microstructural and crystallographic surface changes after grinding zirconia-based dental ceramics. *Journal of Biomedical Materials Research Part B: Applied Biomaterials*, 76, 440-448.
- DEPRICH, R., NAUJOKS, C., OMMERBORN, M., SCHWARZ, F., KÜBLER, N. R. & HANDSCHEL, J. 2012. Current Findings Regarding Zirconia Implants. *Clinical Implant Dentistry and Related Research*.
- DEPRICH, R., OMMERBORN, M., ZIPPRICH, H., NAUJOKS, C., HANDSCHEL, J. R., WIESMANN, H.-P., KÖBLER, N. R. & MEYER, U. 2008. Behavior of osteoblastic cells cultured on titanium and structured zirconia surfaces. *Head Face Med*, 4, 29.
- DEVILLE, S., CHEVALIER, J. R. M. & GREMILLARD, L. 2006. Influence of surface finish and residual stresses on the ageing sensitivity of biomedical grade zirconia. *Biomaterials*, 27, 2186-2192.
- DEVILLE, S., GREMILLARD, L., CHEVALIER, J. R. M. & FANTOZZI, G. 2005. A critical comparison of methods for the determination of the aging sensitivity in biomedical grade yttria-stabilised zirconia. *Journal of Biomedical Materials Research Part B: Applied Biomaterials*, 72, 239-245.
- DEVILLE, S., GUÉNIN, G. & CHEVALIER, J. 2004. Martensitic transformation in zirconia: Part II. Martensite growth. *Acta Materialia*, 52, 5709-5721.
- DEY, A. & MUKHOPADHYAY, A. K. 2014. *Nanoindentation of Brittle Solids*, Taylor & Francis.
- DIN, S.-U. & KALEEM, A. 1998. Vickers hardness study of zirconia partially stabilised with lanthanide group oxides. *Materials Chemistry and Physics*, 53, 48-54.
- DOERNER, M. F. & NIX, W. D. 1986. A method for interpreting the data from depth-sensing indentation instruments. *Journal of Materials Research*, 1, 601-609.
- DONLEY, T. G. & GILLETTE, W. B. 1991. Titanium endosseous implant-soft tissue interface: a literature review. *Journal of Periodontology*, 62, 153-160.
- DRISSI, H., LUC, Q., SHAKOORI, R., CHUVA DE SOUSA LOPES, S., CHOI, J.-Y., TERRY, A., HU, M., JONES, S., NEIL, J. C., LIAN, J. B., STEIN, J. L., VAN WIJNEN, A. J. & STEIN, G. S. 2000. Transcriptional autoregulation of the bone related CBFA1/RUNX2 gene. *Journal of Cellular Physiology*, 184, 341-350.
- DRUMMOND, J. L. 1989. *In Vitro* Aging of Yttria-Stabilised Zirconia. *Journal of the American Ceramic Society*, 72, 675-676.

- DU, J., JIANG, H.-H., MO, J.-J., ZHOU, Z.-H., ZHANG, Z.-Y. & LAI, H.-C. 2012. Effect of hydrophilic titanium surface on the proliferation and differentiation of osteoblasts. *China Journal of Oral and Maxillofacial Surgery*, 3, 005.
- DUCY, P. & KARSENTY, G. 1995. Two distinct osteoblast-specific cis-acting elements control expression of a mouse osteocalcin gene. *Molecular and Cellular Biology*, 15, 1858-69.
- ERIKSEN, E. F. 2010. Cellular mechanisms of bone remodeling. *Reviews in endocrine and metabolic disorders*, 11, 219-227.
- ESPOSITO, M., ARDEBILI, Y. & WORTHINGTON, H. V. 2014. Interventions for replacing missing teeth: different types of dental implants. *The Cochrane Library*.
- ESPOSITO, M., GRUSOVIN, M., COULTHARD, P. & WORTHINGTON, H. 2007. Interventions for replacing missing teeth: different types of dental implants. *Cochrane Oral Health Group*.
- ESPOSITO, M., GRUSOVIN, M., POLYZOS, L., FELICE, P. & WORTHINGTON, H. V. 2010. Timing of implant placement after tooth extraction: immediate, immediate-delayed or delayed implants? A Cochrane systematic review. *Eur J Oral Implantol*, 3, 189-205.
- ESPOSITO, M., GRUSOVIN, M. G., ACHILLE, H., COULTHARD, P. & WORTHINGTON, H. V. 2009. Interventions for replacing missing teeth: different times for loading dental implants. *Cochrane Database Syst Rev*, CD003878-CD003878.
- ESPOSITO, M., MAGHAIREH, H., GRUSOVIN, M., POLYZOS, L. P., ZIOUNAS, L. & WORTHINGTON, H. V. 2012. Interventions for replacing missing teeth: management of soft tissues for dental implants. *Cochrane Database Syst Rev*, 15.
- EVARD, L., WAROQUIER, D. & PARENT, D. 2010. Allergies to dental metals. Titanium: a new allergen. *Rev Med Brux*, 31, 44-49.
- FARGES, G. & DEGOUT, D. 1989. Interpretation of the indentation size effect in vickers microhardness measurements-absolute hardness of materials. *Thin Solid Films*, 181, 365-374.
- FASSINA, P., ZAGHINI, N., BUKAT, A., PICONI, C., GRECO, F. & PIANTELLI, S. 1992. Ytria and calcia partially stabilised zirconia for biomedical applications. *Bioceramics and the Human Body*. Springer.
- FENG C-E., WANG X. & YU Z. 2002. Neural networks modeling of honing surface roughness parameters defined by ISO 13565, *Journal of Manufacturing Systems*, 21 (5) 395-408, [http://dx.doi.org/10.1016/S0278-6125\(02\)80037-1](http://dx.doi.org/10.1016/S0278-6125(02)80037-1).
- FERGUSON, S. J., LANGHOFF, J. D., VOELTER, K., RECHENBERG, B. V., SCHARNWEBER, D., BIERBAUM, S., SCHNABELRAUCH, M., KAUTZ, A. R., FRAUCHIGER, V. M. & MUELLER, T. L. 2008. Biomechanical comparison of different surface modifications for dental implants. *The International journal of oral & maxillofacial implants*, 23, 1037.
- FERRARI, M., VICHI, A. & ZARONE, F. 2015. Zirconia abutments and restorations: From laboratory to clinical investigations. *Dental Materials*.

- FERRARO, J. R. & NAKAMOTO, K. 2012. *Introductory Raman Spectroscopy*, Elsevier Science.
- FISCHER-CRIPPS, A. C. 2011. *Nanoindentation*, Springer.
- FLINN, B. D., DEGROOT, D. A., MANCL, L. A. & RAIGRODSKI, A. J. 2012. Accelerated aging characteristics of three yttria-stabilised tetragonal zirconia polycrystalline dental materials. *The Journal of Prosthetic Dentistry*, 108, 223-230.
- FRÖBERG, K. K., LINDH, C. & ERICSSON, I. 2006. Immediate Loading of Brånemark System Implants®: A Comparison Between TiUnite™ and Turned Implants Placed in the Anterior Mandible. *Clinical Implant Dentistry and Related Research*, 8, 187-197.
- FRANCHI, M., FINI, M., MARTINI, D., ORSINI, E., LEONARDI, L., RUGGERI, A., GIAVARESI, G. & OTTANI, V. 2005. Biological fixation of endosseous implants. *Micron*, 36, 665-671.
- FRANÇOIS, P., VAUDAUX, P., TABORELLI, M., TONETTI, M., LEW, D. P. & DESCOUTS, P. 1997. Influence of surface treatments developed for oral implants on the physical and biological properties of titanium. (II) Adsorption isotherms and biological activity of immobilized fibronectin. *Clinical oral implants research*, 8, 217-225.
- FRANSEN, P. A., CHRISTOFFERSEN, H. & MADSEN, T. 1984. Holding power of different screws in the femoral head: a study in human cadaver hips. *Acta Orthopaedica*, 55, 349-351.
- FULLMAN, R. L. 1953. *Measurement of Particle Sizes in Opaque Bodies*, General Electric Research Laboratory.
- GADELMAWLA, E., KOURA, M., MAKSOUD, T., ELEWA, I. & SOLIMAN, H. 2002. Roughness parameters. *Journal of Materials Processing Technology*, 123, 133-145.
- GAHLERT, M., GUDEHUS, T., EICHHORN, S., STEINHAUSER, E., KNIHA, H. & ERHARDT, W. 2007. Biomechanical and histomorphometric comparison between zirconia implants with varying surface textures and a titanium implant in the maxilla of miniature pigs. *Clinical oral implants research*, 18, 662-668.
- GAHLERT, M., ROEHLING, S., SPRECHER, C. M., KNIHA, H., MILZ, S. & BORMANN, K. 2012. *In vivo* performance of zirconia and titanium implants: a histomorphometric study in mini pig maxillae. *Clinical Oral Implants Research*, 23, 281-286.
- GAILLARD, Y., JIMÁNEZ-PIQUÁ, E., SOLDERA, F., MÁCKLICH, F. & ANGLADA, M. 2008. Quantification of hydrothermal degradation in zirconia by nanoindentation. *Acta Materialia*, 56, 4206-4216.
- GANELES, J., ZÖLLNER, A., JACKOWSKI, J., TEN BRUGGENKATE, C., BEAGLE, J. & GUERRA, F. 2008. Immediate and early loading of Straumann implants with a chemically modified surface (SLActive) in the posterior mandible and maxilla: 1-year results from a prospective multicenter study. *Clinical Oral Implants Research*, 19, 1119-1128.
- GARVIE, R. C., HANNINK, R. H. & PASCOE, R. T. 1975. Ceramic steel? *Nature*, 258, 703-704.

- GARVIE, R. C. & NICHOLSON, P. S. 1972. Phase Analysis in Zirconia Systems. *Journal of the American Ceramic Society*, 55, 303-305.
- GARVIE, R. C., URBANI, C., KENNEDY, D. R. & MCNEUER, J. C. 1984. Biocompatibility of magnesia-partially stabilised zirconia (Mg-PSZ) ceramics. *Journal of Materials Science*, 19, 3224-3228.
- GEHRKE, P., DHOM, G., BRUNNER, J., WOLF, D., DEGIDI, M. & PIATTELLI, A. 2006. Zirconium implant abutments: fracture strength and influence of cyclic loading on retaining-screw loosening. *Quintessence international (Berlin, Germany: 1985)*, 37, 19-26.
- GEIER, D., CARMODY, T., KERN, J., KING, P. & GEIER, M. 2011. A significant relationship between mercury exposure from dental amalgams and urinary porphyrins: a further assessment of the Casa Pia children's dental amalgam trial. *BioMetals*, 24, 215-224.
- GEIGER, B., TOKUYASU, K., DUTTON, A. H. & SINGER, S. 1980. Vinculin, an intracellular protein localized at specialized sites where microfilament bundles terminate at cell membranes. *Proceedings of the National Academy of Sciences*, 77, 4127-4131.
- GILLINGS, B. R. D., GRAHAM, C. H. & DUCKMANTON, N. A. 1973. Jaw movements' in young adult men during chewing. *Journal of Prosthetic Dentistry*, 29, 616-627.
- GLAUSER, R., SAILER, I., WOHLWEND, A., STUDER, S., SCHIBLI, M. & SCHARER, P. 2004. Experimental zirconia abutments for implant-supported single-tooth restorations in esthetically demanding regions: 4-year results of a prospective clinical study. *Int J Prosthodont*, 17, 285-90.
- GOGOTSI, G., MUDRIK, S. & GALENKO, V. 2007. Evaluation of fracture resistance of ceramics: edge fracture tests. *Ceramics international*, 33, 315-320.
- GÓMEZ-FLORIT, M., XING, R., RAMIS, J. M., TAXT-LAMOLLE, S., HAUGEN, H. J., LYGSTADAAS, S. P. & MONJO, M. 2014. Human gingival fibroblasts function is stimulated on machined hydrided titanium zirconium dental implants. *Journal of Dentistry*, 42, 30-38.
- GONG, J., WU, J. & GUAN, Z. 1999. Examination of the indentation size effect in low-load vickers hardness testing of ceramics. *Journal of the European Ceramic Society*, 19, 2625-2631.
- GONZÁLEZ-MARTÍN, M. L., LABAJOS-BRONCANO, L., JAŃCZUK, B. & BRUQUE, J. M. 1999. Wettability and surface free energy of zirconia ceramics and their constituents. *Journal of Materials Science*, 34, 5923-5926.
- GONZÁLEZ, J. E. G. M.-R., J.C 1999. Study of the corrosion behavior of titanium and some of its alloys for biomedical and dental implant applications. *Journal of Electroanalytical Chemistry*, 471, 109-115.
- GREDES, T., KUBASIEWICZ-ROSS, P., GEDRANGE, T., DOMINIAK, M. & KUNERT-KEIL, C. 2014. Comparison of Surface Modified Zirconia Implants With Commercially Available Zirconium and Titanium Implants: A Histological Study in Pigs. *Implant dentistry*, 23, 502-507.

- GREMILLARD, L., CHEVALIER, J., EPICIER, T., DEVILLE, S. & FANTOZZI, G. 2004a. Modeling the aging kinetics of zirconia ceramics. *Journal of the European Ceramic Society*, 24, 3483-3489.
- GREMILLARD, L., CHEVALIER, J. R. M., EPICIER, T., DEVILLE, S. & FANTOZZI, G. 2004b. Modeling the aging kinetics of zirconia ceramics. *Journal of the European Ceramic Society*, 24, 3483-3489.
- GREMILLARD, L., GRANDJEAN, S. & CHEVALIER, J. 2010. A new method to measure monoclinic depth profile in zirconia-based ceramics from X-Ray diffraction data. *International Journal of Materials Research*, 101, 88-94.
- GRINNELL, F. 1978. Cellular adhesiveness and extracellular substrata. *International review of cytology*, 53, 65-144.
- GRÖßNER-SCHREIBER, B., HERZOG, M., HEDDERICH, J., DÜCK, A., HANNIG, M. & GRIEPENTROG, M. 2006. Focal adhesion contact formation by fibroblasts cultured on surface-modified dental implants: an *in vitro* study. *Clinical Oral Implants Research*, 17, 736-745.
- GU, Y.-X., DU, J., SI, M.-S., MO, J.-J., QIAO, S.-C. & LAI, H.-C. 2013. The roles of PI3K/Akt signaling pathway in regulating MC3T3-E1 preosteoblast proliferation and differentiation on SLA and SLActive titanium surfaces. *Journal of Biomedical Materials Research Part A*, 101A, 748-754.
- GUAZZATO, M., ALBAKRY, M., RINGER, S. P. & SWAIN, M. V. 2004. Strength, fracture toughness and microstructure of a selection of all-ceramic materials. Part II. Zirconia-based dental ceramics. *Dental Materials*, 20, 449-456.
- GUAZZATO, M., QUACH, L., ALBAKRY, M. & SWAIN, M. V. 2005. Influence of surface and heat treatments on the flexural strength of Y-TZP dental ceramic. *Journal of Dentistry*, 33, 9-18.
- GUICCIARDI, S., SHIMOZONO, T. & PEZZOTTI, G. 2007. Ageing effects on the nanoindentation response of sub-micrometric 3Y-TZP ceramics. *Journal of Materials Science*, 42, 718-722.
- GUPTA, T. K., BECHTOLD, J. H., KUZNICKI, R. C., CADOFF, L. H. & ROSSING, B. R. 1977. Stabilisation of tetragonal phase in polycrystalline zirconia. *Journal of Materials Science*, 12, 2421-2426.
- GUPTA, T. K., LANGE, F. F. & BECHTOLD, J. H. 1978. Effect of stress-induced phase transformation on the properties of polycrystalline zirconia containing metastable tetragonal phase. *Journal of Materials Science*, 13, 1464-1470.
- HANKER, J. S. & GIAMMARA, B. L. 1988. Biomaterials and biomedical devices. *Science*, 242, 885-892.
- HANNINK, R. H. J., KELLY, P. M. & MUDDLE, B. C. 2000. Transformation toughening in zirconia-containing ceramics. *Journal of the American Ceramic Society*, 83, 461-487.
- HANSSON, H. A., ALBREKTSSON, T. & BRÈSNEMARK, P. I. 1983. Structural aspects of the interface between tissue and titanium implants. *Journal of Prosthetic Dentistry*, 50, 108-113.
- HAO, L. & LAWRENCE, J. 2003. CO₂ laser modification of the wettability characteristics of a magnesia partially stabilised zirconia bioceramic. *Journal of Physics D: Applied Physics*, 36, 1292.

- HAO, L., LAWRENCE, J. & CHIAN, K. 2005. Osteoblast cell adhesion on a laser modified zirconia based bioceramic. *Journal of Materials Science: Materials in Medicine*, 16, 719-726.
- HARAGUCHI, K., SUGANO, N., NISHII, T., MIKI, H., OKA, K. & YOSHIKAWA, H. 2001. Phase transformation of a zirconia ceramic head after total hip arthroplasty. *Journal of Bone & Joint Surgery, British Volume*, 83, 996-1000.
- HARDING, G., KOSANETZKY, J. & NEITZEL, U. 1987. X-ray diffraction computed tomography. *Medical physics*, 14, 515-525.
- HAYFLICK, L. 1974. The longevity of cultured human cells. *Journal of the American Geriatrics Society*, 22, 1-12.
- HEISERMAN, D. L. 1991. *Exploring Chemical Elements and Their Compounds*, Tab Books.
- HELLMANN, J. R. & STUBICAN, V. S. 1983. Phase Relations and Ordering in the Systems MgO-Y₂O₃-ZrO₂ and CaO-MgO-ZrO₂. *Journal of the American Ceramic Society*, 66, 265-267.
- HELLSING, G. 1980. On the regulation of interincisor bite force in man. *Journal of Oral Rehabilitation*, 7, 403-411.
- HELMER, J. & DRISKELL, T. 1969. *Research on Bioceramics. Symposium on Use of Ceramics as Surgical Implants*. Clemson University; South Carolina.
- HELMICK, L., DILLON, S. J., GERDES, K., GEMMEN, R., ROHRER, G. S., SEETHARAMAN, S. & SALVADOR, P. A. 2011. Crystallographic Characteristics of Grain Boundaries in Dense Yttria-Stabilised Zirconia. *International Journal of Applied Ceramic Technology*, 8, 1218-1228.
- HEMPEL, U., HEFTI, T., KALBACOVA, M., WOLF-BRANDSTETTER, C., DIETER, P. & SCHLOTTIG, F. 2010. Response of osteoblast-like SAOS-2 cells to zirconia ceramics with different surface topographies. *Clinical Oral Implants Research*, 21, 174-181.
- HERMANN, J. S., COCHRAN, D. L., BUSER, D., SCHENK, R. K. & SCHOOLFIELD, J. D. 2001a. Biologic Width around one- and two-piece titanium implants. *Clinical oral implants research*, 12, 559-571.
- HERMANN, J. S., SCHOOLFIELD, J. D., SCHENK, R. K., BUSER, D. & COCHRAN, D. L. 2001b. Influence of the Size of the Microgap on Crestal Bone Changes Around Titanium Implants. A Histometric Evaluation of Unloaded Non-Submerged Implants in the Canine Mandible. *Journal of Periodontology*, 72, 1372-1383.
- HERNIGOU, P. & BAHRAMI, T. 2003. Zirconia and alumina ceramics in comparison with stainless-steel heads POLYETHYLENE WEAR AFTER A MINIMUM TEN-YEAR FOLLOW-UP. *Journal of Bone & Joint Surgery, British Volume*, 85, 504-509.
- HERRMANN, K. 2011. *Hardness Testing: Principles and Applications*, ASM International.
- HERZFIELD, H. 1916. *Process for obtaining zirconium dioxide or pure zirconium preparations from natural zirconia earth*. Germany patent application.

- HEYDECKE, G., KOHAL, R. & GLASER, R. 1999. Optimal esthetics in single-tooth replacement with the Re-Implant system: a case report. *The International Journal of Prosthodontics*, 12.
- HISBERGUES, M., VENDEVILLE, S. & VENDEVILLE, P. 2009. Zirconia: Established facts and perspectives for a biomaterial in dental implantology. *Journal of Biomedical Materials Research Part B: Applied Biomaterials*, 88, 519-529.
- HJERPPE, J., NÖRHI, T., FRÜBERG, K., VALLITTU, P. K. & LASSILA, L. V. J. 2008. Effect of shading the zirconia framework on biaxial strength and surface microhardness. *Acta Odontologica*, 66, 262-267.
- HOFFMANN, O., ANGELOV, N., ZAFIROPOULOS, G.-G. & ANDREANA, S. 2011. Osseointegration of zirconia implants with different surface characteristics: an evaluation in rabbits. *The International journal of oral & maxillofacial implants*, 27, 352-358.
- HORMIA, M. & KÖNÖNEN, M. 1994. Immunolocalisation of fibronectin and vitronectin receptors in human gingival fibroblasts spreading on titanium surfaces. *Journal of Periodontal Research*, 29, 146-152.
- HORMIA, M., KÖNÖNEN, M., KIVILAHTI, J. & VIRTANEN, I. 1991. Immunolocalisation of proteins specific for adhaerens junctions in human gingival epithelial cells grown on differently processed titanium surfaces. *Journal of Periodontal Research*, 26, 491-497.
- HUANG, G. T. J., SONOYAMA, W., CHEN, J. & PARK, S. H. 2006. *In vitro* characterization of human dental pulp cells: various isolation methods and culturing environments. *Cell and tissue research*, 324, 225-236.
- ILAVSKY, J. & STALICK, J. K. 2000. Phase composition and its changes during annealing of plasma-sprayed YSZ. *Surface and Coatings Technology*, 127, 120-129.
- INGEL, R. P., LEWIS, D., BENDER, B. A. & RICE, R. W. 1983. Physical, microstructural, and thermomechanical properties of ZrO₂ single crystals. *Science and technology of zirconia II*.
- ISO 10993-1 1992. Biological evaluation of a medical devices guidance on selection of tests, International Standards Organization, Geneva.
- ISO 13356 2008. Implants for surgery – Ceramic materials based on yttria-stabilised tetragonal zirconia (*Y-TZP*) International Organization for Standardization, Geneva (2008).
- ISO 14705 2008. Fine ceramics (advanced ceramics, advanced technical ceramics) Test method for hardness of monolithic ceramics at room temperature.
- ISO 14801 2007. Dentistry-Implants-Dynamic fatigue test for endosseous dental implants.
- ITO, H., SASAKI, H., SAITO, K., HONMA, S., YAJIMA, Y. & YOSHINARI, M. 2013. Response of osteoblast-like cells to zirconia with different surface topography. *Dental materials journal*, 32, 122-129.
- IVANOFF, C. J., SENNERBY, L., JOHANSSON, C., RANGERT, B. & LEKHOLM, U. 1997. Influence of implant diameters on the integration of screw implants:

an experimental study in rabbits. *International journal of oral and maxillofacial surgery*, 26, 141-148.

- JACOBS, J., SKIPOR AK, PATTERSON LM, HALLAB NJ, PAPROSKY WG, BLACK J & JO., G. 1998. Metal release in patients who have had a primary total hip arthroplasty. A prospective, controlled, longitudinal study. *J Bone Jt Surg Am*, 80, 1447-1458.
- JANG, W. G., KIM, E. J., KIM, D. K., RYOO, H. M., LEE, K. B., KIM, S. H., CHOI, H. S. & KOH, J. T. 2012. BMP2 protein regulates osteocalcin expression via Runx2-mediated Atf6 gene transcription. *J Biol Chem*, 287, 905-15.
- JEMT, T. & JOHANSSON, J. 2006. Implant Treatment in the Edentulous Maxillae: A 15-Year Follow-Up Study on 76 Consecutive Patients Provided with Fixed Prosthesis. *Clinical Implant Dentistry and Related Research*, 8, 61-69.
- JENKINS, R. & SNYDER, R. 2012. *Introduction to X-Ray Powder Diffractometry*, Wiley.
- JI, S., KIM, Y., MIN, B. M., HAN, S. H. & CHOI, Y. 2007. Innate immune responses of gingival epithelial cells to nonperiodontopathic and periodontopathic bacteria. *Journal of Periodontal Research*, 42, 503-510.
- JIMÉNEZ-PIQUÉ, EMILIO., RAMOS, A., MUÑOZ-TABARES, J. A., HATTON, A., SOLDERA, F., MÜCKLICH, F. & ANGLADA, M. 2012. Focused ion beam tomography of zirconia degraded under hydrothermal conditions. *Journal of the European Ceramic Society*, 32, 2129-2136.
- JORDAN, H.-J., WEGNER, M. & TIZIANI, H. 1998. Highly accurate non-contact characterization of engineering surfaces using confocal microscopy. *Measurement Science and Technology*, 9, 1142.
- JORGENSON, D., MAYER MH, ELLENBO GEN RG, CENTENO JA, JOHNSON FB, MULLICK FG & PN., M. 1997. Detection of titanium in human tissues after craniofacial surgery. *Plast Reconstr Surg*, 99, 976-979.
- JOSSET, Y., OUM'HAMED, Z., ZARRINPOUR, A., LORENZATO, M., ADNET, J. J. & LAURENT-MAQUIN, D. 1999. *In vitro* reactions of human osteoblasts in culture with zirconia and alumina ceramics. *Journal of Biomedical Materials Research*, 47, 481-493.
- JUM'AH A., WOOD D. & MAGHEIREH H., 2011a. Implant Dentistry: From Titanium to Zirconia *Smile Dental Journal*. 6(2), 8-12.
- JUM'AH, A. A., BEEKMANS, B. M., WOOD, D. J., & MAGHAIREH, H. 2012b. Zirconia Implants: The New Arrival in the Armoury of Successful Aesthetic Implant Dentistry. *Smile Dental Journal*, 7(2), 12-26.
- JUNG, R., SAILER, I., HAMMERLE, C., ATTIN, T. & SCHMIDLIN, P. 2007. *In vitro* color changes of soft tissues caused by restorative materials. *International Journal of Periodontics and Restorative Dentistry*, 27, 251-257.
- JUNG, Y. G., PETERSON, I. M., KIM, D. K. & LAWN, B. R. 2000. Lifetime-limiting strength degradation from contact fatigue in dental ceramics. *Journal of dental research*, 79, 722-731.
- KANG, B.-S., SUL, Y.-T., OH, S.-J., LEE, H.-J. & ALBREKTSSON, T. 2009. XPS, AES and SEM analysis of recent dental implants. *Acta Biomaterialia*, 5, 2222-2229.

- KATZ, G. 1971. X-Ray Diffraction Powder Pattern of Metastable Cubic ZrO₂. *Journal of the American Ceramic Society*, 54, 531-531.
- KAWAHARA, H., HIRABAYASHI, M. & SHIKITA, T. 1980. Single crystal alumina for dental implants and bone screws. *Journal of biomedical materials research*, 14, 597-605.
- KAWAI, Y., UO, M., WANG, Y., KONO, S., OHNUKI, S. & WATARI, F. 2011. Phase transformation of zirconia ceramics by hydrothermal degradation. *Dental materials journal*, 30, 286-292.
- KAZUHISA, B. & IIZUKA, T. 1993. Clinical and animal experiments on stress corrosion of titanium miniplates. *Clin Mater*, 14, 223-227.
- KELLY, J. R. 1997. Ceramics in restorative and prosthetic dentistry 1. *Annual Review of Materials Science*, 27, 443-468.
- KERN, M. & WEGNER, S. M. 1998. Bonding to zirconia ceramic: adhesion methods and their durability. *Dental Materials*, 14, 64-71.
- KEUL, C., LIEBERMANN, A., ROOS, M., UHRENBACHER, J. & STAWARCZYK, B. 2013. The effect of ceramic primer on shear bond strength of resin composite cement to zirconia: A function of water storage and thermal cycling. *Journal of the American Dental Association (1939)*, 144, 1261-1271.
- KEUPER, M., BERTHOLD, C. & NICKEL, K. G. 2014. Long-time aging in 3mol.% yttria-stabilised tetragonal zirconia polycrystals at human body temperature. *Acta Biomaterialia*, 10, 951-959.
- KHERADMANDAN, S., KOUTAYAS, S. O., BERNHARD, M. & STRUB, J. R. 2001. Fracture strength of four different types of anterior 3-unit bridges after thermo-mechanical fatigue in the dual-axis chewing simulator. *Journal of Oral Rehabilitation*, 28, 361-369.
- KIESWETTER, K., SCHWARTZ, Z., DEAN, D. D. & BOYAN, B. D. 1996. The Role of Implant Surface Characteristics in the Healing of Bone. *Critical Reviews in Oral Biology & Medicine*, 7, 329-345.
- KILIARIDIS, S., KJELLBERG, H., WENNEBERG, B. & ENGSTRÉM, C. 1993. The relationship between maximal bite force, bite force endurance, and facial morphology during growth: A cross-sectional study. *Acta Odontologica*, 51, 323-331.
- KIM, H., CHOI, S.-H., RYU, J.-J., KOH, S.-Y., PARK, J.-H. & LEE, I.-S. 2008. The biocompatibility of SLA-treated titanium implants. *Biomedical Materials*, 3, 025011.
- KIMURA, Y., MATSUZAKA, K., YOSHINARI, M. & INOUE, T. 2012. Initial attachment of human oral keratinocytes cultured on zirconia or titanium. *Dental materials journal*, 31, 346-353.
- KIRSTEIN, A. F. & WOOLLEY, R. M. 1967. Symmetrical bending of thin circular elastic plates on equally spaced point supports. *J. Res. Natl. Bur. Stand. C*, 71, 1-10.
- KLEIN, M. O., BIJELIC, A., TOYOSHIMA, T., GOTZ, H., VON KOPPFELS, R. L., AL-NAWAS, B. & DUSCHNER, H. 2010. Long-term response of osteogenic cells on micron and submicron-scale-structured hydrophilic

- titanium surfaces: sequence of cell proliferation and cell differentiation. *Clin Oral Implants Res*, 21, 642-9.
- KLEUKER, U., SUORTTI, P., WEYRICH, W. & SPANNE, P. 1998. Feasibility study of X-Ray diffraction computed tomography for medical imaging. *Physics in medicine and biology*, 43, 2911.
- KNECHTEL, M. C., GARCIA, D. E., RÖDEL, J. R. & CLAUSSEN, N. 1993. Subcritical Crack Growth in Y-TZP and Al₂O₃-Toughened Y-TZP. *Journal of the American Ceramic Society*, 76, 2681-2684.
- KO, H.-C., HAN, J.-S., BÄCHLE, M., JANG, J.-H., SHIN, S.-W. & KIM, D.-J. 2007. Initial osteoblast-like cell response to pure titanium and zirconia/alumina ceramics. *Dental Materials*, 23, 1349-1355.
- KOBAYASHI, K., KUWAJIMA, H. & MASAKI, T. 1981. Phase change and mechanical properties of ZrO₂-Y₂O₃ solid electrolyte after ageing. *Solid State Ionics*, 3-4, 489-493.
- KOHAL, R.-J., ATT, W., BÄCHLE, M. & BUTZ, F. 2008. Ceramic abutments and ceramic oral implants. An update. *Periodontology 2000*, 47, 224-243.
- KOHAL, R.-J., FINKE, H. C. & KLAUS, G. 2009a. Stability of Prototype Two-Piece Zirconia and Titanium Implants after Artificial Aging: An *In Vitro* Pilot Study. *Clinical Implant Dentistry and Related Research*, 11, 323-329.
- KOHAL, R.-J., KLAUS, G. & STRUB, J. R. 2006. Zirconia-implant-supported all-ceramic crowns withstand long-term load: a pilot investigation. *Clinical Oral Implants Research*, 17, 565-571.
- KOHAL, R.-J., KNAUF, M., LARSSON, B., SAHLIN, H. & BUTZ, F. 2012. One-piece zirconia oral implants: one-year results from a prospective cohort study. 1. Single tooth replacement. *Journal of Clinical Periodontology*, 39, 590-597.
- KOHAL, R.-J., WOLKEWITZ, M. & MUELLER, C. 2010. Alumina-reinforced zirconia implants: survival rate and fracture strength in a masticatory simulation trial. *Clinical Oral Implants Research*, 21, 1345-1352.
- KOHAL, R., WOLKEWITZ, M. & TSAKONA, A. 2011. The effects of cyclic loading and preparation on the fracture strength of zirconium-dioxide implants: an *in vitro* investigation. *Clinical Oral Implants Research*, 22, 808-814.
- KOHAL, R. J., BÄCHLE, M., ATT, W., CHAAR, S., ALTMANN, B., RENZ, A. & BUTZ, F. 2013. Osteoblast and bone tissue response to surface modified zirconia and titanium implant materials. *Dental Materials*, 29, 763-776.
- KOHAL, R. J., WENG D, BÄCHLE M & JR, S. 2004. Loaded custom-made zirconia and titanium implants show similar osseointegration: an animal experiment. *Journal of Periodontology*, 75, 1262-1268.
- KOHAL, R. J., WOLKEWITZ, M., HINZE, M., HAN, J.-S., BÄCHLE, M. & BUTZ, F. 2009b. Biomechanical and histological behavior of zirconia implants: an experiment in the rat. *Clinical Oral Implants Research*, 20, 333-339.
- KOHORST, P., BORCHERS, L., STREMPPEL, J. R., STIESCH, M., HASSEL, T., BACH, F.-W. & HÜBSCH, C. 2012. Low-temperature degradation of different zirconia ceramics for dental applications. *Acta Biomaterialia*, 8, 1213-1220.
- KOKUBO, T. 2008. *Bioceramics and their Clinical Applications*, Elsevier Science.

- KORBER, K. H. & LUDWIG, K. 1983. Maximale Kaukraft als Berechnungsfaktor zahntechnischer Konstruktionen. *Dent Lab*, 31, 55-60.
- KOSMAĆ, T., WAGNER, R. & CLAUSSEN, N. 1981. X-Ray Determination of Transformation Depths in Ceramics Containing Tetragonal ZrO₂. *Journal of the American Ceramic Society*, 64, c-72-c-73.
- KOSMAĆ, T., OBLAK, Ä. & MARION, L. 2008. The effects of dental grinding and sandblasting on ageing and fatigue behavior of dental zirconia (**Y-TZP**) ceramics. *Journal of the European Ceramic Society*, 28, 1085-1090.
- KOSMAĆ, T., OBLAK, C., JEVIKAR, P., FUNDUK, N. & MARION, L. 1999. The effect of surface grinding and sandblasting on flexural strength and reliability of **Y-TZP** zirconia ceramic. *Dental Materials*, 15, 426-433.
- KOUTAYAS, S. O., VAGKOPOULOU, T., S. PELEKANOS, P. KOIDIS & STRUB, J. R. 2009. Zirconia in dentistry. Part 2. Evidence-based clinical breakthrough. *The European Journal of Esthetic Dentistry*, 4, 348-380.
- KREJCI, I. & LUTZ, F. 1989. [In-vitro test results of the evaluation of dental restoration systems. Correlation with in-vivo results]. *Schweizer Monatsschrift für Zahnmedizin= Revue mensuelle suisse d'odonto-stomatologie= Rivista mensile svizzera di odontologia e stomatologia/SSO*, 100, 1445-1449.
- KUNZLER, T. P., DROBEK, T., SCHULER, M. & SPENCER, N. D. 2007. Systematic study of osteoblast and fibroblast response to roughness by means of surface-morphology gradients. *Biomaterials*, 28, 2175-2182.
- LAI, H. C., ZHUANG, L. F., LIU, X., WIELAND, M., ZHANG, Z. Y. & ZHANG, Z. Y. 2010. The influence of surface energy on early adherent events of osteoblast on titanium substrates. *Journal of Biomedical Materials Research Part A*, 93, 289-296.
- LALOR, P. A., REVELL, P.A., GRAY, A.B., WRIGHT, S., RAILTON, G.T. & FREEMAN, M.A. 1991. Sensitivity to titanium. A cause of implant failure? *Journal of Bone and Joint Surgery – British*, 73, 25-28.
- LAMBRICH, M. & IGLHAUT, G. 2008. Vergleich der Überlebensrate von Zirkondioxid- und Titanimplantaten. *Zeitschrift für Zahnärztliche Implantologie*, 24, 182-191.
- LANG, N. P., PUN, L., LAU, K. Y., LI, K. Y. & WONG, M. C. M. 2012. A systematic review on survival and success rates of implants placed immediately into fresh extraction sockets after at least 1 year. *Clinical Oral Implants Research*, 23, 39-66.
- LANGE, F. F. 1982. Transformation toughening. *Journal of Materials Science*, 17, 225-234.
- LANGE, F. F., DUNLOP, G. L. & DAVIS, B. I. 1986. Degradation During Aging of Transformation-Toughened ZrO₂-Y₂O₃ Materials at 250°C. *Journal of the American Ceramic Society*, 69, 237-240.
- LANGFORD, R. M. 2006. Focused ion beams techniques for nanomaterials characterization. *Microscopy research and technique*, 69, 538-549.
- LANGFORD, R. M. & CLINTON, C. 2004. *In situ* lift-out using a FIB-SEM system. *Micron*, 35, 607-611.

- LAUER, G., WIEDMANN-AL-AHMAD, M., OTTEN, J. E., HÜBNER, U., SCHMELZEISEN, R. & SCHILLI, W. 2001. The titanium surface texture effects adherence and growth of human gingival keratinocytes and human maxillar osteoblast-like cells in vitro. *Biomaterials*, 22, 2799-2809.
- LAUSMAA, J., KASEMO, B., ROLANDER, U., BJURSTEN, L., ERICSON, L., ROSANDER, L. & THOMSEN, P. 1988. Preparation, surface spectroscopic and electron microscopic characterization of titanium implant materials. *Surface characterization of biomaterials*. Amsterdam: Elsevier, 161-174.
- LAWN, B. & WILSHAW, R. 1975. Indentation fracture: principles and applications. *Journal of Materials Science*, 10, 1049-1081.
- LEE, C. K., KARL, M. & KELLY, J. R. 2009a. Evaluation of test protocol variables for dental implant fatigue research. *Dental Materials*, 25, 1419-1425.
- LEE, J., SIEWEKE, J. H., RODRIGUEZ, N. A., SCHÜPBACH, P., LINDSTRÖM, H., SUSIN, C. & WIKESJÖ, U. M. E. 2009b. Evaluation of nano-technology-modified zirconia oral implants: a study in rabbits. *Journal of Clinical Periodontology*, 36, 610-617.
- LEONI, M., JONES, R. L. & SCARDI, P. 1998. Phase stability of scandia–yttria-stabilised zirconia TBCs. *Surface and Coatings Technology*, 108–109, 107-113.
- LESOT, H. & BROOK, A. H. 2009. Epithelial histogenesis during tooth development. *Archives of oral biology*, 54, S25-S33.
- LEWIS, I. R. & EDWARDS, H. 2001. *Handbook of Raman Spectroscopy: From the Research Laboratory to the Process Line*, CRC Press.
- LI, J.-F. & WATANABE, R. 1998. Phase Transformation in Y2O3-Partially-Stabilised ZrO2 Polycrystals of Various Grain Sizes during Low-Temperature Aging in Water. *Journal of the American Ceramic Society*, 81, 2687-2691.
- LI, J. F., WATANABE, R., ZHANG, B. P., ASAMI, K. & HASHIMOTO, K. 1996. X-ray Photoelectron Spectroscopy Investigation on the Low-Temperature Degradation of 2 mol% Y2O3-ZrO2 Ceramics. *Journal of the American Ceramic Society*, 79, 3109-3112.
- LIAN, J., GARAY, J. E. & WANG, J. 2007. Grain size and grain boundary effects on the mechanical behavior of fully stabilised zirconia investigated by nanoindentation. *Scripta materialia*, 56, 1095-1098.
- LIBMAN, W. J. & NICHOLLS, J. I. 1994. Load fatigue of teeth restored with cast posts and cores and complete crowns. *The International journal of prosthodontics*, 8, 155-161.
- LIN, J-D & DUH J-G. 2003. Fracture toughness and hardness of ceria-and yttria-doped tetragonal zirconia ceramics. *Materials Chemistry and Physics*, 78, 253-261.
- LINDER, L., ALBREKTSSON, T., BRÅNEMARK, P.-I., HANSSON, H.-A., IVARSSON, B., JONSSON, U. & LUNDSTRÖM, I. 1983. Electron microscopic analysis of the bone-titanium interface. *Acta Orthopaedica*, 54, 45-52.
- LINDHE, J. & BERGLUNDH, T. 1998. The interface between the mucosa and the implant. *Periodontology 2000*, 17, 47-54.

- LINDQUIST, L. W., CARLSSON, G. E. & JEMT, T. 1996. A prospective 15-year follow-up study of mandibular fixed prostheses supported by osseointegrated implants. Clinical results and marginal bone loss. *Clinical Oral Implants Research*, 7, 329-336.
- LINKEVICIUS, T., APSE, P., GRYBAUSKAS, S. & PUISYS, A. 2008. The influence of soft tissue thickness on crestal bone changes around implants: a 1-year prospective controlled clinical trial. *The International journal of oral & maxillofacial implants*, 24, 712-719.
- LIPKIN, D. M., KROGSTAD, J. A., GAO, Y., JOHNSON, C. A., NELSON, W. A. & LEVI, C. G. 2013. Phase Evolution upon Aging of Air-Plasma Sprayed t'-Zirconia Coatings: I—Synchrotron X-Ray Diffraction. *Journal of the American Ceramic Society*, 96, 290-298.
- LISTGARTEN, M. A. 1996. Soft and hard tissue response to endosseous dental implants. *The Anatomical Record*, 245, 410-425.
- LIU, S.-Y. & CHEN, I. W. 1991. Fatigue of Ytria-Stabilised Zirconia: II, Crack Propagation, Fatigue Striations, and Short-Crack Behavior. *Journal of the American Ceramic Society*, 74, 1206-1216.
- LIU, S. Y. & CHEN, I. W. 1994. Plasticity-Induced Fatigue Damage in Ceria-Stabilised Tetragonal Zirconia Polycrystals. *Journal of the American Ceramic Society*, 77, 2025-2035.
- LUGHI, V. & SERGO, V. 2010. Low temperature degradation-aging-of zirconia: A critical review of the relevant aspects in dentistry. *Dental Materials*, 26, 807-820.
- LUNDGREN, D. & LAURELL, L. 1986. Occlusal force pattern during chewing and biting in dentitions restored with fixed bridges of cross-arch extension. *Journal of Oral Rehabilitation*, 13, 57-71.
- LUTHARDT, R. G., HOLZHÜTER, M., SANDKUHL, O., HEROLD, V., SCHNAPP, J. D., KUHLISCH, E. & WALTER, M. 2002. Reliability and properties of ground Y-TZP-zirconia ceramics. *Journal of dental research*, 81, 487-491.
- LYONS, M. F. & BAXENDALE, R. H. 1990. A preliminary electromyographic study of bite force and jaw-closing muscle fatigue in human subjects with advanced tooth wear. *Journal of Oral Rehabilitation*, 17, 311-318.
- MACKENZIE, I. C. & TONETTI, M. S. 1995. Formation of Normal Gingival Epithelial Phenotypes Around Osseo-Integrated Oral Implants in Humans. *Journal of Periodontology*, 66, 933-943.
- MAGNANI, G. & BRILLANTE, A. 2005. Effect of the composition and sintering process on mechanical properties and residual stresses in zirconia-alumina composites. *Journal of the European Ceramic Society*, 25, 3383-3392.
- MAI, R., KUNERT-KEIL, C., GRAFE, A., GEDRANGE, T., LAUER, G. N., DOMINIAK, M. & GREDES, T. 2012. Histological behaviour of zirconia implants: An experiment in rats. *Annals of Anatomy-Anatomischer Anzeiger*, 194, 561-566.
- MAMALIS, A. A. & SILVESTROS, S. S. 2011. Analysis of osteoblastic gene expression in the early human mesenchymal cell response to a chemically modified implant surface: an *in vitro* study. *Clin Oral Implants Res*, 22, 530-7.

- MARDAS, N., SCHWARZ, F., PETRIE, A., HAKIMI, A. R. & DONOS, N. 2011. The effect of SLActive surface in guided bone formation in osteoporotic-like conditions. *Clin Oral Implants Res*, 22, 406-15.
- MARTIN, J. Y., SCHWARTZ, Z., HUMMERT, T. W., SCHRAUB, D. M., SIMPSON, J., LANKFORD, J., DEAN, D. D., COCHRAN, D. L. & BOYAN, B. D. 1995. Effect of titanium surface roughness on proliferation, differentiation, and protein synthesis of human osteoblast-like cells (MG63). *Journal of Biomedical Materials Research*, 29, 389-401.
- MASAKI, C., SCHNEIDER, G. B., ZAHARIAS, R., SEABOLD, D. & STANFORD, C. 2005. Effects of implant surface microtopography on osteoblast gene expression
- Der Einfluss der Mikrotopographie von Implantatoberflächen auf die Genexpression von Osteoblasten. *Clinical Oral Implants Research*, 16, 650-656.
- MASAKI, T. 1986. Mechanical properties of Y-PSZ after aging at low temperature. *International Journal of High Technology Ceramics*, 2, 85-98.
- MASSIMI, F., MERLATI, G., SEBASTIANI, M., BATTAINI, P., MENGHINI, P. & BEMPORAD, E. 2012. FIB/SEM and SEM/EDS microstructural analysis of metal-ceramic and zirconia-ceramic interfaces. *Bulletin du Groupement International pour la Recherche Scientifique en Stomatologie et Odontologie*, 50, 1-10.
- MAVROGENIS, A. F., DIMITRIOU, R., PARVIZI, J. & BABIS, G. C. 2009. Biology of implant osseointegration. *J Musculoskelet Neuronal Interact*, 9, 61-71.
- MEIJER, H. J. A., STELLINGSMA, K., MEIJNDERT, L. & RAGHOEBAR, G. M. 2005. A new index for rating aesthetics of implant-supported single crowns and adjacent soft tissues – the Implant Crown Aesthetic Index
- Ein neuer Index zur Wertung der Aesthetik von implantatgetragenen Einzelkronen und der angrenzenden Weichgewebe – der Implantat Kronen Aesthetik Index. *Clinical Oral Implants Research*, 16, 645-649.
- MELLINGHOFF, J. 2006. Erste klinische Ergebnisse zu dentalen Schraubenimplantaten aus Zirkonoxid. *Zeitschrift für Zahnärztliche Implantologie*, 22, 288-293.
- MENEGHINI, F. & BIONDI, P. 2012. *Clinical Facial Analysis: Elements, Principles, and Techniques*, Springer.
- MEYER, U., BUCHTER, A., WIESMANN, H. P., JOOS, U. & JONES, D. B. 2005. Basic reactions of osteoblasts on structured material surfaces. *Eur Cell Mater*, 9, 39-49.
- MILLEDING, P., KARLSSON, S. & NYBORG, L. 2003. On the surface elemental composition of non-corroded and corroded dental ceramic materials *in vitro*. *Journal of Materials Science: Materials in Medicine*, 14, 557-566.
- MISCH, C. E. 2008. *Contemporary Implant Dentistry*. Third ed.: Mosby Elsevier.
- MOLIN, M. K. & KARLSSON, S. L. 2007. Five-year clinical prospective evaluation of zirconia-based Denzir 3-unit FPDs. *The International journal of prosthodontics*, 21, 223-227.

- MORENA, R., BEAUDREAU, G. M., LOCKWOOD, P. E., EVANS, A. L. & FAIRHURST, C. W. 1986. Fatigue of dental ceramics in a simulated oral environment. *Journal of dental research*, 65, 993-997.
- MORRELL, R. & GANT, A. J. 2001. Edge chipping of hard materials. *International Journal of Refractory Metals and Hard Materials*, 19, 293-301.
- MUÑOZ-SALDAÑA, J., BALMORI-RAMÁ-REZ, H., JARAMILLO-VIGUERAS, D., IGA, T. & SCHNEIDER, G. A. 2003. Mechanical properties and low-temperature aging of tetragonal zirconia polycrystals processed by hot isostatic pressing. *Journal of Materials Research*, 18, 2415-2426.
- MUNZ, D. & FETT, T. 1999. *Ceramics: mechanical properties, failure behaviour, materials selection*, Springer.
- MUSTAFA, K., LOPEZ, B. S., HULTENBY, K., WENNERBERG, A. & ARVIDSON, K. 1998. Attachment and proliferation of human oral fibroblasts to titanium surfaces blasted with TiO₂ particles. A scanning electron microscopic and histomorphometric analysis. *Clinical oral implants research*, 9, 195-207.
- MUSTAFA, K., WROBLEWSKI, J., LOPEZ, B. S., WENNERBERG, A., HULTENBY, K. & ARVIDSON, K. 2001. Determining optimal surface roughness of TiO₂ blasted titanium implant material for attachment, proliferation and differentiation of cells derived from human mandibular alveolar bone. *Clinical oral implants research*, 12, 515-525.
- NAKAJIMA, K., KOBAYASHI, K. & MURATA, Y. 1983. Phase stability of Y-PSZ in aqueous solutions. *Science and technology of zirconia II*.
- NANCI, A. 2008. *Ten Cate's Oral Histology: Development, Structure, and Function*, Mosby Elsevier.
- NICKEL, K. G., KEUPER, M. & BERTHOLD, C. 2013. The long-time low-temperature degradation (LTD) kinetics in 3Y-TZP bioceramics. *Key Engineering Materials*, 529, 589-594.
- NIINOMI, M. 1998. Mechanical properties of biomedical titanium alloys. *Materials Science and Engineering*, 243, 231-236.
- NIU, X., YANG, Y. & SOBOYEJO, W. 2008. Contact deformation and cracking of zirconia/cement/foundation dental multilayers. *Materials Science and Engineering: A*, 485, 517-523.
- NORTON, M. R., YARLAGADDA, R. & ANDERSON, G. H. 2002. Catastrophic failure of the Elite Plus total hip replacement, with a Hylamer acetabulum and Zirconia ceramic femoral head. *Journal of Bone & Joint Surgery, British Volume*, 84, 631-635.
- NOTHDURFT, F. & POSPIECH, P. 2010. Prefabricated zirconium dioxide implant abutments for single-tooth replacement in the posterior region: evaluation of peri-implant tissues and superstructures after 12 months of function. *Clinical oral implants research*, 21, 857-865.
- NOTHDURFT, F. P., FONTANA, D., RUPPENTHAL, S., MAY, A., AKTAS, C., MEHRAEIN, Y., LIPP, P. & KAESTNER, L. 2014. Differential Behavior of Fibroblasts and Epithelial Cells on Structured Implant Abutment Materials: A

Comparison of Materials and Surface Topographies. *Clinical Implant Dentistry and Related Research*,

- OHLMANN, B., RAMMELSBERG, P., SCHMITTER, M., SCHWARZ, S. & GABBERT, O. 2008. All-ceramic inlay-retained fixed partial dentures: Preliminary results from a clinical study. *Journal of Dentistry*, 36, 692-696.
- OHNISHI, T., KOIKE H, ISHITANI T, TOMIMATSU S, UMEMURA K & T, K. A new focused-ion beam microsampling technique for TEM observation of site-specific areas. Proceedings of the 25th international symposium for testing and failure analysis, 1999. 449–453.
- OLIVA, J., OLIVA, X. & OLIVA, J. 2007. One-year follow-up of first consecutive 100 zirconia dental implants in humans: a comparison of 2 different rough surfaces. *The International Journal of Oral & Maxillofacial Implants*, 22, 430-435.
- OLIVA, J., OLIVA, X. & OLIVA, J. 2010. Five-year success rate of 831 consecutively placed Zirconia dental implants in humans: a comparison of three different rough surfaces. *Int J Oral Maxillofac Implants.*, 25, 336-344.
- OLIVER, W. C. & PHARR, G. M. 1992. An improved technique for determining hardness and elastic modulus using load and displacement sensing indentation experiments. *Journal of Materials Research*, 7, 1564-1583.
- ONODERA, K., OOYA, K. & KAWAMURA, H. 1993. Titanium lymph node pigmentation in the reconstruction plate system of a mandibular bone defect. *Oral Surg Oral Med Oral Pathol*, 75, 495-497.
- ORIMO, H. 2010. The mechanism of mineralisation and the role of alkaline phosphatase in health and disease. *J Nippon Med Sch*, 77, 4-12.
- ORTORP, A., KIHIL, M. L. & CARLSSON, G. E. 2012. A 3-year retrospective and clinical follow-up study of zirconia single crowns performed in a private practice. *Journal of Dentistry*, 37, 731-736.
- ÖZKURT, Z. & KAZAZOĞLU, E. Clinical Success of Zirconia in Dental Applications. *Journal of Prosthodontics*, 19, 64-68.
- PAE, A., LEE, H., KIM, H.-S., KWON, Y.-D. & WOO, Y.-H. 2009. Attachment and growth behaviour of human gingival fibroblasts on titanium and zirconia ceramic surfaces. *Biomedical Materials*, 4, 025005.
- PALMER, R. 1999. Dental implants: Teeth and implants. *Br Dent J*, 187, 183-188.
- PANALYTICAL, B. V. 2011. X-Ray penetration depth. *Help file*. 3 ed.
- PAOLO FRANCESCO MANICONE, P. R. I., LUCA RAFFAELLI 2007. An overview of zirconia ceramics: Basic properties and clinical applications. *Journal of Dentistry*, 35, 819-826.
- PAPANAGIOTOU, H. P., MORGANO, S. M., GIORDANO, R. A. & POBER, R. 2006. *In vitro* evaluation of low-temperature aging effects and finishing procedures on the flexural strength and structural stability of **Y-TZP** dental ceramics. *The Journal of Prosthetic Dentistry*, 96, 154-164.
- PARK, Y.-S., CHUNG, S.-H. & SHON, W.-J. 2012. Peri-implant bone formation and surface characteristics of rough surface zirconia implants manufactured by

- powder injection molding technique in rabbit tibiae. *Clinical oral implants research*, 24, 586-591.
- PASSERINI, L. 1939. Isomorphism among oxides of different tetravalent metals: CeO₂-ThO₂; CeO₂-ZrO₂; CeO₂-HfO₂. *Gazzet Chim Ital*, 60, 762-76.
- PAUL, A., VAIDHYANATHAN, B. & BINNER, J. G. P. 2011. Hydrothermal Aging Behavior of Nanocrystalline Y³⁺•TZP Ceramics. *Journal of the American Ceramic Society*, 94, 2146-2152.
- PAYER, M., ARNETZL, V., KIRMEIER, R., KOLLER, M., ARNETZL, G. & JAKSE 2012. N. Immediate provisional restoration of single-piece zirconia implants: a prospective case series – results after 24 months of clinical function. *Clin. Oral. Impl. Res.*, 00, 1-7.
- PAYER, M., LORENZONI, M., JAKSE, N., KIRMEIER, R., DOHR, G., STOPPER, M. & PERTL, C. 2010. Cell growth on different zirconia and ti-tanium surface textures: a morphologic *in vitro* study. *J Dental Implant (in German)*, 4, 338-51.
- PEŠŠKOVÁ, V., KUBIES, D., HULEJOVÁ, H. & HIMMLOVÁ, L. 2007. The influence of implant surface properties on cell adhesion and proliferation. *Journal of Materials Science: Materials in Medicine*, 18, 465-473.
- PETIT, F., VANDENEDE, V. & CAMBIER, F. 2009. Ceramic toughness assessment through edge chipping measurements influence of interfacial friction. *Journal of the European Ceramic Society*, 29, 2135-2141.
- PHARR, G. M. & OLIVER, W. C. 1992. Measurement of thin film mechanical properties using nanoindentation. *Mrs Bulletin*, 17, 28-33.
- PHILLIPS, R. W. 1973. *Skinner's Science of Dental Materials*, W. B. Saunders.
- PIANTELLI, S., MACCAURO, G., SPECCHIA, N., MAGGIANO, N., PICONI, C. & GRECO, F. 1992. Effects of ceramic precursors on human lymphocyte mitogenesis. *4th World Biomaterials Congress Transactions*. Berlin, Germany.
- PIATTELLI, A., FARIAS PONTES, A. E., DEGIDI, M. & IEZZI, G. 2011. Histologic studies on osseointegration: Soft tissues response to implant surfaces and components. A review. *Dental Materials*, 27, 53-60.
- PICONI, C., BURGER, W., RICHTER, H. G., CITTADINI, A., MACCAURO, G., COVACCI, V., BRUZZESE, N., RICCI, G. A. & MARMO, E. 1998. **Y-TZP** ceramics for artificial joint replacements. *Biomaterials*, 19, 1489-1494.
- PICONI, C. & MACCAURO, G. 1999. Zirconia as a ceramic biomaterial. *Biomaterials*, 20, 1-25.
- PIGATTO, P. D., GUZZI, G., BRAMBILLA, L. & SFORZA, C. 2009. Titanium allergy associated with dental implant failure. *Clinical Oral Implants Research*, 20, 857-857.
- PIRKER, W. & KOCHER, A. 2008. Immediate, non-submerged, root-analogue zirconia implant in single tooth replacement. *Int. J. Oral Maxillofac. Surg.*, 37, 293-295.
- PIRKER, W., WIEDEMANN, D., LIDAUER, A. & KOCHER, A. A. 2011. Immediate, single stage, truly anatomic zirconia implant in lower molar

- replacement: A case report with 2.5 years follow-up. *Int. J. Oral Maxillofac. Surg*, 40, 212-216.
- PITTAYACHAWAN, P. 2008. *COMPARATIVE STUDY OF PHYSICAL PROPERTIES OF ZIRCONIA BASED DENTAL CERAMICS*. PhD, University College London.
- PITTAYACHAWAN, P., MCDONALD, A., PETRIE, A. & KNOWLES, J. C. 2007. The biaxial flexural strength and fatigue property of Lava Y-TZP dental ceramic. *Dental Materials*, 23, 1018-1029.
- PLETKA, B. J. & WIEDERHORN, S. M. 1982. A comparison of failure predictions by strength and fracture mechanics techniques. *Journal of Materials Science*, 17, 1247-1268.
- PROBST, A. & SPIEGEL, H.-U. 1997. Cellular mechanisms of bone repair. *Investigative Surgery*, 10, 77-86.
- PROFFIT, W. R., FIELDS, H. W. & NIXON, W. L. 1983. Occlusal Forces in Normal- and Long-face Adults. *Journal of Dental Research*, 62, 566-570.
- PULEO, D. A. & NANCI, A. 1999. Understanding and controlling the bone-implant interface. *Biomaterials*, 20, 2311-2321.
- RØNOLD, H. J. & ELLINGSEN, J. E. 2002. Effect of micro-roughness produced by TiO₂ blasting-tensile testing of bone attachment by using coin-shaped implants. *Biomaterials*, 23, 4211-4219.
- RADFORD, K. C. & BRATTON, R. J. 1979. Zirconia electrolyte cells. *Journal of Materials Science*, 14, 59-65.
- RAFFAELLI, L., IOMMETTI, P. R., PICCIONI, E., TOESCA, A., SERINI, S., RESCI, F., MISSORI, M., DE SPIRITO, M., MANICONE, P. F. & CALVIELLO, G. 2008. Growth, viability, adhesion potential, and fibronectin expression in fibroblasts cultured on zirconia or feldspatic ceramics *in vitro*. *Journal of Biomedical Materials Research Part A*, 86A, 959-968.
- RALL, W. 1947. *The exact masses of the zirconium isotopes*, Technical Information Division, Oak Ridge Operations.
- RAU, U., ABOU-RAS, D. & KIRCHARTZ, T. 2011. *Advanced Characterization Techniques for Thin Film Solar Cells*, Wiley.
- RHO, J.-Y., TSUI, T. Y. & PHARR, G. M. 1997. Elastic properties of human cortical and trabecular lamellar bone measured by nanoindentation. *Biomaterials*, 18, 1325-1330.
- RICE, P. M. & STOLLER, R. E. Correlation of nanoindentation and conventional mechanical property measurements. MRS Proceedings, 2000. Cambridge Univ Press, Q7. 11.
- RIGOLIN, M. 2014. Influence of different abutments implants surfaces on OBA-09 epithelial cells adhesion: an *in vitro* study. *Annual Congress of the European Association for Osseointegration*. Italy.
- RIMONDINI, L., CERRONI, L., CARRASSI, A. & TORRICELLI, P. 2002. Bacterial colonization of zirconia ceramic surfaces: an *in vitro* and *in vivo* study. *International Journal of Oral & Maxillofacial Implants*, 17.

- RITCHIE, R. O. & DAUSKARDT, R. H. 1991. Cyclic fatigue of ceramics: a fracture mechanics approach to subcritical crack growth and life prediction. *Nippon seramikku kyokai gakujutsu ronbunshi*, 99, 1047-1062.
- RITTER, J. E. 1978. Engineering design and fatigue failure of brittle materials. *Crack Growth and Microstructure*, 667-686.
- RITTER, J. E., VICEDOMINE, M., BREDEK, K. & JAKUS, K. 1985. Dynamic fatigue of indented, soda-lime glass as a function of temperature. *Journal of Materials Science*, 20, 2868-2872.
- ROMPEN, E., DOMKEN, O., DEGIDI, M., FARIAS PONTES, A. E. & PIATTELLI, A. 2006. The effect of material characteristics, of surface topography and of implant components and connections on soft tissue integration: a literature review. *Clinical oral implants research*, 17, 55-67.
- ROTH, V. 2006. Available from; <http://www.doubling-time.com/compute.php>. [Last accessed on 25 August 2014].
- RUFF, O. & EBERT, F. 1929. Ceramics of highly refractory materials. *Z. Anorg. Allgem. Chem*, 180, 19-41.
- RUFF, O., EBERT, F. & STEPHEN, E. 1929. Contributions to the ceramics of highly refractory materials: Ii. System zirconia-lime. *Z Anorg Allg Chem*, 180, 215-24.
- RUIZ, L. & READEY, M. J. 1996. Effect of Heat Treatment on Grain Size, Phase Assemblage, and Mechanical Properties of 3 mol% Y-TZP. *Journal of the American Ceramic Society*, 79, 2331-2340.
- RUPP, F., SCHEIDELER, L., OLSHANSKA, N., DE WILD, M., WIELAND, M. & GEIS-GERSTORFER, J. 2006. Enhancing surface free energy and hydrophilicity through chemical modification of microstructured titanium implant surfaces. *Journal of Biomedical Materials Research Part A*, 76A, 323-334.
- RUPP, F., SCHEIDELER, L., REHBEIN, D., AXMANN, D. & GEIS-GERSTORFER, J. 2004. Roughness induced dynamic changes of wettability of acid-etched titanium implant modifications. *Biomaterials*, 25, 1429-1438.
- SAILER, I., FEHER, A., FILSER, F., GAUCKLER, L. J., LUTHY, H. & HAMMERLE, C. H. F. 2007. Five-year clinical results of zirconia frameworks for posterior fixed partial dentures. *International Journal of Prosthodontics*, 20, 383.
- SAMMONS, R. L., LUMBIKANONDA, N., GROSS, M. & CANTZLER, P. 2005. Comparison of osteoblast spreading on microstructured dental implant surfaces and cell behaviour in an explant model of osseointegration. *Clinical Oral Implants Research*, 16, 657-666.
- SANON, C., CHEVALIER, J. R. M., DOUILLARD, T., KOHAL, R. J., COELHO, P. G., HJERPPE, J. & SILVA, N. R. F. A. 2013. Low temperature degradation and reliability of one-piece ceramic oral implants with a porous surface. *Dental Materials*, 29, 389-397.
- SANTOS, E. M., VOHRA, S., CATLEDGE, S. A., MCCLENNY, M. D., LEMONS, J. & MOORE, K. D. 2004. Examination of surface and material properties of explanted zirconia femoral heads. *The Journal of arthroplasty*, 19, 30-34.

- SATO, T. & SHIMADA, M. 1985. Transformation of Yttria-Doped Tetragonal ZrO₂ Polycrystals by Annealing in Water. *Journal of the American Ceramic Society*, 68, 356-356.
- SAULACIC, N., ERDÖSI, R., BOSSHARDT, D. D., GRUBER, R. & BUSER, D. 2014. Acid and Alkaline Etching of Sandblasted Zirconia Implants: A Histomorphometric Study in Miniature Pigs. *Clinical Implant Dentistry and Related Research*, 16, 313-322.
- SCARANO, A., PIATTELLI, M., CAPUTI, S., FAVERO, G. & PIATTELLI, A. 2004. Bacterial Adhesion on Commercially Pure Titanium and Zirconium Oxide Disks: An *In Vivo* Human Study *Journal of Periodontology*, 75, 292-296.
- SCHLIEPHAKE, H., HEFTI, T., SCHLOTTIG, F., GÉDET, P. & STAEDT, H. 2010. Mechanical anchorage and peri-implant bone formation of surface-modified zirconia in minipigs. *Journal of Clinical Periodontology*, 37, 818-828.
- SCHMAUDER, S. & SCHUBERT, H. 1986. Significance of Internal Stresses for the Martensitic Transformation in Yttria-Stabilised Tetragonal Zirconia Polycrystals During Degradation. *Journal of the American Ceramic Society*, 69, 534-540.
- SCHMIDILIN, P. R., MULLER, P., ATTIN, T., WIELAND, M., HOFER, D. & GUGGENHEIM, B. 2013. Polyspecies biofilm formation on implant surfaces with different surface characteristics. *Journal of Applied Oral Science*, 21, 48-55.
- SCHMITTER, M., MUSSOTTER, K., RAMMELSBERG, P., STOBBER, T., OHLMANN, B. & GABBERT, O. 2009. Clinical performance of extended zirconia frameworks for fixed dental prostheses: two-year results. *Journal of Oral Rehabilitation*, 36, 610-615.
- SCHNEIDER, D., GRUNDER, U., ENDER, A., HÄMMERLE, C. H. F. & JUNG, R. E. 2011. Volume gain and stability of peri-implant tissue following bone and soft tissue augmentation: 1-year results from a prospective cohort study. *Clinical Oral Implants Research*, 22, 28-37.
- SCHUBERT, H. & FREY, F. 2005. Stability of *Y-TZP* during hydrothermal treatment: neutron experiments and stability considerations. *Journal of the European Ceramic Society*, 25, 1597-1602.
- SCHWARZ, F., BECKER, J., WIELAND, M. & DARD, M. 2007a. One-Part Implant with a Hydroxylated Soft Tissue Contact Surface. Google Patents.
- SCHWARZ, F., HERTEN, M., SAGER, M., WIELAND, M., DARD, M. & BECKER, J. 2007b. Bone regeneration in dehiscence-type defects at chemically modified (SLActive®) and conventional SLA titanium implants: a pilot study in dogs. *Journal of Clinical Periodontology*, 34, 78-86.
- SCHWARZ, S., LENZ, J. & SCHWICKERATH, H. 1988. Zur Festigkeit des metallkeramischen Verbundes bei der Biegeprüfung. *Dtsch ZahnÄrztl*, 43, 1152-1158.
- SCHWICKERATH, H. 1986. Dauerfestigkeit von Keramik. *Dtsch ZahnÄrztl*, 264-266.

- SCOTT, H. G. 1975. Phase relationships in the zirconia-yttria system. *Journal of Materials Science*, 10, 1527-1535.
- SENNERBY, L., DASMAH, A., LARSSON, B. & IVERHED, M. 2005. Bone Tissue Responses to Surface-Modified Zirconia Implants: A Histomorphometric and Removal Torque Study in the Rabbit. *Clinical Implant Dentistry and Related Research*, 7, 13-20.
- SENNERBY, L., THOMSEN, P. & ERICSON, L. E. 1991. A morphometric and biomechanic comparison of titanium implants inserted in rabbit cortical and cancellous bone. *The International journal of oral & maxillofacial implants*, 7, 62-71.
- SERGO, V. & CLARKE, D. R. 1995. Deformation Bands in Ceria-Stabilised Tetragonal Zirconia/Alumina: II, Stress-Induced Aging at Room Temperature. *Journal of the American Ceramic Society*, 78, 641-644.
- SERGO, V., CLARKE, D. R. & POMPE, W. 1995. Deformation Bands in Ceria-Stabilised Tetragonal Zirconia/Alumina: I, Measurement of Internal Stresses. *Journal of the American Ceramic Society*, 78, 633-640.
- SETZER, B., BÄCHLE, M., METZGER, M. C. & KOHAL, R. J. 2009. The gene-expression and phenotypic response of hFOB 1.19 osteoblasts to surface-modified titanium and zirconia. *Biomaterials*, 30, 979-990.
- SHALABI, M. M., GORTEMAKER, A., HOF, M. A. V. T., JANSEN, J. A. & CREUGERS, N. H. J. 2006. Implant Surface Roughness and Bone Healing: a Systematic Review. *Journal of Dental Research*, 85, 496-500.
- SHIMIZU, K., OKA, M., KUMAR, P., KOTOURA, Y., YAMAMURO, T., MAKINOUCI, K. & NAKAMURA, T. 1993. Time-dependent changes in the mechanical properties of zirconia ceramic. *Journal of Biomedical Materials Research*, 27, 729-734.
- SHOJAI, F. & MÄNTYLÄ, T. A. 2001. Chemical stability of yttria doped zirconia membranes in acid and basic aqueous solutions: chemical properties, effect of annealing and ageing time. *Ceramics international*, 27, 299-307.
- SICILIA, A., CUESTA, S., COMA, G., ARREGUI, I., GUIASOLA, C., RUIZ, E. & MAESTRO, A. 2008. Titanium allergy in dental implant patients: a clinical study on 1500 consecutive patients. *Clinical Oral Implants Research*, 19, 823-835.
- SIEGELE, D. & SOLTESZ, U. 1988. Numerical investigations of the influence of implant shape on stress distribution in the jaw bone. *The International journal of oral & maxillofacial implants*, 4, 333-340.
- SIGNORE, A., BENEDECENTI, S., KAITZAS, V., BARONE, M., ANGIERO, F. & RAVERA, G. 2009. Long-term survival of endodontically treated, maxillary anterior teeth restored with either tapered or parallel-sided glass-fibre posts and full-ceramic crown coverage. *Journal of Dentistry*, 37, 115-121.
- SILVA, N. R. F. A., COELHO, P. G., FERNANDES, C. A. O., NAVARRO, J. M., DIAS, R. A. & THOMPSON, V. P. 2009. Reliability of one-piece ceramic implant. *Journal of Biomedical Materials Research Part B: Applied Biomaterials*, 88, 419-426.

- SIMONIS, P., DUFOUR, T. & TENENBAUM, H. 2010. Long-term implant survival and success: a 10–16-year follow-up of non-submerged dental implants. *Clinical Oral Implants Research*, 21, 772-777.
- SIMPSON, J. P. & STEINEMANN, S. G. 2002. Surface-modified implant with improved osteointegration. Google Patents.
- SINGER, I. I. 1982. Association of fibronectin and vinculin with focal contacts and stress fibres in stationary hamster fibroblasts. *The Journal of cell biology*, 92, 398-408.
- SOBCZAK, N., KUDYBA, A., NOWAK, R., RADZIWIŁŁ, W. & PIETRZAK, K. 2007. Factors affecting wettability and bond strength of solder joint couples. *Pure and Applied Chemistry*, 79, 1755-1769.
- STADLINGER, B., HENNIG, M., ECKELT, U., KUHLISCH, E. & MAI, R. 2010. Comparison of zirconia and titanium implants after a short healing period. A pilot study in minipigs. *International journal of oral and maxillofacial surgery*, 39, 585-592.
- STANFORD, C. M. & KELLER, J. C. 1991. The concept of osseointegration and bone matrix expression. *Critical Reviews in Oral Biology & Medicine*, 2, 83-101.
- STEELE, J., TREASURE, E., O'SULLIVAN, I., MORRIS, J. & MURRAY, J. 2012. Adult dental health survey 2009: Transformations in British oral health 1968–2009. *British dental journal*, 213, 523-527.
- STEIGENGA, J. T., AL-SHAMMARI, K. F., NOCITI, F. H., MISCH, C. E. & WANG, H.-L. 2003. Dental implant design and its relationship to long-term implant success. *Implant dentistry*, 12, 306-317.
- STERNER, T., SCHUTZE, N., SAXLER, G., JAKOB, F. & RADER, C. 2004. Effects of clinically relevant alumina ceramic, zirconia ceramic and titanium particles of different sizes and concentrations on TNF-*alpha* release in a human macrophage cell line. *Biomed Tech (Berl)*, 49, 340-344.
- STÜBINGER, S., HOMANN, F., ETTER, C., MISKIEWICZ, M., WIELAND, M. & SADER, R. 2008. Effect of Er: YAG, CO₂ and diode laser irradiation on surface properties of zirconia endosseous dental implants. *Lasers in surgery and medicine*, 40, 223-228.
- STUDART, A. R., FILSER, F., KOCHER, P. & GAUCKLER, L. J. 2007a. Fatigue of zirconia under cyclic loading in water and its implications for the design of dental bridges. *Dental Materials*, 23, 106-114.
- STUDART, A. R., FILSER, F., KOCHER, P. & GAUCKLER, L. J. 2007b. *In vitro* lifetime of dental ceramics under cyclic loading in water. *Biomaterials*, 28, 2695-2705.
- SUBBARAO, E. C., MAITI, H. S. & SRIVASTAVA, K. K. 1974. Martensitic transformation in zirconia. *physica status solidi (a)*, 21, 9-40.
- SUENAGA, K., BOUCHET, D., COLLIEX, C., THOREL, A. & BRANDON, D. G. 1998. Investigations of alumina/spinel and alumina/zirconia interfaces by spatially resolved electron energy loss spectroscopy. *Journal of the European Ceramic Society*, 18, 1453-1459.
- SUNDGREN, J. E., BODÖ, P. & LUNDSTRÖM, I. 1986. Auger electron spectroscopic studies of the interface between human tissue and implants of

- titanium and stainless steel. *Journal of Colloid and Interface Science*, 110, 9-20.
- SUZUKI, K., AOKI, K. & OHYA, K. 1997. Effects of surface roughness of titanium implants on bone remodeling activity of femur in rabbits. *Bone*, 21, 507-514.
- SWAIN, M. V. 1985. Inelastic deformation of MgO—PSZ and its significance for strength-toughness relationship of zirconia toughened ceramics. *Acta Metallurgica*, 33, 2083-2091.
- SYKARAS, N., IACOPINO, A. M., MARKER, V. A., TRIPLETT, R. G. & WOODY, R. D. 1999. Implant materials, designs, and surface topographies: their effect on osseointegration. A literature review. *The International journal of oral & maxillofacial implants*, 15, 675-690.
- TABORELLI, M., JOBIN, M., FRANÇOIS, P., VAUDAUX, P., TONETTI, M., SZMUKLER-MONCLER, S., SIMPSON, J. P. & DESCOUTS, P. 1997. Influence of surface treatments developed for oral implants on the physical and biological properties of titanium. (I) Surface characterization. *Clinical Oral Implants Research*, 8, 208-216.
- TAKAMORI, E. R., CRUZ, R., GONÇALVEZ, F., ZANETTI, R. V., ZANETTI, A. & GRANJEIRO, J. M. 2008. Effect of Roughness of Zirconia and Titanium on Fibroblast Adhesion. *Artificial Organs*, 32, 305-309.
- TANAKA, K., TAMURA, J., KAWANABE, K., NAWA, M., UCHIDA, M., KOKUBO, T. & NAKAMURA, T. 2003. Phase stability after aging and its influence on pin-on-disk wear properties of Ce-TZP/Al₂O₃ nanocomposite and conventional *Y-TZP*. *Journal of Biomedical Materials Research Part A*, 67A, 200-207.
- TARKANIAN, M. L., NEUMANN, J. P. & RAYMOND, L. 1973. Determination of the temperature dependence of {100} and {112} slip in tungsten from Knoop hardness measurements. *The Science of Hardness Testing and Its Research Application*. Westbook JH, Conrad H, Eds. American Society for Metals, 187-198.
- THE ACADEMY OF PROSTHODONTICS 2005. Glossary of Prosthodontic Terms. *Journal of Prosthetic Dentistry*, 94.
- TORAYA, H., YOSHIMURA, M. & SOMIYA, S. 1984. Calibration Curve for Quantitative Analysis of the Monoclinic-Tetragonal ZrO₂ System by X-Ray Diffraction. *Journal of the American Ceramic Society*, 67, C-119-C-121.
- TRUSTRUM, K. & JAYATILAKA, A. D. S. 1979. On estimating the Weibull modulus for a brittle material. *Journal of Materials Science*, 14, 1080-1084.
- TSUKUMA, K. & SHIMADA, M. 1985. Strength, fracture toughness and Vickers hardness of CeO₂-stabilised tetragonal ZrO₂ polycrystals (Ce-TZP). *Journal of Materials Science*, 20, 1178-1184.
- UGO COVANI, C. B., ANTONIO BARONE, AND DR. LUDOVICO SBORDONE 2004. Bucco-Lingual Crestal Bone Changes After Immediate and Delayed Implant Placement *Journal of Periodontology*, 75, 1605-1612.
- USTUNDAG, E. & FISCHMAN, G. S. 2009. *23rd Annual Conference on Composites, Advanced Ceramics, Materials, and Structures - B: Ceramic Engineering and Science Proceedings*, Wiley.

- VAGKOPOULOU T, K. S., KOIDIS P, STRUB JR. 2009. Zirconia in dentistry: part 1. Discovering the nature of an upcoming bioceramic. *Eur J Esthet Dent*, 4, 130-151.
- VAN BRAKEL, R., CUNE, M., VAN WINKELHOFF, A., DE PUTTER, C., VERHOEVEN, J. & VAN DER REIJDEN, W. 2011. Early bacterial colonization and soft tissue health around zirconia and titanium abutments: an *in vivo* study in man. *Clinical Oral Implants Research*, 22, 571-577.
- VAN NOORT, R. 2014. *Introduction to Dental Materials*, Elsevier Health Sciences UK.
- VANASUPA, L., JOO, Y.-C., BESSER, P. R. & PRAMANICK, S. 1999. Texture analysis of damascene-fabricated Cu lines by X-Ray diffraction and electron backscatter diffraction and its impact on electromigration performance. *Journal of applied physics*, 85, 2583-2590.
- VAREZ, A., GARCIA-GONZALEZ, E., JOLLY, J. & SANZ, J. 2007. Structural characterization of Ce-ZrO₂ samples prepared at 1650 C by solid state reaction: A combined TEM and XRD study. *Journal of the European Ceramic Society*, 27, 3677-3682.
- VIRKAR, A. V., HUANG, J. L. & CUTLER, R. A. 1987. Strengthening of Oxide Ceramics by Transformation-Induced Stress. *Journal of the American Ceramic Society*, 70, 164-170.
- VIRKAR, A. V. & MATSUMOTO, R. L. K. 1986. Ferroelastic domain switching as a toughening mechanism in tetragonal zirconia. *Journal of the American Ceramic Society*, 69, 224-226.
- VON STEYERN, P., EBBESSON, S., HOLMGREN, J., HAAG, P. & NILNER, K. 2006. Fracture strength of two oxide ceramic crown systems after cyclic loading and thermocycling. *Journal of oral rehabilitation*, 33, 682-689.
- WACHTMAN, J. B., CANNON, W. R. & MATTHEWSON, J. 2009. *Mechanical Properties of Ceramics*, Wiley.
- WANG, G., MENG, F., DING, C., CHU, P. K. & LIU, X. 2010. Microstructure, bioactivity and osteoblast behavior of monoclinic zirconia coating with nanostructured surface. *Acta biomaterialia*, 6, 990-1000.
- WANG, J., ZHENG, X. H. & STEVENS, R. 1992. Fabrication and microstructure-mechanical property relationships in Ce-TZPs. *Journal of Materials Science*, 27, 5348-5356.
- WARREN, B. E. 2012. *X-Ray Diffraction*, Dover Publications.
- WATTS, D. C., ISSA, M., IBRAHIM, A., WAKIAGA, J., AL-SAMADANI, K., AL-AZRAQI, M. & SILIKAS, N. 2008. Edge strength of resin-composite margins. *Dental Materials*, 24, 129-133.
- WEIBULL, W. 1951. A Statistical Distribution Function of Wide applicability. *Journal of applied mechanics*.
- WEILER, W. 1989. Hardness testing--a new method for economical and physically meaningful microhardness testing. *Br. J. Non-Destr. Test.*, 31, 253-258.

- WELANDER, M., ABRAHAMSSON, I. & BERGLUNDH, T. 2008. The mucosal barrier at implant abutments of different materials. *Clinical oral implants research*, 19, 635-641.
- WENNERBERG, A. & ALBREKTSSON, T. 2009. Effects of titanium surface topography on bone integration: a systematic review. *Clinical oral implants research*, 20, 172-184.
- WENNERBERG, A., GALLI, S. & ALBREKTSSON, T. 2011. Current knowledge about the hydrophilic and nanostructured SLActive surface. *Clinical, Cosmetic and Investigational Dentistry*, 3, 59-67.
- WENNERBERG, A., OHLSSON, R., ROSÉN, B.-G. & ANDERSSON, B. 1996. Characterizing three-dimensional topography of engineering and biomaterial surfaces by confocal laser scanning and stylus techniques. *Medical engineering & physics*, 18, 548-556.
- WENZ, H. J., BARTSCH, J., WOLFART, S. & KERN, M. 2008. Osseointegration and clinical success of zirconia dental implants: a systematic review. *The International Journal of Prosthodontics*, 21, 27-36.
- WHITEHEAD, S. A., SHEARER, A. C., WATTS, D. C. & WILSON, N. H. F. 1995. Comparison of methods for measuring surface roughness of ceramic. *Journal of Oral Rehabilitation*, 22, 421-427.
- WIEDERHORN, S. M. 1967. Influence of Water Vapor on Crack Propagation in Soda • Lime Glass. *Journal of the American Ceramic Society*, 50, 407-414.
- WILLIAMS, D. F. 1999. *The Williams Dictionary of Biomaterials*, Liverpool University Press.
- WILLMOTT, P. 2011. *An Introduction to Synchrotron Radiation: Techniques and Applications*, Wiley.
- WURST, J. C. & NELSON, J. A. 1972. Lineal Intercept Technique for Measuring Grain Size in Two-Phase Polycrystalline Ceramics. *Journal of the American Ceramic Society*, 55, 109-109.
- YAHYAPOUR, N., ERIKSSON, C., MALMBERG, P. & NYGREN, H. K. 2004. Thrombin, kallikrein and complement C5b-9 adsorption on hydrophilic and hydrophobic titanium and glass after short time exposure to whole blood. *Biomaterials*, 25, 3171-3176.
- YAMADA, K. M., YAMADA, S. S. & PASTAN, I. 1976. Cell surface protein partially restores morphology, adhesiveness, and contact inhibition of movement to transformed fibroblasts. *Proceedings of the National Academy of Sciences*, 73, 1217-1221.
- YAMANO, S., MA, A., SHANTI, R. M., KIM, S.-W., WADA, K. & SUKOTJO, C. 2010. The influence of different implant materials on human gingival fibroblast morphology, proliferation, and gene expression. *The International journal of oral & maxillofacial implants*, 26, 1247-1255.
- YAMASHITA, I., TSUKUMA, K., TOJO, T., KAWAJI, H. & ATAKE, T. 2008. Synchrotron X-Ray Study of the Crystal Structure and Hydrothermal Degradation of Ytria-Stabilised Tetragonal Zirconia Polycrystal. *Journal of the American Ceramic Society*, 91, 1634-1639.

- YASHIMA, M., SASAKI, S., KAKIHANA, M., YAMAGUCHI, Y., ARASHI, H. & YOSHIMURA, M. 1994. Oxygen-induced structural change of the tetragonal phase around the tetragonal-cubic phase boundary in ZrO₂-YO₁. 5 solid solutions. *Acta Crystallographica Section B: Structural Science*, 50, 663-672.
- YILDIRIM, M., EDELHOFF, D., HANISCH, O. & SPIEKERMANN, H. 2000. Ceramic abutments--a new era in achieving optimal esthetics in implant dentistry. *The International journal of periodontics & restorative dentistry*, 20, 81-91.
- YIN, H., GAO, M. & WEI, R. P. 1995. Phase transformation and sustained load crack growth in ZrO₂, 3 mol% Y₂O₃: Experiments and kinetic modeling. *Acta metallurgica et materialia*, 43, 371-382.
- YOSHIMURA, M., NOMA, T., KAWABATA, K. & SŌMIYA, S. 1987. Role of H₂O on the degradation process of **Y-TZP**. *Journal of Materials Science Letters*, 6, 465-467.
- YOUNG, T. 1805. An Essay on the Cohesion of Fluids. *Philosophical Transactions of the Royal Society of London*, 95, 65-87.
- YOVANOVICH, M. M. Micro and macro hardness measurements, correlations, and contact models. 44th AIAA Aerospace Sciences Meeting and Exhibit, 2006. 1-28.
- YUAN, Y. & LEE, T. R. 2013. Contact angle and wetting properties. *Surface science techniques*. Springer.
- ZEMBIC, A., S., I., J., R.E. & HAMMERLE, C. H. 2009. Randomized-controlled clinical trial of customised zirconia and titanium implant abutments for single-tooth implants in canine and posterior regions: 3-year results. *Clinical Oral Implants Research*, 20, 802-808.
- ZEMBIC, A., BÖSCH, A., JUNG, R. E., HÄMMERLE, C. H. F. & SAILER, I. 2013. Five-year results of a randomized controlled clinical trial comparing zirconia and titanium abutments supporting single-implant crowns in canine and posterior regions. *Clinical oral implants research*, 24, 384-390.
- ZEMBIC, A., PHILIPP, A. O. H., HÄMMERLE, C. H. F., WOHLWEND, A. & SAILER, I. 2014. Eleven-Year Follow-Up of a Prospective Study of Zirconia Implant Abutments Supporting Single All-Ceramic Crowns in Anterior and Premolar Regions. *Clinical Implant Dentistry and Related Research*, n/a-n/a.
- ZHANG, A. 2014. *CGF osseointegration* [Online]. Available: <https://www.youtube.com/watch?v=4YM7TkAM7Fo> [Accessed 06/01/2015 2015].
- ZHANG, Y. & LAWN, B. R. 2005. Fatigue sensitivity of **Y-TZP** to microscale sharp-contact flaws. *Journal of Biomedical Materials Research Part B: Applied Biomaterials*, 72, 388-392.
- ZHANG, Y., LAWN, B. R., REKOW, E. D. & THOMPSON, V. P. 2004a. Effect of sandblasting on the long-term performance of dental ceramics. *Journal of Biomedical Materials Research Part B: Applied Biomaterials*, 71, 381-386.
- ZHANG, Y., PAJARES, A. & LAWN, B. R. 2004b. Fatigue and damage tolerance of Y-TZP ceramics in layered biomechanical systems. *Journal of Biomedical Materials Research Part B: Applied Biomaterials*, 71, 166-171.

- ZHAO, G., SCHWARTZ, Z., WIELAND, M., RUPP, F., GEIS-GERSTORFER, J., COCHRAN, D. & BOYAN, B. 2005. High surface energy enhances cell response to titanium substrate microstructure. *Journal of Biomedical Materials Research Part A*, 74, 49-58.
- ZIDAN, O., ASMUSSEN, E. & JÜRGENSEN, K. D. 1980. Tensile strength of restorative resins. *European Journal of Oral Sciences*, 88, 285-290.
- ZINGER, O., ANSELME, K., HABERSETZER, P. & LANDOLT, D. 2003. Time-dependent adhesion and morphology of osteoblastic cells on titanium model surfaces featuring scale-dependent topography. *Eur Cell Mater*, 5, 21-3.
- ZÖLLNER, A., GANELES, J., KOROSTOFF, J., GUERRA, F., KRAFFT, T. & BRÄGGER, U. 2008. Immediate and early non-occlusal loading of Straumann implants with a chemically modified surface (SLActive) in the posterior mandible and maxilla: interim results from a prospective multicenter randomized-controlled study. *Clinical Oral Implants Research*, 19, 442-450.

Appendix A

maxon motor		
maxon motor group	Prozessbeschreibung Process description	S-Qw_F66 Index 04 Seite 1 / 3

Projekt: (project)	<i>Implantate</i>
Hersteller: (Equipment Manufacturer)	maxon motor GmbH
Kunde: (customer)	White Implants Development Corp B.V.
Standort: (Location)	maxon motor GmbH, Sexau
Bereich: (Departement)	maxon dental

1Zielsetzung (<i>Objective</i>)	2
2Prozessschritte	2

maxon motor		
maxon motor group	Prozessbeschreibung Process description	S-Qw_F66 Index 04 Seite 2 / 3

1 Zielsetzung

Objective

Das Dokument beschreibt den allgemeinen Herstellungsvorgang eines Keramikimplantates für White Implants Development Corp B.V.

This document describes the general manufacturing process of a ceramic implant for WIDC.

2 Prozessschritte

Process steps

- **Pulver und Binder = Compound**

Das hochfeine Keramikpulver wird mit einem Bindersystem zu einem spritzgießfähigen Material vermischt und anschließend granuliert. Das entstandene Compound lässt sich mit ähnlichen Freiheitsgraden wie beim Kunststoffspritzguss verarbeiten.

Powder + Binder = Compound

The ultra-fine ceramic powder is mixed with a binder system into an injection moldable material and subsequently granulated. The resulting compound can be processed with similar degrees of freedom as with plastic injection.

- **Keramikpulverspritzgießen CIM**

Bei diesem Verfahren wird das Compound auf speziell ausgerüsteten Spritzgießmaschinen verarbeitet. Dabei wird das Compound aufgeschmolzen und Spritzgußform gefüllt. Die gespritzten Teile werden als Grünlinge bezeichnet. Es sind ähnliche Geometrien wie beim Kunststoffspritzguss realisierbar.

Ceramic Injection Molding

With this method, the compound is processed in specially equipped injection molding machines. The compound is melted and filled into the injection molds. The molded parts are referred to as green bodies. Similar geometries as in plastic injection are realized.

- **Entbinderung**

Bei der Entbinderung wird das Bindermaterial aus dem Grünling thermisch herausgelöst. Dabei reduziert sich das Gewicht des Grünlings.

Debinding

When debinding, the binder material is thermally removed from the green bodies, thereby reducing their weight.

- **Sinterung**

Anschließend wird das entbinderte Teil im Sinterofen bei ungefähr 1450°C gesintert. Das Teil unterliegt dabei einer Schwindung von ca. 30%.

Sintering

Subsequently the binder-free part is sintered in a sintering furnace at approximately 1450°C. The part is thereby shrinking about 30%.

maxon motor		
maxon motor group	Prozessbeschreibung Process description	S-Qw_F66 Index 04 Seite 3 / 3

- **Oberflächenbehandlung**

Nach der Sinterung findet eine Oberflächenbehandlung statt. Dabei wird durch ein Ätzverfahren die Oberfläche des Implantates aufgeraut.

Surface treatment

After the sintering process follows a surface treatment. The surface of the implants is roughened by an etching process.

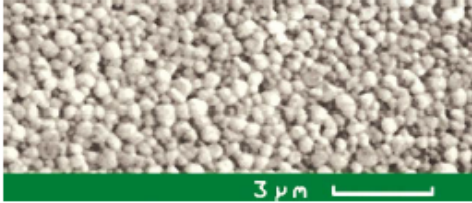
- **Kontrolle**

Ein gut implementiertes Qualitätsmanagementsystem sowie Prüf- und Messtechnik auf neuestem Niveau stellt die Prozess- und Produktqualität sicher.

Control

A well implemented quality management system, as well as testing and measurement equipment meeting the latest standards, ensure a high process and product quality.

Appendix B

Mechanische Eigenschaften / Mechanical properties :			
• Elastizitätsmodul / <i>E-modulus</i>		2×10^5	$\frac{\text{N}}{\text{mm}^2}$
• Biegefestigkeit / <i>bending strength</i>			
• gesintert / <i>sintered</i>		600 - 800	$\frac{\text{N}}{\text{mm}^2}$
• poliert / <i>polished</i>		800 - 1.000	$\frac{\text{N}}{\text{mm}^2}$
• geHIPt / <i>HIPed</i>		1.200 - 1.400	$\frac{\text{N}}{\text{mm}^2}$
• Härte / <i>hardness</i>		~1350	HV
• Bruchzähigkeit / <i>fracture toughness</i>		6 - 9	$\text{MPa}\sqrt{\text{m}}$
• Dichte / <i>density</i>		$\geq 6,02$	$\frac{\text{g}}{\text{cm}^3}$
• mögliche Oberfläche / <i>surface</i>		$\leq \text{Ra } 0,05$	
Thermische Eigenschaften / Thermal properties :			
• Ausdehnungskoeffizient / <i>thermal expansion coefficient</i>		10×10^{-6}	$\frac{1}{\text{K}}$
• Wärmeleitfähigkeit / <i>thermal conductivity</i>		2	$\frac{\text{W}}{\text{mK}}$
• Thermoschockbeständigkeit / <i>resistance to thermal shock</i>		350	$^{\circ}\text{C}$
Elektrische Eigenschaften / Electrical properties :			
• Widerstand / <i>resistance</i>		10^8	Ωm
• Dielektrische Konstante / <i>relative permittivity</i>		22	[-]
Zusammensetzung nach dem Sintern / Composition after sintering :			
		> 94,4 %	ZrO ₂
		5,0% - 5,3%	Y ₂ O ₃
		0,2% - 0,3%	Al ₂ O ₃
Gefüge / microstructure:		Mittlere Korngröße / <i>middle grain size:</i>	0,5µm
Vorteile / advantages :	<ul style="list-style-type: none"> • Exzellente Oberflächengüte • Sehr gute Gleiteigenschaften • Verschleißbeständig mit hoher Festigkeit • Gute Biegefestigkeit • Biokompatibel • Thermischer Isolator • Elektrischer Isolator 	<ul style="list-style-type: none"> • <i>excellent surface quality</i> • <i>very good sliding character</i> • <i>wear-resistant with a high strength</i> • <i>good bending strength</i> • <i>biocompatible</i> • <i>thermal isolator</i> • <i>electrical isolator</i> 	
Artikel-Nr. / part no		167989	
Ind. / rev.		01	
AFD-Nr. / change		605041 29.07.2005	
Werkstoff / material		Zirkonoxid TZP (ZrO ₂)	
<small>Änderungen in der Hersteiltechnologie, Geometrie und Material nur in Absprache mit maxon motor GmbH Sexau Modifications in production technology, geometry and materials only by agreement with maxon motor GmbH Sexau</small>		Benennung / title Materialspezifikation Zirkonoxid Material specification of zirconium oxide	
<small>Für dieses Dokument behalten wir uns alle Rechte vor. We reserve all rights for this document.</small>		maxon motor GmbH D-79350 Sexau	
Datum / date	Name	Dokument-Nr. / document no	ind. / rev.
29.07.2005	REIM	771673	01
29.07.2005	ZD		
EDV:	77167301.pdf	Blatt / sheet	1 / 1
Freigabe:	605941	Ersatz für:	Ersetzt durch:

Appendix C

12 EMCM 4

CYCLE VALIDATION PROTOCOL			
Implementation of generic cycle # 14/15 and 24/25 for ETO processing of EMCM Ovabloc catheter and C-ment direct			
Sterigenics	Protocol No. P 2008-007	Revision 0	Page 8 of 22

7.1.2 Nominal full cycle parameters

Parameter	Set-point	Min. spec.	Max. spec.
Preconditioning			
Load temperature prior to preconditioning start	≤ 20°C	N/A	20
Temperature	38°C	33	43
RH	60%	50	80
Time	16 hours	16	72
Transfer preconditioning → sterilizer	Maximum 45 minutes	N/A	45
Sterilization cycle (re-circulation blower steered 'on')			
Sterilization temperature	42°C	40	50
Initial vacuum	75 mbarA	70	80
Leak test	≤15 mbar/10 min	0	15
Steam injection	40 mbar	35	45
Humidity dwell pressure range	115-122 mbarA	105	130
Steam dwell time	15 minutes	15	30
Nitrogen injection #1	230 mbarA	225	235
ETO injection	650 mbarA	645	655
ETO minimum weight	> 22.7 kg	23	N/A
Nitrogen injection #2	750 mbarA	745	755
Nitrogen injection time	13 minutes	13	20
Calculated ETO concentration at gas dwell start (pV = nRT)	690 mg/l	660	720
Gas dwell pressure	720-750 mbarA	715	765
ETO dwell time	Cycle 14/15: 02h15 Cycle 24/25: 04h00	Cycle 14/15: 02h15 Cycle 24/25: 04h00	Cycle 14/15: 03h15 Cycle 24/25: 05h00
Evacuation pressure	75 mbarA	70	80
Nitrogen wash A: 75 → 700 → 75 mbarA	75-700 mbarA	70	705
Nitrogen wash B: 75 → 800 → 85 mbarA	75-800 mbarA	70	805
Final air inlet	950 mbarA	945	955

Appendix D

Fitting Functions

```
a=5.708e-10%0.0439245
b=-sqrt(0.71399)%-1.33293
c=0.209999999%0.259398
d=-b%1.31288%0.798526
%pi=3.14159
%a=0.0
%b=-2.305
%c=1
%d=2.5
syms s t
%symfun f
%for the exponential decrease
f=(s*a-b*c*d)/(s-b*d)
f2=(a/s+c*d)/(1+s*d)
%load ahmad.dat
%for the Gausssian decrease
%f=sqrt(2*pi)/2*(-2.305)*2.5/s*(1-erf(-
sqrt(2)/2*(2.305)*2.5/s))*exp(2.305^2*2.5^2/(2.*s^2))
%f=erf(s)
g=ilaplace(f2)
%lin = -0.158 *s + 0.2594
lin = -0.258 *s + 0.21
fp = matlabFunction(f);
gp = matlabFunction(g);
linp = matlabFunction(lin);
q=0:0.1:10;
%dg = matlabFunction(diff(gp,q))
dlmwrite('test.txt', [q', fp(q)',gp(q)',linp(q)],'delimiter','t')
ezplot(f,[0, 10])
hold on
p=ezplot(g,[0,10])
set(p,'Color','red')
lp=ezplot(lin,[0,10])
set(lp,'Color','black')
ylim([0,0.3])
hold off
```

Inverse Laplace Transform

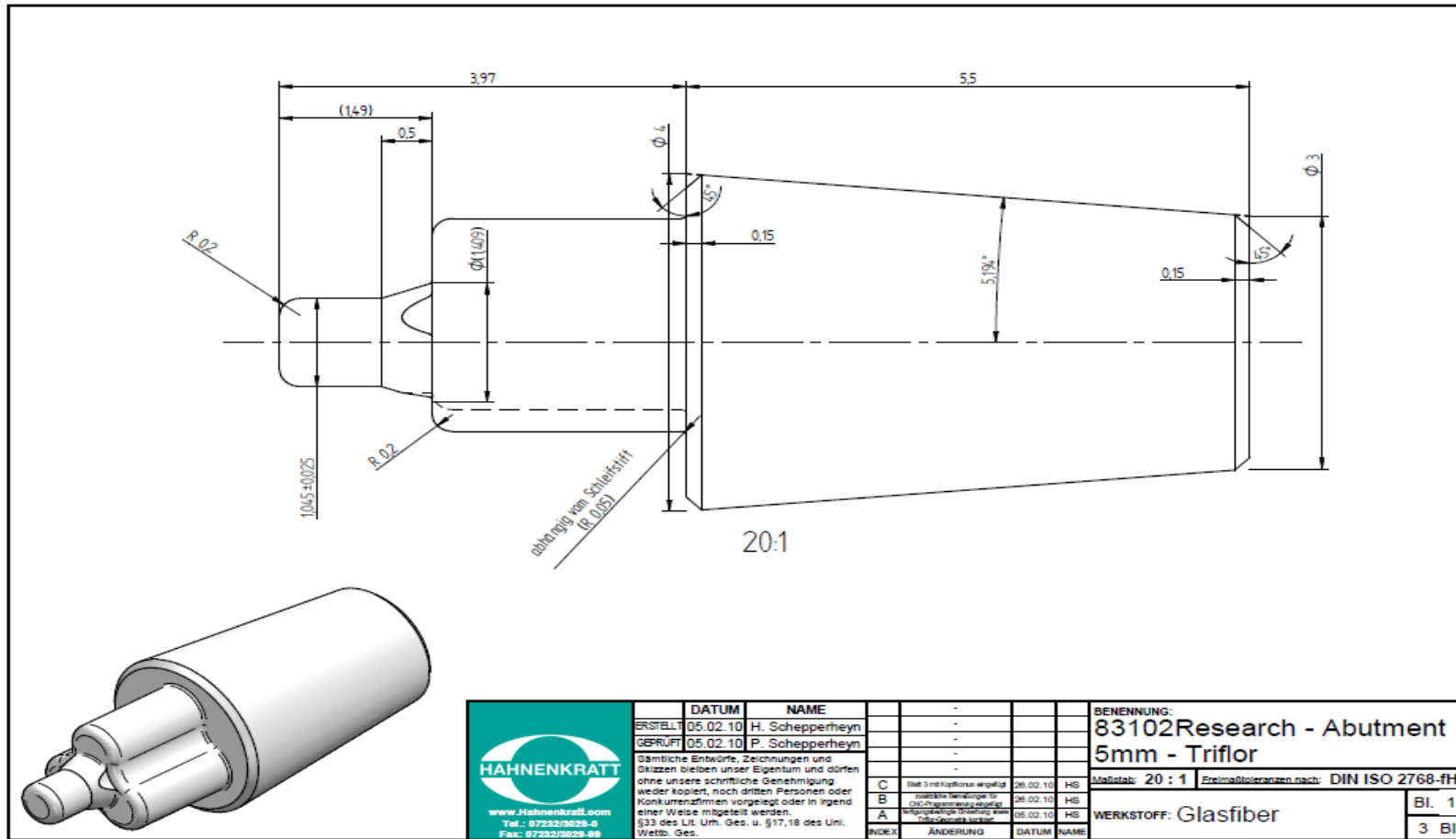
```
FIT_LIMIT=1e-10
set style line 1 lt 1 lw 2 pt 3
set style line 2 lt 8 lw 2 pt 3
set style line 3 lt 3 lw 2 pt 3
set style line 4 lt 5 lw 2 pt 3
set xlabel 'D,z'
set ylabel 'x_m(D)'
```

```

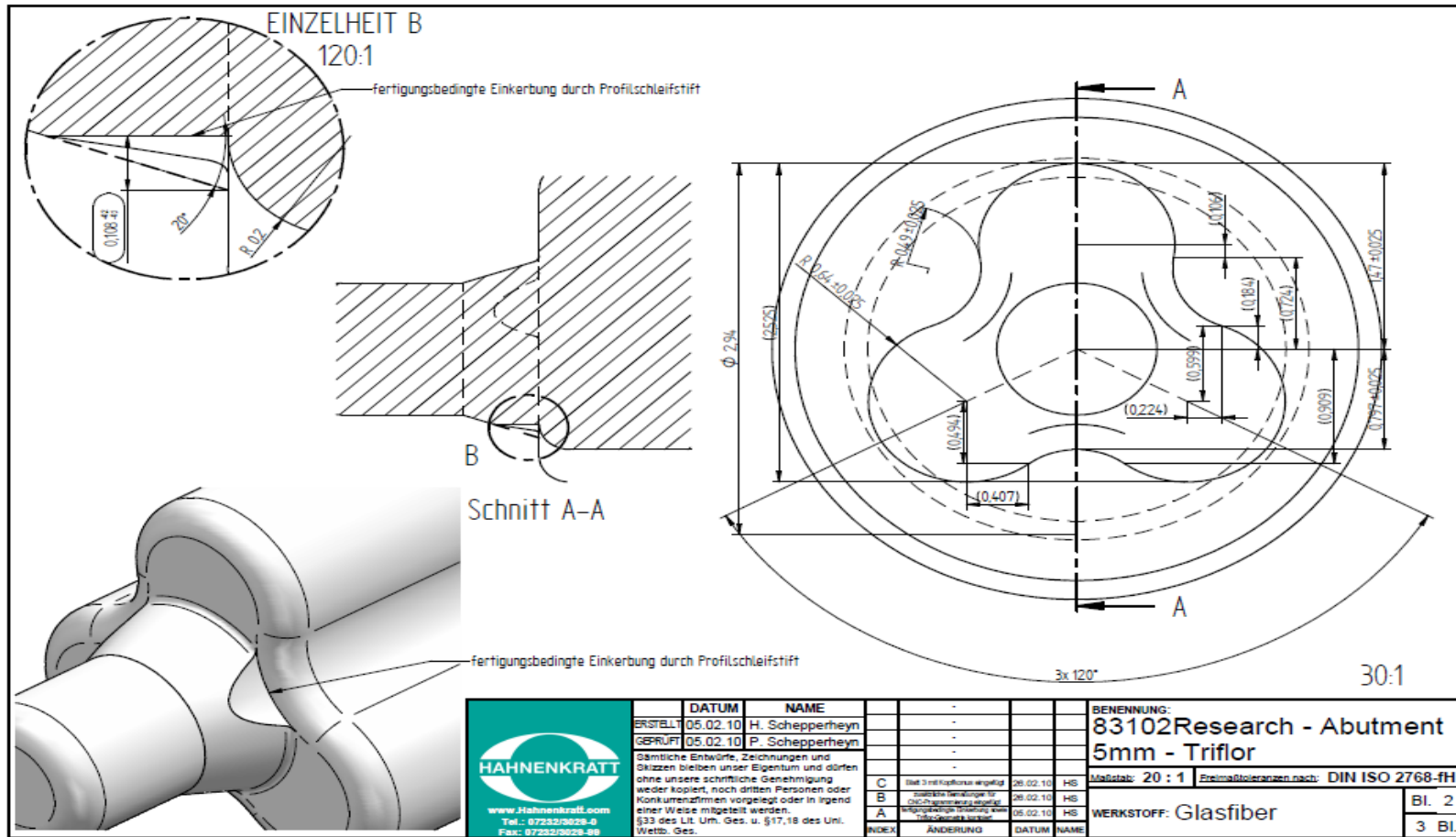
A1(x)=sin(x)**2
C1(x)=sin(x)**2
E1(x)=x**2
f1(x)=(A1(a1)*x+E1(e1)*C1(c1))/(x+E1(e1))
f1b(x)=A1(a1b)+sqrt(2*pi)/2*E1(e1b)*(C1(c1b)-
A1(a1b))/x*erfc(sqrt(2)/2*E1(e1b)/x)*exp(E1(e1b)**2/2/x**2)
A2(x)=sin(x)**2
C2(x)=0.21*sin(x)**2
E2(x)=x**2
f2(x)=(A2(a2)*x+E2(e2)*C2(c2))/(x+E2(e2))
f2b(x)=A2(a2b)+sqrt(2*pi)/2*E2(e2b)*(C2(c2b)-
A2(a2b))/x*erfc(sqrt(2)/2*E2(e2b)/x)*exp(E2(e2b)**2/2/x**2)
fit f1(x) 'ahmad2.dat' u 1:2 via a1,c1,e1
#fit f1b(x) 'ahmad2.dat' u 1:2 via a1b,c1b,e1b
pause -1
fit f2(x) 'ahmad2.dat' u 1:3 via a2,c2,e2
#fit f2b(x) 'ahmad2.dat' u 1:3 via a2b,c2b,e2b
set xrange [0 to 10]
#set yrange [0 to 0.3]
p 'ahmad2.dat' u 1:2 lt -1 lw 2 ps 2 ti " " u 1:3 lt -1 lw 2 ps 2 ti " , f1(x) ls 1 ti
'expo' ,f2(x) ls 3 ti 'expo'
#p 'ahmad2.dat' u 1:2 lt -1 lw 2 ps 2 ti " , " u 1:3 lt -1 lw 2 ps 2 ti " , f1(x) ls 1 ti
'expo' , f1b(x) ls 2 ti 'gauss',f2(x) ls 3 ti 'expo' , f2b(x) ls 4 ti 'gauss'
print 'fitting parameters for set 2 (exponential)'
print A1(a1),C1(c1),E1(e1)
#print 'fitting parameters for set 2 (gauss)'
#print A1(a1b),C1(c1b),E1(e1b)
print 'fitting parameters for set 3 (exponential)'
print A2(a2),C2(c2),E2(e2)
#print 'fitting parameters for set 3 (gaussian) '
#print A2(a2b),C2(c2b),E2(e2b)


```

Appendix E



<p style="font-size: 8px; margin: 0;">www.hahnenkratt.com Tel.: 07232/3029-0 Fax: 07232/3029-99</p>	ERSTELLT	DATUM	NAME							BENENNUNG: 83102Research - Abutment 5mm - Triflor	
	GEPRÜFT	05.02.10	H. Schepperheyh							Maßstab: 20 : 1	Ermittlungsnorm nach: DIN ISO 2768-fH
Sämtliche Entwürfe, Zeichnungen und Skizzen bleiben unser Eigentum und dürfen ohne unsere schriftliche Genehmigung weder kopiert, noch dritten Personen oder Konkurrenzfirmen vorgelegt oder in irgend einer Weise mitgeteilt werden. §33 des Lit. Um. Ges. u. §17, 18 des Uni. Wettb. Ges.											
C	Blatt 3 mit Kopfkorn angefügt	26.02.10	HS								
B	zusätzliche Verzögerung für CAD-Zwischenprüfung angefügt	26.02.10	HS								
A	hängigkeitsmäßige Verzögerung durch CAD-Zwischenprüfung angefügt	05.02.10	HS								
INDEX	ÄNDERUNG	DATUM	NAME								
										WERKSTOFF: Glasfiber	Bl. 1
											3 Bl.



 www.hahnenkrott.com Tel.: 07232/36229-0 Fax: 07232/36229-99	DATUM 05.02.10	NAME H. Schepperheyh					BENENNUNG: 83102Research - Abutment 5mm - Triflor	Maßstab: 20 : 1 Einzelzeichnungen nach: DIN ISO 2768-fH	Bl. 2
	ERSTELLT 05.02.10	GEFÜHRT 05.02.10	P. Schepperheyh					WERKSTOFF: Glasfaser	3 Bl.
Sämtliche Entwürfe, Zeichnungen und Skizzen bleiben unser Eigentum und dürfen ohne unsere schriftliche Genehmigung weder kopiert, noch dritten Personen oder Konkurrenzfirmen vorgelegt oder in irgend einer Weise mitgeteilt werden. §33 des Lit. Um. Ges. u. §17,18 des Unt. Wettb. Ges.			C Blatt 3 mit Konformitätsgang	28.02.10	HS				
			B alle Änderungen in CAD/PLM-Systemen bestätigt	28.02.10	HS				
			A eingetragene Zeichnung ohne Nachbearbeitung	05.02.10	HS				
	INDEX	ÄNDERUNG	DATUM	NAME					

Appendix F



Primers data sheet

As part of our unique service we provide the primer sequences for our custom real-time PCR kits to help improve the integrity of your research. We support the MIQE guidelines: The MIQE guidelines: minimum information for publication of quantitative real-time PCR experiments. Clin Chem. 2009 Apr;55(4):611-22. Epub 2009 Feb 26. Bustin SA *et al*

Homo sapiens fibronectin 1 (FN1), transcript variant 3, mRNA.

Accession Number	Official gene symbol	Sequence Length
NM_002026	FN1	8,449

Amplicon Details				
Product Length	Tm	Distance from 3' end of sequence	Single Exon	Structure
100	74.5	2681	ND	

Primer Details					
Sense Primer	Position	Tm	GC%	3'dG	Dimer
GAGAACCAAGACTGAGACGAT	5,768	55.4	47.6	-3.5	0
Anti-sense Primer	Position	Tm	GC%	3'dG	Dimer
GCTTCTGACATCTGGCTTGA	5,867	55.9	50	-3.6	0

Further information

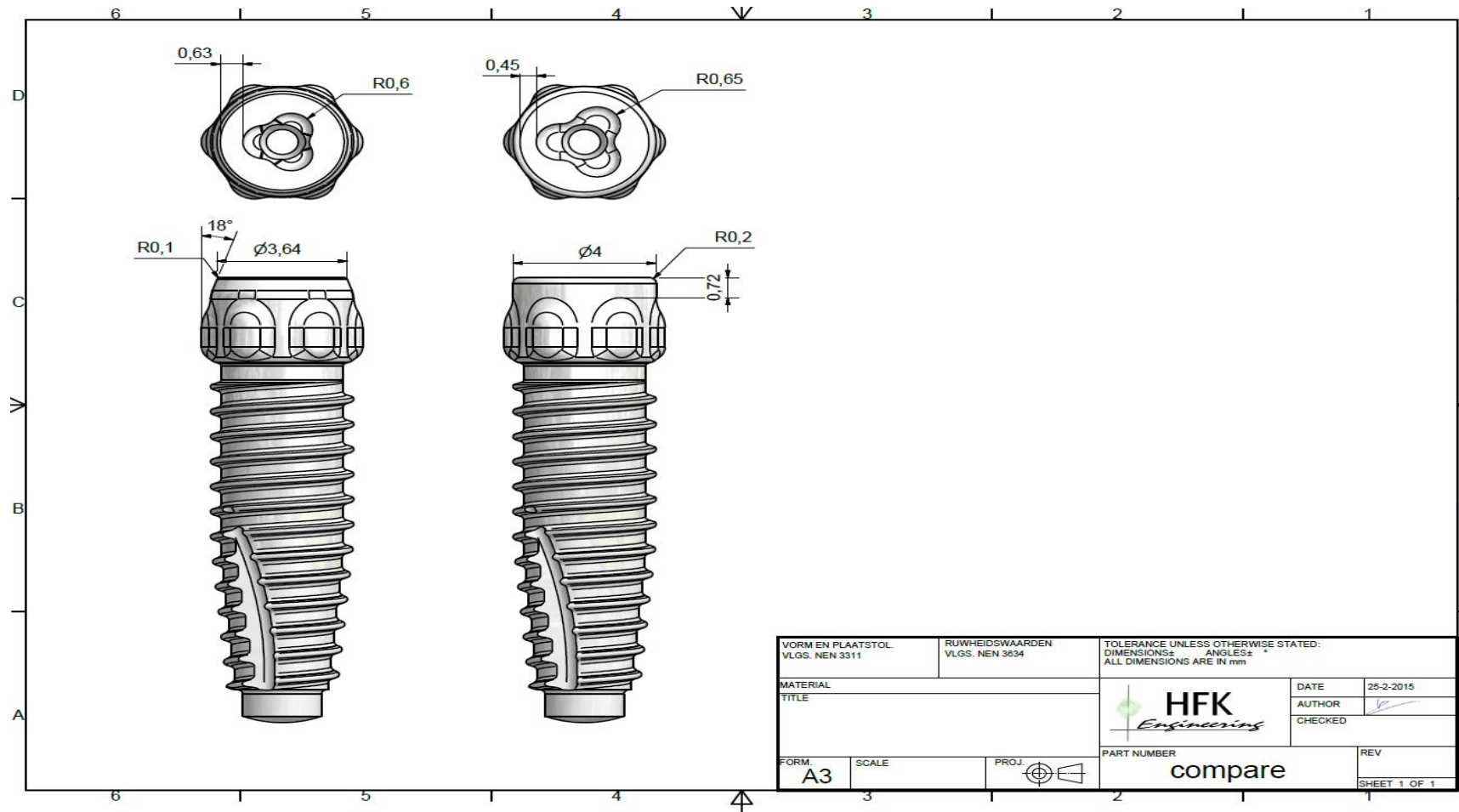
Terms and conditions of use

The use of Primerdesign Custom gene detection kits data sheets is subject to the following terms and conditions:

- 1) Primer sequences may only be stored in the form of this data sheet and not incorporated into any other database.
- 2) Primer sequences may not be displayed on any website or uploaded to any public online database.
- 3) When primer sequences are published in journal articles, Primerdesign Ltd must be cited as the source of the design and gene detection kit in the materials and methods section.
- 4) The primer sequences on this data sheet may not be used to synthesis replacement primers either 'in house' or by ordering them from an alternative supplier.

The primers displayed on this data sheet remain the intellectual property of Primerdesign Ltd and are protected by international copyright laws.
© Primerdesign Ltd 2015

Appendix G



PROPRIETARY AND CONFIDENTIAL. THE INFORMATION CONTAINED IN THIS DRAWING IS THE SOLE PROPERTY OF HFK ENGINEERING. ANY REPRODUCTION IN PART OR AS A WHOLE WITHOUT THE WRITTEN PERMISSION OF HFK ENGINEERING IS PROHIBITED.